Hematite-based epitaxial thin films as photoanodes for solar water splitting

Maxime Rioult

Doctoral thesis in Physics

Maxime Rioult

Hematite-based epitaxial thin films as photoanodes for solar water splitting

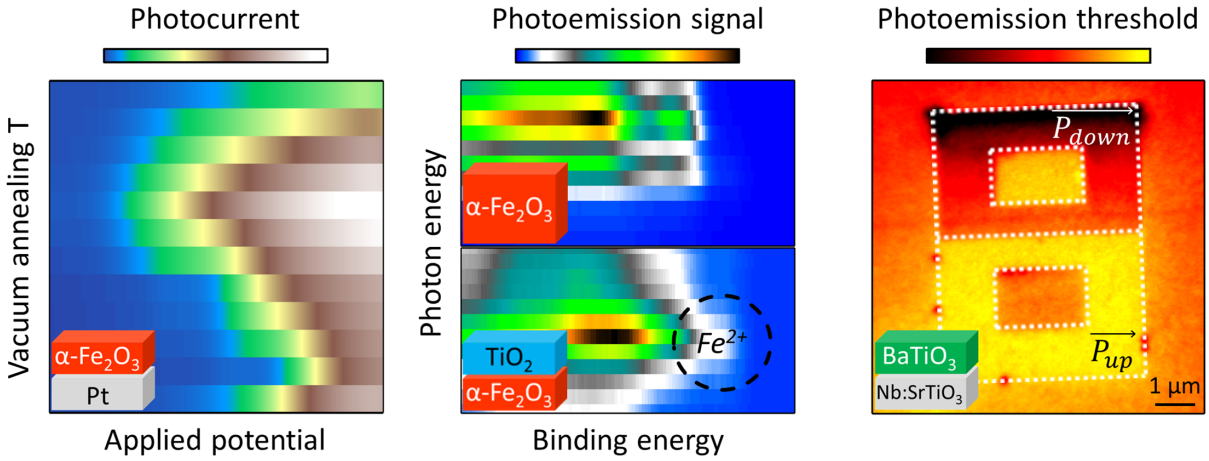

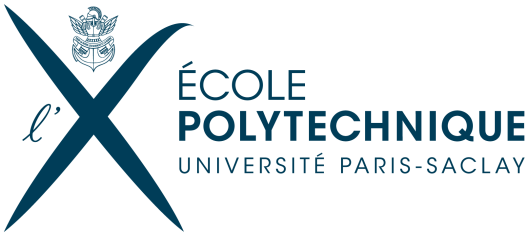

Thèse de doctorat présentée en vue d'obtenir le grade de :

Docteur de l'École Polytechnique

Spécialité : Physique

par Maxime Rioult

Hematite-based epitaxial thin films as photoanodes for solar water splitting

Travail réalisé au Service de Physique de l'État Condensé (SPEC),

CEA-CNRS UMR 3680, CEA-Saclay, Université Paris-Saclay

Soutenue publiquement le 24 septembre 2015 devant le jury composé de :

Dr. Dominique Chandesris	Présidente
Pr. Bruno Domenichini	Rapporteur
Dr. Valérie Keller	Rapporteur
Pr. Pere Roca i Cabarrocas	Examinateur
Dr. Antoine Barbier	Directeur de thèse
Dr. Hélène Magnan	Co-directrice de thèse

"J'investirais bien mon argent dans le soleil et l'énergie solaire. Quelle source d'énergie !
J'espère que nous n'allons pas devoir attendre la fin du pétrole
et du charbon avant de nous y attaquer."
Thomas Edison, 1931.

Remerciements

En premier lieu, je tiens à exprimer ma gratitude à ma co-directrice de thèse et encadrante Hélène Magnan, ainsi qu'à mon directeur de thèse Antoine Barbier. J'espère que nos chemins se croiseront encore pour le meilleur.

Hélène, grâce à toi j'ai pu démarrer mon stage de fin d'études dans l'équipe et continuer en thèse. Je te remercie pour ton accompagnement constant, ton soutien indéfectible, et surtout ta confiance au cours de l'accomplissement de ce travail et plus largement du projet photo-électrolyse.

Antoine, l'évolution du sujet nous a amenés à fusionner deux projets de recherche pour découvrir un nouveau terrain scientifique plein de promesses. Ta présence, notamment au cours des runs synchrotrons où nous avons tant échangé, a pour beaucoup contribué à la réussite de cette thèse.

Je remercie chaleureusement les membres du jury pour leurs remarques et éclaircissements relatifs à ce manuscrit ainsi qu'à la soutenance de thèse : les rapporteurs Bruno Domenichini (ICB - Université de Bourgogne, Dijon) et Valérie Keller (ICPEES, Strasbourg), ainsi que les examinateurs Pere Roca i Cabarrocas (Ecole Polytechnique, Palaiseau) et Dominique Chandesris (LPS - Université Paris-Sud, Orsay, présidente de jury).

Dans le groupe Oxydes, je dois également beaucoup à Dana Stanescu dont le travail sur la MBE, la lithographie, l'AFM/PFM - et j'en passe - a été d'une aide indispensable. Merci également à notre technicien Frédéric Merlet, qui nous a permis de démêler moult situations problématiques, de la maintenance de la MBE-Oxydes à l'impression de posters ...

Au sein de l'IRAMIS du CEA de Saclay (SPEC et NIMBE/LICSEN), je remercie aussi Cindy Rountree, Jean-Baptiste Moussy, Luc Barbier, Myriam Pannetier-Lecoeur, Claude Fermon, Fabien Silly, Renaud Cornut, Dominique Martinotti, Yannick Dappe, Sylvain Latil, Cyrille Barreteau, Daniel Bonamy ; les chefs de service Serge Palacin et François Daviaud. Que ce soit dans le cadre d'expériences, de discussions scientifiques ou d'échange plus informels, vous avez contribué au bon déroulement de cette thèse.

Merci pour son aide au personnel de secrétariat avec qui j'ai interagi, en particulier pour les procédures administratives et l'impression du manuscrit : Christine Prigian, Catherine Julien, Nathalie Royer, Corinne Kopec-Coelho.

Je remercie également les synchrotronistes avec qui j'ai collaboré dans le cadre de ce travail, notamment pendant les runs synchrotron, qui m'ont conforté dans mon envie de travailler dans cet environnement si particulier : à SOLEIL, Rachid Belkhou, Stefan Stanescu, Sufal Swaraj et Adrien Besson de la ligne HERMES, Patrick Le Fèvre de la ligne CASSIOPEE, Emiliano Fonda de la ligne SAMBA, et à DIAMOND, Francesco Maccherozzi de la ligne I-06 (Nanoscience).

Grâce à une ribambelle de jeunes doctorants/post-doctorants/ingénieurs à qui je ne souhaite que le meilleur, mon temps de présence au CEA a été sublimé en une magnifique expérience humaine. Jelle, merci pour nos passionnantes discussions, scientifiques ou parfois un peu "déplacées", qui, sans aucun doute, me manqueront ! Tiphaine, merci pour tous ces moments dans le bus, ces discussions entre un physicien qui fait de la chimie et une chimiste qui fait de la physique. Thomas, j'ai été plus que ravi de t'avoir comme compagnon doctorant, je me rappellerai longtemps de ces moments de détente à échanger sur le sport, les séries, l'actualité, les jeux vidéo, et bien sûr la science ! Romain B., je te souhaite bon courage pour terminer ta thèse ! Merci aussi à Sara, bonne fin de thèse à toi ! Je pense aussi à Sukanya Datta, Romain Lebrun, Lisa Levasseur, Claire Soum, Patrick Hsia, David Peyrot, Jean-Yves Chauleau, Julien Rault, Guillaume Nataf, Cédric Zobrist, Thomas Baubeau, Dongzhe Li, Martin Rudolph, Marina Barlet, Jérémy Hieulle, Jonathan Barès et Parwana Habibi.

J'adresse aussi mes remerciements à la section Basket du CEA de Saclay, dont ce fut un plaisir d'être le responsable. Je ne garde que des bons souvenirs de jeu et d'échanges sur le basket, la thèse ou encore la recherche. J'espère pouvoir continuer autant que faire se peut !

Je remercie également mes parents, mon frère et ma sœur évidemment, Axel, Pierre et les autres Phelma, les agros et les Caennais (qui ne sont plus caennais que d'origine maintenant, ils se reconnaîtront !).

Valentin, si un jour tu lis ceci, sache que sans t'en rendre compte tu as contribué à ta façon au bon déroulement de la fin de cette thèse, en arrivant à me faire décompresser ou à me débloquer pendant la rédaction (à n'importe quelle heure du jour et de la nuit). Merci beaucoup ! Enfin je remercie ma femme Charlène pour son soutien, son aide et ses encouragements des plus constants, grâce auxquels le bonheur tiré cette aventure s'en est vu maximisé.

Contents

1 General introduction **1**

2 Solar water splitting with semiconducting photoanodes **7**
2.1 Solar water splitting systems using photoelectrodes . . . 8
2.2 Semiconductor/electrolyte contact . . . 12
2.2.1 The semiconductor . . . 12
2.2.2 The electrolyte . . . 16
2.2.3 Semiconductor/electrolyte contact in the dark . . . 17
2.2.4 Semiconductor/electrolyte contact upon illumination . . . 21
2.3 n-SC photoanode requirements . . . 22
2.3.1 Stability, low cost and abundance . . . 24
2.3.2 Band positions . . . 24
2.3.3 Light absorption . . . 26
2.3.4 Electron-hole pair recombinations . . . 27
2.4 Strategies to improve metal oxide photoanodes . . . 28
2.4.1 Reducing bulk recombination . . . 29
2.4.2 Improving light absorption . . . 31
2.4.3 Improving surface kinetics . . . 32

3 Experimental techniques **35**
3.1 Thin films preparation . . . 35
3.1.1 Oxygen plasma assisted molecular beam epitaxy (OPA-MBE) . . . 35
3.1.2 Substrates used for thin films deposition . . . 37
3.1.3 UV and laser lithography . . . 38
3.2 Laboratory characterization tools . . . 39
3.2.1 Reflexion high energy electron diffraction (RHEED) . . . 39
3.2.2 X-ray photoelectron spectroscopy (XPS) . . . 42
3.2.3 Atomic and piezoresponse force microscopy (AFM and PFM) . . . 46
3.2.4 Low energy electron microscopy (LEEM) . . . 48
3.3 Synchrotron radiation characterization techniques . . . 49
3.3.1 X-ray absorption spectroscopy (XAS) . . . 49
3.3.2 Extended X-ray absorption fine structure (EXAFS) . . . 51
3.3.3 Resonant photoemission spectroscopy (RPES) . . . 56
3.3.4 X-ray photoemission electron microscopy (X-PEEM) . . . 58
3.4 Photoelectrochemical characterization . . . 60
3.4.1 Experimental setup . . . 61
3.4.2 I-V voltammetry . . . 64
3.4.3 Incident photon to current efficiency (IPCE) . . . 65

3.4.4 Optical chopper + lock-in amplifier (OCLIA) characterization 66

4 Single layers of undoped hematite 69

4.1 Iron oxides films of different structures 71
4.1.1 Presentation of the iron oxides grown by OPA-MBE 71
4.1.2 Growth followed by *in situ* RHEED 73
4.1.3 *In situ* XPS 74
4.1.4 Investigation of the γ*-Fe_2O_3 / Nb:$SrTiO_3$ (001) film structure 75
4.1.5 Photocurrent measurements 79
4.2 Air annealing of Fe_3O_4 films 80
4.2.1 *Ex situ* RHEED 80
4.2.2 *Ex situ* XPS 82
4.2.3 Photocurrent measurements 83
4.3 Hematite films annealed in vacuum 84
4.3.1 *Ex situ* XPS 84
4.3.2 *In situ* EXAFS 85
4.3.3 Photocurrent measurements 91
4.3.4 Discussion 92
4.4 Summary 92

5 Single layers of Ti-doped hematite 95

5.1 Ti-doping and thickness effects on hematite films properties 97
5.1.1 Ti-doped hematite films growth followed by RHEED 97
5.1.2 Crystallographic structure investigation by EXAFS 100
5.1.3 Electronic structure investigation by XPS 102
5.1.4 Electronic structure investigation by RPES 106
5.1.5 Ti-doping effects on the photocurrent 107
5.1.6 Thickness effects on photoelectrochemical properties 108
5.1.7 Discussion 112
5.2 Surface chemical etching 113
5.2.1 Photocurrent 114
5.2.2 AFM 115
5.2.3 X-PEEM 116
5.2.4 Discussion 119
5.3 Summary 120

6 Photoanode heterojunctions 123

6.1 Growth and structure 125
6.1.1 RHEED 125
6.1.2 XPS 127

6.2 Electronic structure investigation by RPES . . . 131
6.2.1 RPES at the Fe L_3 edge . . . 131
6.2.2 RPES at the Ti L_3 edge . . . 133
6.2.3 Discussion about RPES results . . . 136
6.3 Photocurrent measurements . . . 137
6.3.1 Photocurrent under steady white light illumination . . . 137
6.3.2 Photocurrent under monochromatic light . . . 139
6.4 Photocurrent scenarii for the different heterojunctions . . . 146

7 Ferroelectric layers as photocurrent enhancers 149
7.1 Ferroelectricity physics - applications in photovoltaics and photochemistry . 149
7.1.1 Ferroelectricity physics in $BaTiO_3$ . . . 149
7.1.2 Ferroelectricity applications in photovoltaics and photochemistry . . . 153
7.1.3 Our approach . . . 154
7.2 Growth and structure . . . 154
7.2.1 *In situ* RHEED . . . 154
7.2.2 *In situ* XPS . . . 156
7.3 Photoelectrolysis as a function of $BaTiO_3$ internal polarization . . . 157
7.3.1 Mouting and poling procedures . . . 157
7.3.2 Electrochemical poling procedure . . . 159
7.3.3 On-Off current density measurements . . . 161
7.3.4 Effect of EC-poling on the XPS peaks . . . 163
7.4 Piezoresponse Force Microscopy (PFM) . . . 164
7.5 X-PEEM measurements . . . 166
7.5.1 Photoemission threshold KE_0 . . . 168
7.5.2 MEM-LEEM transition Φ_S . . . 169
7.5.3 XAS at the Ba $M_{4,5}$ edge . . . 170
7.5.4 XAS at the Ti $L_{2,3}$ edge . . . 171
7.6 Discussion . . . 172

8 Conclusion and outlook 175

A Appendixes 181
A.1 Estimation of the Xe arc lamp flux . . . 181
A.2 More details about the functioning of a potentiostat . . . 183
A.3 γ^*-Fe_2O_3 photocurrent contribution in γ^*-Fe_2O_3 / Nb:$SrTiO_3$ . . . 184

References 187

1 General introduction

The global energy consumption continuously increases, being directly the consequence of the overall population growth and the need of a social welfare for as many as possible. Currently our annual energy consumption rate is *ca.* 17 TW and is estimated to increase to 30 TW by 2050 [1]. 87% of our energy needs are covered by fossil fuels burning [1]. This share granted to energy vectors detrimental for the global climate change (through the greenhouse effect) and accelerating the resource shortage is completely unbalanced with the available energy mix on Earth (depicted on figure 1.1, data from 2010). Other energy sources have to be considered to fulfil our appetite for energy and to avoid harmful climate changes. Solar energy is expected to provide *ca.* 10,000 times our energy needs [2, 3]. With these considerations, enough solar energy strikes Earth in one hour to meet the actual energy demands for one year. Hence solar energy development appears as one of the most promising solutions toward a sustainable energy consumption and a weaker dependence on fossil fuels. However, sunlight intermittence is a serious impediment to the inclusion of the photovoltaic technology in the electricity network. It imposes a viable solar energy storage solution, since it is highly desirable to synchronize supply with demand.

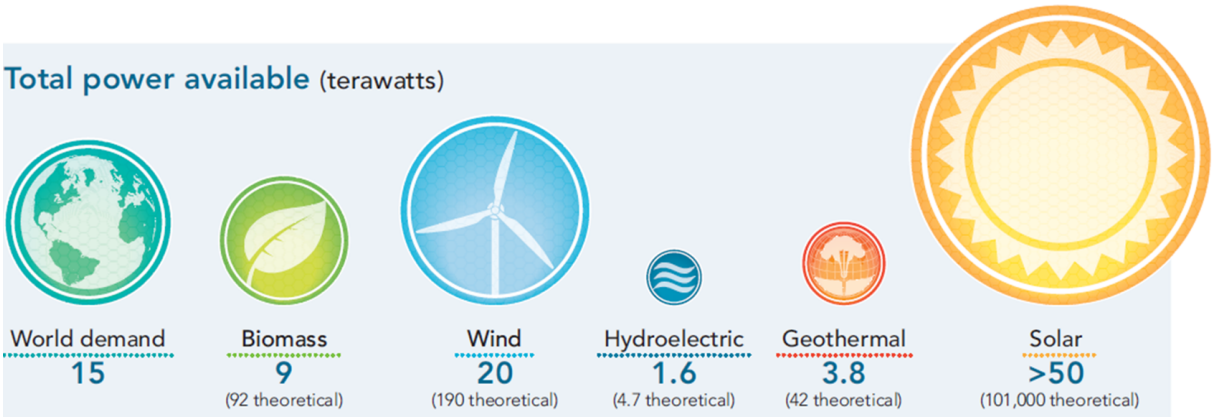

Figure 1.1: Total power available on Earth (in TW). From [2].

Hydrogen has amazing physico-chemical properties that let it appear as the most serious energy vector candidate for solar energy storage and also for an alternative fuel to oil and coal. Hydrogen has the highest specific density (*ca.* 120 MJ/kg) as compared to gasoline (*ca.* 46 MJ/kg) and lithium air batteries (*ca.* 8 MJ/K) [4]. In addition, chemical energy storage has the advantage to decouple the production and consumption sites, whereas electricity transport induces considerable losses and complex distribution and storage infrastructures. Finally, thanks to the long-standing use of hydrogen in the chemical industry, hydrogen storage and transport technologies maturity is ensured.

Fuel cells allow using hydrogen as a clean fuel, only producing water and heat as coproducts, without any greenhouse gas [5]. Hydrogen used in fuel cells has a great potential of scalability, offering a wide range of applications, including the tens of W scale (daily electronic devices), the hundreds of kW scale (vehicles) and the hundreds of MW scale (power plants) [6].

Therefore, more than a solar energy storage solution, hydrogen appears as one of the best alternatives to oil for the transport sector. As a matter of fact, about a quarter of the global CO_2 emissions are due to the transport sector, which relies at 95% on oil as fuel[1]. The commercialization in 2015 of the hydrogen car Mirai by Toyota[2] is a first step toward a hydrogen-based transport sector. By the way the number of orders for this fuel cell vehicle was immediately far above Toyota's expectations[3]. Moreover a substantial number of hydrogen filling stations are already operating all over California and the East Coast in the United States and also in Japan and Europe where enormous efforts are made, especially in United Kingdom and Germany[4]. Lastly, the tremendous benefits of the introduction of hydrogen in the energy market motivated most advanced industrial countries to set up specific roadmaps for hydrogen. We can cite at the European level the HyWays project[5], with a target strategy which started in 2002 and extends into 2050. In particular by 2030, 25 million of fuel cell vehicles are expected in Europe, with an H_2 cost of 3 €/kg and a fuel cell cost of 50 €/kW, which makes the hydrogen solution perfectly competitive for an oil barrel price around 50-60 $. A net employment effect of 200000 to 300000 labour per year has been estimated by 2030 in the HyWays report. This illustrates that hydrogen as a fuel is not any more a dream vision.

However to consider the direct use of hydrogen as a fuel produced from sunlight and water, solar hydrogen production has to be competitive with existing hydrogen production routes.

Hydrogen production presents a major advantage: it can be produced from all energy resources, such as hydrocarbons, biomass, wind and solar energy [7, 8]. This grants an adaptive production relying on the resources available in a given region or country.

Nowadays hydrogen is produced at a rate of *ca.* 50 millions of tons per year. More than 95% of this production depends on the fossil fuels industry (mainly steam methane reforming) [6, 7, 9]. Steam methane reforming is very mature, and its low cost *ca.* 1-2 $/kg of H_2 dominates any other hydrogen production method [10, 11]. However the carbon impact is tremendous: for one ton of H_2 produced from hydrocarbons, 2.5 tons of CO_2 are released in the atmosphere [4]. Hydrogen is also produced by water electrolysis, where electricity is

[1] http://www.airliquide.com/en/hydrogen-a-vector-of-clean-energy.html
[2] http://www.toyota.com/mirai/fcv.html.
[3] http://urlz.fr/2aR1
[4] See www.h2stations.org for the location of hydrogen filling stations worldwide.
[5] http://www.hyways.de/

used in electrolysers to split water in hydrogen and oxygen (water splitting). Nonetheless to produce the same amount of hydrogen, water electrolysis requires 5 times more input energy than steam reforming [4], and this energy may originate from fossil fuels. However it is an elegant way to store the intermittent photovoltaic electricity.

An economy based on hydrogen as clean fuel should consistently rely on clean hydrogen production methods to become sustainable in the long term. Figure 1.2 gives examples of carbon-free hydrogen production paths [6]. The direct solar-to-hydrogen conversion through solar water splitting in hydrogen and oxygen, named as a "Holy Grail in chemistry" by Bard in 1995 [12, 13], appears to be the most seductive idea considering that:

- solar energy has the highest share in the energy mix offered by Earth (*cf.* figure 1.1);
- it allows chemical solar energy storage, with all the benefits described earlier;
- intermediate losses are limited (direct conversion);
- it limits to the minimum the amount of used resources.

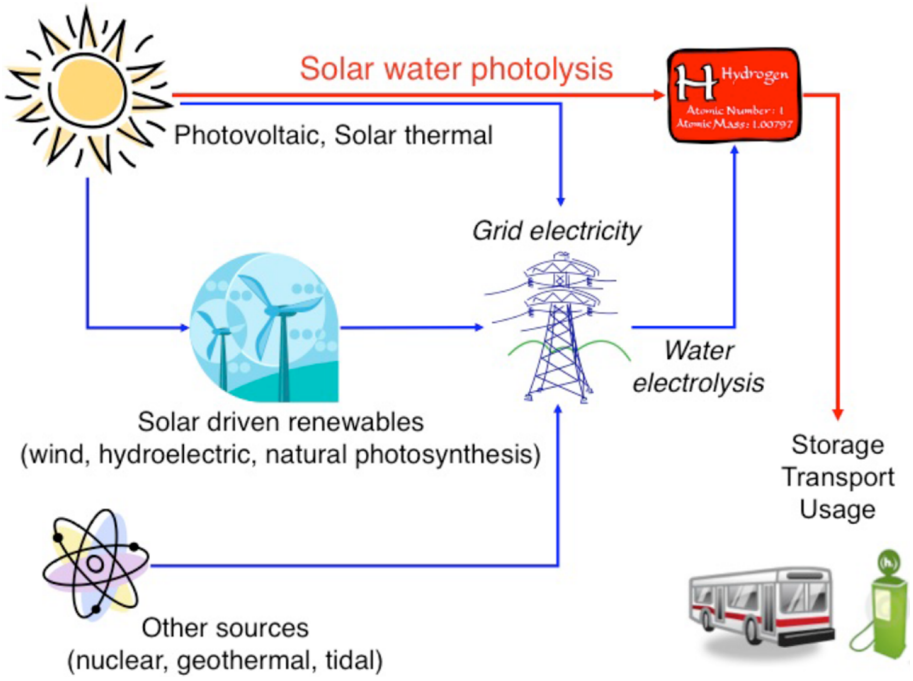

Figure 1.2: Carbon-free hydrogen production paths. From [6].

A first route so realize solar water splitting is to couple a solar cell and a conventional electrolyser. This perspective can be encouraging considering the maturity of the photovoltaic industry and of the electrolysis technology. However a device using a solar cell and an electrolyser with up-to-date efficiencies of 15 % and 85 % respectively is limited to a

solar-to-hydrogen efficiency of 13% and the hydrogen production cost can be estimated to 4-10 $/kg of H_2 [9, 10]. This is way higher that what is currently achieved through steam reforming. Moreover the separation of the solar energy harvesting and water oxido-reduction parts increases the overall complexity of the device and hence its cost.

Another way, inspired by natural photosynthesis, is water photoelectrolysis where hydrogen and oxygen are produced directly at a semiconductor/water interface, without intermediates, in systems called photoelectrochemical cells [14] (direct solar water splitting). During the process, electron-hole pairs are generated upon solar light absorption in a semiconducting photoelectrode. These charges are subsequently used to promote the oxido-reduction reactions of water at the semiconductor surface. In 1972, direct solar water splitting has been demonstrated by the pioneering study of Fujishima and Honda where titanium dioxide TiO_2 was used as photoactive semiconductor [15]. As a matter of fact 40 years later, no single material able to directly split water into oxygen and hydrogen at its surface without external assistance has been found. Indeed the material requirements are very challenging. Splitting the problem into two parts facilitates the approach. Dedicating the semiconductor to either water oxidation or water reduction lowers the specifications, since the material has to meet the requirements only for water oxidation or water reduction. In this case, water is oxidized in O_2 at one photoelectrode (the photoanode) and is reduced in H_2 at another photoelectrode (the photocathode). This allows a wider choice of materials and architectures and a possibly lower cost.

Transition metals oxide semiconductors like α-Fe_2O_3 (hematite) or TiO_2 are the most interesting materials to be considered as photoanodes in terms of stability, availability, low cost and band structure. Indeed, these materials are among the most stable in aqueous environments in oxidation conditions and are abundant on Earth [1], meeting the low cost criterion as well. This makes them perfect in a environment-friendly approach. Concerning hematite, its greatest asset is its band gap of *ca.* 2 eV, allowing it to absorb 40 % of the solar spectrum, which is quasi optimal for direct solar water splitting applications [5]. Indeed such a band gap is predicted to give a solar-to-hydrogen efficiency of 17 % [16].This places hematite among the top candidates for solar water splitting. Better competitiveness with the steam methane reforming can be found by using this kind of stable and low cost materials, which could drop the hydrogen production cost down to 1.6-2 $/kg H_2 [9, 10]. As it was reported recently by Protti et al., it should also be noted that a significant number of patents concerning direct solar water splitting are granted since 1980 [17], showing that this hydrogen production method is getting closer to the market.

Our approach at the Service de Physique de l'Etat Condensé (SPEC) consists in the elaboration of nanometric single crystalline thin films based on hematite, in order to focus on the fundamental understanding of the involved mechanisms determining the photoelectrochemical properties of hematite-based photoanodes (water oxidation, oxygen production). In addition, for metal oxides (and especially hematite) the short collection length of photogenerated charges limits the effective thickness of the material to tens of nm, imposing nanometric geometries to avoid material waste [18]. Our films are deposited by oxygen plasma assisted molecular beam epitaxy (OPA-MBE), which makes possible the elaboration of highly controlled systems (dopants concentration, crystallographic structure) suitable for model studies. The use of high-end characterization techniques, in particular using a synchrotron radiation light source, makes possible the determination of the relevant physical parameters affecting the photoelectrochemical properties. In addition, a photoelectrochemical characterization setup was developed throughout the project, allowing the correlation between physical and water splitting properties on the very same sample.

This work is divided in seven chapters. In chapter 2, the basic concepts of solar water splitting with semiconducting photoanodes are presented (systems and physics), as well as the latest developments concerning the different strategies to improve the photoelectrochemical properties of metal oxide photoanodes. Chapter 3 presents the experimental techniques used for the elaboration and characterization of our thin films (OPA-MBE, laboratory and synchrotron characterization techniques, photoelectrochemical characterization setup). Chapters 4 to 7 contain the contribution of this PhD to the research effort in the field of hematite-based photoanodes. Chapter 4 presents results about undoped iron oxides thin films, where we benefited from the versatility of the OPA-MBE technique to investigate the effects of the crystallographic structure and oxygen stoichiometry. In Chapter 5 we study the effects of Ti-doping on the hematite properties (crystallographic and electronic structures, photoelectrochemical and electronic properties), unravelling the intimate crystallographic structure of Ti-doped hematite and demonstrating the existence of an optimal doping level and an increase of the charges diffusion length inducing a high photocurrent gain. In addition the effect of a surface chemical treatment with HCl is studied, enabling a further improvement of the water splitting performances of Ti-doped hematite. Chapter 6 is dedicated to Ti-doped α-Fe_2O_3 - TiO_2 heterojunctions, where the electronic structure and the surface recombination dynamics are characterized, highlighting concomitant effects due to heterostructuting. In chapter 7, we show results concerning ferroelectric films of $BaTiO_3$, which are foreseen to act on hematite water splitting performances through the internal electric polarization. A first step concerning the understanding of the relation between photocurrent and ferroelectric polarization is made. Lastly, chapter 8 provides a general conclusion and presents some open new perspectives.

2 Solar water splitting with semiconducting photoanodes

Water splitting (or water electrolysis) is an oxido-reduction reaction where water molecules are split into gaseous oxygen and hydrogen. More precisely water, which is amphoteric, is oxidized to O_2 and reduced to H_2 according to equation 2.1:

$$H_2O \rightarrow H_2 + \frac{1}{2}O_2 \tag{2.1}$$

The two corresponding half reactions are the oxidation of the O_2/OH^- couple and the reduction of the H_2O/H_2 couple according to (in basic environments, pH $>$ 7):

$$\begin{cases} 4OH^- \rightarrow 2H_2O + O_2 + 4e^- \\ 4H_2O + 4e^- \rightarrow 4OH^- + 2H_2 \end{cases} \tag{2.2}$$

Their sum gives equation 2.1 and the overall process to produce one molecule of O_2 and two molecules of H_2 involves 4 electrons. Water splitting is realized in systems called electrochemical cells, containing an aqueous solution (called the electrolyte) and two electrodes where the water oxidation and reduction reactions occur. The electrode where water is oxidized is called the anode and the electrode where water is reduced is called the cathode. In addition a reference electrode is used in order to have a potential reference.

The water splitting reaction has a Gibbs free energy of change of + 237.2 kJ (endoenergetic), which is equivalent to a minimum required potential of 1.23 V [5]. This value is given by the difference between the energy levels of the water oxidation and reduction reactions. Therefore, input energy is needed to yield oxygen and hydrogen from water. Oxido-reduction (redox) reactions involve the exchange of electronic charges (electrons). The concept of solar water splitting is to provide these charges by using solar energy through the creation of electron-hole pairs by illumination of semiconductors: an electron of the valence band is promoted to an energy state in the conduction band, leaving an electron vacancy (hole) in the valence band. The charges created by illumination can subsequently be used to realize water oxidation at the anode and water reduction at the cathode (equation 2.2).

The first section of this chapter (2.1) presents a quick overview of the existing solar water splitting systems. Since my work is in the framework of semiconducting anodes (photoanodes) based on metal oxides and in particular hematite, the physics of the semiconductor/electrolyte interface in this context is of top interest. This will be discussed in section 2.2. In the light of this, section 2.3 gives the requirements for metal oxide photoanodes. The strategies developed to improve the photoanodes performances are presented section 2.4.

2.1 Solar water splitting systems using photoelectrodes

Solar water splitting using photoelectrodes is realized in systems called photoelectrochemical cells. The term "photoelectrode" designates the complete architecture of a photoactive electrode. O_2 evolution will involve an electron (e^-) transfer from the electrolyte to the photoelectrode (*i.e.* a hole (h^+) transfer from the photoelectrode to the electrolyte), whereas H_2 evolution will involve an electron transfer from the photoelectrode to the electrolyte. A photoelectrode can be composed of:

- a conductive substrate on which the photoactive material(s) will be assembled;
- a semiconducting material which furnishes the charges for water oxido-reduction. It is often referred to as photocatalyst, since it catalyses water oxidation or reduction through light absorption;
- a cocatalyst, which has no photoactivity but is a catalyst for water oxidation or reduction reactions (it helps to reduce the amount of required input energy);
- a surface coating (or layer) which acts as a reaction kinetics enhancer or as a passivation layer to protect the photoelectrode (against corrosion for instance if it is not stable in aqueous environments).

A photoelectrode rarely includes all these components at once, in general studies focus on one or two components, without incorporating the others (or without modifying them).

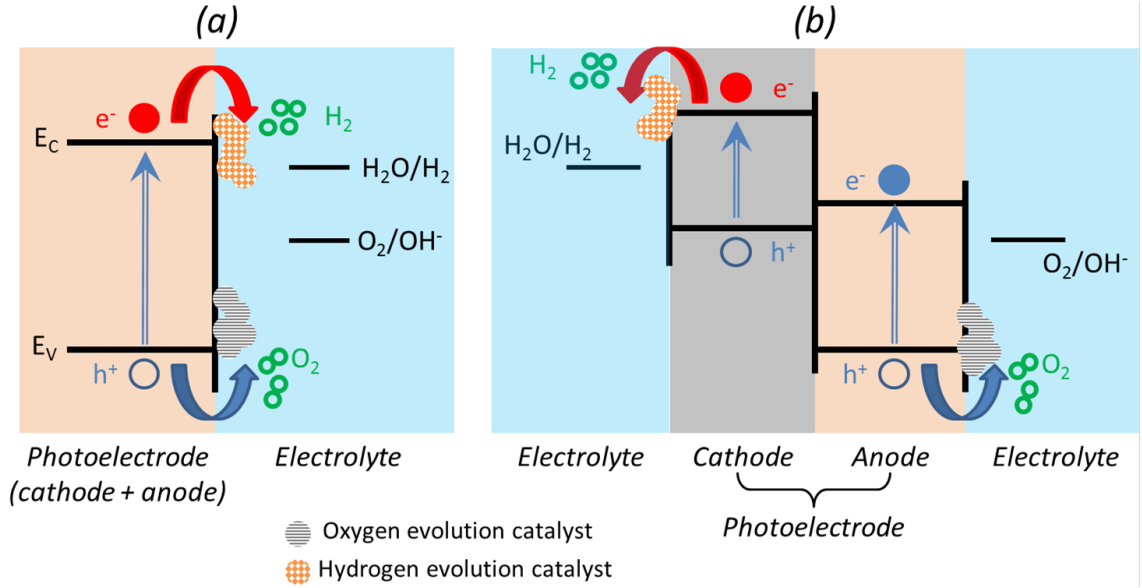

Figure 2.1: Illustrative band diagram of a solar water splitting system with a single semiconductor realizing both water oxidation and reduction (a) at the same location or (b) at different sides, using cocatalysts. E_V and E_C stand for the top of the valence band and the bottom of the conduction band of the semiconductor, respectively. The substrate is not shown.

Figure 2.1 shows solar water splitting systems using an ideal single photoelectrode which can realize water oxidation and water reduction. Here the creation of an electron-hole pair is depicted, as well as the transfer of the photogenerated charges to the electrolyte and evolving H_2 and O_2 gases. Cocatalysts for water oxidation and reduction are also represented. The configuration shown on figure 2.1.a uses a single semiconductor able to directly split water at its surface. This is usually realized with photocatalyst particles dispersed in an electrolyte. Lu et al. reported unassisted water splitting under visible light using nanometric particles of a solid solution of mixed zinc and gallium oxides [19], featuring a solar-to-hydrogen efficiency of *ca.* 2.5% at a wavelength of 440 nm.

The configuration shown on figure 2.1.b uses a single photoelectrode where hydrogen is evolved on one side and oxygen is evolved on the other side. An example of such an architecture has been reported by the group of Prof. Nocera in 2011 [20, 21], under the name of "artificial leaf" (*cf.* figure 2.2). The photoelectrode is not a single material, but consists in a triple silicon junction solar cell combined with cocatalysts for both hydrogen and oxygen evolution (*cf.* figure 2.2.c). The reported solar-to-hydrogen efficiency was 2.5 %.

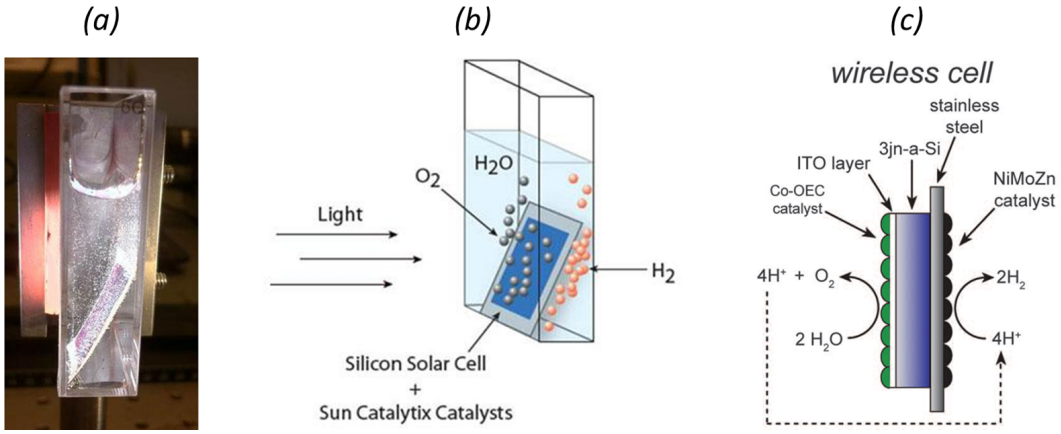

Figure 2.2: The "artificial leaf". (a) functioning artificial leaf, evolving hydrogen and oxygen upon illumination without additional external input energy. (b) illustration of the device (c) detail of the artificial leaf architecture. From [20, 21].

However solar water splitting with a single photoelectrode remains extremely challenging because the system has to fulfil the requirements for both water oxidation (which will be detailed later in this chapter, *cf.* 2.3) and reduction. Hence the price of the system is very high, and the reported efficiencies remain low. In addition, the oxygen and hydrogen production sites are not separated, which requires an additional system to separate the gases (*e.g.* membranes) [22]. This not only represents a safety issue, but also increases the energy cost of the systems and lowers its efficiency [5].

Another type of system, often referred to as tandem systems [11], consists in combining several systems together to realize solar water splitting, like solar cells and cocatalysts materials. Ager et al. published very recently a review about tandem systems featuring spontaneous solar water splitting [23]. In particular they presented a state-of-the-art chart, shown on figure 2.3, providing the solar-to-hydrogen efficiency as a function of the year since 1976. We can cite Luo et al. who reported in 2014 the use of a low cost system made of two metallic electrodes coated with a cocatalyst able to catalyse both water oxidation and reduction, the photogenerated charges being supplied by two perovskite solar cells (one for each metallic electrode) [24]. They reported a solar-to-hydrogen efficiency of 12.3 %.

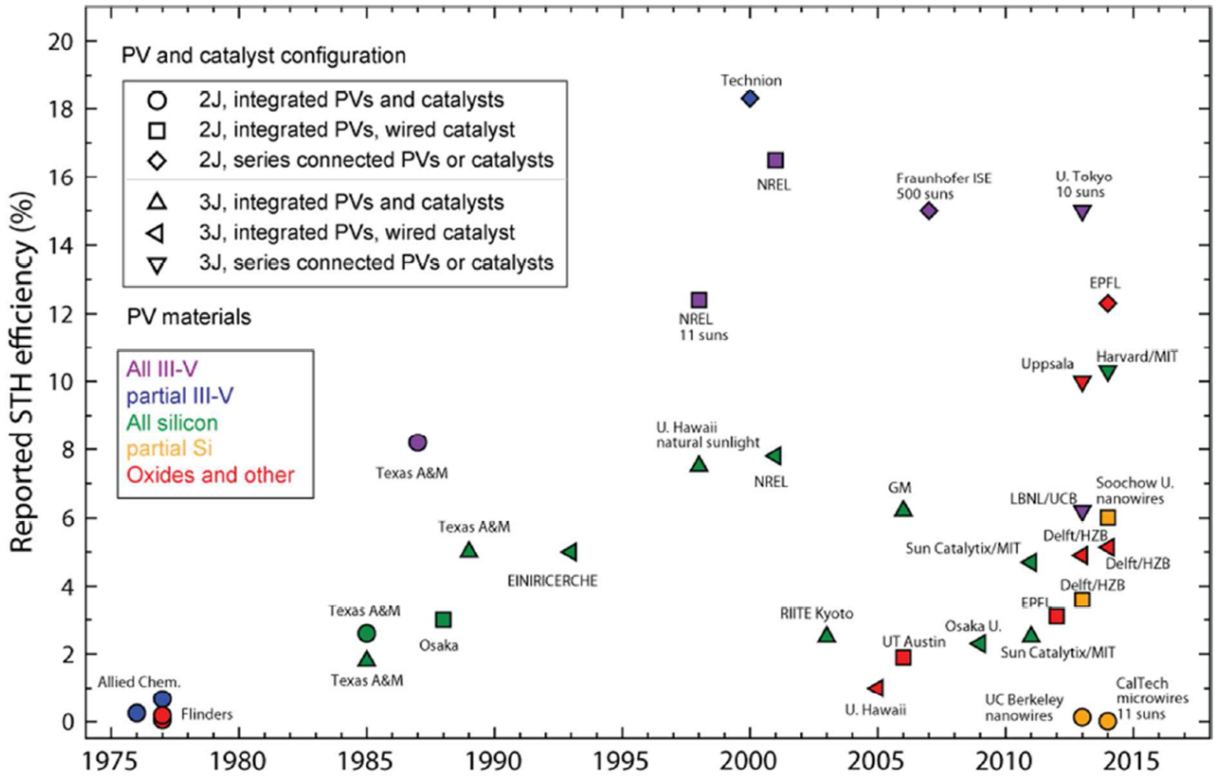

Figure 2.3: Reported solar-to-hydrogen (STH) conversion efficiencies as a function of year and sorted by the number of photovoltaic junctions used in tandem (2 or 3). The degree of integration of photovoltaic and catalyst elements is also indicated (PV and catalyst configuration box). The fill colour represents the semiconductor materials used in the photovoltaic portion of the device (PV materials box). From [23].

Another example of interest is the use of two photoelectrodes (figure 2.4.a): one for water oxidation (photoanode) and one for water reduction (photocathode). O_2 evolution will involve an electron transfer from the electrolyte to the photoanode (*i.e.* a hole transfer from the photoanode to the electrolyte), whereas H_2 evolution will involve an electron transfer from the photocathode to the electrolyte. An external circuit closes the current loop. This

lowers the specifications for both photoelectrodes, which only have to meet the requirements for water oxidation or water reduction respectively. This allows a wider choice of materials and architectures, hence a lower cost. Moreover the oxygen production can be spatially separated from the hydrogen production, allowing a built-in separation of the produced gases.

Extra input energy may be required to drive the charges transfer from the photoelectrodes to the electrolyte. It can be furnished through the application of an external bias (figure 2.4.b) by a generator or a solar cell (in the external circuit or directly assembled with the photoelectrodes).

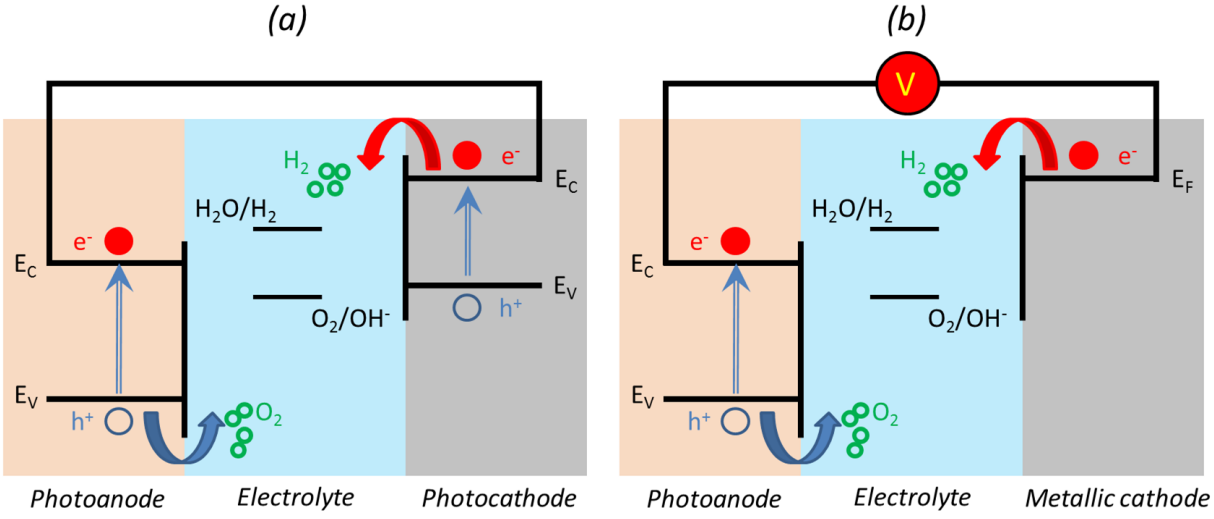

Figure 2.4: Illustrative band diagram of: (a) solar water splitting system using a photoanode and a photocathode and (b) dual-electrode solar water splitting system using a photoanode, a metallic cathode, and an external bias to assist the reaction. The substrates are not shown.

In the following, we will focus on the solar water splitting system illustrated on figure 2.4.b (photoanode + metallic cathode) where the eventual external bias is applied by an external power supply unit.

2.2 Semiconductor/electrolyte contact

In this section the physics of the contact between a semiconductor and an electrolyte are presented through the building of band diagrams [5, 6, 8, 25–28].

2.2.1 The semiconductor

2.2.1.a Energy bands in solids

For an isolated atom ($n_{at} = 1$ on figure 2.5), the energy states occupied by electrons are discrete and defined by quantum mechanics. The electron energy axis is usually reported *vs.* the absolute vacuum scale (AVS). The Pauli's exclusion principle prevents two electrons to have the same energy state. If two identical atoms assemble together ($n_{at} = 2$ on figure 2.5), a given energy level will split into two discrete energy levels so that the Pauli's exclusion principle is fulfilled. When the number of identical atoms further increases ($n_{at} = 4$ on figure 2.5), the energy levels continue to split and are more and more close to each other. For a large number of identical atoms (*e.g.* in solids, $n_{at} >> 1$ on figure 2.5), a group of authorized energy levels can be associated to a continuous energy band. Two energy bands are separated from each other by a forbidden band, also called band gap.

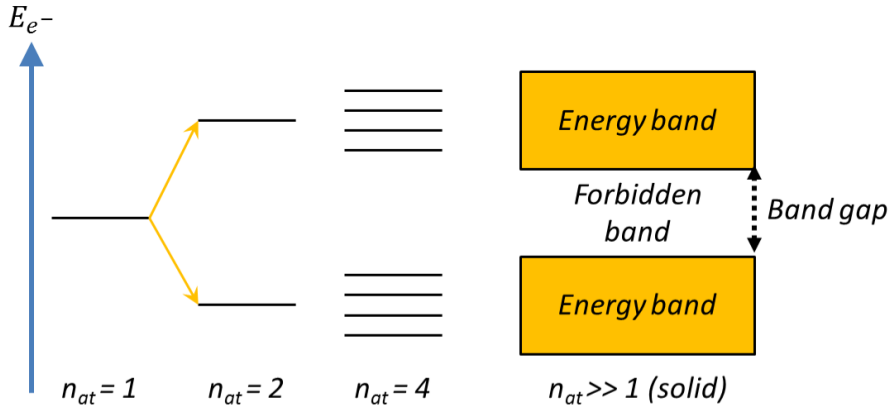

Figure 2.5: Electron energy level splitting upon assembly of n atoms.

In terms of energy, the highest occupied band is called the valence band (VB) and the lowest unoccupied one is called the conduction band (CB). The band gap between the VB and the CB is noted E_g. The conductivity of a material is highly related to the density of electrons in the conduction band: the more electrons in the conduction band, the more conductive the material is. If the VB and the CB overlap (figure 2.6.a), which is the case for metals, a high number of electrons are in the conduction band, which explains why metals are conductive. In insulators, E_g is large (typically higher than 5 eV) so that the VB and the CB are well apart (figure 2.6.b). Therefore no electron is present in the conduction

band. When the VB and the CB are separated by a smaller band gap, typically between 0.5 and 4 eV, some electrons from the VB may be promoted in the CB (leaving an electron vacancy (hole) in the VB), leading to some conduction (figure 2.6.c). These materials are called semiconductors.

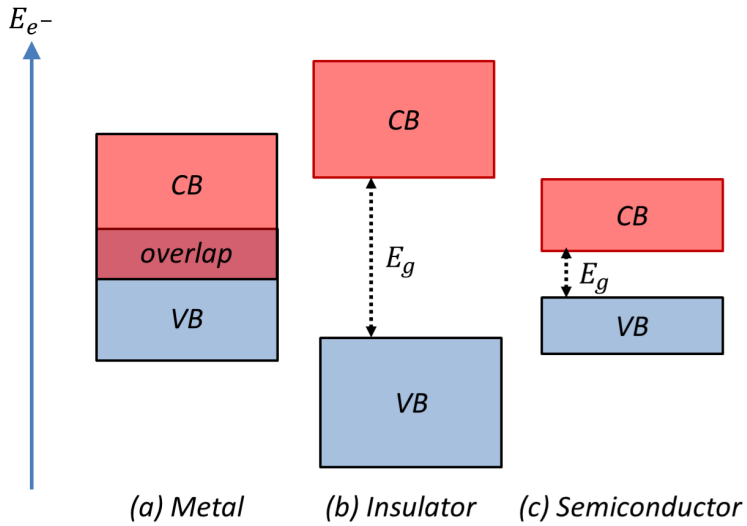

Figure 2.6: Valence band (VB) and conduction band (CB) relative positions for (a) a metal, (b) an insulator and (c) a semiconductor.

2.2.1.b Intrinsic semiconductors

The densities of electrons in the CB (n) and holes in the VB (p) (carriers densities) are basic properties of semiconductors (for intrinsic semiconductors, $n = p$). They are given by [28]:

$$n = \int_{E_{C,bot}}^{E_{C,top}} D_C(E) \times f(E) \times dE \; ; \; p = \int_{E_{V,bot}}^{E_{V,top}} D_V(E) \times (1 - f(E)) \times dE \tag{2.3}$$

Where $D_C(E)$ is the density of states at the energy E in the CB, $D_V(E)$ is the density of states at the energy E in the VB, $E_{C,bot}$ and $E_{C,top}$ are the positions of the bottom and top of the CB, $E_{V,bot}$ and $E_{V,top}$ are the positions of the bottom and top of the VB and $f(E)$ is the probability to find an electron having an energy of E. Accordingly, the probability of finding a hole (*i.e.* no electrons) at an energy of E is $1 - f(E)$. $E_{C,bot}$ and $E_{V,top}$ will be referred as E_C and E_V in the rest of the manuscript. $f(E)$ is given by the Fermi-Dirac statistics according to [28]:

$$f(E) = \frac{1}{1 + \exp\left(\frac{(E - E_F)}{k_B T}\right)} \tag{2.4}$$

Where E_F is the Fermi level and k_B is the Boltzmann constant. E_F is defined as the energy level with a probability of occupation of 0.5 and corresponds to the chemical potential of electrons in the solid. In semiconductors and insulators the Fermi level of electrons is located within the band gap. For the Boltzmann statistics case, *i.e.* if E_F lies several $k_B T$ below E_C and several $k_B T$ above E_V ($E_C - E_F \gg k_B T$ and $E_F - E_V \gg k_B T$, for non degenerated semiconductors) and considering the density of states given by the free electron gas model (Jellium model) [28], equation 2.3 becomes:

$$n = N_C \exp\left(-\frac{(E_C - E_F)}{k_B T}\right) \;;\; p = N_V \exp\left(-\frac{(E_F - E_V)}{k_B T}\right) \tag{2.5}$$

Where N_C and N_V are the effective densities of states in the CB and in the VB respectively. Equation 2.5 allows determining the position of the Fermi level within the band gap if the electrons and hole densities are known, according to:

$$E_F = E_C - k_B T \ln\left(\frac{N_C}{n}\right) = E_V + k_B T \ln\left(\frac{N_V}{p}\right) \tag{2.6}$$

In addition, it is worth noting that the product $n \times p$ is constant:

$$n \times p = N_C N_V \exp\left(-\frac{E_g}{k_B T}\right) \tag{2.7}$$

Equation 2.7 can be understood as a law of mass action, so that an increase in n implies a decrease in p and reciprocally. This is analogous to the self ionization of water where in pure water some hydroxide ions (OH^-) and protons (H_3O^+) are present for which $[OH^-] \times [H_3O^+] = 10^{-14}$ mole per litre and $[OH^-] = [H_3O^+]$. Thus the protons concentration in "intrinsic" water is 10^{-7} mole per litre, which corresponds to a pH of 7 (pure water).

The Fermi level position within the band gap for intrinsic semiconductors (E_{Fi}) can be obtained from equation 2.6 with $n = p = n_i$ and is given by:

$$E_{Fi} = \frac{E_C + E_V}{2} + \frac{k_B T}{2} \ln\left(\frac{N_V}{N_C}\right) \tag{2.8}$$

At room temperature, $k_B T$ is *ca.* 26 meV, which is negligible with respect to usual E_g values for semiconductors (> 1 eV). Hence $E_{Fi} \approx \frac{E_C + E_V}{2}$, which leads to an E_{Fi} position at the middle of the band gap. In this case, the intrinsic carrier density and can then be

obtained from equations 2.6 and 2.7:

$$\begin{aligned} n_i &= N_C \exp\left(-\frac{(E_C - E_{Fi})}{k_B T}\right) \\ &= N_V \exp\left(-\frac{(E_{Fi} - E_V)}{k_B T}\right) \\ &= \sqrt{N_C N_V} \exp\left(-\frac{E_g}{2k_B T}\right) \end{aligned} \tag{2.9}$$

2.2.1.c Doped semiconductors

Intrinsic semiconductors can be doped so that their electron (or hole) density is increased, leading thus to a conductivity increase. The conductivity type (by electrons, n-type, or holes, p-type) can be tuned by doping. Dopants increasing the electron density are called (electron) donors (D) and arise n-type doping of the semiconductor which is then labelled as n-type semiconductor (n-SC). Dopants increasing the hole density are called (electron) acceptors (A) and arise p-type doping of the semiconductor which is then labelled as p-type semiconductor (p-SC).

A dopant breaks the lattice symmetry, which can create a discrete energy level within the band gap. A donor level should be 2 - 3 $k_B T$ below E_C so that thermal agitation at room temperature allows the ionization of the dopant (promotion of one or several electrons in the conduction band). An acceptor level should be 2 - 3 $k_B T$ above E_V so that thermal agitation at room temperature allows the ionization of the dopant (promotion of one or several electrons from the valence band to the acceptor level, *i.e.* creation of holes in the valence band). The dopant concentration (called doping level) is noted N_D for the donors and N_A for the acceptors and corresponds to the added electron (or hole) density by doping. The doped semiconductor is therefore labelled as n-type or p-type semiconductor.

With the assumption that all dopants are ionized at room temperature, the electron density in an n-SC semiconductor can then be written as:

$$n = n_i + N_D \tag{2.10}$$

For large doping levels (with respect to the intrinsic carrier concentration), we obtain $n \approx N_D$. The use of equations 2.6 and 2.9 allows determining the Fermi level (E_F) position within the band gap by:

$$E_F = E_C - k_B T \ln\left(\frac{N_C}{N_D}\right) \Longleftrightarrow E_F = E_{Fi} + k_B T \ln\left(\frac{N_D}{n_i}\right) \tag{2.11}$$

Accordingly for a p-SC with the analogous assumptions we obtain:

$$p = p_i + N_A \approx N_A \tag{2.12}$$

$$E_F = E_V + k_B T \ln\left(\frac{N_V}{N_A}\right) \Longleftrightarrow E_F = E_{Fi} - k_B T \ln\left(\frac{N_A}{n_i}\right) \tag{2.13}$$

Therefore, the higher n-doped a SC is, the closer to the CB E_F is. Reciprocally, the higher p-doped a SC is, the closer to the VB E_F is, as it is illustrated on figure 2.7.

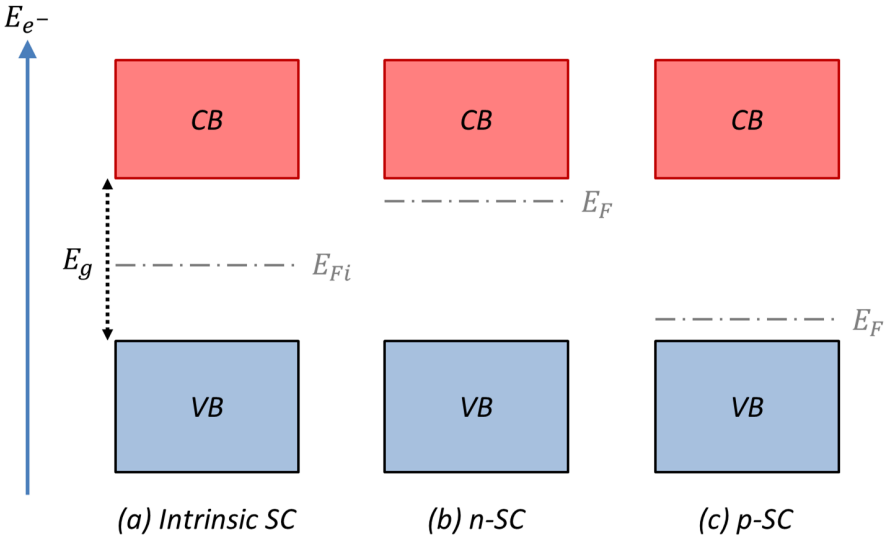

Figure 2.7: Illustrated scheme showing the Fermi level position within the band gap in the case of (a) intrinsic, (b) n-type and (c) p-type semiconductor.

2.2.2 The electrolyte

In ionic solutions, the analogue of the Fermi level in solids is referred to as the electrochemical potential E_{redox}. It depends on the energy levels of the present redox couples. In an electrolyte containing a single redox couple involving a single electron process, the position of the redox couple is given by the Nernst relation [26]. The electrolyte we used during the present work was sodium hydroxide (NaOH) with a concentration of 0.1 mole per litre (noted 0.1 M, corresponding to a pH of 13). In our case, since the objective is to realize the water oxidation at the semiconductor / electrolyte interface, the relevant redox couple is O_2/OH^- [29]. The water oxidation reaction being a multi-electron process, the exact position of the redox level is tricky to calculate, however considering the high $[OH^-]$ concentration in NaOH 0.1 M, we can assume that the redox level is located very close to the O_2/OH^- energy level [26].

Electrochemical potentials are usually reported on a potential scale *vs.* the standard hydrogen electrode potential corresponding to the chemical reaction $2H^+ + 2e^- \rightarrow H_2$. It is the "zero volt" reference in electrochemistry. The practical realization of this electrode is called the normal hydrogen electrode (NHE). Its potential *vs.* the absolute vacuum scale (used in the solid state physics community) is -4.5 eV [8]. In our case we used Ag/AgCl reference electrodes (V *vs.* Ag/AgCl = + 0.197V *vs.* NHE), therefore we have:

$$\begin{aligned} V_{vs.\,Ag/AgCl} &= V_{vs.\,NHE} + 0.197 \\ &= V_{vs.\,vacuum} - 4.5 + 0.197 \\ &= V_{vs.\,vacuum} - 4.303 \end{aligned} \tag{2.14}$$

2.2.3 Semiconductor/electrolyte contact in the dark

When an n-type semiconductor (n-SC) is brought in contact with an electrolyte, electron transfers will occur at the n-SC / electrolyte interface until the electrochemical potentials (or Fermi levels) of the electrons within the semiconductor and within the electrolyte are equal [25]. Hereafter we will speak indifferently of electrochemical potential and Fermi level. Usually, the Fermi level of the conventional n-SC used as photoanodes is higher than the redox level of an electrolyte having a basic pH [5, 8, 25, 29]. Then to reach the thermodynamic equilibrium, electrons from the semiconductor will be transferred to the electrolyte. On the electrolyte side, a charge layer called the Helmholtz layer is formed. It consists of a continuous dense layer of anions, which balances the induced excess positive charges at the surface of the semiconductor [6].

Upon Fermi levels equalization, a zone depleted in electrons will arise close to the surface of the n-SC (with respect to the bulk): this zone is called the space charge layer. The extent of this space charge layer in the semiconductor is noted w. The electron depletion within this space charge layer induces a positive potential difference between the bulk and the surface of the semiconductor. This potential gradient $\overrightarrow{gradV}$ bends the energy bands upward at the surface with respect to the bulk. The associated electric field $\overrightarrow{E} = -\overrightarrow{gradV}$ points towards the semiconductor surface. Because of the associated electric force $\overrightarrow{F} = -e \times \overrightarrow{E}$ (where $e = 1.6\times10^{-19}$ C is the elementary charge), any electron (e^-) within the space charge layer is driven toward the volume of the n-SC. Analogously, any hole (h^+) within the space charge layer is driven toward the semiconductor / electrolyte interface. The interface behaves like a Schottky contact (semiconductor/metal). This is illustrated by figure 2.8:

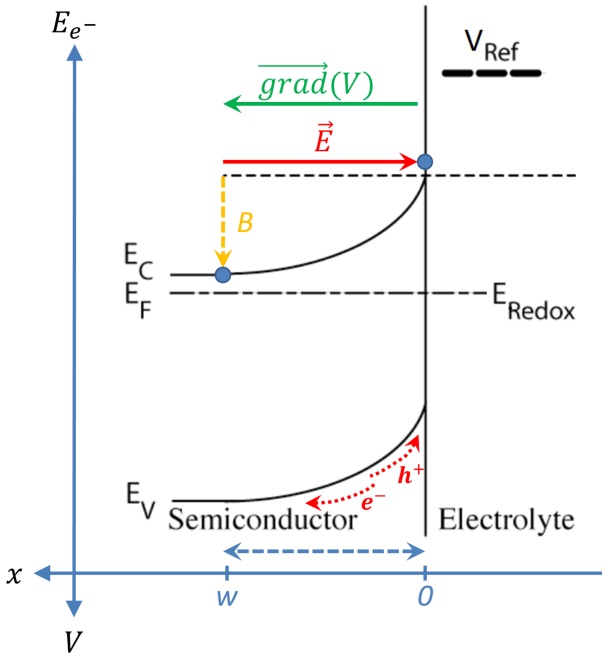

Figure 2.8: n-SC / electrolyte contact in the dark. Reproduced from [8].

As it was explained in 2.1, the water oxidation reaction involves a hole transfer from the photoanode to the electrolyte. The upward band bending in an n-SC in contact with an electrolyte facilitates this hole transfer, showing that n-SCs are suitable as photoanodes. Analogously the water reduction reaction involves an electron transfer from the photocathode to the electrolyte. The downward band bending in a p-SC in contact with an electrolyte facilitates this electron transfer, showing that p-SCs are suitable as photocathodes.

The value of the band bending is noted B on figure 2.8. It is equal to the Fermi levels difference between the semiconductor and the electrolyte before the contact. For an n-SC, upward band bending can be reduced through the application of a potential on the semiconductor inducing an increase of E_F with respect to E_{redox} (cathodic potential, forward biased junction) [27], as it can be seen on figure 2.9.c below. The potential for which the bands are unbent is called the flat band potential and is noted V_{fb}. This potential is always measured *vs.* a potential reference (*e.g.* a reference electrode).

The potential profile $V(x)$ as a function of the distance x from the surface is of importance. It can be derived by solving the Maxwell-Gauss equation in one dimension in the n-SC:

$$div(\vec{E}) = \frac{dE}{dx} = \frac{\rho(x)}{\varepsilon_r \varepsilon_0} \tag{2.15}$$

Where ε_r is the relative permittivity (or dielectric constant) of the n-SC and ε_0 is the vacuum permittivity and $\rho(x)$ is the volumetric charge density. Ionized donors are positive fixed charges (they furnished extra conduction electrons to the material) whereas acceptors are negative fixed charges (they seized conduction electrons from the material). For a n-SC $\rho(x) = e \times (p_i + N_D - n_i - N_A) \approx eN_D$. Since $\overrightarrow{E} = -\overrightarrow{grad}V$, equation 2.15 becomes the Poisson's equation:

$$\frac{d^2V}{dx^2} = -\frac{eN_D(x)}{\varepsilon_r\varepsilon_0} \tag{2.16}$$

If N_D is uniform within the whole space charge layer, the resolution of equation 2.16 is simplified. We chose the following conventions and boundary conditions:

- $x = 0$ at the surface, $x = \infty$ for the bulk of the material;
- $V(\infty) = 0$ (the potential reference is taken with respect to the unbent situation in the bulk), so that $V(0) = -B$;
- $\frac{dV}{dx}(x \geq w) = 0$ (flat band conditions beyond the space charge layer).

The potential profile $V(x)$ as a function of the distance x from the surface is then described by:

$$V(x) = -\frac{eN_D}{2\varepsilon_r\varepsilon_0}(x - w)^2 \tag{2.17}$$

The length of the space charge layer w is then given by $V(0) = -B$:

$$w = \sqrt{\frac{2\varepsilon_r\varepsilon_0|-B|}{eN_D}} \tag{2.18}$$

The space charge layer behaves like a capacitance C, which is given by:

$$C = \frac{\varepsilon_r\varepsilon_0 A}{w} = \sqrt{\frac{eN_D\varepsilon_r\varepsilon_0 A^2}{2|-B|}} \tag{2.19}$$

Where A is the contact area between the n-SC and the electrolyte.

Let us now consider the situation where a potential V_{bias} is applied on the n-SC. By convention, an applied potential inducing an increase of E_F with respect to E_{redox} is positive and said anodic, whereas an applied potential inducing an increase of E_F with respect to E_{redox} is negative and said cathodic. The boundary condition for the potential at the surface ($x = 0$) is modified so that $V(0) = -(B + V_{bias})$. Therefore equation 2.18 becomes:

$$w = \sqrt{\frac{2\varepsilon_r\varepsilon_0|-(B+V_{bias})|}{eN_D}} \tag{2.20}$$

We can then calculate the flat band potential V_{fb} by considering the case where bands are redressed or when $w \to 0$, giving $V_{fb} = -B$. We can then write the expressions of w and C as a function of the applied potential V_{bias} (noted V for simplicity) and the flat band potential (expressions valid whatever the potential reference):

$$w(V) = \sqrt{\frac{2\varepsilon_r\varepsilon_0}{eN_D}|V - V_{fb}|} \tag{2.21}$$

$$C(V) = \sqrt{\frac{eN_D\varepsilon_r\varepsilon_0 A^2}{2|V - V_{fb}|}} \tag{2.22}$$

The effect of an applied potential on the band bending is illustrated on figure 2.9. An anodic bias (reverse biased junction) decreases E_F with respect to E_{redox}. This increases the band bending (and w), which intensifies the electron depletion (*i.e.* hole accumulation) at the n-SC / electrolyte interface [27] (figure 2.9.b). The reversed phenomena occur in the case of a cathodic bias (figure 2.9.c).

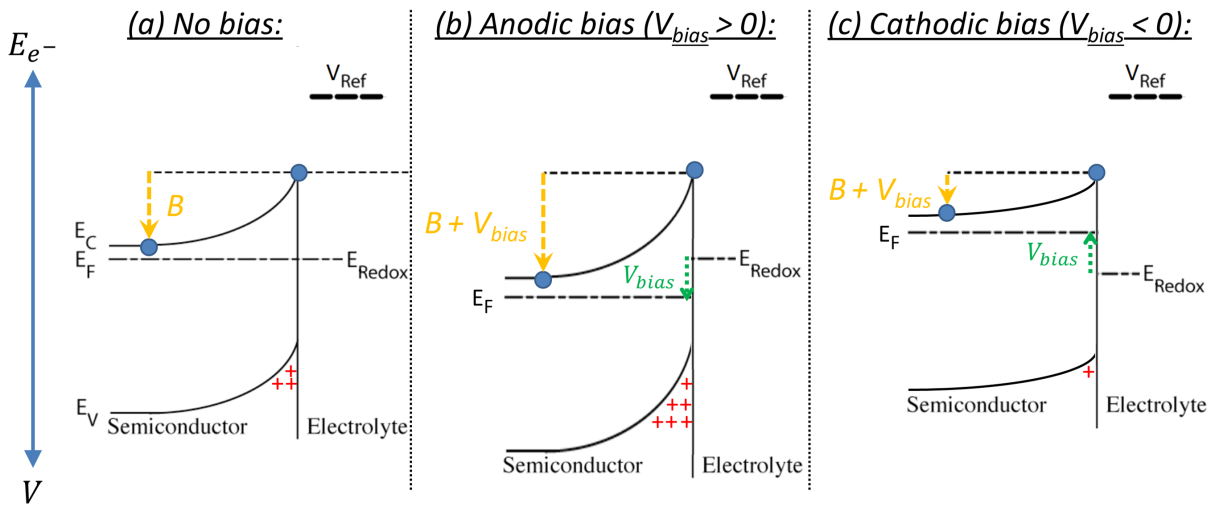

Figure 2.9: Band diagram for an n-SC / electrolyte interface (a) with no bias and upon the application of (b) an anodic bias (decrease of E_F with respect to E_{redox}) or (c) a cathodic bias (increase of E_F with respect to E_{redox}). Reproduced from [8].

Equation 2.22 can also be written to obtain the Mott-Schottky equation:

$$\frac{A^2}{C^2}(V) = \frac{2}{eN_D\varepsilon_r\varepsilon_0} \times (V - V_{fb}) \tag{2.23}$$

Here the calculations assume a uniform charge density within the depletion layer in the n-SC. A more realistic model modifies the Mott-Schottky equation as follows [28]:

$$\frac{A^2}{C^2}(V) = \frac{2}{eN_D\varepsilon_r\varepsilon_0} \times \left(V - V_{fb} - \frac{k_BT}{e}\right) \tag{2.24}$$

Mott-Schottky plots ($\frac{A^2}{C^2} = f(V)$) are often used to determine V_{fb} and N_D [30], which are respectively given by the x-intercept at y = 0 and by the slope of the Mott-Schottky plot, if ε_r is known.

2.2.4 Semiconductor/electrolyte contact upon illumination

When photons of an energy higher than E_g are absorbed by the semiconductor, electron-hole pairs are created. The basic phenomenon can be described as follows: an electron from the valence band is promoted to an energy state in the conduction band, leaving an electron vacancy (hole) in the valence band. If no electric field is present to drive the spatial separation of the electron and the hole, the electron-hole pair will recombine, meaning that the electron will take back an energy state in the valence band. A usual assumption, which we will make here, consists in considering that any electron-hole pair created outside of the space charge layer, *i.e.* where flat-band conditions are met, will recombine instantaneously (no electric field drives the separation of the photogenerated carriers). The creation of electron-hole pairs increases the electron and hole densities by the same quantity (carrier injection), noted n^* and p^* ($n^* = p^*$). This can be seen as semiconductor photoconductivity or "photodoping". Because of the break of equilibrium by illumination, the Fermi level is no more equal for electrons and holes and splits into two quasi Fermi levels: $E_{F,n}$ for the electrons and $E_{F,p}$ for the holes. They are given by equation 2.25 (analogous to equation 2.11) [28]:

$$\begin{cases} E_{F,n} = E_F + k_BT \times \ln\left(\dfrac{n_i + N_D + n^*}{n_i}\right) \approx E_F + k_BT \times \ln\left(\dfrac{N_D}{n_i}\right) \\ E_{F,p} = E_F - k_BT \times \ln\left(\dfrac{p_i + N_A + p^*}{n_i}\right) \approx E_F - k_BT \times \ln\left(\dfrac{p_i + p^*}{n_i}\right) \end{cases} \tag{2.25}$$

Indeed for an n-SC in low-injection conditions, $n^* = p^* \approx n_i$, hence $n^* \ll N_D$ and $p^* \gg N_A$. Therefore the quasi Fermi level of electrons remains constant or barely increases with respect to the Fermi level in the dark. However the quasi Fermi level of holes strongly decreases with respect to the Fermi level in the dark. As a consequence upon illumination of an n-SC, the reorganization of charges concentration is mainly due to the change in holes density [8]. The slight increase of the electrons Fermi level will induce a reduction of the band bending with respect to the dark conditions [25]. The value of the band bending reduction is

the photovoltage V_{ph} and is given by the difference between the quasi Fermi level of electrons and the redox level of the electrolyte [8, 25, 31]. It is also referred to as the open circuit potential of the n-SC / electrolyte junction under illumination.

The n-SC / electrolyte interface band diagram upon illumination is drawn on figure 2.10:

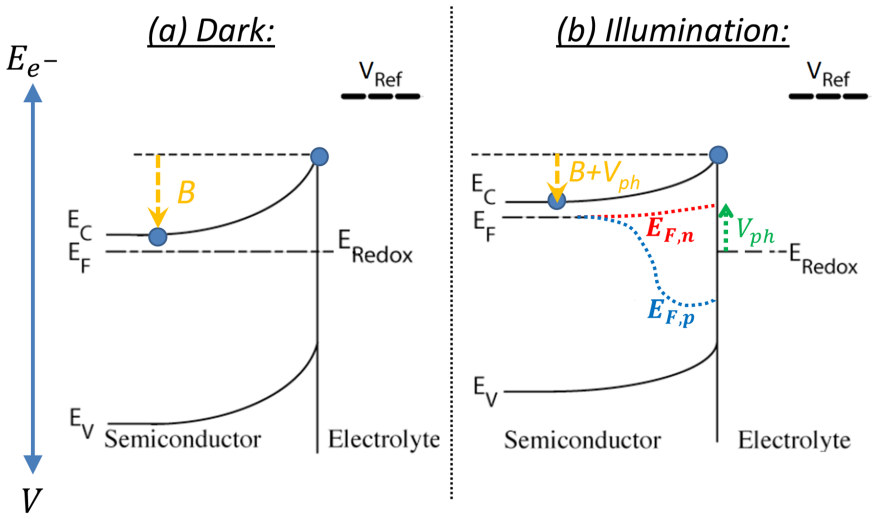

Figure 2.10: n-SC / electrolyte interface band diagram (a) in dark conditions and (b) upon illumination. Reproduced from [8].

In addition (*cf.* 2.2.3), applying an anodic bias will facilitate the separation of photogenerated electron-hole pairs through the increase of the band bending and also drive more efficiently the accumulation of holes at the n-SC / electrolyte interface to realize water oxidation (O_2 evolution).

The quasi Fermi level of holes corresponds (roughly) to the oxidizing power of holes [6]: the more negative $E_{F,p}$, the higher the oxidizing power of holes, which is crucial for water splitting photoanodes. On figure 2.10.b it can be seen that thanks to illumination the quasi Fermi level of holes is more negative than the redox level of the electrolyte, favouring thermodynamically the transfer of photogenerated holes from the semiconductor to the electrolyte, which was not the case in dark conditions. Photoanodes (and more generally photoelectrochemical cells) are based on this photoactivation of chemical reactions.

2.3 n-SC photoanode requirements

To characterize the performances of a solar water splitting device, one can measure the (photo)current flowing between the anode and the cathode, which is expected to be directly the image of the water oxido-reduction. It is also possible to measure directly the amount of produced H_2 and O_2 by mass spectrometry or gas chromatography. This can be a difficult

task because the photoelectrochemical cell needs to be sealed extremely properly to enable accurate quantification and high photocurrent is required [16].

In this section we will focus on systems where water oxidation is realized at a n-type photoanode, and water reduction at a metallic cathode. An external bias may be required to assist water electrolysis (*i.e.* to obtain a substantial photocurrent). The band diagram of the system is shown on figure 2.10:

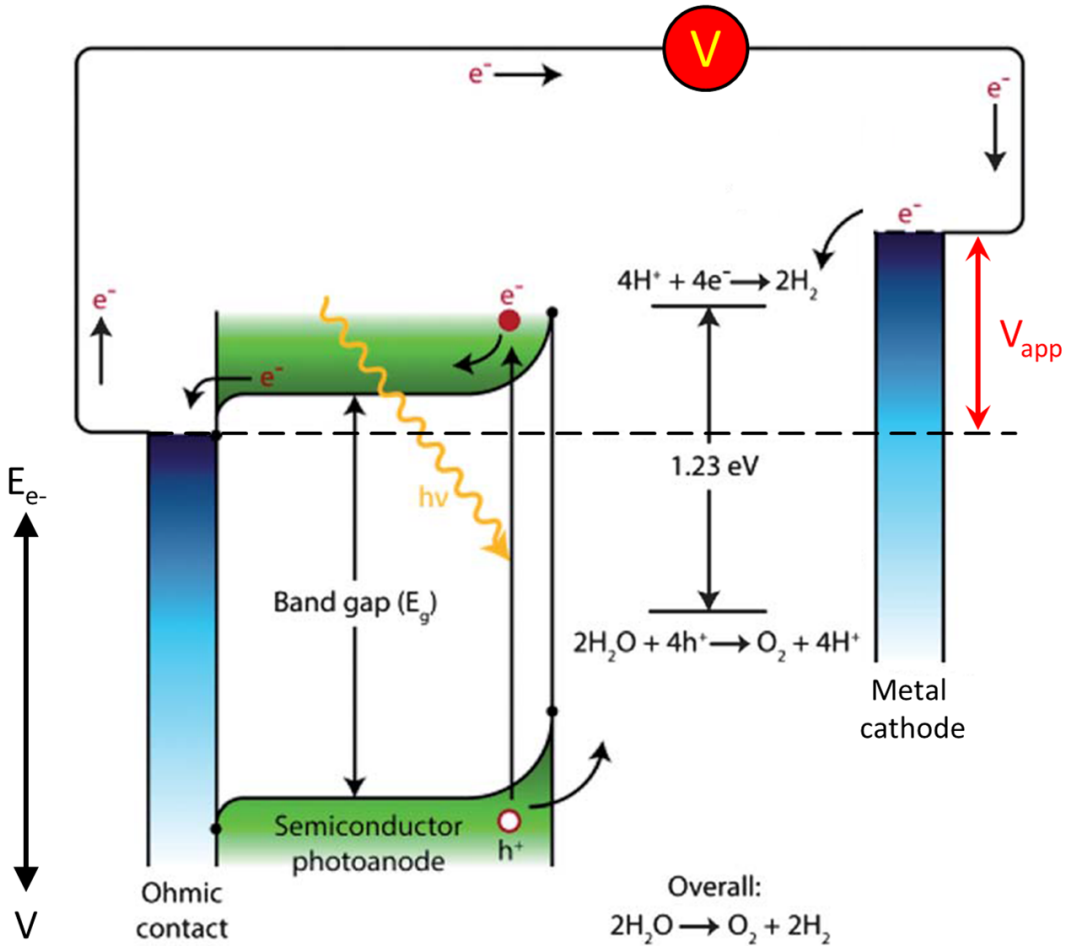

Figure 2.11: Schematic band diagram of a solar water splitting consisting of a semiconductor photoanode, a metallic cathode and an external circuit providing an anodic bias V_{app} to assist water oxido-reduction. Reproduced from [9].

n-type photoanodes for solar water splitting should meet the following requirements, developed in the next subsections:

- stability in aqueous environments (oxidation conditions), low cost and material abundance (2.3.1);
- band positions straddling the water oxidation and reduction potentials (2.3.2);

– strong (visible) light absorption (2.3.3);

– efficient charge transport and weak electron-hole pairs recombination rate (2.3.4).

2.3.1 Stability, low cost and abundance

First of all, an obvious criterion for the choice of n-type photoanodes is the stability of materials against (photo)corrosion in aqueous environments, in oxidation conditions. Non-oxide semiconductors may either decompose or form an oxide surface layer which can be tremendous for the charge transfer to the electrolyte [5]. For instance, a silicon surface will oxidize to form an insulating SiO_2 native oxide. On the contrary, most metal oxides are stable in aqueous solutions under oxidation conditions. For instance, TiO_2 and Fe_2O_3 are usually cited as very stable [32], whereas ZnO always decomposes in aqueous environments [5]. Stability issues may be solved using a protective layer, but the latter will influence the photoelectrochemical properties. In addition to this, the stability of the gas production is highly desirable in order to design long-term functioning solar water splitting devices. To be competitive against usual hydrogen production methods in terms of cost, the lifetime of solar water splitting systems should be in the order of magnitude of 10 years [9, 10].

Secondly, in the framework of sustainable development and resource shortage, the choice of resource critical and expensive materials is unsuited. Materials to be considered should meet the entangled low cost and abundance criteria. Metal oxides have the advantage to meet these requirements together with a good stability in aqueous environments.

2.3.2 Band positions

Water oxidation realized by the transfer of a hole from the photoanode to the electrolyte will occur only if the quasi Fermi level of holes is below the energy level of the O_2 / OH^- reaction, so that the transfer is thermodynamically favourable. This imposes the top of the valence band E_V to be below the O_2 / OH^- energy level (which is necessary but may not be sufficient). Kinetic overpotentials and thermodynamic losses also have to be taken into account [29], which imposes an even lower valence band minimum position. It should be noted that the overpotential necessary for water oxidation is *ca.* 0.4V whereas the one necessary for water reduction is *ca.* 0.05 eV [8]. Then driving efficiently water oxidation appears as a strong challenge, and explains why the use of cocatalysts, expected to reduce the kinetic overpotentials, is a widely explored route.

The electrons photogenerated in the photoanode upon light absorption are transferred to the metallic cathode through the external circuit. Water reduction realized by the transfer of an electron from the metallic cathode to the electrolyte will occur only if the electron energy is higher than the energy level of the H_2O / H_2 reaction, so that the transfer is thermodynamically favoured. This condition can be fulfilled by applying an external anodic bias using a solar cell or (like in our case) a potential generator. Indeed applying an anodic

bias will lower the Fermi level of the n-SC whereas the Fermi level of the metallic cathode will be increased. A sufficient anodic bias will bring the metallic cathode Fermi level above the H_2O / H_2 level, favouring the water reduction reaction. Alternatively the metallic cathode could be replaced by a photocathode having the bottom of the conduction band E_C above the H_2O / H_2 energy level.

VB and CB edges for various semiconductors in contact with an aqueous basic electrolyte (pH = 14) are shown on figure 2.12 [5]:

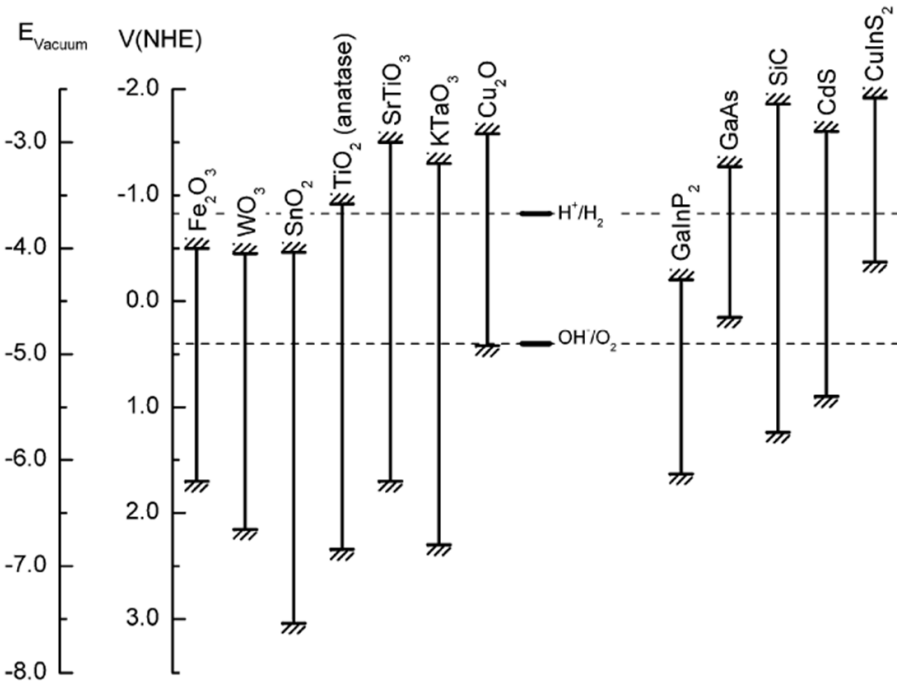

Figure 2.12: VB and CB edges for various semiconductors in contact with an aqueous basic electrolyte (pH = 14). Reproduced from [5].

Metal oxide semiconductors (left panel on figure 2.12) are mainly n-type, which is due to a slight oxygen deficiency acting as donor doping. We can see from figure 2.12 that their VB energy level is usually well below the O_2 / OH^- energy level, which will favour the water oxidation reaction. Such materials can be used as photoanodes. The E_C value for TiO_2, $SrTiO_3$ or $KTaO_3$ is above the H_2O / H_2 energy level, making these materials usable as photocathodes as well. However their large band gap limits their photoconversion efficiency to a few % only [29].

2.3.3 Light absorption

In order to create electron-hole pairs, the semiconductor has to absorb photons in the useful energy range (solar spectrum). To do so, the energy of the photons has to be at least equal to the band gap (E_g). Moreover, E_g has to be greater than 1.23 eV which is the minimum energy required to split water. Taking into account water splitting kinetic overpotentials and thermodynamic losses, it was reported that the optimal band gap should lie between 1.9 et 3.1 eV, with an optimal value *ca.* 2 eV [5, 29]. A semiconductor with such a band gap would absorb photons with wavelengths below 620 nm and ideally features a solar-to-hydrogen efficiency of 16.8 % [5]. Figure 2.13.a shows the AM 1.5 solar spectrum (in temperated zones, taking into account atmosphere absorptions). The band gap constraint limits the efficiency in solar water splitting. A way to tackle this issue can be to use multiple band gap systems in tandem configuration [11, 33]. If these systems show high efficiencies, their potential in scale-up and industrialization may be weak (*e.g.* III-V multijunctions). We can see on figure 2.13.b that hematite (alpha Fe_2O_3), considering a band gap of 2.15 eV, can reach a theoretical solar-to-hydrogen efficiency of *ca.* 15%, which makes it a serious candidate as metal oxide n-type photoanode.

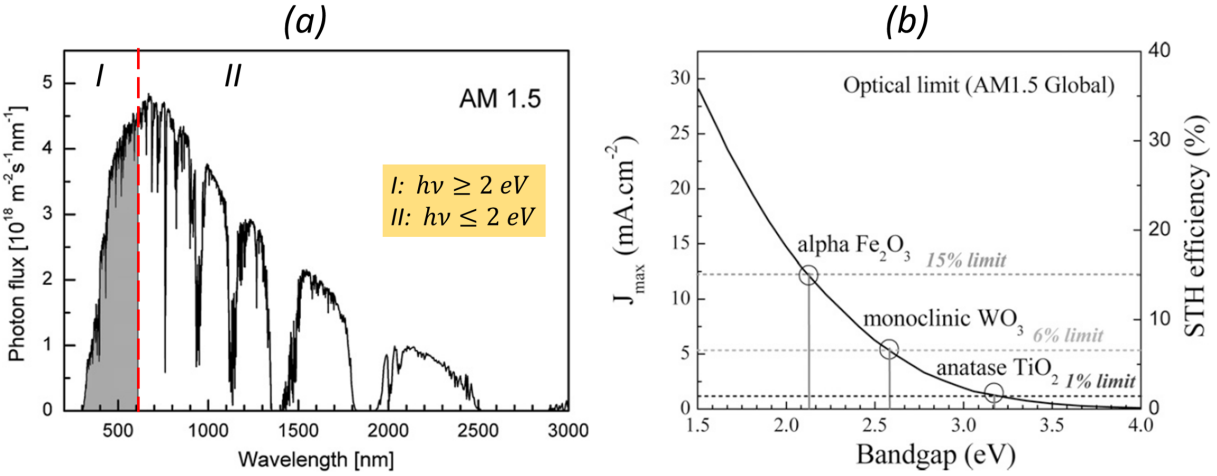

Figure 2.13: (a) AM 1.5 solar spectrum. Zone I (II) corresponds to the part of the solar spectrum absorbed by a semiconductor having a gap superior (inferior) to 2 eV. The energy / wavelength equivalence is given by $E = hc/\lambda$. Reproduced from [5]. (b) Theoretical maximum photocurrent and solar-to-hydrogen (STH) efficiency *vs.* band gap. From [16].

2.3.4 Electron-hole pair recombinations

When an electron (of an electron-hole pair) promoted in the conduction band takes back an energy state in the valence band, it is the recombination of the electron-hole pair. It is a net loss in the charge carrier density, which implies a net loss in the photocurrent, limiting strongly the water splitting efficiency. A lot of effort is made in order to reduce the charges losses due to recombination.

When an n-SC is in contact with an electrolyte, electron-hole pairs recombinations can occur within the bulk of the n-SC, within the space charge layer, or at its surface. This is illustrated on figure 2.14.

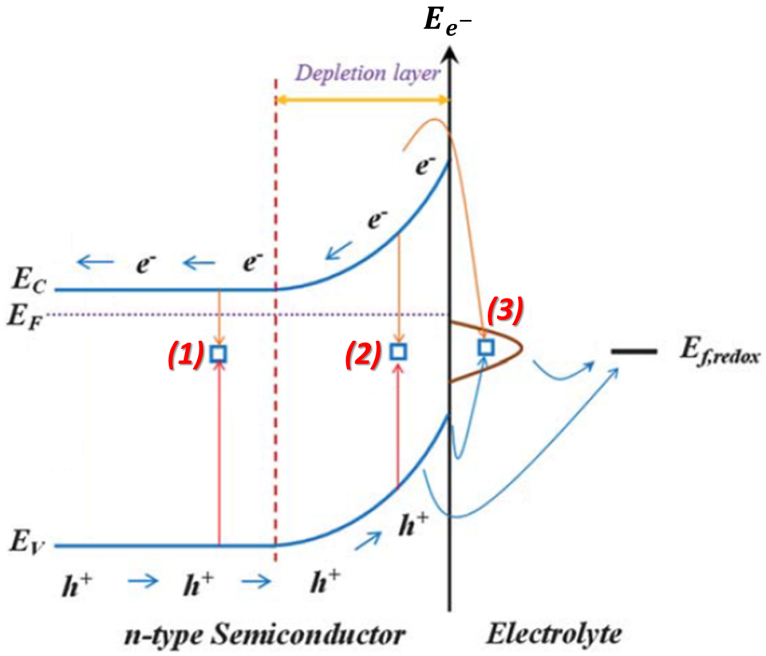

Figure 2.14: Main recombination paths of photogenerated holes and electrons for an n-type semiconductor in contact with an electrolyte: (1) bulk recombination, (2) space charge layer recombination (2), and surface recombination (3). The generation of electron-hole pairs by photon absorption is not represented for the sake of clarity. Reproduced from [34].

A physical property sensing the tendency for bulk electron-hole pairs recombination is the minority carriers diffusion length [34]. The diffusion length is the average distance a carrier can move from its point of generation until it recombines. For an n-SC, the minority carriers are the holes. The holes diffusion length L_p in an n-SC is given by [28]:

$$L_p = \sqrt{\frac{k_B T}{e} \mu_p \tau_p} \tag{2.26}$$

Where μ_p and τ_p are the holes mobility and lifetime respectively. The holes lifetime is the average duration between generation and recombination.

In general the recombination in the space charge layer can be neglected with respect to bulk and surface recombination, since the electric field induced by the band bending drives the electron-hole pairs separation. The effective diffusion length of holes is then the sum of the diffusion length L_p given by equation 2.26 and of the space charge layer width w (*cf.* section 2.2). Defects in the material (impurities, structural defects, grain boundaries) can induce discrete energy levels within the band gap which will favour carrier recombination since the carriers lifetime is inversely proportional to the defect density in the material [28]. These trapping levels are usually located near the middle of the band gap. Energy levels introduced by n-type (or p-type) doping are not considered as trapping levels since they are very close to E_C and E_V respectively.

Recombination exists also at the surface of the photoanode because of intra band gap electronic states located at the n-SC / electrolyte interface which act as preferred recombination centers [6, 35]. They can be due to ion adsorption or surface reconstruction for example. Such states drastically limits the kinetics of the water oxidation reaction. To overcome this phenomenon, one can deposit an overlayer to passivate these trapping states or use cocatalyst species (detailed in 2.4.3).

2.4 Strategies to improve metal oxide photoanodes

The pioneering experimental discovery of water photoelectrolysis was made by Fujishima and Honda in 1972 using TiO_2 photoanodes [15]. For more than 40 years, numerous materials and strategies were developped in order to improve the photoanodes photoelectrochemical performances [5, 29, 32, 34, 36]. TiO_2 [14, 37, 38] and hematite (α-Fe_2O_3) [32, 39] are the most extensively studied metal oxides. Other oxides, like WO_3 [40, 41], $BiVO_4$ [42, 43], $SrTiO_3$ [44–46] and tantalum oxi-nitrides [34, 47, 48] are also the subject of numerous studies. As inorganic photoanode material, we can cite graphitic carbon nitride [49].

In this section, the strategies developed to improve the metal oxide photoanodes water splitting performances are presented, providing state-of-the-art examples from the literature, considering mainly hematite-based photoanodes which is the focus of this PhD. Figure 2.15 shows the major explored routes for improving the water splitting performances of metal oxide photoanodes in general, which can be applied for hematite-based photoanodes.

The major leads can be classified in three approaches:

- reducing the bulk recombination rate (due to small diffusion lengths);
- light absorption optimization (counter the high-band gap drawback);
- surface kinetics improvement (linked to high kinetic overpotentials / surface recombination).

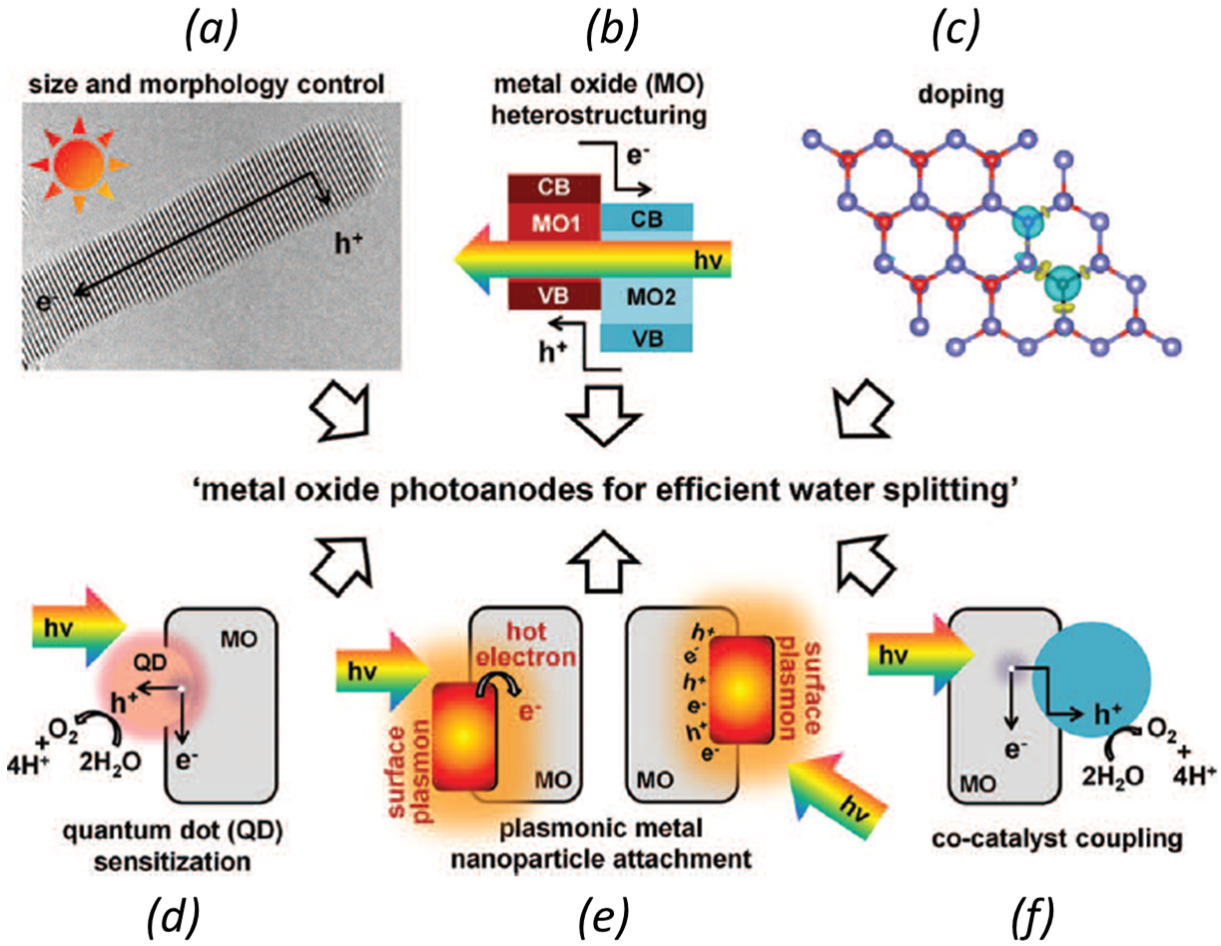

Figure 2.15: Explored routes for improving the water splitting performances of metal oxide photoanodes. Reproduced from [36].

2.4.1 Reducing bulk recombination

The recombination of electron-hole pairs is crucial in photoanodes. As it was detailed in 2.3.4, recombination induces a net loss in the photocurrent and is linked in particular to the ability to separate the charge carriers (through electric fields) and to the diffusion length (the higher the diffusion length is, the lower the recombination rate is).

2.4.1.a Doping

Increasing the n-type doping of photoanodes is a very convenient way to increase the conductivity and carriers mobilities. It is also expected to change the Fermi level position within the band gap (closer to the bottom of the conduction band with respect to the undoped position), which will increase the flat band potential and thus the band bending in contact with the electrolyte. Reported dopants in the case of hematite are essentially transition metals such as Ti [50–60], Sn [60, 61], Al [62], Cu [63], Cr [64], Mg [65], Mn [66],

Mo [64], Ni [67], Pt [68, 69], Zn [63], or Si [51, 59, 70] and Cd [71]. Multiple doping is also studied [51, 54, 59]. Upon doping, the overall photocurrent can increase up to more than two orders of magnitude. In chapter 5, we investigated the effects of Ti-doping on the properties of hematite epitaxial films (crystallographic and electronic structures, photoelectrochemical properties).

Doping metal oxides through oxygen vacancies, which are reported as donor species [72–77], is also common. We explored this possibility in chapter 4, through the study of single layers based on iron oxides of different crystallographic structures and oxygen stoichiometries.

2.4.1.b Internal electric field

Another widely explored route is to benefit from an internal electric field (spontaneous or remnant) to reduce the recombination rate. Thanks to this electric field, charge carriers can be well separated and driven to the appropriate interface.

In semiconductors junctions, a built-in electric field exists due to Fermi level equalization upon contact between the materials. This is the basic functioning principle of a p-n junction and allows a drastic drop in the recombination rate. Numerous attempts to build a p-n junction architecture as photoanode exist in the literature. Wang et al. reported the use of a junction made of amorphous p- or n-Si and crystalline intrinsic Si, which can be used as photoanode or photocathode [78]. Several articles reported results about the study of p-n metal oxides junction, *e.g.* p-$CoAl_2O_4$ - n-Fe_2O_3 nanocomposites [79] or p-$CaFe_2O_4$ / Fe_2O_3 [80] or / $BiVO_4$ [81] or / TaON [82] heterojunctions. Heterojunctions involving two conventional metal oxide photoanodes have also been reported in the literature, like $BiVO_4$ / WO_3 [83], Fe_2O_3 / WO_3 [84], p-Fe_2O_3 / n-Fe_2O_3 (p-type doping achieved upon doping with Mg) [65]. We can finally cite the Fe_2O_3 - TiO_2 system [85–90], which we investigated in chapter 6 through the characterization of the electronic structure and of the surface recombination dynamics.

The use of ferroelectricity to provide an internal electric field has also been considered. Indeed ferroelectric materials exhibit a spontaneous internal electric polarization [91], which has been proven to drive the separation of photogenerated carriers in the field of photovoltaics [92] and to induce band bending favouring oxidation or reduction reactions for photocatalysis applications [93, 94], depending on the ferroelectric polarization orientation. In the framework of solar water splitting, the use of such materials is very promising, yet little studied [93, 95]. In chapter 7, we studied as a first step the influence of the ferroelectric polarization of the prototypical $BaTiO_3$ on the photoelectrochemical properties of photoanodes systems based on thin films of $BaTiO_3$ deposited on Nb:$SrTiO_3$ single crystals.

2.4.1.c Nanostructuration

Nanostructuration is a widely used method to compensate the small carrier diffusion lengths [96–98]. The principle is to reduce the travel distance of carriers without diminishing too much the overall volume of the material so that the same quantity of light is absorbed (decoupling of the directions of charge collection and light absorption). In this way, the recombination rate decreases since holes reach the surface before recombining. Another complementary advantage is the increase of the surface area between the photoanode and the electrolyte, increasing the overall photocurrent. The literature is very rich concerning nanostructuration geometries in hematite-based photoanodes [32]. We can cite nanometric thin films, [52–55, 63, 65, 99, 100], nanowires [101], nanorods, [66, 102, 103], nanopellets [63, 102, 104], nanoparticles [105–107], or a honeycomb nanostructure [98].

2.4.1.d Interfacial layers

Studies concerning the use of interfacial layers between the substrate and the photoanode material in the framework of heterostructures have also been reported to help reducing the recombination rate. Here the principle is to use the underlayer as a structural template to improve the crystalline quality of the photoanode film, or as a potential barrier to prevent the transfer of holes from the photoanode to the substrate (back injection). In the case of hematite, Ga_2O_3, SiO_2, TiO_2 or Nb_2O_5 underlayers were reported to reduce the required applied potential by 0.2V in average [18, 108, 109].

2.4.2 Improving light absorption

Photon absorption is the first step in the solar water splitting process. Its efficiency relies on the band gap value of the photoanode: the lower the band gap is, the higher the number of absorbed photons is, hence the higher the photoanode efficiency is (*cf.* 2.3.3).

2.4.2.a Doping

Nitrogen doping can arise band gap narrowing by modification of the valence band positions while keeping the conduction band edges almost unaltered [36]. This strategy has been used mostly on metal oxide semiconductors with a band gap larger than 3 eV, like TiO_2 [110] or on the tantalum oxi-nitrides family [47].

2.4.2.b Heterostructuring

Combining materials with various gaps in heterostructures will increase the absorption efficiency of the whole system by utilizing the maximum number of incident photons. A widely explored route is to combine a conventional photoanode with Si which has a small band gap of 1.12 eV. This solution is highly desirable to increase the efficiency of photoanodes using wide band gap oxides like TiO_2 [111] and ZnO [112] and some reports are dedicated to α-Fe_2O_3 / Si architectures [113–115]. The case of the Fe_2O_3 - TiO_2 system is considered in

chapter 6. Indeed one can expect to conjugate the advantageous absorption of Fe_2O_3 (band gap around 2.2 eV) with the well suited band positions of TiO_2.

2.4.2.c Quantum dots

Another lead to increase the light absorption concern quantum dots. Quantum dots are semiconducting nanocrystals for which the electrical and optical properties (in particular the band gap) can be tuned by the nanocrystal size (through the quantum confinement effect). The use of quantum dots as sensitizers can arise photoactivity upon visible light or infrared illumination of wide band gap semiconductors [36]. Also Holmes et al. reported that the quantum confinement effect governs the water splitting properties of CdSe quantum dots immersed in an electrolyte [116].

2.4.2.d Plasmonic metal nanoparticles

Lastly, for materials featuring a very short holes diffusion length (*e.g.* below 10 nm in hematite) as compared to the light penetration depth (*ca.* hundreds of nm), absorbing all the incoming photons within the first 10 nm below the surface is a solution to increase the efficiency [117]. This can occur upon strong light scattering, induced by surface plasmon resonance of metal nanoparticles deposited on hematite or embedded in it [118]. Metal nanoparticles (*e.g.* Au) support surface plasmons (collective conduction electron oscillations), which at specific wavelengths (*i.e.* in resonant conditions) produce intense light fields near the metal and cause strong light scattering [36]. Metal particles can then be seen as optical antennas.

2.4.3 Improving surface kinetics

The water oxidation reaction is very challenging because the kinetic overpotential is high as compared to the one for water reduction reaction (*cf.* 2.3.2). Moreover surface recombination may drastically limit the oxygen production rate (*cf.* 2.3.4).

2.4.3.a Cocatalysts

Cocatalysts materials can decrease the overpotential required to oxidize water [119] so that the water oxidation kinetics are improved. Among the reported cocatalysts for photoanodes, we can cite iridium oxide [120, 121], cobalt oxide [122], mixed cobalt-nickel-iron oxides [123, 124], cobalt phosphate (often referred as "Co-Pi") [125], or Ru-based materials [126].

2.4.3.b Passivating overlayers

One of the drawbacks of photoanodes like hematite is the high recombination rate of holes at their surface because of intra band gap trapping states. Therefore a high anodic potential is required to drive water oxidation. To counter this, overlayers can be deposited on the photoanode surface to "passivate" these surface trapping states and thus reduce the required

applied bias potential [119, 127]. Since these overlayers do not have a catalytic activity when used alone, this strategy is different from using a cocatalyst. Michael Grätzel's group at EPFL published several studies where overlayers of Al_2O_3, Ga_2O_3 or In_2O_3 deposited on hematite succesfully reduced the required applied potential by 0.2V in average [108, 128–130]. Yang et al. reported that an ultra-thin (*ca.* 1 nm thick) TiO_2 film deposited on hematite featured the same effects [131]. In chapter 6, we compared the surface recombinations dynamics of TiO_2 - Ti-doped hematite heterojunctions, when the surface layer is TiO_2 or Ti-doped hematite. Overlayers can also be used to prevent (photo)-corrosion [127].

3 Experimental techniques

This chapter is dedicated to the presentation of the main experimental techniques that I used. A lot of apparatuses function in ultra high vacuum conditions (UHV, base pressure *ca.* 10^{-10} mbar). Such a vacuum is reached thanks to a combination of pumping devices (turbomolecular, ionic and titanium sublimation pumps). At this pressure, it is possible to elaborate clean epitaxial thin films. Moreover, surface probing techniques as well as electronic structure investigation techniques also require such experimental conditions.

To realize our thin films, we used oxygen plasma assisted molecular beam epitaxy as deposition method (presented in 3.1.1). A large panel of characterization tools were used. I chose here to present them as laboratory techniques (3.2), techniques using synchrotron radiation (3.3) and a specific section is dedicated to the photoelectrochemical properties measurement setup which was developed all along the PhD (3.4).

3.1 Thin films preparation

In this section, I will present the thin film deposition technique that I used to prepare the epitaxial layers (OPA-MBE). In addition, the substrates on which the thin films were deposited are described, as well as the lithography process performed for particular studies.

3.1.1 Oxygen plasma assisted molecular beam epitaxy (OPA-MBE)

Metal oxides thin films can be elaborated using a wide range of procedures. In addition to (electro)chemical routes, we can cite pulsed laser deposition or sputtering techniques, where stoichiometric targets of the desired materials are transferred onto a substrate. However here we chose OPA-MBE since this technique features a high control of the growth parameters, such as the stoichiometry or the growth rate.

OPA-MBE is a thin film growth technique functioning in UHV conditions. The low base pressure in the chamber (*ca.* 10^{-10} mbar) makes the environment reasonably exempt of polluting molecules (*e.g.* water, carbon) and oxygen. It is therefore possible to grow epitaxially thin films with top chemical and structural qualities and to use *in situ* characterization tools such as RHEED or XPS (which will be presented later in this chapter). This technique is well mastered in the Oxide group at SPEC which is expert in the epitaxial growth of oxide films by OPA-MBE.

In our OPA-MBE apparatus, the metal oxide elaboration consists in evaporating separately each metal (co-evaporation) and to use a dedicated oxidation source. This allows a complete control of the stoichiometry and of the growth rate. The oxidation source consists of an atomic oxygen plasma created by a radiofrequency excitation of oxygen gas within a quartz cavity (350W power). The oxygen plasma contains electrons, molecular and monoatomic oxygen (*ca.* 80% and 20% respectively). The latter is very reactive and

grants excellent oxidation conditions. Practically the oxygen flux penetrating in the quartz cavity is controlled by a BARATRON ®, which is a pressure controller device made by the MKS company. The gas penetrates the OPA-MBE chamber by exiting the quartz cavity through a hole of 200 µm diameter. Therefore we can control the flux of monoatomic oxygen by changing the BARATRON ® parameter expressed in turns (the higher the turns, the higher the oxygen partial pressure).

Concerning the evaporation of metals, we use individual Knudsen cells, each containing a high purity metal (99.99% grade) in a crucible. The crucibles are heated at a temperature for which the material is in the vapor state in UHV according to its vapor pressure. For instance, the corresponding temperatures for iron and barium are around 1050°C and 350°C respectively. The metal vapor then condensates on the sample surface and forms an oxide film by reaction with the plasma. The metal vapor flux is controlled by the temperature of the cell (heated by a filament) and calibrated using a quartz microbalance. The change in the quartz resonance frequency of the microbalance is related to the quantity of deposited matter. Knowing the density of the deposited material, it is possible to derive the growth rate on the microbalance. During the calibration, the microbalance is placed at the same position as the sample. A scheme and a picture of the OPA-MBE deposition chamber are depicted on figure 3.1.

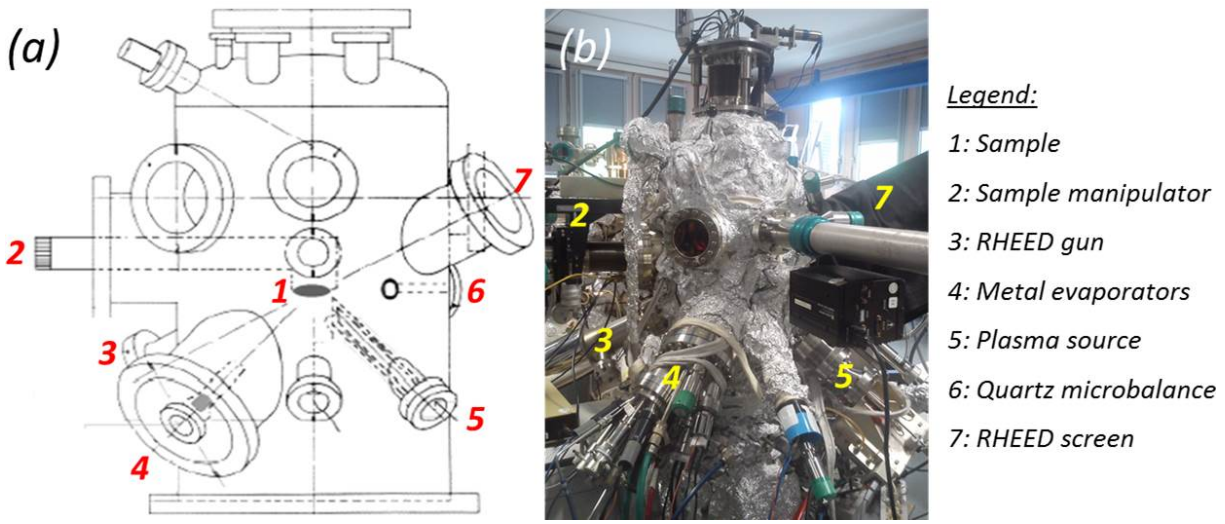

Figure 3.1: OPA-MBE deposition chamber : (a) scheme and (b) picture.

The deposition starts only after the metals evaporation fluxes are perfectly stabilized, *i.e.* when the Knudsen cells temperatures are constant with opened shutters (this stabilization takes *ca.* one hour). During this stabilization process, the sample surface is kept hidden and its temperature is *ca.* 300°C. Just before the deposition begins, the BARATRON ® is set to the desired oxidation conditions. For instance, the perfect oxidation of hematite layers

was obtained with a BARATRON ® set to 3.1 turns, corresponding to a pressure in the 10^{-7} mbar range in the OPA-MBE chamber. Lastly, the sample is heated at a temperature of *ca.* 600°C, favoring the atoms diffusion on the surface and rotates around its normal to ensure an homogeneous growth.

One of the major drawbacks of OPA-MBE is the slow growth rate (*ca.* 8 nm per hour) compared to other thin film deposition techniques in UHV like pulsed laser deposition, where growth rates *ca.* 100 nm per hour can be achieved.

To summarize, OPA-MBE grants an excellent control of the thin film properties (stoichiometry, doping, structure, thickness, ...) and is therefore a powerful epitaxial thin film engineering technique, thanks to the tuning of metal fluxes and the oxidation power, monitored by *in situ* characterizations.

3.1.2 Substrates used for thin films deposition

I used several substrates during my PhD work. Substrates for epitaxial thin films dedicated to photoelectrochemical measurements should meet the following conditions:

- lattice parameter and structure should be adapted to promote 2D growth, and good epitaxy conditions for the chosen phase (*i.e.* low lattice mismatch and compatible crystalline structure);
- it should not be a photoactive material to avoid mingled photoelectrochemical measurements;
- it should be a good electrical conductor (as it will be justified in the photoelectrochemical measurement presentation).

Hematite single layers (studied in chapters 4 and 5) and Ti-doped hematite - TiO_2 heterojunctions (studied in chapter 6) were grown on Pt (111) single crystals (8 or 10 mm diameter, 1 mm thickness). Pt crystallizes in the face-centered cubic system (FCC, space group $Fm3m$), with a lattice parameter of 0.392 nm. For the Pt (111) orientation, an hexagonal-like lattice can be used with a surface lattice parameter of a = 0.277 nm [132, 133]. The Pt (111) substrates can be reused: the oxide layer can be removed using a chlorhydric acid bath (HCl 38%, performed in clean room). A smooth and well-ordered surface can be retrieved performing an Ar^+ ion beam etching (at a pressure of 10^{-5} mbar with an energy beam of 4 kV) followed by a high temperature electron beam annealing (1000°C).

$BaTiO_3$ films studied in chapter 7 were grown on 1 at.% Nb-doped $SrTiO_3$ (001) (Nb:$SrTiO_3$) single crystals (squares of 1×1 cm^2, 1 mm thickness). Nb:$SrTiO_3$ is a cubic perovskite (ABO_3 structure) with a lattice parameter of 0.3905 nm. Nb doping grants a very good electrical conductivity contrary to bare $SrTiO_3$, the latter being fairly insulating. Nb:$SrTiO_3$ substrates cannot be cleaned and reused as the Pt (111) substrates. Before using Nb:$SrTiO_3$

substrates, they were annealed in air at a temperature of 950°C for three hours to remove the polishing induced surface defects and to restore a perfect stoichiometry.

Prior each deposition, the substrates were annealed at 600°C by radiative heating and cleaned using to the oxygen plasma in order to eliminate the chemisorbed surface contamination such as water or carbon. This cleaning is done during one hour with the BARATRON ® set to 1.3 turns, corresponding to a pressure in the 10^{-8} mbar range in the OPA-MBE chamber. Auger electron and X-ray photoelectron spectroscopies measurements showed that this protocol is very efficient to obtain clean surfaces [133], for both Pt (111) and Nb:$SrTiO_3$ (001).

3.1.3 UV and laser lithography

We performed lithography on some of our thin films for the following purposes:

- applying landmarks for microscopy experiments (*e.g.* Ti/Au lines);
- studying nanostructuration effects;
- avoiding mechanical strains on the $BaTiO_3$ films upon the mounting for photoelectrochemical measurements.

Lithography was realized in the clean room SPEC-NANOFAB[6]. We used both MJB3 Karl Suss Photomask Aligner and Dilase 650 Direct laser writing KLOE to pattern the samples. Dana Stanescu designed the patterns, defined the protocols and performed the lithography. The protocol can be summarized as following. A photoresist is deposited on the sample surface by spin coating. After the resist annealing at 110°C, we irradiated it through a Cr mask or by a laser beam. The irradiation of the photoresist polymerizes particular zones and make them soluble in a developer solution (positive photoresist). Then the pattern is transferred on the sample by chemical etching (in 38% HCl for hematite films) or lift-off (for Ti/Au marks). Finally, the not polymerized photoresist is removed. We used UV lithography and laser lithography.

The main advantage of UV lithography is the possibility to transfer a pattern from a physical Cr mask on the entire surface of the sample (global patterning). It should be noted that with the SPEC mask aligner and exposer, we were able to draw motifs with typical sizes down to 5 µm. However, the process requires a physical contact by pressing the mask against the sample, resulting in mechanical stresses or contamination of the sample. Also once the mask is fabricated, it cannot be modified, a new mask has to be fabricated if a new pattern is needed.

The main advantage of laser lithography is the possibility to create patterns on demand without using a mask. Patterns are created within a software and then the laser beam

[6]SPEC Clean Room web site: http://nanofab-spec/

draws it by scanning the sample surface. However for complicated patterns, the drawing can take unrealistic amounts of time. Then, either the written surface has to be reduced or the pattern has to be simplified or more smartly defined. For the used laser lithography apparatus available in SPEC, the laser beam diameter could be set down to 1 µm, but we used a beam with a diameter of 10 µm.

3.2 Laboratory characterization tools

In this section I present the main in-lab characterization techniques that I used:

- Reflexion High Energy Electron Diffraction (RHEED), used to monitor the crystal structure and quality as well as the surface roughness *in situ* during the growth or after an *ex situ* treatment like annealing (3.2.1);
- X-ray Photolectron Spectroscopy (XPS), as a chemical characterization tool to analyze the stoichiometry and doping level of our films *in situ* just after deposition or after an *ex situ* treatment (*e.g.* annealing) (3.2.2);
- Atomic and piezoresponse force microscopy (AFM & PFM), to characterize the topography and ferroelectricity of our films when required (3.2.3);

3.2.1 Reflexion high energy electron diffraction (RHEED)

RHEED is an electron diffraction technique that provides structural and morphological informations. The apparatus is embedded in the OPA-MBE chamber and dedicated to sample characterization during thin film deposition (*in situ*). A scheme of the physical principle and of the geometry[7] is shown on figure 3.2.

A beam of high energy electrons (30 keV in our case) strikes the sample surface with an incidence angle of a few degrees (grazing incidence). In these conditions, only the first atomic layers are probed (the electrons mean free path is *ca.* 5 Å), ensuring the characterization of the growing thin film. When the incident beam is perpendicular to a particular low Miller index direction of the surface reciprocal lattice, the beam is diffracted and the electrons are collected on a fluorescent screen, providing the surface diffraction pattern in this azimuth. It allows monitoring and controlling the quality of the surface morphology and structure of the growing film.

[7] Reproduced from http://www.material.tohoku.ac.jp/~kaimenb/B_RHEED.html

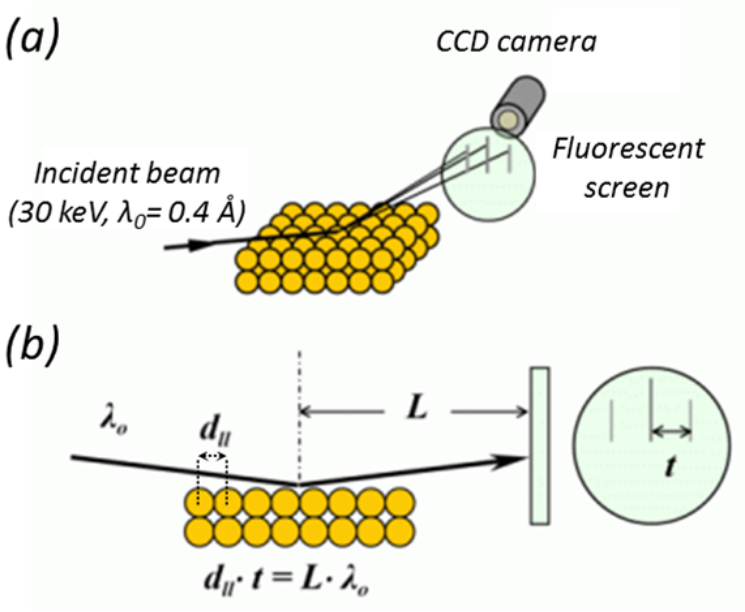

Figure 3.2: RHEED geometry: the incident electron beam is diffracted by the surface reciprocal lattice and we obtain a picture on a fluorescent screen. A camera linked to a computer makes possible the saving of images. (a) General view, (b) side view (© Graduate School of Engineering, Tohoku University)

The expected RHEED patterns are given on figure 3.3. They correspond to the intersection between the Ewald sphere and the surface reciprocal lattice. In optimal conditions (figure 3.3.a), the Ewald sphere is extremely thin (monokinetic high energy electrons) and the reciprocal lattice of a perfect surface consists of a 2D network of extremely thin rods. Therefore the intersection between the Ewald sphere and the reciprocal lattice rods are points (figure 3.3.c). In real conditions (figure 3.3.b), the Ewald sphere has a finite width because electrons are not perfectly monokinetic. Moreover the reciprocal lattice of a surface with in-plane disorder (real surface) consists of a 2D network of rods with a finite width (figure 3.3.b). Then the intersection between the Ewald sphere and the reciprocal lattice lines are streaks with a finite width (figure 3.3.d).

The expected RHEED pattern in real conditions depends on the growth mode :

- Layer-by-layer (2D, Frank-van der Merwe mode): a network of more or less thick lines (figure 3.3.d);
- Layer-plus-islands (intermediate, Stranski-Krastanov mode): dots along more or less thick lines (figure 3.3.e), since 3D diffraction occurs on islands resulting in dots on the pattern.
- Islands (3D, Volmer-Weber mode): dots network without lines (figure 3.3.f).

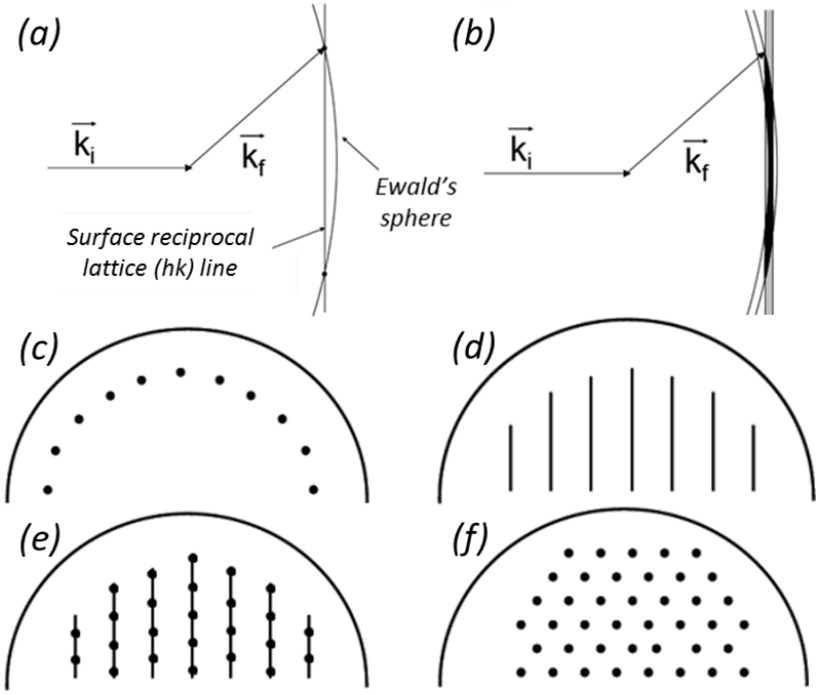

Figure 3.3: Optimal (a) and real (b) diffraction conditions and corresponding expected RHEED patterns: optimal (c) and real (d) layer-by-layer growth, (e) layer-plus-islands and (f) islands.

In addition to the structural phase identification we can also derive from the RHEED patterns the in-plane lattice parameter and therefore analyse relaxation phenomena upon the growth process [55, 132]. The analysis principle is shown on figure 3.4 in the case of the Pt (111) surface. The surface reciprocal lattice can be described using a primitive 2D base defined by two vectors, $\overrightarrow{a_s^*}$ and $\overrightarrow{b_s^*}$, where the $*$ superscript stands for reciprocal lattice, and the s subscript stands for surface lattice. Any direction can be described using a linear combination of these two directions and can be noted $(pq)_s^* = p \times \overrightarrow{a_s^*} + q \times \overrightarrow{b_s^*}$ where p and q are integers. For instance on figures 3.4.a and 3.4.b, the $(10)_s^*$ and $(11)_s^*$ directions are shown for the Pt (111) surface. A RHEED pattern is obtained when the incident electron beam has an azimuth angle perpendicular to a low index diffracting direction. In the case of Pt (111) the surface reciprocal lattice is an hexagonal network: on figures 3.4.a and 3.4.b, the small blue squares represents the network nodes and the bigger transparent blue parallelogram represent the primitive cell. When the RHEED pattern is obtained (figures 3.4.c and 3.4.d), the measurement of the spacing between lines is homothetic to the lattice parameter. Pratically, we integrate the RHEED pattern along the streak direction, according to the integration box highlighted on figures 3.4.c and 3.4.d, and then calibrate the pixel/Å equivalence (figures 3.4.e and 3.4.f) knowing that the Pt (111) surface lattice parameter is 0.277 nm in the $(10)_s$ direction [132].

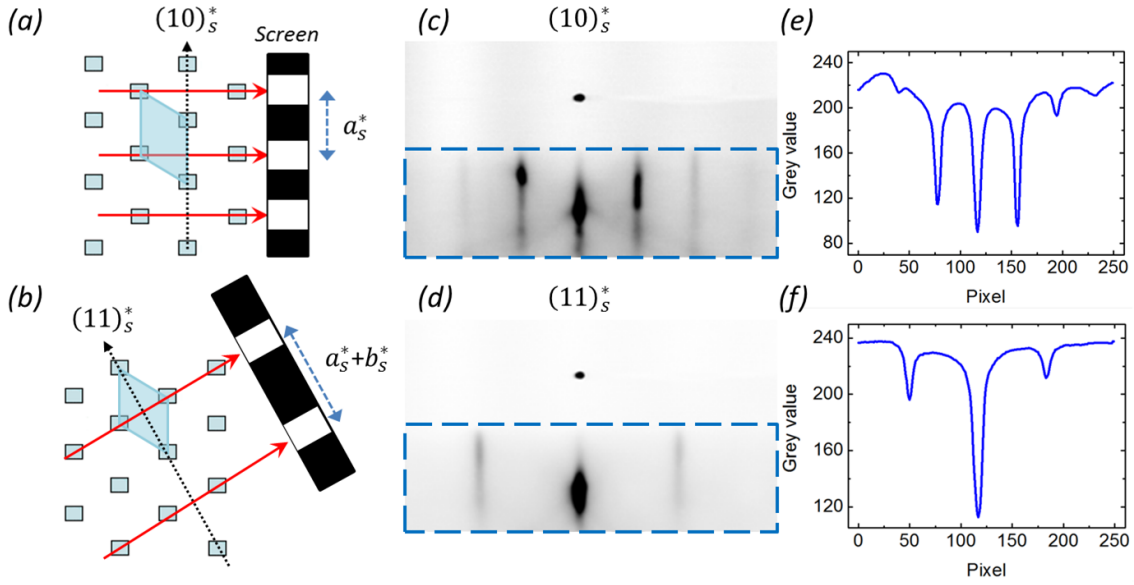

Figure 3.4: Principle of RHEED pattern analysis in order to calculate the surface lattice parameters in the case of the Pt (111) surface: (a) and (b) RHEED geometry for two different azimuths as well as the screen pattern and the accessible lattice parameter (the red solid lines stand for the incident electron beam and the black dotted line for the diffraction direction of the surface reciprocal lattice), (c) and (d) corresponding RHEED image (negative) with blue dashed rectangles highlighting the integration box used to obtain the curves of the integrated RHEED images, shown on (e) and (f).

To conclude, RHEED allows to characterize qualitatively a growth (symmetry, lattice, roughness) and to follow the lattice parameter evolution (if we know the crystallographic structure). Nonetheless, no chemical information can be extracted from this technique.

3.2.2 X-ray photoelectron spectroscopy (XPS)

X-ray photoelectron spectroscopy (XPS) is a common UHV chemical characterization technique. It relies on the photoemission process, where an electron is ejected from an atom after being excited by an incident photon with an energy at least equal to the binding energy (E_b) of the electron (photon in, electron out process). This ejected electron is called a photoelectron and its kinetic energy is noted E_k. The photoemission process is illustrated on figure 3.5.

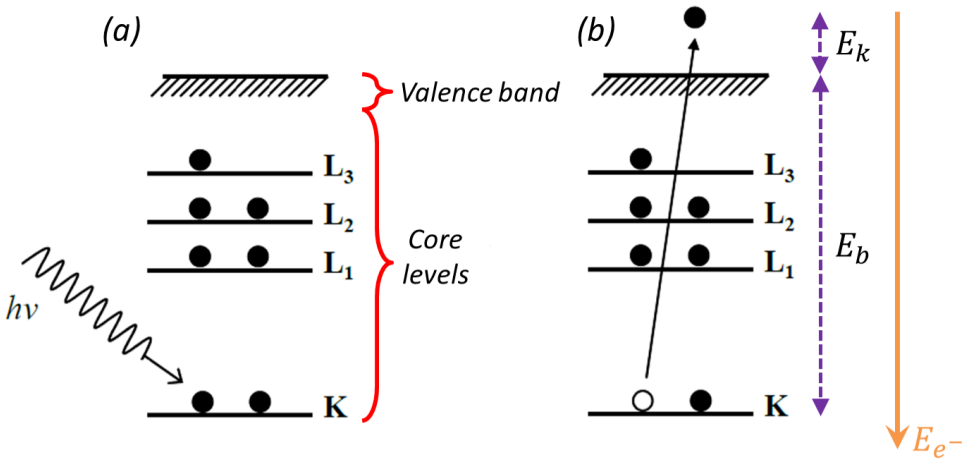

Figure 3.5: Photoemission principle: excitation by a X-ray photon (a) and photoemission (b). The electrons energy axis is sketched (orange solid arrow) and the binding and kinetic energies (E_b and E_k) of the photoelectron are also shown (dashed black arrows).

The X-ray photons source is an X-ray tube, where a metallic anode is irradiated by high energy electrons, resulting in the emission of X-ray photons having a wide range of energies, depending on the electronic structure of the metallic anode. In general, the most intense radiation is used (the one having the highest cross-section), *i.e.* the K_α radiation (containing both $K_{\alpha 1}$ and $K_{\alpha 2}$ energies). In our case, the energy used was the Al K_α radiation (1486.7 eV energy).

The photoelectrons come out of the probed matter and their kinetic energy is measured by an energy analyser which also amplifies the signal (thanks to channeltrons). The kinetic energy is expressed by the energy balance given by equation 3.1 [133]:

$$E_k = h\nu - E_b - W_a \tag{3.1}$$

Where $h\nu$ is the incident photons energy (h is the Planck constant and ν is the frequency of the photons) and W_a is the analyser work function (the minimum energy required for an electron to penetrate into the analyser). In XPS, charge build-up occurs with non-conductive samples: the charges created by photoemission (remaining holes after photoelectron ejection) are difficult to evacuate. This induces a positive charge density at the surface which decelerates the leaving photoelectrons (*i.e.* reduces their kinetic energy), resulting in a shift of the XPS peaks toward higher binding energies. To get rid of these effects, one can either determining the energy shift knowing the binding energy of a photoemission peak of the sample or neutralize these "photoemission" charges using an electron gun.

As it is the case for all electron-based techniques, XPS measurements are performed within a UHV vacuum chamber. In our case, the XPS chamber is attached in UHV conditions to the OPA-MBE chamber, making possible *in situ* measurements.

Spectra acquisition and treatment were performed using the AVANTAGE software (photoemission intensity *vs.* binding energy data). The binding energy is specific to the element to which the photoelectron belonged. It is thus possible to match the binding energy with a particular energetic transition and a specific chemical species, *e.g.* the binding energy of an electron on the Fe *2p* orbital. The corresponding peak is called Fe*2p*. For each sample, the following acquisitions can be performed just after deposition:

- A wide scan, scanning a large range of binding energies (this spectra is acquired very fast with poor statistics, the point is to determine the binding energy windows for each relevant photoemission peak);
- Specific spectra of the material core levels (*e.g.* for undoped hematite : Fe*2p* and O*1s*) acquired with good statistics so that the binding energy can be well derived;
- A spectra scanning very low binding energies ($<$ 10 eV) to analyse the electronic structure of the valence band.

Figure 3.6 shows some examples of acquired XPS spectra.

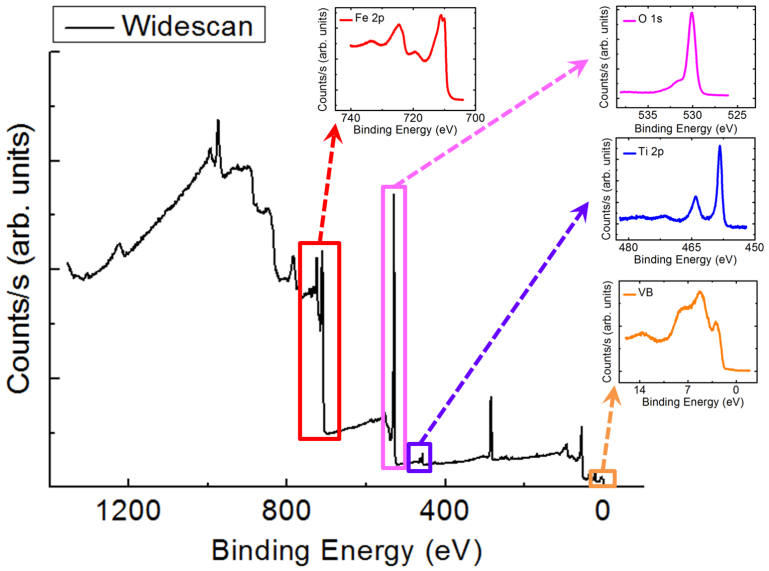

Figure 3.6: Examples of XPS spectra : widescan (black), Fe*2p* (red), O*1s* (pink), Ti*2p* (blue) core levels and valence band spectra (orange). Sample : 54 nm thick 5.8 at.% Ti-doped α-Fe_2O_3 / Pt (111) film.

The probed depth in XPS is limited by the photoelectron inelastic mean free path which is typically below 10 nm, so it is mainly surface sensitive. Also XPS is a suitable tool to observe the electronic structure changes as for example due to various oxidation states. For instance, by analysing the fine structure of Fe*2p* lines, one can determine the iron oxidation state (Fe metal, Fe^{2+} or Fe^{3+}) [134] as it is illustrated on figure 3.7. Indeed depending on the Fe valence state, one observes a shift of the Fe*2p* peaks as well as different characteristic shake-up satellites (shown by arrows on figure 3.7).

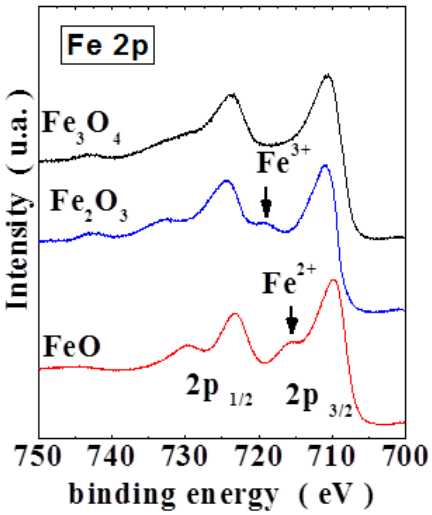

Figure 3.7: Different Fe*2p* lines and characteristic shake-up satellites (shown by arrows) as a function of the iron valence state in iron oxides [134].

Another interesting feature in XPS is the measurement of doping levels (atomic concentrations) deduced from the XPS lines intensities. For instance in the case of Ti-doped hematite, one can measure the atomic doping level by calculating:

$$at.\%(Ti) = \frac{A_N(Ti2p_{3/2})}{A_N(Ti2p_{3/2}) + A_N(Fe2p_{3/2})} \tag{3.2}$$

Where $A_N(Ti2p_{3/2})$ and $A_N(Fe2p_{3/2})$ are respectively the Ti$2p_{3/2}$ and Fe$2p_{3/2}$ peaks normalized areas considering a linear background. For a given element, the peak area is normalized with respect to (i) the tabulated Scofield cross-section factor linked to the probability of photoemission for the corresponding core level, (ii) the photoelectron inelastic mean free path dependent on the probed element and on the kinetic energy and (iii) a transmission function dependent on the measurement conditions and specific to the XPS apparatus.

To conclude, XPS is a powerful chemical characterization technique, giving access to numerous material properties (stoichiometry, valence state, surface composition). Contrary

to RHEED, classical XPS (without angular resolution) does not give structural information at all, which makes the two techniques complementary as *in situ* characterizations during and after the growth.

3.2.3 Atomic and piezoresponse force microscopy (AFM and PFM)

Atomic force microscopy (AFM) and piezoresponse force microscopy (PFM) are surface scanning probe microscopy techniques. They are performed in an AFM environment where a tip (attached to a cantilever) is approached to the sample surface and scans the latter thanks to a piezoelectric scanner. The force felt by the tip will bend the cantilever up or down. This bending is measured by detecting the deflection of a laser sent on the cantilever, projected on a four-sectional photodiode. It is then possible to go back to the force felt by the tip by recording the changes in the photodiode voltage. The working principle of scanning probe microscopy is illustrated on figure 3.8.

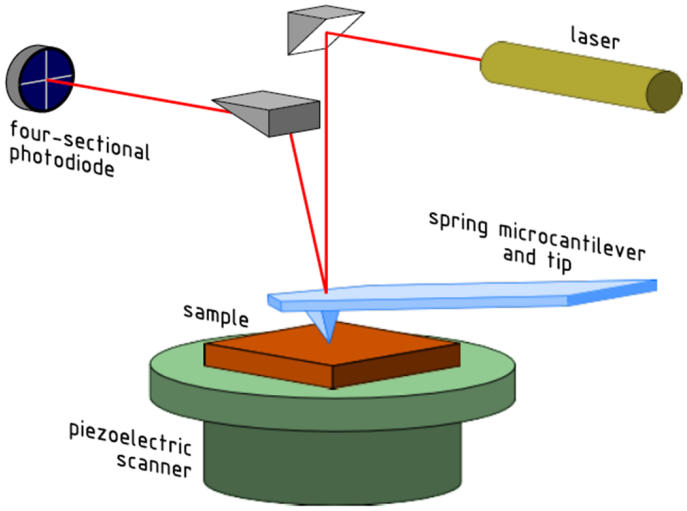

Figure 3.8: Working principle of surface scanning probe microscopy apparatus [135].

Various surface scanning probe microscopy techniques exist. One of the most known is AFM where topographic discontinuities bend the cantilever, making possible the sketching of topography maps and the analysis of roughness for instance. In particular we used AFM to characterize precisely the lithography patterns applied on our samples (etching depth, motif form). We acquired AFM images in contact mode using a Brüker^{TM} FASTSCAN head and Nanoscope V controller. The Brüker's FastScan-A cantilevers utilize a 27 µm long triangular silicon nitride cantilever with a force constant of 17 N/m. The silicon tip used to collect the topography measurements had an extremely sharp tip radius of 5 nm.

PFM is commonly used to detect and/or apply polarization states on ferroelectric materials (which are piezoelectric) using an electrically conductive tip attached on a cantilever. It can be performed in reading mode (detecting polarization states) or writing mode (applying an electric field between the tip and the back of the sample). In reading mode, a sinusoidal electric signal (drive amplitude) is applied to the sample, with a tip bias at 0V. The apparatus detects the piezoelectric deformations of the sample submitted to the electric field created by the conductive tip [136]. The periodic vibrations of the sample surface (the induced deformations) are transmitted to the tip, and the resulting oscillations of the cantilever are recorded using a lock-in amplifier. The lock-in amplifier measures the amplitude and the phase difference of this response signal with respect to a reference signal which is the drive amplitude. Figure 3.9 illustrates the amplitude and phase evolution as a function of the polarization vector direction of a ferroelectric material surface. Qualitatively the differences in the ferroelectric polarization orientation can be seen by contrast in PFM phase images. Quantitative considerations should involve careful calibrations. In writing mode (applying a polarization), a DC bias is applied between the tip and the piezoelectric scanner table, in order to polarize the sample. The tip scans the sample surface following a user-defined bias *vs.* position pattern. The chosen bias should exceed the required bias to reverse the ferroelectric polarization (coercive bias). To study our ferroelectric-based systems, PFM was a technique of choice to locally apply and detect polarization states.

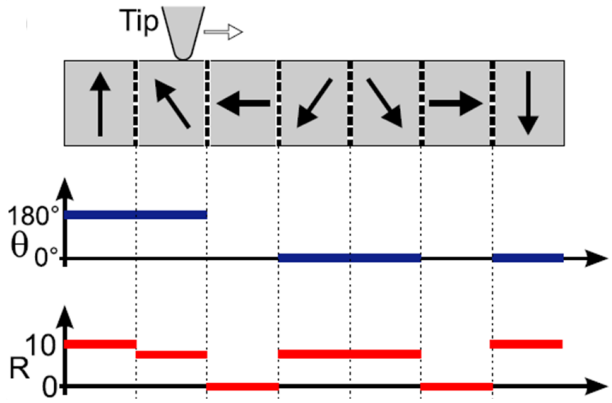

Figure 3.9: Phase (θ, blue) and amplitude (R, red) signals obtained in PFM reading mode on a sample as a function of the polarization vector direction in a ferroelectric material. Reproduced from [136].

PFM images were acquired using a Brüker dimension ICON head and nanoscope V controller. PFM requires a contact mode for the measurements. The tip used for the PFM measurements was Bruker's SCM-PIT, a Platinum - Iridium coated tip with a quoted radius of 20 nm on an Antimony (Sb) doped Si cantilever. During the writing procedure, the sample was connected to the ground. The tip velocity was 5.5 µm/s and the writing resolution was

20 nm. After the writing process, we measured the PFM phase contrast (in reading mode) by applying on the sample a drive amplitude of 4000 mV (sinusoidal potential) and on the tip a potential of 0V.

3.2.4 Low energy electron microscopy (LEEM)

Low Energy Electron Microscopy (LEEM) is a UHV electron microscopy technique where the interaction between an electron beam of low kinetic energy (few eV) and a solid material surface is studied [135]. The primary beam is composed of electrons accelerated with a 20 kV potential generated within an electron gun. After the interaction with the sample, the electrons beam forms an image on a fluorescent screen. A simplified scheme of a LEEM apparatus[8] is shown on figure 3.10.

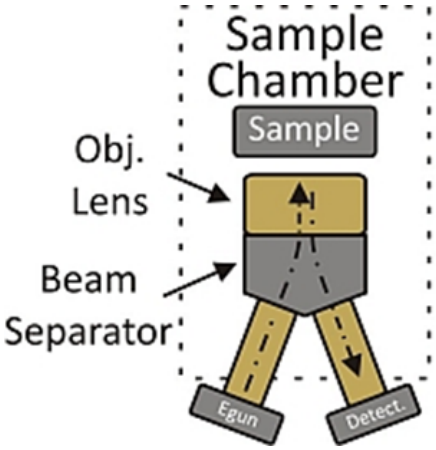

Figure 3.10: Simplified geometry of a LEEM apparatus. Reproduced from Elmitec-GmbH website.

If the incident electrons kinetic energy is not sufficient to penetrate into the sample, they are just reflected by the surface. This is the mirror electron microscopy regime (MEM). For higher kinetic energies, incident electrons may go through the surface and then interact with the sample. They can be back-scattered by the sample depending on the material electronic properties. The analysis of this back-scattering (LEEM regime) can give insights about some sample properties. In particular, if we examine the electron intensity *vs.* the electron kinetic energy curve (also called the reflectivity curve), we can have access to the MEM-LEEM transition energy, which is the minimum energy for which electrons can penetrate in the sample. This particular energy can be linked to various factors, such as topography variations, work function differences or surface electric fields (*e.g.* differences in doping, equivalent to surface potential differences).

[8] From http://www.elmitec-gmbh.com/

3.3 Synchrotron radiation characterization techniques

The synchrotron radiation is a high brilliance photons flux with a wide range of energies, obtained within a synchrotron which is a particular type of particle accelerator. The use of a photons beam with a tunable energy (through monochromatization) as excitation source opens a great scope of new characterization tools. Another degree of freedom offered by synchrotron radiation is given by the photons polarization. Synchrotron radiation is natively linearly polarized in the accelerator plane. By using undulators, one can obtain various photons polarizations, for instance linear horizontal (LH) or linear vertical (LV). Due to the anisotropic shape of thin films, it is often interesting to have the photons linear polarization vector either parallel or perpendicular to the film surface.

In the following subsections, I will present the four absorption and photoemission spectroscopy techniques that I mainly used:

- X-ray absorption spectroscopy (XAS, 3.3.1);
- analysis of the local atomic environment for a particular species by extended X-ray absorption fine structure (EXAFS, 3.3.2);
- chemically selective photoemission using resonant photoemission spectroscopy (RPES, 3.3.3);
- local electronic structure using X-ray photoemission electron microscopy (X-PEEM, 3.3.4).

During the PhD, we performed measurements using the synchrotron radiation at synchrotron SOLEIL, Saint-Aubin, France[9], and at Diamond Light Source, Didcot, United Kingdom[10].

3.3.1 X-ray absorption spectroscopy (XAS)

When a photons beam irradiates a material, photons are absorbed according to the cross-section of the process if their energy matches the binding energy of an electron belonging to an atom (*e.g.* a core level binding energy): the electron is then ejected (electron photoemission), the atom is excited. The efficiency of the absorption process is given by the absorption coefficient of the material, μ, which varies with the photons energy. XAS consists in measuring this absorption coefficient as a function of the incident photons energy. A tunable photons energy source, like the one provided by the synchrotron radiation, is required to perform this measurement. XAS is ideally realized in transmission conditions. The XAS signal can also be obtained by measuring the photons or electrons arising from deexcitation of the material after the photon absorption (the relevant processes are shown on figure 3.11).

[9] Synchrotron SOLEIL website: http://www.synchrotron-soleil.fr/
[10] Diamond Light Source website: http://www.diamond.ac.uk/

The photon absorption creates an electron vacancy (a hole), which leaves the atom in an excited state (*cf.* figure 3.11.a). The core hole can relax in two ways:

- Auger deexcitation, also called auto-ionization process (an electron from an upper core level fills the hole and another one, the Auger electron, is ejected from the material, *cf.* figure 3.11.b);
- X-ray fluorescence (*cf.* figure 3.11.c).

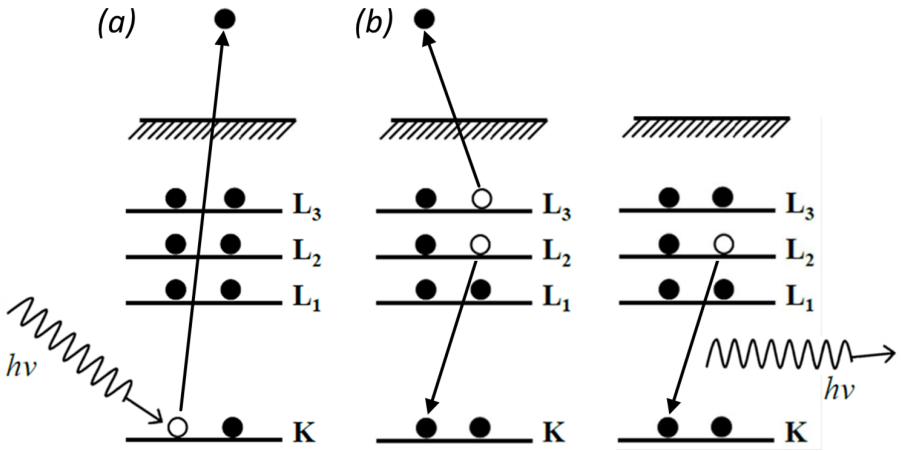

Figure 3.11: Relevant processes for XAS experiments : (a) photon absorption by a core level, resulting in photoelectron emission, leaving a core level hole, relaxation by (b) Auger electron emission and by (c) X-ray fluorescence.

The mean free path of electrons being low, Auger electrons and photoelectrons can create other electrons through inelastic processes. These electrons are called secondary electrons. It has been shown that the secondary electrons and fluorescence intensities are proportional to the absorption coefficient [137]. Therefore XAS can be obtained by counting the photons or electrons emitted by the sample. Practically for our EXAFS experiments the XAS at the Fe and Ti K edges were recorded by measuring the X-ray fluorescence of the samples. In the case of XAS measurements done within an X-PEEM apparatus, we recorded the signal of electrons emitted by the sample, selecting a particular electron kinetic energy close to the photoemission threshold (very low kinetic energy electrons, corresponding mainly to secondary electrons). The output data was the number of the recorded electrons as a function of the incident photons energy.

The great advantage of XAS relies on its chemical selectivity. Moreover since for a given species different absorption edges can have different selection rules, it is possible to focus on specific electronic properties by choosing the absorption edge. For instance, the XAS spectra at the Fe $L_{2,3}$ edge are different for all iron oxides (including metal Fe) because the

structure and the valence state of iron changes. Figure 3.12 presents the XAS for metal Fe and different iron oxides elaborated by Fe sputtering followed by a thermal oxidation [138].

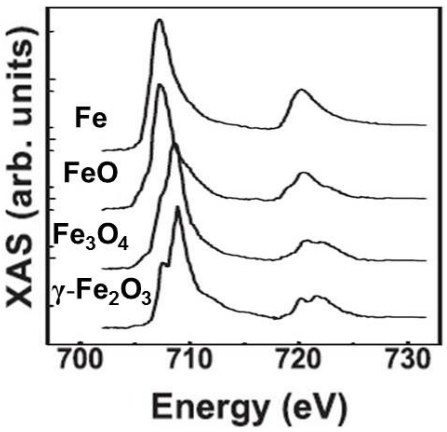

Figure 3.12: XAS at Fe $L_{2,3}$ edge for metal Fe and different iron oxides elaborated by Fe sputtering followed by a thermal oxidation [138].

3.3.2 Extended X-ray absorption fine structure (EXAFS)

EXAFS is a particular XAS technique used to derive the local crystallographic structure around the absorbing atom (also called central atom) by studying the oscillations of the absorption coefficient above a particular edge. Our EXAFS experiments were performed on the SAMBA beamline at synchrotron SOLEIL[11] at room temperature, by detecting the XAS signal in the fluorescence mode. For K edges of solid materials (excitation of the *1s* core level), the XAS signal can be described in three regions [139], which is illustrated on figure 3.13:

- when the photon does not have a sufficient energy to be absorbed by the K core level, it is the pre-edge region. However, it can be absorbed by core levels with lower binding energies;
- when the photon energy is sufficiently high to be absorbed by the K core level, the absorption coefficient greatly increases and a peak appears: it is the absorption edge. The value of this increase is proportional to the quantity of absorbing atoms. Just after the edge the absorption coefficient can feature various evolutions. This regime is called XANES, standing for X-ray absorption near edge structure;
- for photons energies between 40 and 1000 eV after the edge, the absorption coefficient features oscillations called EXAFS.

[11] SAMBA beamline web page: http://www.synchrotron-soleil.fr/Recherche/LignesLumiere/SAMBA

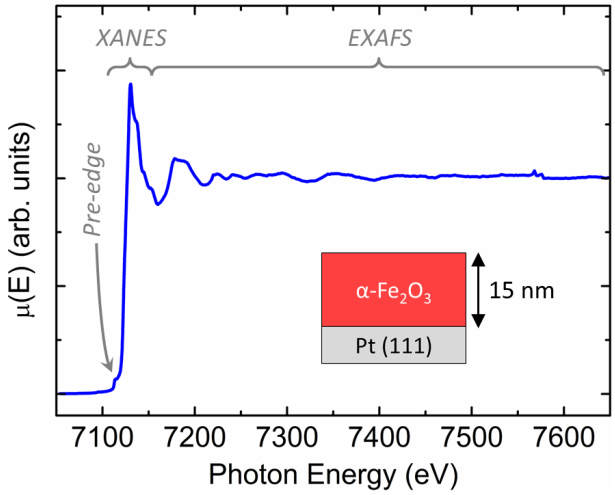

Figure 3.13: Fe K edge absorption spectra for a 15 nm α-Fe_2O_3 / Pt (111) film (data acquired on the SAMBA beamline at synchrotron SOLEIL). The different regions are highlighted in grey.

The EXAFS oscillations originate from interferences and arise from the wavelike nature of the photoelectron emitted by the absorbing atom. The photoelectron can be seen as an outgoing spherical wave centered at the excited atom. Its wave vector as a function of the photons energy is given by:

$$k(E) = \sqrt{\frac{2m}{h^2} \times (E - E_0)} = \frac{2\pi}{\lambda} \tag{3.3}$$

Where m is the electron mass (9.11×10^{-31} kg), E_0 the absorption edge energy and λ the electron wavelength. This electron wave is scattered by neighbour atoms and the new waves issuing from each scattering site interfere with the outgoing wave. By increasing the photons energy E, $k(E)$ increases and constructive and destructive interferences occur alternatively. Therefore the EXAFS oscillations are linked to the absorbing atom environment (number, type and distance of the neighbours). EXAFS takes advantage of the chemical selectivity of the X-ray absorption process. For instance, in the case of Ti:α-Fe_2O_3, the EXAFS signal measured just after the Fe (resp. Ti) K edge will give insights about the chemical environment of Fe (resp. Ti).

To conduct a quantitative analysis of EXAFS, one has to sketch the EXAFS oscillations $\chi(E)$ spectrum, expressed as a function of the raw data $\mu(E)$ by:

$$\chi(E) = \frac{\mu(E) - \mu_0(E)}{\mu_0(E)} \tag{3.4}$$

Where $\mu_0(E)$ is the $\mu(E)$ spectrum background. In the "single scattering" approach (scattering by only one neighbour before interfering with the initial electron wave), the EXAFS oscillations as a function of the photoemitted electron wave number k for well-ordered crystals can then be expressed as [139]:

$$k\chi(k) = \sum_i \frac{N_i}{r_i^2} \times e^{-2\sigma_i^2 k^2} \times e^{-2r_i/\lambda(k)} \times F_i(k) \times \sin(2kr_i + \varphi_i(k)) \tag{3.5}$$

Where:

- The index i corresponds to the current shell of neighbours composed of N_i atoms (if i=1 the term corresponds to the first neighbour(s)) at a r_i distance of the absorbing atom and having a Debye-Waller factor σ_i;
- $F_i(k)$ and $\varphi_i(k)$ are the backscattering amplitude and phase for the shell of neighbours i surrounding the central atom ($\varphi_i(k)$ also depends on the central atom);
- $e^{-2\sigma_i^2 k^2}$ corresponds to the Debye-Waller term taking into account the damping due to thermal or structural disorder;
- $e^{-2r_i/\lambda(k)}$ corresponds to the damping factor due to the electron mean free path at the $\lambda(k)$ wavelength.

For K edges, when the incident photons beam is linearly polarized, N_i can be replaced by N_i^* according to [139]:

$$N_i^* = \sum_j^{N_i} 3\cos^2\left(\alpha_j^i\right) \tag{3.6}$$

Where α_j^i is the angle between the polarization vector of the incident photons beam and the bond between the central atom and the atom j of the current layer of neighbours i. Therefore when the photons polarization is perpendicular to a bond, the EXAFS signal corresponding to this bond is zero, whereas when the photons polarization is parallel to the bond, the corresponding EXAFS signal is maximized. On the SAMBA beamline, instead of changing the photons beam polarization with undulators, the sample is rotated so that the photons polarization vector is either parallel or perpendicular to the sample surface, as it is illustrated on figure 3.14. The synchrotron radiation is natively LH-polarized. In normal incidence the polarization vector will be parallel to the basal plane of the sample, arising a preferential probing of the in-plane structure (*cf.* figure 3.14.a). In grazing incidence, the polarization vector will be almost perpendicular to the basal plane, arising a preferential probing of the out-of-plane structure (*cf.* figure 3.14.b).

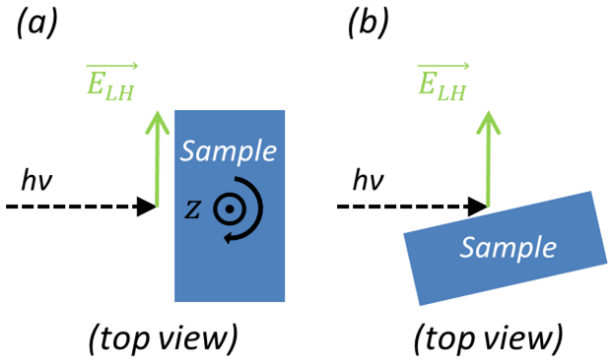

Figure 3.14: EXAFS measurement geometries using LH photons polarization: (a) normal incidence (*i.e.* in-plane structure probing), (b) grazing incidence (*i.e.* out-of-plane structure probing).

The expression of the EXAFS oscillations given by equation 3.5 is valid in the single scattering approach. This approximation is valid only for the first nearest neighbour shell. For a more accurate analysis, "multiple scattering" approaches have been developed using the FEFF 8 codes [140–142].

The quantitative EXAFS data analysis is done using the DEMETER © software suite developed by Bruce Ravel [141] including the ATHENA & ARTEMIS softwares[12] according to the following steps (illustrated on figure 3.15):

1. "Deglitching": experimental spectra may feature artefact sharp peaks due to the diffraction of the incident beam by the substrate. These peaks are called "glitch" and are present because we are using single crystalline substrates. A slight change of the incidence angle (1-2°) will change the position of these peaks in the spectra, making possible the reconstruction of a "glitch-free" experimental spectra from raw spectra obtained at various incidence angles (figure 3.15.a).

2. Determining the absorption edge energy E_0 in order to derive $k_0 = k(E_0) = 0$ (*cf.* equation 3.3).

3. Converting $\mu(E)$ data (raw absorption spectra) into $\chi(k)$ data (EXAFS oscillations, *cf.* figure 3.15.b): the background removal and axis conversion is done using the ATHENA software.

4. EXAFS oscillations simulation (figure 3.15.b): this is done using the ARTEMIS software and FEFF calculations (with HORAE and FEFF 8.4 codes [140–142]). More details are given herein.

[12] Demeter software suite web site: http://bruceravel.github.io/demeter/

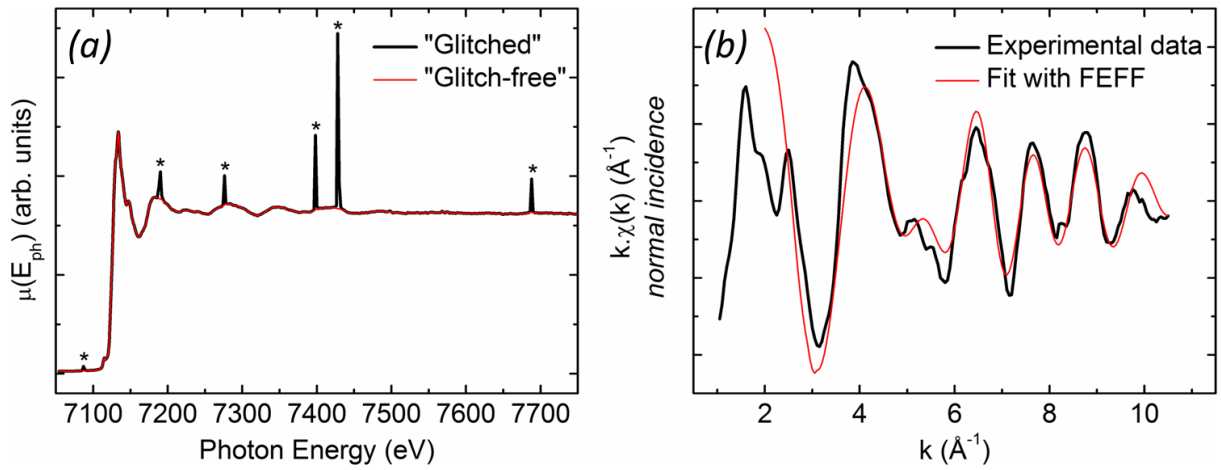

Figure 3.15: Fe K edge EXAFS data post-processing illustration: (a) raw absorption spectra recorded in normal incidence with glitches (black thick line, glitches are indicated by asterisks) and glitch-free (red thin line), (b) corresponding experimental EXAFS oscillations obtained by the ATHENA software (black thick line) and fit of the data by FEFF calculations assuming a corundum crystallographic structure (red thin line) using the ARTEMIS software. Sample : 15 nm α-Fe_2O_3 / Pt (111) annealed in UHV at 200°C for 15 minutes.

FEFF8 files are used by the ARTEMIS software to simulate the EXAFS oscillations ($\chi(k)$ data). To generate a FEFF8 file, the user enters the supposed crystallographic structure (absorbing atom type, neighbours type and positions) and other parameters (absorption edge type, temperature, incident beam polarization). Then FEFF8 determines for these conditions the possible single and multiple scattering paths (distance and atom(s) type) from the absorbing atom and calculates their contribution to the EXAFS signal. Afterwards in the software ARTEMIS, the user has to choose the used paths to simulate the experimental data. In our case (iron oxide), we noted that the signal corresponding to multiple scattering paths was negligible so we did not retain these paths. Also in order to limit the fitting parameters we chose to use paths of lengths up to 3.8 Å around the absorbing atom. The fitting parameters for each path corresponding to a shell of neighbours are the amplitude for the path, the distance between the neighbour and the absorbing atom and the Debye-Waller factor. To reduce further the number of fitting parameters for our iron oxide films, we supposed that the crystallographic structure is known (*e.g.* corundum structure for hematite) and allowed only structural expansion by introducing two expansion parameters: α parallel to the surface of the film and β perpendicular to it.

3.3.3 Resonant photoemission spectroscopy (RPES)

Resonant PhotoEmission Spectroscopy conditions are fulfilled when we realize XPS using excitation photons of an energy close to the absorption threshold of a core level (previously determined by XAS), which provides (in a simple picture) chemically selective photoemission. It is a useful technique for the investigation of valence band features in solids [143]. For instance we used this technique to acquire resonant photoemission spectra of the valence band region at the L_3 absorption edge for oxides incorporating Fe and/or Ti. In an atomic picture, there are two ways to extract an electron from the valence band using photons energies close to the L_3 edge:

- direct photoemission from the valence band ("usual" photoemission of the valence band region after photon absorption);
- Auger relaxation (auto-ionization process) following the $2p \rightarrow 3d$ core excitation (only possible with an incident photons energy exactly at the L_3 absorption edge).

The resonant photoemission is caused by the final-state coherent interference between the two corresponding electron waves. The processes are sketched on figure 3.16.

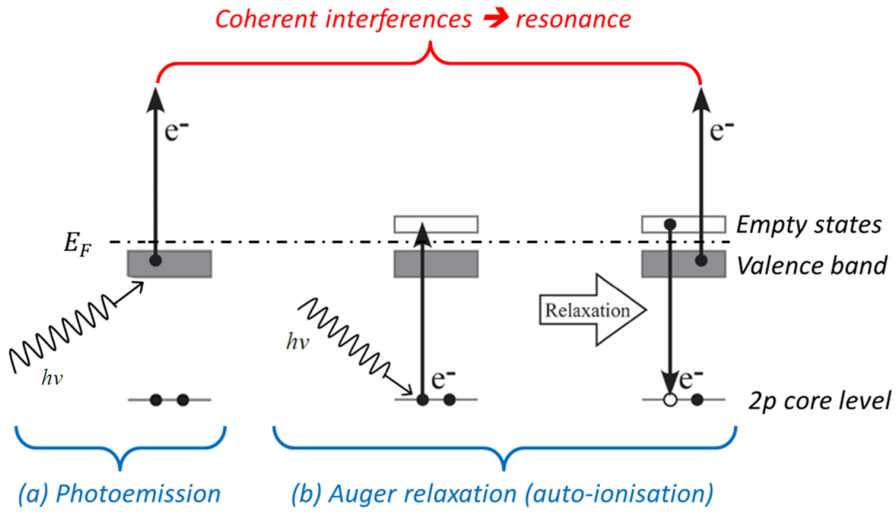

Figure 3.16: Resonant phenomena when investigating the valence band in RPES: interference between (a) direct photoemission from the valence band and (b) Auger relaxation. E_F stands for the Fermi level of the sample.

Therefore, by choosing the right photons energy, one can expect an increase of the photoemission signal coming from the atoms for which the excitation energy matches the L_3 absorption edge, thanks to the coherent interferences phenomena. For instance, illumination with photons of energy corresponding to the Fe L_3 absorption edge will result in the emission

of photoelectrons coming in majority from Fe atoms. In the case of α-Fe_2O_3, we recorded increases of the valence band photoemission signal of a factor of 10 in resonant conditions at the Fe L_3 edge with respect to the signal obtained in non resonant conditions. In the case of TiO_2, the increase of the valence band photoemission signal at the Ti L_3 edge is only a factor of 4. Therefore RPES can be used to characterize dopants in the case of a doped material (*e.g.* Ti:α-Fe_2O_3) or buried layers in the case of multi-layers architectures (*e.g.* (Ti):α-Fe_2O_3-TiO_2 heterojunctions). RPES can be seen as a chemically selective photoemission process enhanced by the resonance phenomena. However, it should be noted that this technique is limited to nanometric thin film geometries, since the probed depth will be given by the electrons mean free path ($<$ 10 nm at a kinetic energy of 800 eV). The use of a high brilliance tunable photons energy source such as synchrotron radiation is required to perform RPES. Our RPES experiments were carried out on the CASSIOPEE beamline at synchrotron SOLEIL (Saint-Aubin, FRANCE)[13].

RPES spectra acquisition and post-processing are illustrated on figure 3.17 with the example of data recorded at the Fe L_3 edge for a 10 nm TiO_2 / 10 nm 2 at.% Ti:α-Fe_2O_3 / Pt (111) sample. The acquisition of a complete set of RPES spectra is done in four steps:

1. acquisition of the XAS corresponding to a specific element and definition of the relevant photons energies for the XPS spectra acquisition (*cf.* 3.17.a);
2. selection of the photons energy;
3. acquisition of the XPS spectrum;
4. repetition of steps 2 and 3 for all photons energies chosen in step 1.

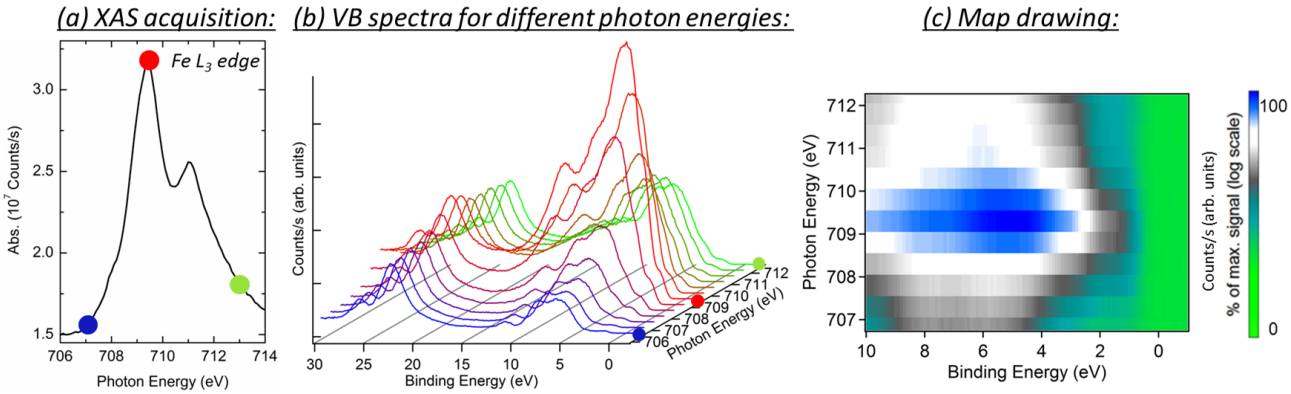

Figure 3.17: RPES spectra acquisition and post-processing: (a) Fe L_3 XAS acquisition and energy selection (coloured disks), (b) valence band XPS spectra acquisition, (c) drawing of a RPES map. Sample : 10 nm TiO_2 / 10 nm Ti:α-Fe_2O_3 / Pt (111). Data acquired at the CASSIOPEE beamline on synchrotron SOLEIL.

[13] CASSIOPEE beamline web site: http://www.synchrotron-soleil.fr/Recherche/LignesLumiere/CASSIOPEE

RPES data can be represented in multiple ways. We can either represent a selection of spectra (*cf.* figures 3.17.b) or draw RPES maps for which the X axis is the binding energy, the Y axis is the photons energy and the colour scale is determined by the photoemission signal (*cf.* figure 3.17.c). On the one hand, the use of a selection of spectra makes a quantitative analysis of changing features possible (*e.g.* peak shift, increasing component, appearing states within the gap). On the other hand, maps allow a facile qualitative vision of changes in the valence band photoemission as a function of the photons energy position in the absorption spectra.

3.3.4 X-ray photoemission electron microscopy (X-PEEM)

Conventional XPS does not provide spatial information below the probe size, *i.e.* tens of µm scale. If the same information is needed with a spatial resolution in the µm scale, X-ray photoemission electron microscopy (X-PEEM) is the characterization technique of choice. Zones which underwent different treatments (*e.g.* chemical etching, patterning, PFM polarization) can be compared immediately and on the very same sample, excluding any variation from one thin film deposition to the other.

X-PEEM is a full-field X-ray spectromicroscopy technique based on the photoemission process, in the same way as conventional XPS (photon in, electron out). The synchrotron radiation beam of tunable photons energy is the primary excitation source. Photoemitted electrons are guided through an electron microscope column which is similar to what is used for a LEEM. Then their energy is analysed within an analyser and finally they are projected on a screen providing a pattern at a given electron kinetic energy (*cf.* figure 3.18, from synchrotron SOLEIL HERMES beamline website[14]). The whole apparatus works under UHV conditions.

Output results are then an XPS images stack where each image corresponds to one electron kinetic energy and the colour scale is given by the intensity of the photoemission signal. From this stack we can define a region of interest (ROI) and do the sum of the intensity of each pixel of this ROI, for each image and for the whole stack, obtaining the XPS spectra for this ROI (analogous to XPS spectra in non-spatially resolved configurations). It gives simultaneously spectroscopic and microscopic information at scales that can reach tens of nm at best. This procedure is illustrated on figure 3.19.

[14]HERMES beamline web site: http://www.synchrotron-soleil.fr/Recherche/LignesLumiere/HERMES

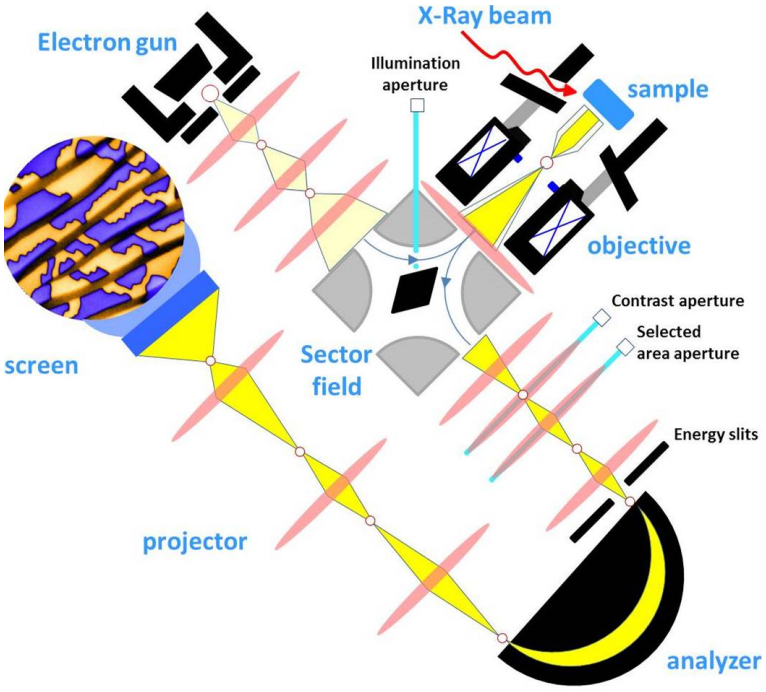

Figure 3.18: Scheme of the 90° X-PEEM apparatus available on the HERMES beamline at synchrotron SOLEIL (also featuring LEEM) (from Hermes beamline website)

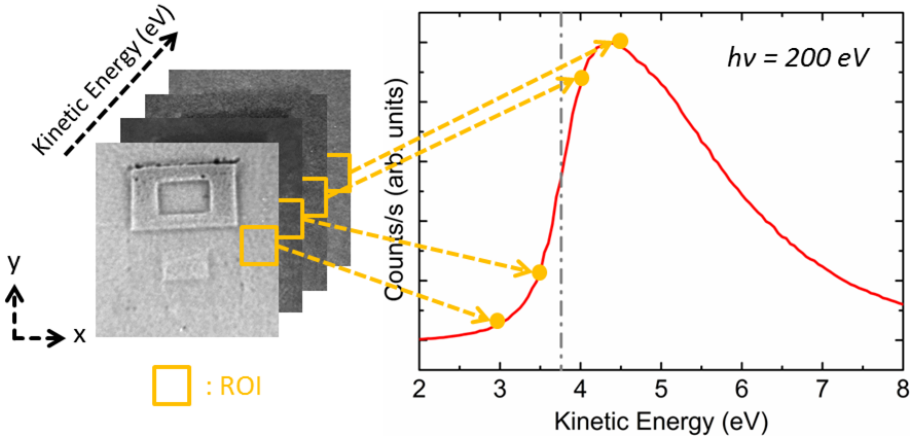

Figure 3.19: Photoemission treshold spectra extraction from an image stack at various kinetic energies through the integration of the signal of a region of interest (ROI). Sample: 15 nm $BaTiO_3$ / Nb:$SrTiO_3$ (001).

The use of synchrotron radiation in an X-PEEM setup grants a very useful degree of freedom by giving the possibility of tuning the incident photons energy. This makes possible the acquisition of RPES or XAS images stacks where each image corresponds to one electron kinetic energy or one incident photons energy (analogous to RPES or XAS spectra in non-spatially resolved configurations). Also, given the possibility to use various photons polarizations, we could perform dichroism experiments. Using two different photons polarizations, linear horizontal (LH) or linear vertical (LV), one can obtain the photons polarization vector either parallel (LH) or perpendicular (LV) to the sample surface, arising predominant in-plane or out-of-plane probing. The measurement geometry is shown on figure 3.20. We performed our X-PEEM experiments at the Nanoscience beamline (I06)[15] at the Diamond Light Source (UK).

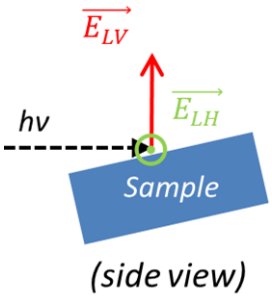

Figure 3.20: X-PEEM geometry offering in-plane sensitivity with LH photons polarization and out-of-plane sensitivity with LV photons polarization.

3.4 Photoelectrochemical characterization

The final application of the studied samples in my PhD is their use as photoanodes for solar water splitting. The performances of our materials for this application can be measured by photoelectrochemical characterization. A complete photoelectrochemistry experiment was set up and developed all along the PhD to perform photoelectrochemical measurements on our systems. The basic principle in photoelectrochemistry characterization is to study the evolution of the (photo)current flowing between a working electrode and a counter electrode as a function of the potential applied on the working electrode (with respect to a reference electrode). This occurs within a photoelectrochemical cell containing the three electrodes and an aqueous electrolyte. The photocurrent is defined as the difference between the current recorded without illumination (dark) and the one under illumination. Best photoanodes are expected to have the highest photocurrent for the lowest applied potential. Depending on the illumination regimes and voltage application conditions, one can access various material properties. The chosen current sign convention was the following:

[15] I-06 beamline web site: http://www.diamond.ac.uk/Beamlines/Surfaces-and-Interfaces/I06.html

- A positive current is said anodic: it corresponds to an electron flow from the counter electrode toward the working electrode through the electrolyte. Electrons are transferred from the counter electrode to the electrolyte (electrolyte reduction) and from the electrolyte to the working electrode (electrolyte oxidation);
- A negative current is said cathodic and flows the reverse way.

Therefore, since the photoanode is the location where electrolyte oxidation occurs for solar water splitting, the working electrode is the photoanode (the metal oxide semiconductor) and the counter electrode is the cathode (a Pt wire in our case). Oxido-reduction reactions are electrons exchange reactions, manifesting themselves as current flowing. Since solar water splitting is water oxido-reduction using charges generated by light absorption within the photoanode, the current measured in photoelectrochemical characterization is directly linked to the solar water splitting efficiency: the higher the current, the higher the evolved gas quantity.

3.4.1 Experimental setup

The experimental setup is illustrated on figure 3.21 and features the following devices (their use and functions will be detailed hereafter if needed):

- An illumination source (Newport 1000 W Xe Arc Lamp);
- A photoelectrochemical cell where the electrodes are dipped in the electrolyte (custom-made by Veral);
- A potentiostat (Princeton Applied Research (PAR) 263A);
- A monochromator (Cornerstone model 74004 from Newport);
- A power meter (model 1918-R from Newport) used for the light flux calibration (not shown on figure 3.21);
- A lock-in amplifier (PAR 5210, not shown on figure 3.21);
- One manual and one automatic optical chopper (model 71445 from Newport and MC-2000 from Thorlabs respectively);
- A computer to collect data and control the instruments (not shown on figure 3.21).

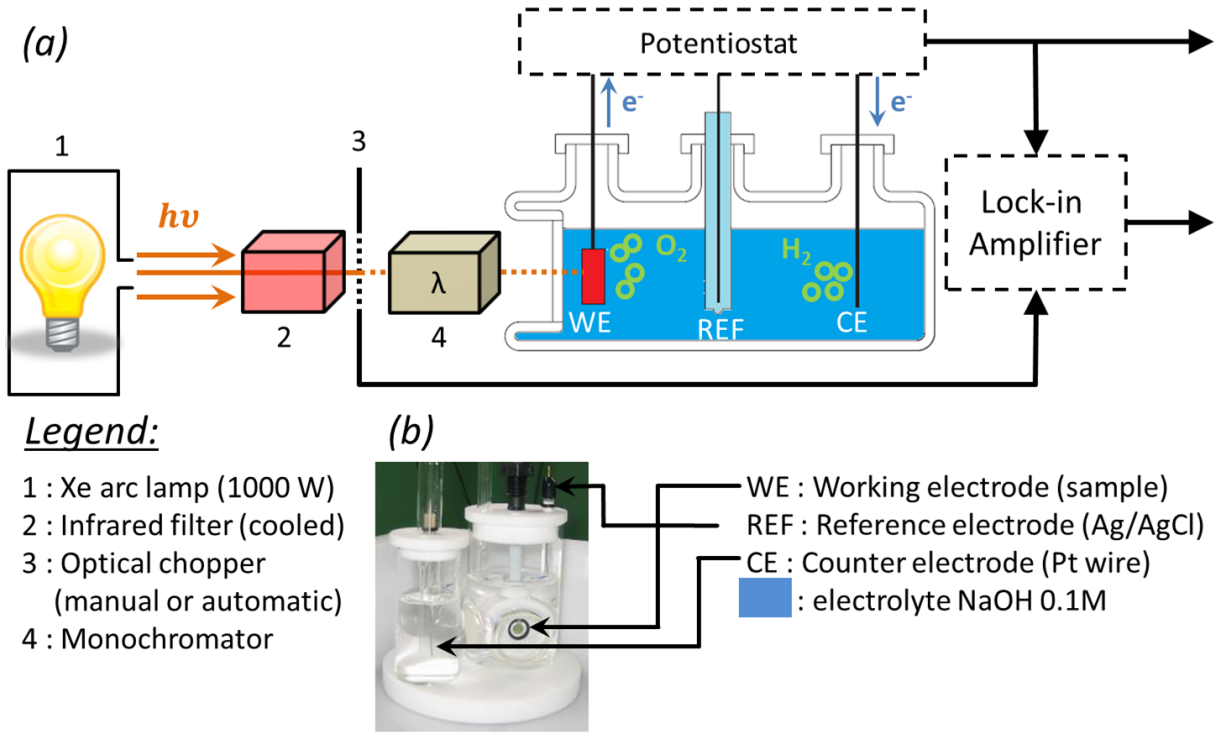

Figure 3.21: (a) Photoelectrochemistry setup, and (b) details of the mounting within the cell.

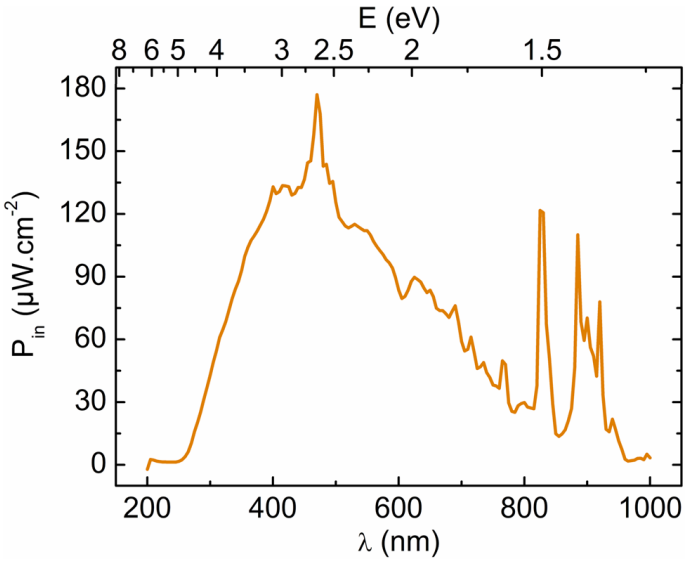

Figure 3.22: Light flux of the Xe arc lamp after the monochromator as a function of the photons energy (top axis) and wavelength (bottom axis).

3.4.1.a The illumination source

The illumination source provides a light flux mimicking the solar spectrum. Solar simulators exist (featuring a AM 1.5 filter), however in our case we used an ozone-free Xe arc lamp. Our lamp outgoing flux was calibrated using the monochromator and the power meter (*cf.* figure 3.22). We measured a mean monochromatic flux outgoing from the monochromator *ca.* 55 mW/cm^2 (between 200 and 1000 nm). We have evaluated (*cf.* appendix A.1) that it corresponds to a white light flux incoming on the monochromator *ca.* 104 mW/cm^2 ($\pm$ 5%). This is very close to the incoming AM 1.5 solar light flux at midday for mid-latitudes (equal to 100 mW/cm^2). Infrared radiations are filtered just after the lamp output to avoid inconvenient heating of the next elements.

3.4.1.b The photoelectrochemical cell (PEC)

The photoelectrochemical cell (PEC) contains the electrolyte, which is the aqueous chemical solution where water electrolysis occurs. We used a sodium hydroxide solution (NaOH) at a concentration of 0.1 M (pH = 13). In this electrolyte, three electrodes are dipped:

- The (photo)anode or working electrode (our sample), which was mounted using a dedicated sample holder that allows the contact only between the sample surface and the electrolyte;
- The cathode or counter electrode (a Pt wire);
- The reference electrode, mandatory to have an absolute potential reference, which was an Ag/AgCl reference electrode ($V_{Ag/AgCl}$ = +0.197V *vs.* NHE).

The sample is irradiated through a quartz window by the light flux coming from the lamp (eventually modified by the optical chopper and/or the monochromator). The sample is illuminated at the thin film side (front-side). The electrical contact with the external circuit is taken at the back of the sample (bottom of the substrate), which justifies the use of a good conductor as subtrate. All electrochemical measurements were performed at room temperature.

3.4.1.c The potentiostat

The potentiostat controls (and applies) the potential between the working and reference electrodes and measures the current flowing between the working and counter electrodes within a circuit external to the cell[16]. We used a Princeton Applied Research (PAR) 263A model. It was controlled by the Power Suite software (dedicated to electrochemistry) or by home-made LabView programs, in particular when several instruments were used and controlled at the same time (*e.g.* the potentiostat and the monochromator).

[16] More details about the functioning of a potentiostat are given in appendix A.2

In the continuation of this manuscript, the applied potential between the working and reference electrodes will be simply referred to as applied potential (or potential) and the current flowing between the working and counter electrodes will be simply referred as current.

3.4.2 I-V voltammetry

I-V voltammetries are the basic measurements of the photoelectrochemical properties. Here we measure the current as a function of the swept applied potential. In order to increase the signal/noise ratio, we acquire several $I(V)$ curves (typically 10) without illumination (in dark conditions, $I_{Dark} = I_D$) and under illumination (with light, $I_{Light} = I_L$). Curves are subsequently averaged and the current I in A is converted in current density J in mA/cm^2 (taking into account the illuminated surface). The photocurrent is then calculated using $J_{ph} = J_L - J_D$, and is exactly the sample answer to the incident light. Then to compare samples with each other, one can select the photocurrent at a particular potential (0.6V *vs.* Ag/AgCl for instance). It is possible to measure $J(V)$ curves with an On-Off chopped light obtained with an optical chopper (manual or automatic) in order to underline transient phenomena and to visualize easily the illumination effect on the current. Figure 3.23 shows J_D, J_L (with permanent and chopped light) and J_{ph} curves examples. On this figure an increase of the current thanks to the illumination is obvious. Also we can approximately derive the onset potential (applied potential for which the water electrolysis starts) which is *ca.* 0.4V *vs.* Ag/AgCl under illumination, and superior to 0.8V *vs.* Ag/AgCl in dark conditions.

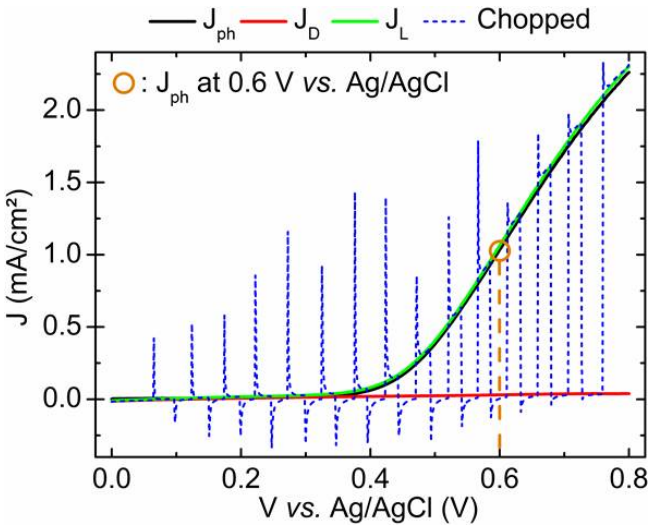

Figure 3.23: $J_{ph}(V)$ (black) , $J_D(V)$ (red) and $J_L(V)$ (for constant (green) and On-Off chopped (blue dots) illumination) curves. The photocurrent at 0.6V *vs.* Ag/AgCl is indicated. Sample: 16 nm 2.1 at.% Ti:α-Fe_2O_3 / Pt (111).

The applied potential was swept at 50 mV/s. The sweeping speed has an effect on the measured data (*cf.* figure 3.24). However as it can be seen on figure 3.24, the overall photocurrent does not vary with the applied potential sweeping speed (this was repeated on three samples).

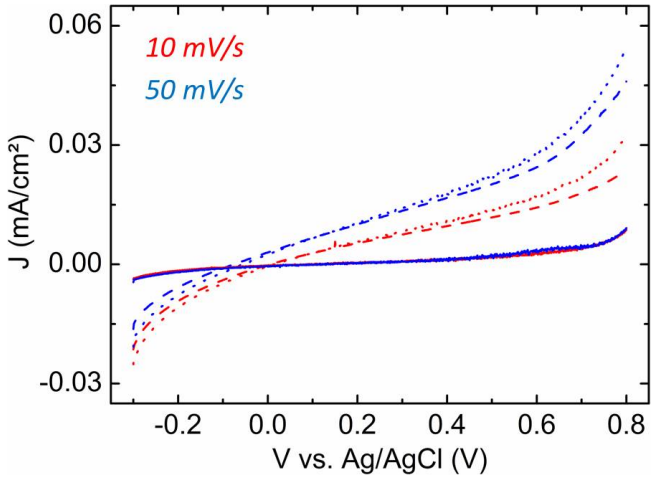

Figure 3.24: Applied potential sweep speed effect shown on $J(V)$ curves. The current in dark conditions (dashed lines), with light (dotted lines) and the photocurrent (solid lines) are shown for sweep speeds of 10 mV/s (red curves) and 50 mV/s (blue curves). Sample : 27 nm α-Fe_2O_3 / Pt (111).

For the I-V voltammetries performed in this PhD, the applied potential window varied from [0 ; +0.8] to [-1 ; +0.8] (in V *vs.* Ag/AgCl), depending on the samples measured.

3.4.3 Incident photon to current efficiency (IPCE)

Current density measurements as a function of the incident light wavelength with monochromatic light (using our monochromator), noted $J(\lambda)$, keeping the applied potential constant defines the incident photon to current efficiency (IPCE). IPCE provides insights about the photoanode efficiency and is given by equation 3.7 [55]:

$$IPCE\,(\lambda)\,[\%] = \frac{h \times c}{\lambda\,[m]} \times \frac{J_{ph}\,(\lambda)\,[mA/cm^2]}{e \times P\,(\lambda)\,[mW/cm^2]} \times 100\% \tag{3.7}$$

Where $J_{ph}(\lambda)$ is the photocurrent density, $P(\lambda)$ the incident power density, λ the wavelength of the incident light and c the light velocity (3×10^8 m/s). IPCE (between 0 and 100%) corresponds for each wavelength to the fraction of incident photons which effectively participates to the water electrolysis photocurrent.

IPCE data were extracted from $J(\lambda)$ data. The latter were obtained using a home-made LabView program. The wavelength was varied between 200 and 1000 nm, with 10

nm steps. This corresponds to the relevant range of wavelength which can be absorbed by semiconductors dedicated to solar water splitting. In order to minimize the transient signals due to the voltage application, the potential was held constant during 200 s prior to $J(\lambda)$ data acquisition. Figure 3.25 shows the evolution of the current density under white light illumination as a function of the time after voltage application. We can notice a transient variation of the current density after the voltage application (quick variation at the beginning, then progressive stabilization). A $J(\lambda)$ measure lasts *ca.* 3.5 minutes and according to figure 3.25 the integrated current density variation during this period is less than 5% if the measure starts 200 s after the voltage application.

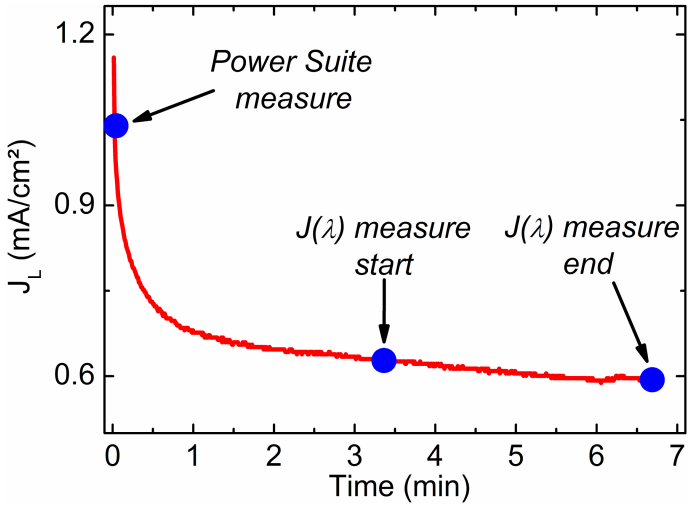

Figure 3.25: Current density *vs.* time curve for white light illumination at a potential of 0.6V *vs.* Ag/AgCl. Sample: 16 nm 2.1 at.% Ti:α-Fe_2O_3 / Pt (111).

3.4.4 Optical chopper + lock-in amplifier (OCLIA) characterization

Transient variations of the photocurrent (also simply called transients), visible using chopped incident light, are related in part to bulk and surface recombination phenomena [6, 35]. When a hole reaches the semiconductor surface, there is a competition between the water oxidation reaction (transfer from the hole to the electrolyte) and the recombination of the hole at the surface (with electrons from the conduction band). If the water oxidation kinetic is too slow, holes will accumulate at the interface and the recombination risk is very high. Surface recombination can also be intensified if intra band gap states exist (due to ion adsorption or surface reconstruction for instance). The surface charge dynamics related to transient phenomena due to chopped illumination are shown on figure 3.26. The left panel shows ideal and real photocurrent profiles under chopped light as a function of the time at a given applied potential. The real photocurrent profile after the light is set to ON can be divided

into four regimes for which the physical phenomena are illustrated in the form of a simplified band diagram on the right panel of figure 3.26:

- a: ideal behaviour, no surface recombination: maximal photocurrent (large green arrows);
- b: progressive hole trapping at the surface: photocurrent limitation (small red arrows);
- c: steady state regime: balance between surface recombination (red arrows) and photocurrent (green arrows);
- d: no light: recombination with valence band electrons, cathodic (photo)current (red).

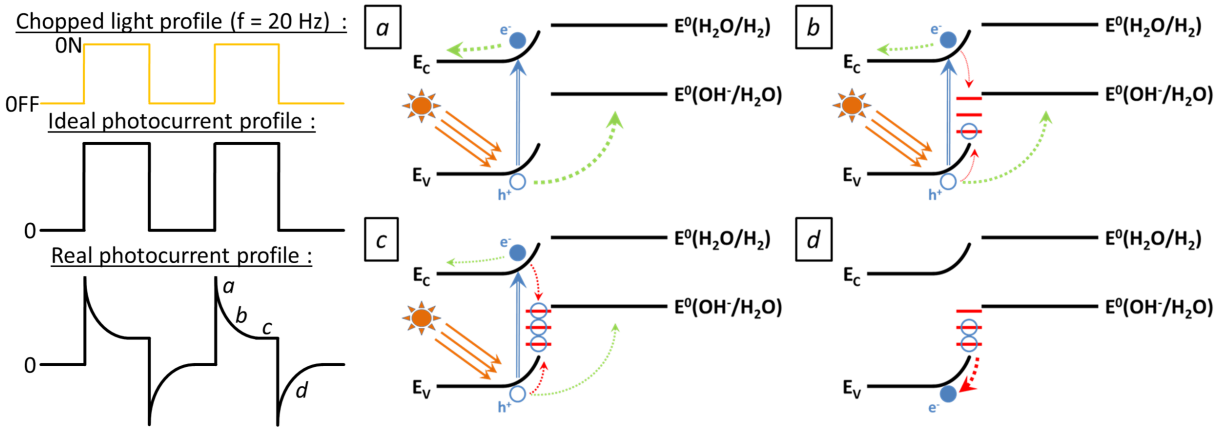

Figure 3.26: Chopped light induced transient phenomena. Left panel: chopped light profile and associated ideal and real photocurrent profiles. Right panel (a→d): surface charges dynamics for the four different situation during transients.

When increasing the applied potential on the photoanode, the transients diminish because the driving force given by the potential accelerates the water oxidation kinetics.

To characterize the more or less important limitation of the photocurrent by surface hole trapping, one should measure the difference of photocurrent between step a and step c. The photocurrent during step c (steady state regime) is easily measurable contrary to the photocurrent during step a since the duration of step a is very short. Using an automatic Optical Chopper and a Lock-In Amplifier (OCLIA acronym), the photocurrent during step a (and perhaps step b) can be measured. The former is used to obtain a chopped light illumination at a controlled frequency and the latter to realize a phase sensitive detection of the resulting photocurrent. Indeed the lock-in amplifier detects the response signal (the transient photocurrent) which is at the same frequency than the reference signal (the optical chopper opening and closing, equivalent to the chopped light profile). For this purpose we used a PAR 5210 lock-in amplifier and an optical chopper from THORLABS at a reference

frequency of 20 Hz. The integration is done during the transient regime (steps a and b). A home-made LabView program was used to perform these experiments. Unfortunately, we were not able to write a LabView program allowing the measurement of the OCLIA signal in white light excitation conditions. Therefore, the OCLIA measurements were done using monochromatic light. Our OCLIA method is a particular case of intensity-modulated photocurrent spectroscopy (IMPS). In IMPS experiments, the frequency response of the photocurrent to a sinusoidal modulation of the light around a particular flux value (contrary to a ON/OFF modulation in our case) is measured [35].

The OCLIA method also allows the measurement of the IPCE for samples having a very low photocurrent thanks to the increased signal-to-noise ratio due the lock-in detection (*e.g.* our bare hematite films for which the photocurrent transients are high). It is then noted PSIPCE for phase sensitive IPCE.

4 Single layers of undoped hematite

Hematite (α-Fe_2O_3) has attracted much attention for application as photoanode since the first report by Hardee and Bard back in 1976 [144]. Indeed due to its quasi-ideal band gap ($\approx$ 2.2 eV) for solar water splitting applications, this material is able to absorb *ca.* 40% of the solar light spectrum and its theoretical solar-to-hydrogen conversion yield reaches 13 % [5]. It is abundant on earth [1] and very stable in aqueous environments, which makes it a serious candidate in the framework of green energy production [32]. Moreover, the valence band edge of hematite is located below the OH^- / O_2 redox potential which favours the water oxidation reaction [96].

Unfortunately, hematite has also drawbacks. It has been demonstrated that it has weak transport properties (low conductivity and low hole diffusion length *ca.* 2-4 nm) [50, 51] and poor surface kinetics [145] due to hole recombination at the surface [128]. Besides of this, the conduction band edge of α-Fe_2O_3 is well below the H_2O / H_2 redox level (*cf.* 2.3.2), thus a significant external bias is necessary to promote water splitting [120]. Various strategies, detailed in 2.4, can be employed to improve the performances of hematite-based photoanodes.

Kay et al. reported in 2006 a benchmark photocurrent density value of 2.2 mA/cm^2 at an applied potential of *ca.* 0.2V *vs.* Ag/AgCl for undoped dendritic hematite photoanodes [96]. Using multiple strategies provides the state-of-the-art performance of hematite photonoades. To the best of our knowledge, the highest photocurrent density ever recorded using hematite photoanodes is 4.32 mA/cm^2 at an applied potential of *ca.* 0.2V *vs.* Ag/AgCl. This result was reported in 2013 by Kim et al. [69] who studied Pt-doped wormlike hematite photoanodes coated with a cobalt phosphide cocatalyst. Very recently Jang et al. reported unassisted solar water splitting using an amorphous Si photocathode (coated with a TiO_2 layer and a Pt-based cocatalyst) and a hematite photoanode (coated with a mixed Ni-Fe oxide cocatalyst), with a solar-to-hydrogen efficiency of 0.9 % [115]. Gurudayal et al. realized unassisted solar water splitting using a tandem configuration consisting in a photoanode made of Mn-doped hematite nanorods coated with a cobalt-phosphide cocatalyst in series with a halide perovskite solar cell (2.4 % solar-to-hydrogen efficiency) [66]. These results are encouraging for the use of hematite as photoanode in low cost devices.

This chapter presents results about iron oxides thin films of different crystallographic structures and various oxygen stoichiometries. The crystallographic structure of iron oxide is a key point when it comes to photoelectrochemical properties. Also the oxygen stoichiometry is a key parameter for the optimization of iron oxide photoanodes. Oxygen vacancies are expected to act as shallow donor dopants in hematite [72–77] (energy states close to the conduction band minimum). The creation of an oxygen vacancy, ejecting the gaseous oxygen, leaves two electrons by oxygen atom. This will increase the overall carrier concentration and therefore the conductivity. However the introduction of two extra electrons is expected to

reduce Fe^{3+} into Fe^{2+} [146]. This iron reduction can be beneficial or detrimental in the framework of solar water splitting. On the one hand, since the conduction mechanism in non ideal hematite (*i.e.* oxygen deficient) is attributed to polaron hopping conduction thanks to Fe^{3+}/Fe^{2+} mixed valence (electrons "hop" from Fe^{3+} to Fe^{2+}) [34], oxygen vacancies can be expected to indirectly increase the conductivity [73] and the carrier mobility [147]. On the other hand, at too high concentrations, Fe^{2+} sites may serve as recombination centers for photoexcited holes because of the presence of electronic states within the band gap [143], which could lower the photocurrent [32, 72]. The increase or decrease in photocurrent will be the result of the competition between these two concomitant phenomena. In addition to this, beyond a particular concentration of oxygen vacancies in hematite a phase transition toward the not photoactive magnetite Fe_3O_4 can occur.

The effect of crystallographic structure and oxygen stoichiometry on photoelectrochemical properties for iron oxide films is a tricky issue to tackle. Indeed, a very good control of the global samples properties is expected in order to conduct properly this kind of study. For instance, in the case of polycrystalline films, annealings can result in changes in (i) crystallites size, (ii) predominant crystallographic orientation, (iii) surface roughness and morphology. Entangled properties prevent from studying the effect of a single parameter. The use of single crystalline films allows to overcome this issue.

We present firstly in section 4.1 results concerning iron oxide thin films of constant thickness (15 nm) having different crystallographic structures, grown by OPA-MBE. They were obtained by changing either the substrate or the oxidizing plasma conditions (*i.e.* the BARATRON ® diaphragm opening).

In sections 4.2 and 4.3 results about iron oxides having different oxygen vacancies concentration are shown. Oxygen vacancies can be obtained by different ways. A first solution is to elaborate an under-stoichiometric iron oxide film and then anneal it under a more or less O_2 rich atmosphere. We explored this method in section 4.2 by performing ambient air annealings on 15 nm thick Fe_3O_4 (111) films grown by OPA-MBE. A second solution consists in creating oxygen vacancies by annealing stoichiometric hematite in oxygen-deficient atmospheres. To do so, we performed *ex situ* UHV annealings on 15 nm α-Fe_2O_3 (0001) films grown by OPA-MBE and we characterized these films by EXAFS (4.3). It should be noted that our annealings were performed with relatively low temperatures (200-450°C range) compared to what is reported in the literature concerning oxygen vacancies engineering in hematite [148, 149]. For a broader view one may note that oxygen vacancies can also be generated through the elaboration of hematite under a mixed oxygen-hydrogen atmosphere [149] or through the deposition of an "oxygen scavenger" material, *e.g.* a carbon layer [150].

When possible, each sample was analysed by *in/ex situ* RHEED and *in/ex situ* XPS, and the photocurrent was measured.

4.1 Iron oxides films of different structures

We exploited the versatility of the OPA-MBE technique to grow iron oxides films of different structures. To keep our model systems approach, the selected structures had to fulfil epitaxial growth conditions.

4.1.1 Presentation of the iron oxides grown by OPA-MBE

Using Pt (111) and Nb:$SrTiO_3$ (001) substrates (Nb doping level of 1 at.%), we elaborated the following iron oxides.

Hematite α-Fe_2O_3. Hematite is the most stable iron oxide [8, 151]. It has a corundum structure (space group $R\bar{3}C$, rhombohedral primitive cell). The lattice parameter of the primitive rhombohedral cell is 0.543 nm and the α angle equals 55.3°. It consists in a compact hexagonal piling of oxygen O^{2-} anions along the c axis (vertical axis, (0001) direction). Fe^{3+} cations occupy two thirds of the octahedral sites which are slightly distorted. The lattice parameters of the primitive hexagonal cell are $a = b = 0.504$ nm and $c = 1.375$ nm. A scheme of the structure is given figure 4.1. Like most of the metal oxide semiconductors, hematite is a n-type semiconductor, due to a slight deviation of the oxygen stoichiometry from its ideal value. Using Pt (111) as substrate in highly oxidizing conditions (BARATRON ® set to 3.1 turns), we expect the growth of α-Fe_2O_3 (0001) with a compressive lattice mismatch of 5 % assuming an epitaxial relationship of $\sqrt{3}\times\sqrt{3}$R30° [132, 152].

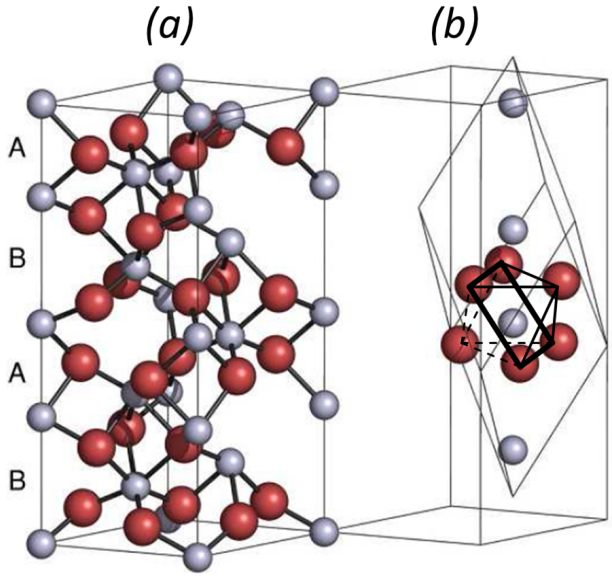

Figure 4.1: Hematite primitive cell in the (a) hexagonal system and in the (b) rhombohedral system. The small blue spheres stand for iron cations and the large red ones for oxygen anions. The oxygen octahedron is also highlighted in black on (b). Reproduced from [133].

Magnetite Fe_3O_4. Magnetite (Fe_3O_4) has an inverse spinel structure (space group $Fd\bar{3}m$) [151] with a bulk lattice parameter of 0.8395 nm [153, 154]. In this structure, Fe cations are surrounded by oxygen anions forming tetrahedra (Fe tetra site) or octahedra (Fe octa site). The occupancy ratio of tetrahedral and octahedral sites is 1:2. On tetrahedral sites, Fe cations are in the Fe^{3+} valence state and on octahedral sites, Fe cations are either in the Fe^{2+} or Fe^{3+} valence state, with a 50 % ratio. The chemical formula can be written as $[Fe^{3+}]_{tetra}[Fe^{3+}Fe^{2+}]_{octa}O_4$ [151]. The elementary cell is shown on figure 4.2. It is a ferrimagnetic and half metallic material [133]. The lattice parameter of the Fe_3O_4 (111) surface is 0.593 nm and the one of the Pt (111) surface is 0.277 nm ($= \frac{0.554}{2}$ nm). Therefore using Pt (111) as substrate in weakly oxidizing conditions (BARATRON ® set to 1.3 rounds), the expected iron oxide phase grown is Fe_3O_4 (111) with a compressive lattice mismatch of 6 % assuming a cube-on-cube epitaxial relationship.

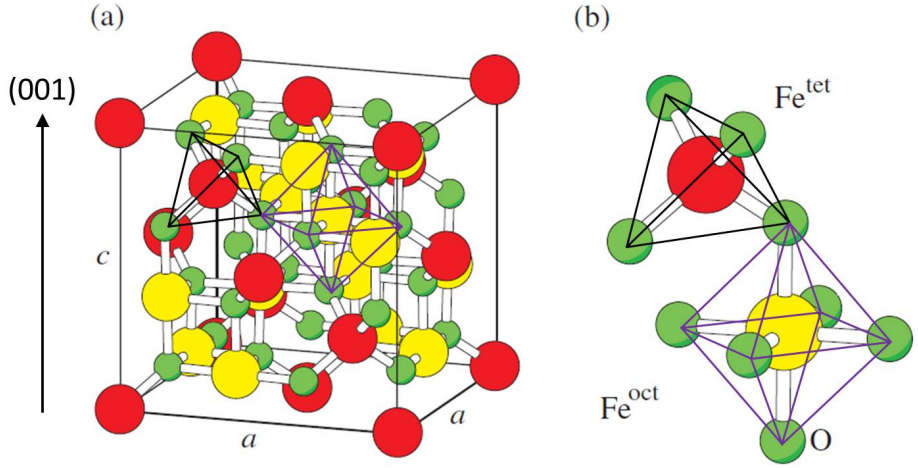

Figure 4.2: Magnetite crystallographic structure: (a) elementary cubic cell and (b) detail of the tetrahedral and octahedral sites. Large red (resp. yellow) spheres stand for iron in tetrahedral (resp. octahedral) sites whereas small green spheres stand for oxygen anions. Tetrahedral (resp. octahedral) sites are highlighted in black (resp. blue) [155].

Maghemite γ-Fe_2O_3. Maghemite (γ-Fe_2O_3) can be seen as a Fe^{2+}-deficient magnetite where octahedral sites are no more occupied by either Fe^{2+} or Fe^{3+} ions like in Fe_3O_4 (1:1 ratio), but by either Fe^{3+} ions or cation vacancies (5:1 ratio), with a reported lattice parameter of 0.835 nm [153, 154]. Hence the maghemite chemical formula is $[Fe^{3+}]_{tetra}[Fe^{3+}_{5/3}\square_{1/3}]_{octa}O_4$ [151] which is equivalent to $[Fe^{3+}_{3/4}]_{tetra}[Fe^{3+}_{5/4}\square_{1/4}]_{octa}O_3 = Fe_2O_3$. In bulk γ-Fe_2O_3 the tetrahedral/octahedral occupancy ratio is therefore 1:$\frac{5}{3}$ (*vs.* 1:2 for bulk Fe_3O_4). Using Nb:$SrTiO_3$ (001) (lattice parameter of 0.3905 nm $= \frac{0.781}{2}$ nm) as substrate in highly oxidizing condi-

tions (BARATRON ® set to 3.1 turns), we can expect the growth of γ-Fe_2O_3 (001) with a compressive lattice mismatch of 6.5 % assuming a cube-on-cube epitaxial relationship.

Amorphous Fe_2O_3. In addition we used a Pt foil (laminated Pt) as substrate in order to grown an amorphous or polycrystalline Fe_2O_3 film (am-Fe_2O_3) in highly oxidizing conditions (BARATRON ® set to 3.1 turns).

4.1.2 Growth followed by *in situ* RHEED

Figure 4.3 and 4.4 present the RHEED patterns of the various iron oxide structures grown by OPA-MBE on Pt (111) and Nb:$SrTiO_3$ (001) substrates respectively. No RHEED patterns (only a uniform background) were obtained for the am-Fe_2O_3 film grown on a Pt foil, accounting for an amorphous structure. All other samples showed RHEED patterns with straight lines, accounting for a 2D growth (Frank-van der Merwe mode), at least up to a thickness of 15 nm.

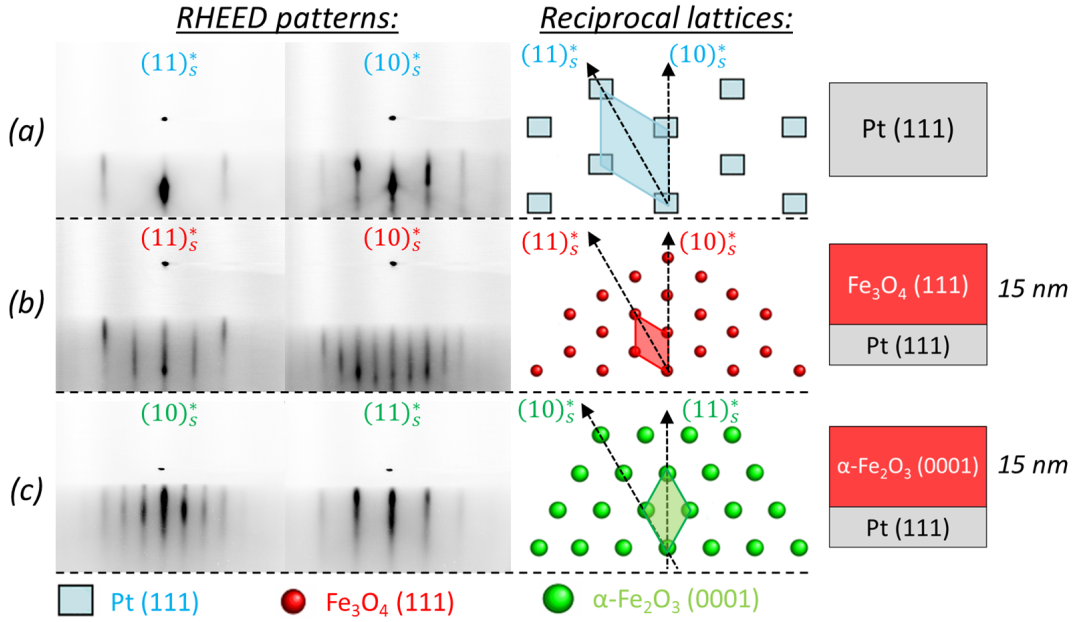

Figure 4.3: (Left panel) RHEED patterns along two particular azimuths corresponding to the two reciprocal space surface diffraction directions of lowest Miller indexes and (right panel) corresponding surface reciprocal lattices for various iron oxides of 15 nm thickness grown by OPA-MBE: (a) Pt (111) substrate, (b) Fe_3O_4 (111) / Pt (111), α-Fe_2O_3 (0001) / Pt (111). The elementary cell (in the reciprocal space) is also shown with the same colour than the corresponding reciprocal lattice.

On figure 4.3, the derived surface reciprocal lattice is consistent with the expected growths of Fe_3O_4 (111) on Pt (111) (spinel, figure 4.3.b) and α-Fe_2O_3 on Pt (111) (corundum, figure 4.3.c) [132]. In the case of the γ*-Fe_2O_3 (001) / Nb:$SrTiO_3$ (001) growth[17] (figure 4.4.a,

[17] The use of the γ*-Fe_2O_3 terminology is justified later in this section (see 4.1.4).

bottom line), the RHEED patterns correspond to the ones expected for maghemite γ-Fe_2O_3 (spinel structure lines) and are fuzzy. This is maybe due to the fact that the structure contains defects because it is a metastable oxide. In addition we plotted on figure 4.4.c the integrated RHEED patterns (along the streak direction) corresponding to the $(11)^*_s$ direction of the Nb:$SrTiO_3$ (001) surface reciprocal lattice. One observes that the spacing between the streaks is divided by two, accounting for a γ*-Fe_2O_3 (001) elementary cell in the direct space twice larger than the one of Nb:$SrTiO_3$ (001).

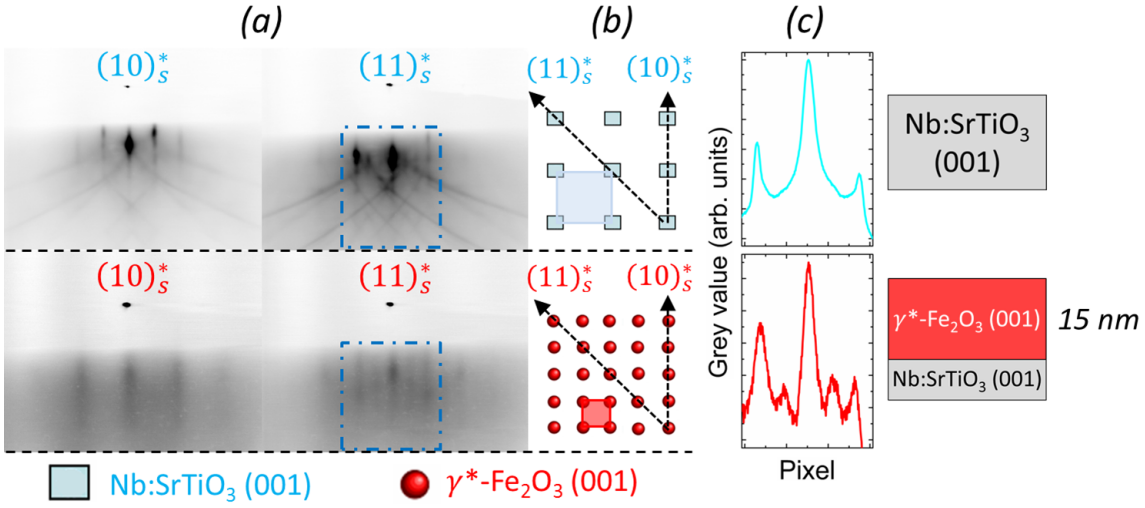

Figure 4.4: (a) RHEED patterns along two particular azimuths corresponding to the two reciprocal space surface diffraction directions of lowest Miller indexes, (b) corresponding surface reciprocal lattices and (c) curves of the $(11)^*_s$ RHEED patterns integrated along the streak direction, according to the dash-dotted blue integration box highlighted on (a). The upper (resp. bottom) line shows the data for the Nb:$SrTiO_3$ (001) substrate (resp. γ*-Fe_2O_3 (001) / Nb:$SrTiO_3$ (001) film). The elementary cell (in the reciprocal space) is also shown with the same colour than the corresponding reciprocal lattice.

4.1.3 *In situ* XPS

The reference of binding energies[18] was obtained through a Pt Fermi level measurement on an ultra-thin iron oxide film (thickness below 5 nm) deposited on Pt (111) (internal energy reference) resulting in an O*1s* line position at 530.1 eV for hematite.

The Fe*2p* core levels of our iron oxides samples of different structures are shown on figure 4.5.a. Fe*2p* lines and shake-up satellites give insights about the iron valence state in the oxide (*cf.* figure 3.7 subsection 3.2.2) [134]. More precisely a shake-up satellite closer to the Fe$2p_{1/2}$ (resp. Fe$2p_{3/2}$ line) stands for a Fe^{2+} (resp. Fe^{3+}) valence state. The Fe_3O_4 sample showed classical features for a Fe^{2+}/Fe^{3+} mixed iron valence state with broad Fe$2p_{1/2}$ and

[18] The requirement for a binding energy reference was discussed in 3.2.2.

Fe$2p_{3/2}$ lines *ca.* 710.7 eV and 723.7 eV binding energy respectively and no visible shake-up satellite [134]. Other films, expected to exhibit a Fe^{3+} valence state only (Fe_2O_3 chemical formula), present narrow Fe$2p_{1/2}$ and Fe$2p_{3/2}$ lines *ca.* 711.2 eV and 724.7 eV binding energy respectively, as well as the typical Fe^{3+} shake-up satellite around 719.2 eV binding energy. The Fe$2p_{1/2}$ and Fe$2p_{3/2}$ lines positions are respectively at 0.5 eV and 1 eV higher binding energies than Fe_3O_4, which is in agreement with previous works of the group [134]. Valence band spectra (figure 4.5.b) show that Fe_3O_4 features a metallic behaviour whereas other samples have *ca.* the same band gap than hematite.

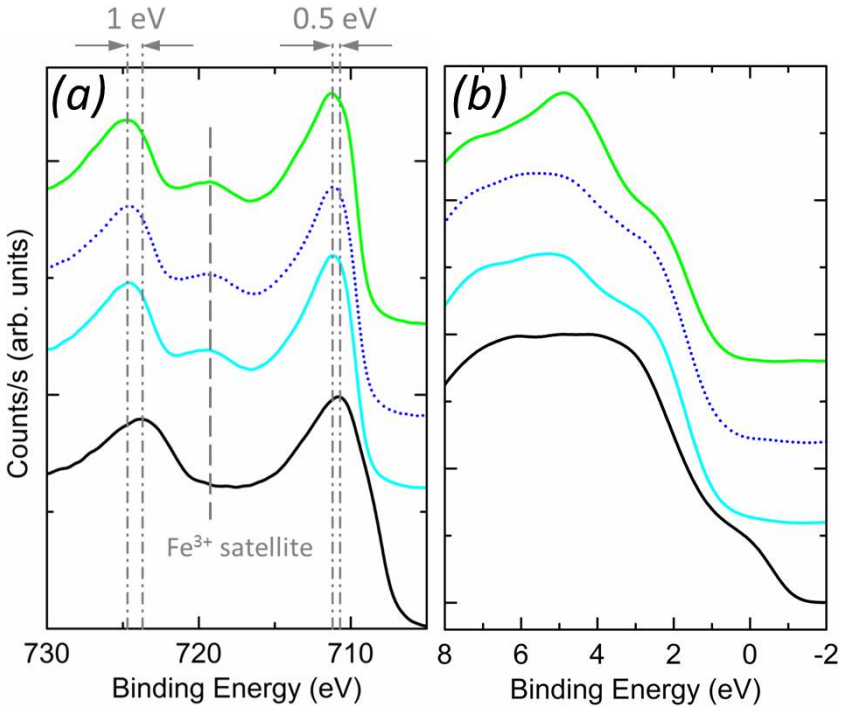

Figure 4.5: (a) Fe$2p$ core levels and (b) valence band XPS spectra of iron oxides of different crystallographic structures grown by OPA-MBE. From bottom to top: Fe_3O_4 (111) (black solid line), γ*-Fe_2O_3 (001) (cyan solid line), am-Fe_2O_3 (blue dotted line), α-Fe_2O_3 (0001) (green solid line).

4.1.4 Investigation of the γ*-Fe_2O_3 / Nb:$SrTiO_3$ (001) film structure

The choice of Nb:$SrTiO_3$ (001) as substrate is well adapted for the growth of γ-Fe_2O_3. Indeed the RHEED patterns feature the spinel lines (*cf.* figure 4.3.c) and the XPS analysis proves the absence of detected Fe^{2+} for this film (*cf.* figure 4.5.a). We investigated more quantitatively the crystallographic structure through RHEED and EXAFS analysis.

From the RHEED patterns obtained during the growth, we derived the in-plane lattice parameter (*cf.* 3.2.1) [55, 132]. We represented a generic lattice parameter p which is calculated by measuring the spacing between streaks in the RHEED patterns obtained over

the particular diffraction direction $(11)_s^*$ of the Nb:$SrTiO_3$ (001) surface reciprocal lattice. Its evolution *vs.* the deposited film thickness is depicted on figure 4.6. Here the in-plane parameter p is equal to:

- the in-plane lattice parameter in the case of $SrTiO_3$ (001) (0.393 nm at the deposition temperature of 900K [156]);
- $a_{\gamma-Fe_2O_3}/2$ in the case of γ-Fe_2O_3 (001) (where $a_{\gamma-Fe_2O_3}$ is the in-plane lattice parameter of γ-Fe_2O_3 (001), assuming a cube-on-cube epitaxial relationship with Nb:$SrTiO_3$ (001) and a γ-Fe_2O_3 (001) elementary cell in the direct space twice larger than the one of Nb:$SrTiO_3$ (001));

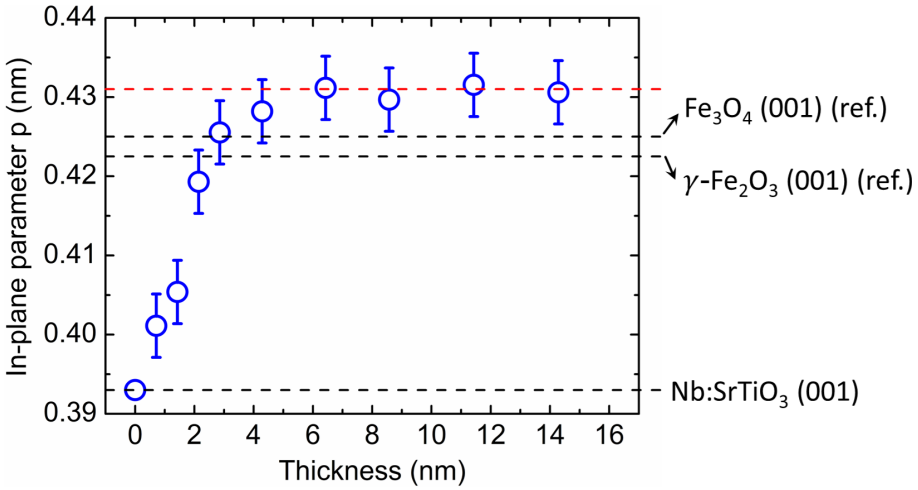

Figure 4.6: In-plane lattice parameter p derived from the $(11)_s^*$ direction of the Nb:$SrTiO_3$ (001) surface reciprocal lattice in RHEED patterns as a function of the film thickness for our 15 nm γ*-Fe_2O_3 (001) film grown by OPA-MBE. Black dashed lines stand for the lattice parameter p of the substrate Nb:$SrTiO_3$ (001) and of references γ-Fe_2O_3 (001) and Fe_3O_4 (001) (bulk values taken from literature). Thermal expansion was taken into account.

The in-plane parameter p progressively increases from the substrate lattice parameter to an asymptotic value. This asymptotic value is estimated to be 0.431 ± 0.004 nm, corresponding to a lattice parameter of 0.862 ± 0.008 nm at the deposition temperature of 900K. Considering the same thermal expansion coefficient of 2.06×10^{-5} K^{-1} for our γ*-Fe_2O_3 / Nb:$SrTiO_3$ film than for bulk magnetite (and bulk maghemite since they have the same crystallographic structure) [157], we obtain a lattice parameter of 0.851 ± 0.008 nm at room temperature. Therefore, considering lattice parameters value of 0.835 nm and 0.8395 nm for bulk maghemite (resp. magnetite) at room temperature [153, 154], we observe a dilatation of the in-plane parameter of about 2 % (resp. 1.4 %) with respect to the bulk maghemite (resp. magnetite) value although we expected a compression (*cf.* 4.1.1).

RHEED is sensitive to the first atomic layers beyond the surface. To go further in the crystallographic structure investigation, we measured the EXAFS spectra of this γ*-Fe_2O_3 (001) / Nb:$SrTiO_3$ (001) film. They were recorded at the Fe K edge in normal incidence (linear photons polarization parallel to the film surface) and grazing incidence (linear photons polarization perpendicular to the film surface)[19], at room temperature on the SAMBA beamline at synchrotron SOLEIL. The EXAFS raw data were analysed according to the approach detailed in 3.3.2. The spectra were fitted with HORAE and FEFF 8.4 codes [140–142] assuming a magnetite (Fe_3O_4) structure (spinel). We did not differentiate Fe^{2+} from Fe^{3+}. However, to perform the data fitting using FEFF, we used a structure with Fe in tetrahedral site as central atom and another structure with Fe in octahedral site as central atom. Then we imposed the maghemite occupancy ratio of tetra:octa $= 1:\frac{5}{3}$ for the calculation. We fitted the two incidences together and used paths of length up to 3.8 Å around the absorbing Fe atoms, corresponding to the nearest neighbours shells. We checked that multiple scattering is negligible. In order to take into account the strain due to epitaxy and to reduce the number of parameters, we introduced two structural expansion factors: α parallel to the (001) basal plane of the bulk magnetite structure (*i.e.* parallel to the film surface) and β perpendicular to it. These expansion factors are used for all paths, including the first shell of oxygen neighbours. The other fitting parameters are the Debye-Waller factors corresponding to each shell and type of neighbour to take into account additional structural disorder. EXAFS oscillations spectra and the corresponding fits are presented on figure 4.7. One can notice that experimental spectra in normal and grazing incidences are almost identical, accounting for an isotropic crystallographic structure. The best fits are represented figure 4.7, showing that the supposed spinel structure is accurate for this film.

Interatomic distances for the first shell of neighbours and corresponding Debye-Waller (DW) factors as well as the expansion factors (α and β) are given in table 4.1. It can be seen that the best fit was obtained with an isotropic structural expansion of *ca.* 2.4 ± 0.5 % with respect to bulk magnetite. This is in agreement with the in-plane lattice parameter obtained by RHEED for this film, which is *ca.* 1.4 % higher than the bulk magnetite lattice parameter. Also the DW factors values show that the environment of iron in octahedral site is highly perturbed with respect to bulk magnetite (the higher the DW, the stronger the perturbation).

[19] See figure 3.14 in subsection 3.3.2 for more details.

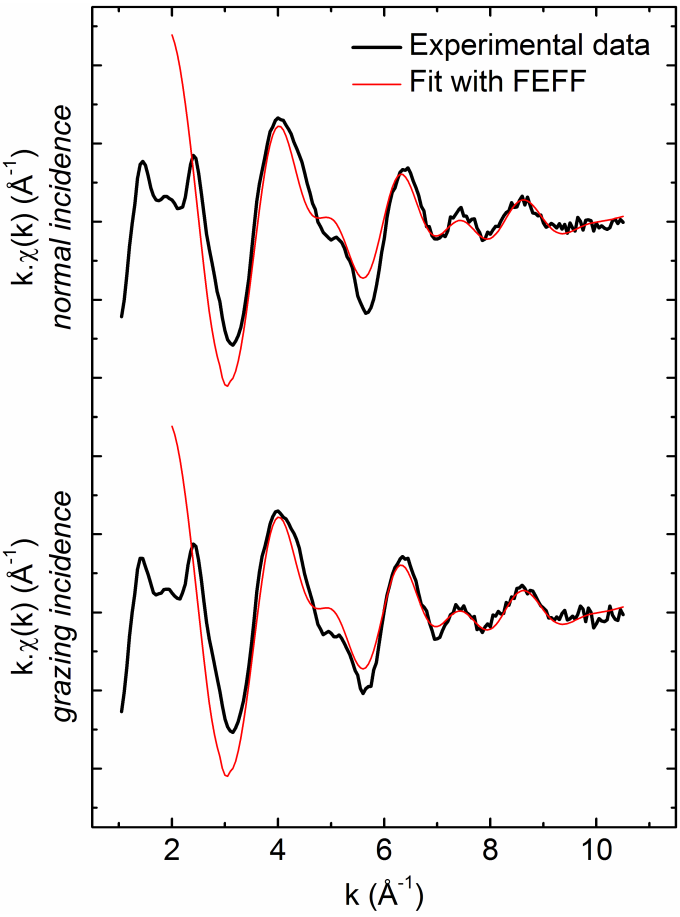

Figure 4.7: Experimental (black thick line) $k\chi(k)$ EXAFS oscillations and fit (red thin line) by FEFF calculations (assuming a spinel structure) obtained in normal (upper curves) and grazing (lower curves) incidences. Sample : 15 nm γ*-Fe_2O_3 (001) / Nb:$SrTiO_3$ (001).

Sample	Fe site	Fe-O		Fe-Fe tetra		Fe-Fe octa		α	β
		R	DW	R	DW	R	DW		
γ*-Fe_2O_3 (001)	tetra	1.93	0.001	3.72	0.072	3.56	0.072	2.4	2.4
	octa	2.11	0.025	3.56	0.072	3.04	0.012		
Bulk magnetite	tetra	1.89		3.63		3.48			
	octa	2.06		3.48		2.97			

Table 4.1: Interatomic distances (R) and Debye-Waller factors (DW) obtained by EXAFS simulations for our 15 nm γ*-Fe_2O_3 (001) / Nb:$SrTiO_3$ (001) film and corresponding lengths in bulk magnetite, at the Fe K edge. The R (resp. DW) values are given in Å (resp. Å^{-2}), the error bar is $\pm$ 0.03 Å (resp. $\pm$ 10%). The expansion factors (α and β) are expressed in % and the error bar is $\pm$ 0.5%.

The lattice parameter of our 15 nm γ*-Fe_2O_3 (001) / Nb:$SrTiO_3$ (001) film, calculated using RHEED (resp. EXAFS) data, is 1.4 % (resp. 2.4 %) higher than the reported values for bulk Fe_3O_4 [153, 154] and Fe_3O_4 (001) films grown on $SrTiO_3$ (001) by pulsed laser deposition [158]. In addition our calculated lattice parameter (using the RHEED data) is 2 % higher than the reported values for bulk γ-Fe_2O_3 [153, 154] and γ-Fe_2O_3 (001) films grown on MgO (001) by molecular beam epitaxy [159]. The XPS analysis showed clearly the presence of Fe^{3+} only and did not reveal any interdiffusion from the Nb:$SrTiO_3$ substrate that may play a role in increasing the lattice parameter with respect to bulk references. Moreover RHEED and EXAFS results are compatible with a spinel structure. This led us to consider that we obtained a structure which has the characteristics of maghemite (stoichiometry and crystallographic structure), except for the particular lattice parameter which deviates of *ca.* 2 % with respect to the bulk value, which is why we used the γ*-Fe_2O_3 terminology for this structure. A lattice parameter of $a_{\gamma*-Fe_2O_3} = 0.851 \pm 0.008$ nm corresponds to a lattice mismatch with Nb:$SrTiO_3$ (001) *ca.* 8.2 %. This can explain the very fast lattice parameter relaxation (within the first 5 nm, *cf.* figure 4.6), the fuzzy RHEED patterns (*cf.* figure 4.3.c) and the high DW factors for this sample (*cf.* table 4.1).

4.1.5 Photocurrent measurements

First of all, it should be noted that Nb:$SrTiO_3$ has been reported in the literature as a photoanode material [45, 46]. As a consequence, the 15 nm γ*-Fe_2O_3 / Nb:$SrTiO_3$ sample should be considered as a semiconductor heterojunction, where both γ*-Fe_2O_3 and Nb:$SrTiO_3$ participate to the photocurrent. Therefore care should be taken about the photocurrent results for this sample. Nonetheless Nb:$SrTiO_3$ (001) was the substrate of choice for the growth of γ*-Fe_2O_3. To extract the photocurrent contribution specific to the γ*-Fe_2O_3 layer in the 15 nm γ*-Fe_2O_3 / Nb:$SrTiO_3$ sample, we used the fact that γ*-Fe_2O_3 is expected to have a lower band gap than Nb:$SrTiO_3$, so that the signal specific to γ*-Fe_2O_3 can be extracted from monochromatic photocurrent measurements. This is detailed in appendix A.3.

Figure 4.8 presents the photocurrent measurements obtained for the iron oxides of different crystallographic structures grown by OPA-MBE considered in this subsection. The first information is that hematite (corundum structure) shows the best photocurrent at any bias. Secondly, the Fe_3O_4 sample features almost zero photocurrent, which confirms its metallic behaviour. This was seen already from the valence band XPS analysis (figure 4.5.b) where the Fe_3O_4 layer showed no gap, also the absence of photoactivity for Fe_3O_4 is a widely accepted fact [72]. The γ*-Fe_2O_3 film, which has the same crystallographic structure than Fe_3O_4 but the same band gap than α-Fe_2O_3 features a very weak photocurrent. This shows that the spinel (001) structure is much less favourable than the corundum (0001) structure for water photoelectrolysis. Moreover one observes that the photocurrent of the am-Fe_2O_3 sample is low, indeed amorphous Fe_2O_3 is known to show poor performances compared to

single crystalline hematite [70]. This is likely due a poor conductivity which drastically limits the photocurrent [51]. We can conclude that for fully oxidized iron oxide the corundum (0001) structure is the most efficient for solar water splitting.

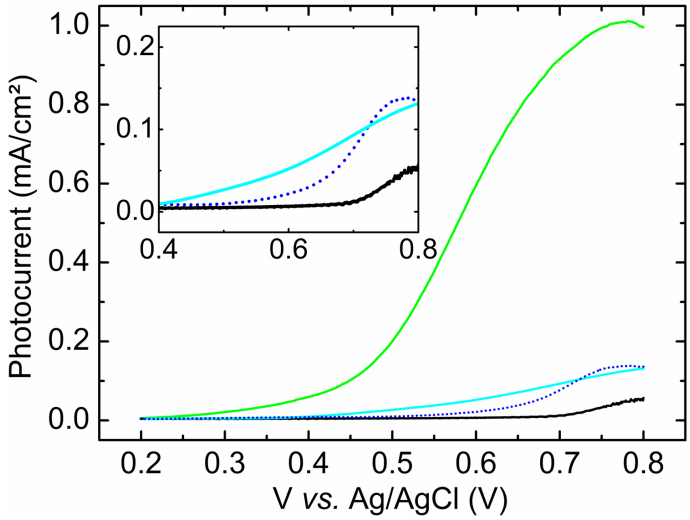

Figure 4.8: Photocurrent for various iron oxide structures grown by OPA-MBE: Fe_3O_4 (111) (bottom, black solid line), γ^*-Fe_2O_3 (001) (cyan solid line), am-Fe_2O_3 (blue dotted line), α-Fe_2O_3 (0001) (top, green solid line). Inset: magnified view of the [0.4V; 0.8V] *vs.* Ag/AgCl window.

4.2 Air annealing of Fe_3O_4 films

As seen previously, Fe_3O_4 is an iron oxide with a metallic behaviour and a mixed valence Fe^{3+}/Fe^{2+}. This material is not photoactive as we saw previously in 4.1 [72]. However upon air annealing, one can expect to increase the oxygen content, resulting in an increase in the Fe^{3+}/Fe^{2+} ratio and in a gap opening, leading to increasing photocurrents. Also it is interesting to study the structural modifications occurring upon air annealing, before photocurrent measurements. The samples were 15 nm Fe_3O_4 (111) films deposited on Pt (111) by OPA-MBE, as in 4.1. One sample was annealed in air (air-annealed) at 180°C for 23 hours and a second one at 220°C for 23 hours. We studied these samples by RHEED, XPS and photocurrent measurements. The air-annealed samples are noted T-air where T is the annealing temperature in °C.

4.2.1 *Ex situ* RHEED

The RHEED results are presented on figure 4.9. We recorded the RHEED patterns along the azimuth corresponding to the $(11)^*_s$ direction for Fe_3O_4 (111) and to the $(10)^*_s$ direction for α-Fe_2O_3 (0001) (figure 4.9.a). For a clear comparison we also show the RHEED pattern of α-Fe_2O_3 (0001). RHEED patterns are shown along with the corresponding surface reciprocal

lattices for each sample (figure 4.9.b). It is clear that upon air annealing of Fe_3O_4: (i) additional lines corresponding to the hematite lattice are more and more visible and (ii) the lines specific to Fe_3O_4 tend to disappear. This is even clearer when one analyses the integrated profile of the RHEED patterns (figure 4.9.c). On these profiles the peaks specific to Fe_3O_4 and α-Fe_2O_3 are highlighted with grey and green rectangles respectively. It is clear that upon air annealing of Fe_3O_4: (i) the peaks specific to α-Fe_2O_3 progressively appear and become more visible and (ii) the peaks specific to Fe_3O_4 progressively disappear.

This means that upon annealing, the crystallographic structure changes from the pure Fe_3O_4 spinel structure to a mix of iron oxides made of corundum and spinel structures leading asymptotically to a pure Fe_2O_3 corundum structure. However since Fe_3O_4 and γ-Fe_2O_3 have both a spinel structure, it is not straightforward to conclude if upon air annealing the Fe_3O_4 film becomes a mix of Fe_3O_4 and α-Fe_2O_3 or a mix of γ-Fe_2O_3 and α-Fe_2O_3.

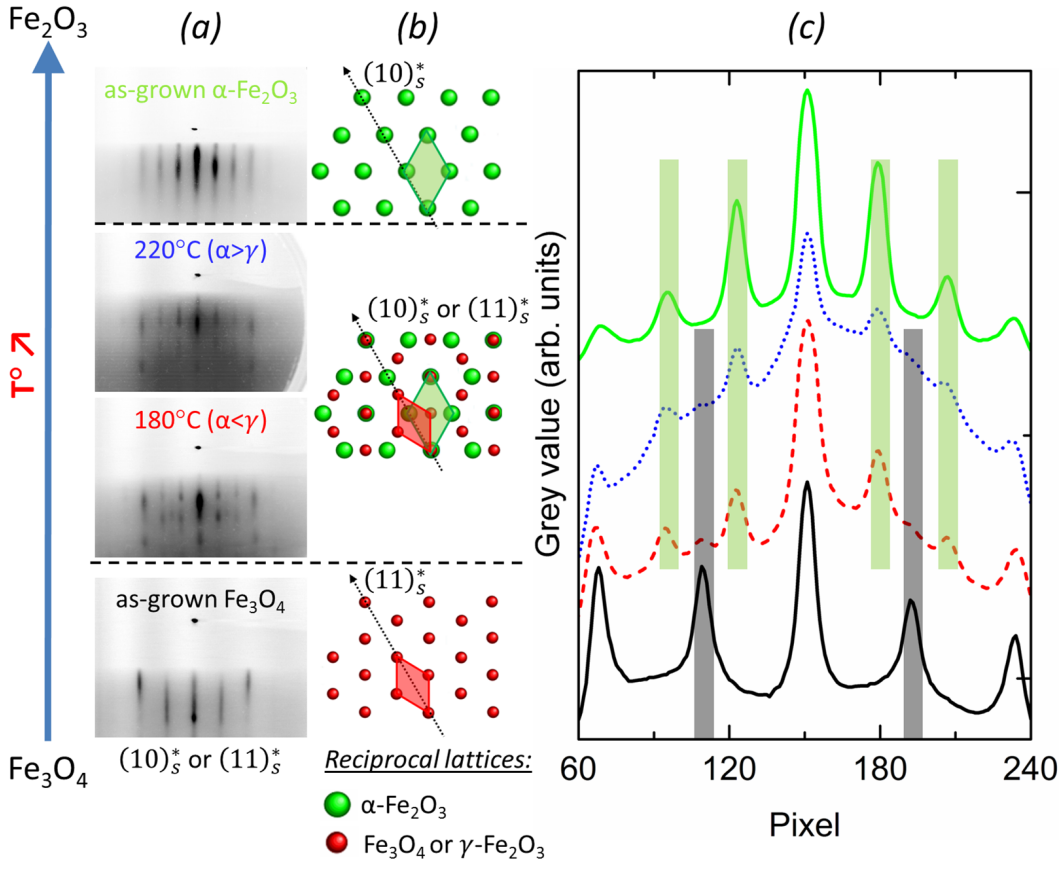

Figure 4.9: RHEED patterns obtained along the azimuth given by the arrows on (b): (a) RHEED patterns, (b) corresponding surface reciprocal lattices and (c) RHEED patterns integrated profiles. From bottom to top: as-grown Fe_3O_4 (black), 180-air (red) and 220-air (blue) samples and a reference α-Fe_2O_3 film (green). The elementary cell (in the reciprocal space) is also shown on (b) with the same colour than the corresponding reciprocal lattice. On (c), the transparent grey (resp. green) rectangles highlight RHEED lines specific to Fe_3O_4 (resp. α-Fe_2O_3).

4.2.2 *Ex situ* XPS

The Fe*2p* core levels analysis[20] (figure 4.10.a) shows that upon air annealing, the oxidation state of iron starts from a Fe^{3+}/Fe^{2+} mix in pure Fe_3O_4 (consistent with previous results shown in subsection 4.1) and moves closer to only Fe^{3+} like in pure hematite. This is seen on the one hand by the occurrence and the increase of the typical Fe^{3+} shake-up satellite around 719.2 eV binding energy and on the other hand by the shift of the Fe$2p_{1/2}$ and Fe$2p_{3/2}$ lines (resp. 0.5 eV and 1 eV) toward higher binding energies.

The valence band analysis (figure 4.10.b) informs about a gap opening upon air annealing. Indeed one can notice that Fe_3O_4 features a metallic behaviour as seen previously (4.1). For air-annealed samples we highlighted in grey the integral of the valence band spectra between the valence band minimum cut-off and the baseline (no photoelectron recorded). The bigger this integral, the higher the number of electronic states available within the band gap.

In Fe_3O_4, electronic states in the gap are induced by Fe^{2+} ions [143]. We observe that air annealing oxidizes these Fe^{2+} into Fe^{3+} (*cf.* Fe*2p* core level analysis), explaining why the number of electronic states within the gap decreases upon air annealing. Since for the air-annealed samples only Fe^{3+} species were detected, we can unravel the uncertainty left after the RHEED analysis about the phase mix for annealed samples: the mix seems to be a (α/γ)-Fe_2O_3 mix rather than a mix of Fe_3O_4 and α-Fe_2O_3.

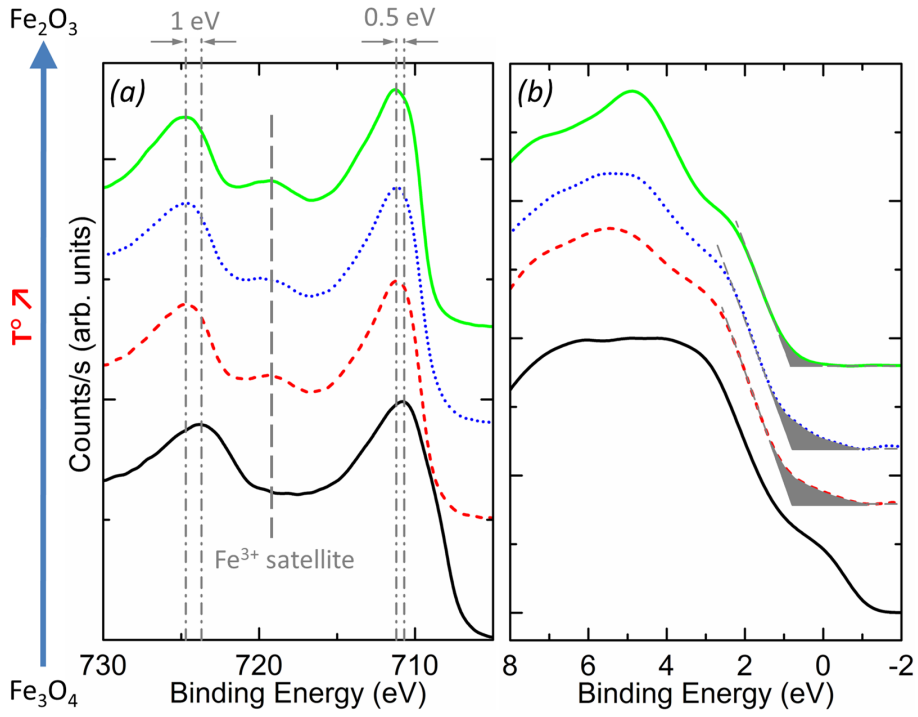

Figure 4.10: (a) Fe*2p* core level and (b) valence band XPS spectra. From bottom to top: as-grown Fe_3O_4 (black solid line), 180-air (red dashed line) and 220-air (blue dotted line) samples and a reference α-Fe_2O_3 film (green solid line).

[20] As previously (*cf.* 4.1.3), the reference of binding energies was taken considering the O*1s* line position at 530.1 eV.

4.2.3 Photocurrent measurements

Figure 4.11 presents the photocurrent of the air-annealed Fe_3O_4 films, compared with a Fe_3O_4 and hematite reference films. We observe that air-annealed samples feature a lower photocurrent than the reference hematite film, but higher than the Fe_3O_4 reference film.

Concerning the electronic structure for air-annealed samples, we saw a non negligible quantity of available electronic states within the gap (higher for the 180-air sample than for the 220-air sample). These states can act as trapping states where photogenerated carriers recombine, explaining the lower photocurrent. In addition to this, the RHEED analysis showed that annealed samples have a mix of crystallographic structures (α/γ mix, *cf.* figure 4.9). This is not desirable since it may likely induce crystallographic defects, resulting in carriers recombination and a loss in photocurrent. Moreover we have shown earlier in this chapter (subsection 4.1.5) that the γ-Fe_2O_3 structure is not favourable for water photoelectrolysis.

Also, the more annealed is the sample, the more oxidized it is, the less electronic states in the gap are recorded in XPS, and the more hematite predominant is the structure. This explains why the 220-air sample shows a higher photocurrent than the 180-air one.

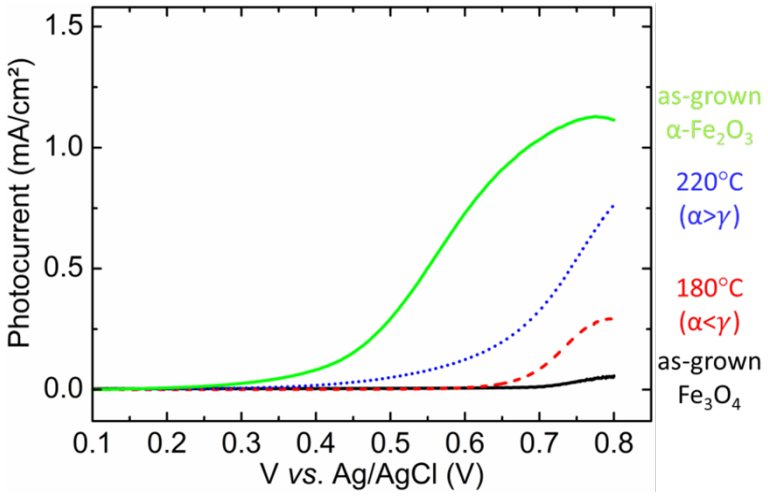

Figure 4.11: Photocurrent for air-annealed Fe_3O_4 films grown on Pt (111): as-grown (black solid line), 180-air (red dashed line) and 220-air (blue dotted line) samples and a reference α-Fe_2O_3 film (green solid line).

4.3 Hematite films annealed in vacuum

In the previous subsection, it appeared that the presence of a large concentration of Fe^{2+} in iron oxides (like in Fe_3O_4) drastically decreases the photocurrent. However as it was highlighted at the beginning of this section, Fe^{2+} presence in hematite is ambivalent. To investigate if a beneficial effect of oxygen vacancies introduction exists for our systems, we chose to study a set of samples for which the introduced oxygen vacancies concentration was kept low. In this subsection we studied hematite films grown by OPA-MBE and annealed for 15 minutes at various temperatures (200-450°C range) in UHV at a pressure of 10^{-9} mbar (vac-annealed). The vac-annealed samples will be noted T-vac where T is the annealing temperature. They were characterized by *ex situ* XPS (4.3.1) and *in situ* EXAFS after vac-annealing (4.3.2) and their photocurrent was measured (4.3.3).

4.3.1 *Ex situ* XPS

Fe*2p* core level XPS spectra[21] are shown on figure 4.12.

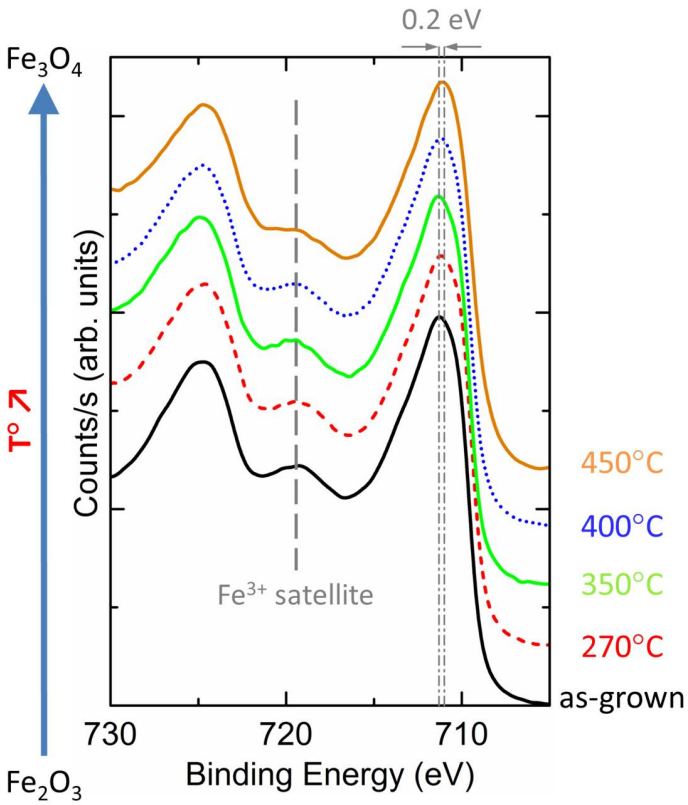

Figure 4.12: XPS after 15 min UHV annealing of 15 nm hematite films grown on Pt (111). From bottom to top: as-grown (black solid line), 270-vac (red dashed line), 350-vac (green solid line), 400-vac (blue dotted line) and 450-vac (orange solid line) samples.

[21] The reference of binding energies was taken considering the O*1s* line position at 530.1 eV (*cf.* 4.1.3).

As explained before, an oxygen vacancy is expected to reduce Fe^{3+} into Fe^{2+}. For UHV annealing temperatures up to 350°C, we saw no changes in the Fe*2p* spectra, meaning that the introduced oxygen vacancies concentration, if any, is not sufficient to induce a detectable amount of Fe^{2+} by XPS. The area of the satellite starts to decrease for an annealing temperature of 400°C, accounting for detected Fe^{2+} species. For a temperature of 450°C, we can also notice a very slight shift of the Fe*2p* lines toward lower binding energies, of 0.2 eV in the case of the Fe$2p_{3/2}$ peak. This difference is smaller than what we observed earlier by comparing the Fe$2p_{3/2}$ peaks of α-Fe_2O_3 and Fe_3O_4 films (subsection 4.2.2).

4.3.2 *In situ* EXAFS

In situ EXAFS spectra were recorded in normal incidence (linear photons polarization parallel to the film surface) and grazing incidence (linear photons polarization perpendicular to the film surface)[22] just after the UHV annealing for all samples, at room temperature, on the SAMBA beamline at synchrotron SOLEIL. The XANES for the as-grown and 450-vac samples and the pre-edge regions for the as-grown, 350-vac, 400-vac and 450-vac samples are shown on figure 4.13.

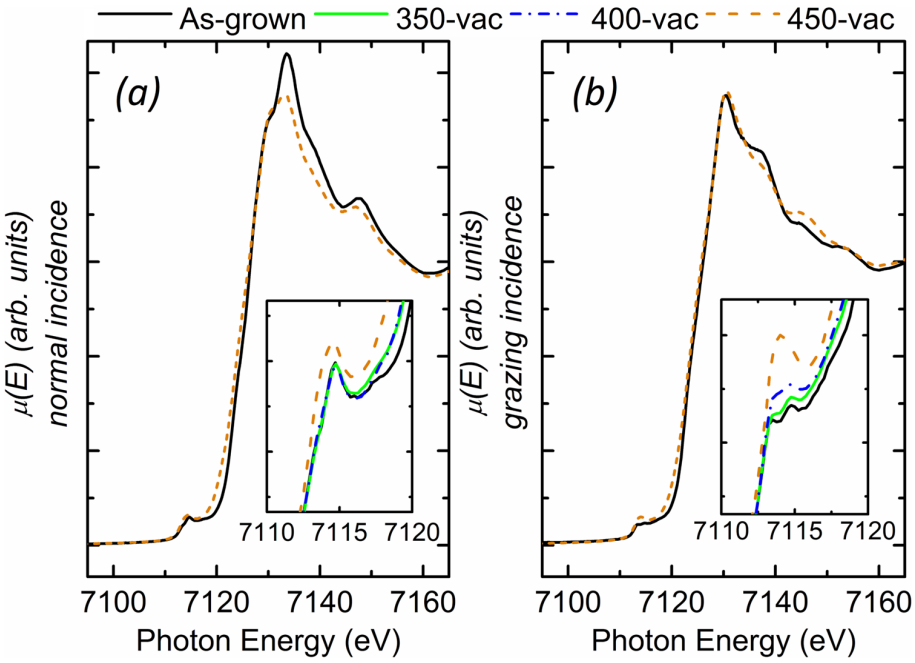

Figure 4.13: *In situ* experimental XANES spectra in (a) normal and (b) grazing incidences for 15 nm thick as-grown (black solid line) and 450-vac (orange dashed line) hematite films. Insets show a zoom of the pre-edge region where the data for the 350-vac (green solid line) and 400-vac (blue dash-dotted line) samples were added.

[22] See figure 3.14 in subsection 3.3.2 for more details.

The data for other samples are not shown for the sake of clarity and because their relevance for this figure was limited. Firstly, the overall XANES shapes are different, meaning that a 450°C annealing in UHV modifies the iron oxide structure and the overall iron valence state. Indeed the spectra recorded in normal and grazing incidences are very different for the as-grown sample, accounting for a strong anisotropic structure (expected for hematite), whereas for the 450-vac sample differences are lighter, accounting for a less anisotropic structure with respect to the as-grown structure. Secondly, we can see a slight shift of the XANES spectra toward lower photons energies for the 450-vac sample with respect to the as-grown one, meaning that the valence state of iron is not only Fe^{3+}, but a mix of Fe^{2+} and Fe^{3+} [160], which is consistent with the XPS observations. On the pre-edge region, the data recorded in normal incidence are almost equivalent for all samples (except for the 450-vac sample), whereas in grazing incidence, significant changes are seen for the 400-vac and 450-vac sample, accounting for iron reduction in these samples with respect to the as-grown sample [160]. 200-vac and 270-vac samples featured shapes similar to the as-grown sample.

EXAFS data were analysed according to the approach detailed in 3.3.2. Figure 4.14 gives the experimental $k\chi(k)$ EXAFS oscillations spectra for all samples.

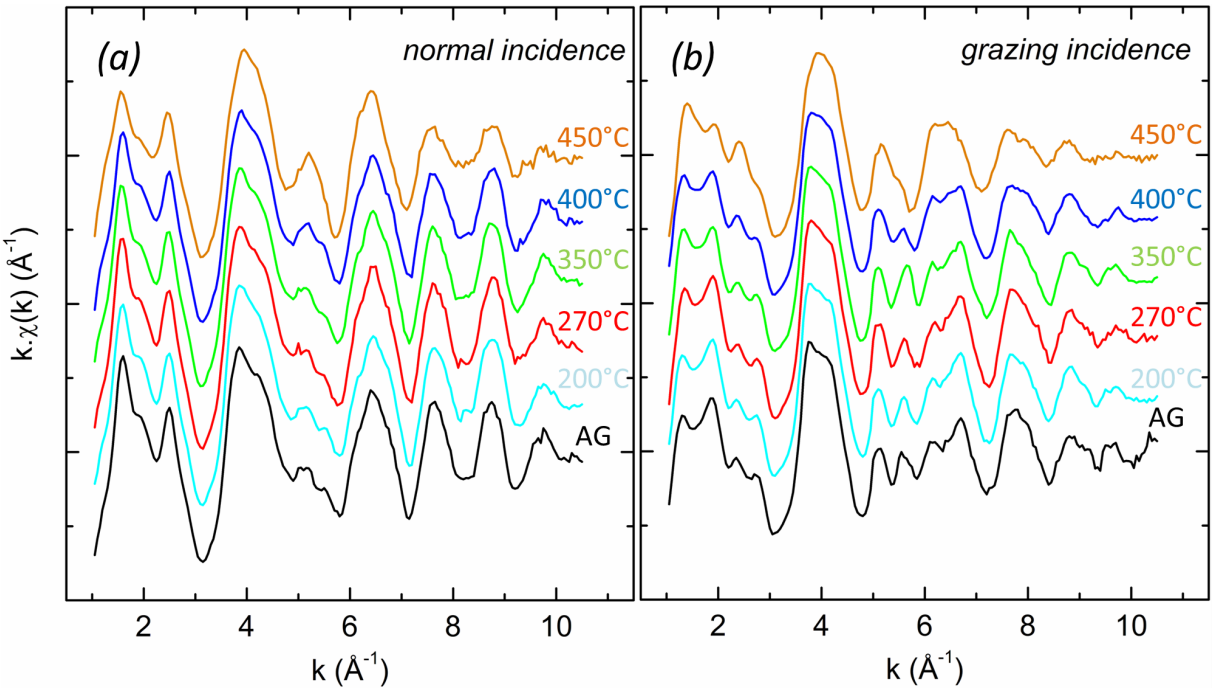

Figure 4.14: *In situ* experimental $k\chi(k)$ EXAFS oscillations spectra in (a) normal and (b) grazing incidences for 15 nm thick hematite films annealed in UHV at various temperatures. From bottom to top: as-grown (black), 200-vac (cyan), 270-vac (red), 350-vac (green), 400-vac (blue) and 450-vac (orange) samples.

Upon UHV annealing, the structure slightly changes with respect to as-grown hematite.

This is more visible for grazing incidence spectra, meaning that (qualitatively) the out-of-plane structure is more modified than the in-plane structure upon UHV annealing. Also when increasing the annealing temperature, the differences between spectra recorded in normal and grazing incidence are less and less important, meaning that the structure is less and less anisotropic. More precisely, visible changes occur starting from an annealing temperature of 400 °C. This is in agreement with the previous observations of the XANES and pre-edge regions.

To investigate the crystallographic structure changes upon UHV annealing, we started by studying the 450-vac sample. For this sample, XPS showed that the Fe*2p* spectra is not identical to the one of pure Fe_3O_4, meaning that this annealing did not create enough oxygen vacancies to reach the Fe^{3+}/Fe^{2+} ratio of Fe_3O_4. Also the EXAFS data of the 450-vac sample are not similar to the EXAFS data of the spinel-like γ*-Fe_2O_3 / Nb:$SrTiO_3$ (001) studied in subsection 4.1 (figure 4.7).

To have a first look into the possible crystallographic structure of the 450-vac sample, we compared its experimental EXAFS spectra with FEFF calculations for pure α-Fe_2O_3 (0001) and pure Fe_3O_4 (111). The results are depicted on figure 4.15. It can be seen that the 450-vac sample has qualitatively an in-plane (resp. out-of-plane) structure resembling the one of pure α-Fe_2O_3 (0001) (resp. pure Fe_3O_4 (111)).

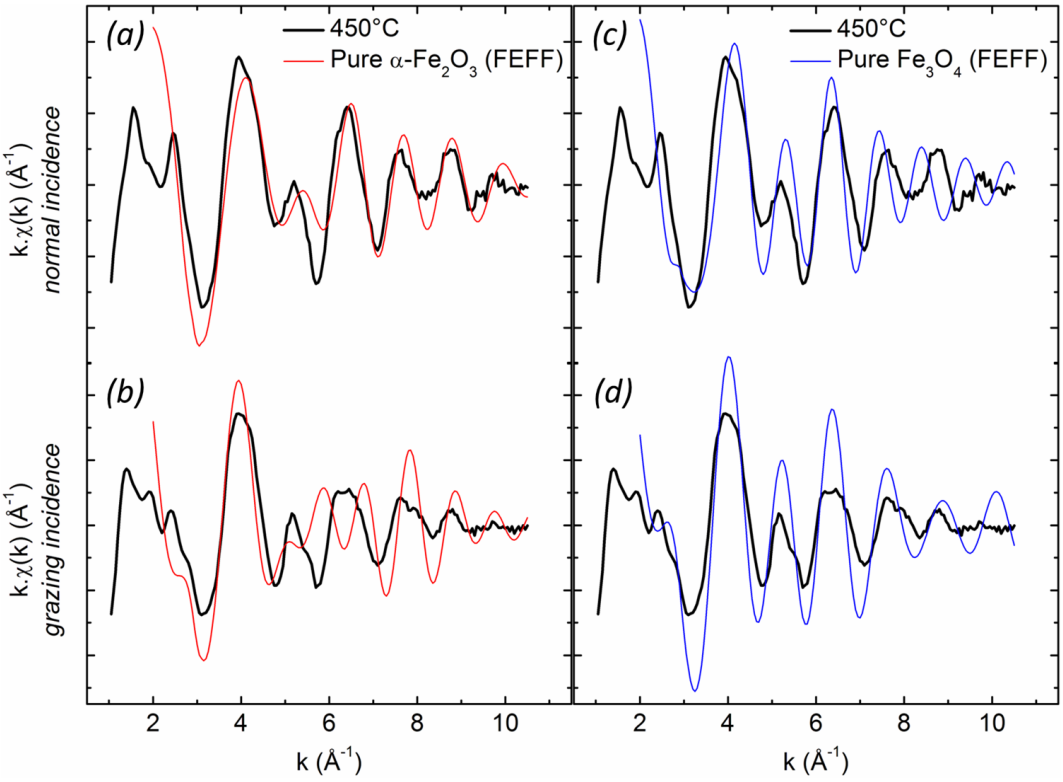

Figure 4.15: Experimental $k\chi(k)$ EXAFS oscillations spectra of the 450-vac hematite film (thick black line) compared with the ones of pure α-Fe_2O_3 (thin red line) and Fe_3O_4 (thin blue line) in normal (a and c, in-plane sensitive) and grazing (b and d, out-of-plane sensitive) incidences obtained by FEFF calculations.

Attempts to fit the EXAFS spectra of the 450-vac sample with a Fe_3O_4 structure (in the same manner than explained in subsection 4.1 for the maghemite-like γ*-Fe_2O_3 / Nb:$SrTiO_3$ (001) sample) were unsuccessful, in particular the output fit parameters were physically meaningless (negative DW factors).

Then we made the hypothesis of a hematite structure for the 450-vac sample. The EXAFS spectra were fitted assuming a hematite structure (*i.e.* corundum, scheme of the structure shown on figure 4.16). More precisely, we fitted the normal and grazing incidences data together and used paths of length up to 3.8 Å around the absorbing Fe atom, corresponding to the nearest neighbours shells. We firstly eliminated multiple scattering paths after checking that they are negligible and we considered only the most intense remaining paths. We fitted the data with the ARTEMIS software, using 11 parameters. The fitting parameters are the amplitude for each path, the distances of the octahedral shell of oxygen (first and second oxygen neighbours, noted O1 and O2, *cf.* figure 4.16 below) and the corresponding Debye-Waller (DW) factors. The more distant shells (first and second iron neighbours, noted Fe1 and Fe2, and all shells until 3.8 Å) were fitted in a single scattering approach. In order to take into account the strain due to epitaxy without increasing the number of parameters we introduced two structural expansion factors: α parallel to the (0001) basal plane of the bulk hematite structure and β perpendicular to it (in the same way as in subsection 4.1.4). For these more distant shells, we have also introduced DW factors to take into account additional structural disorder (total of 4).

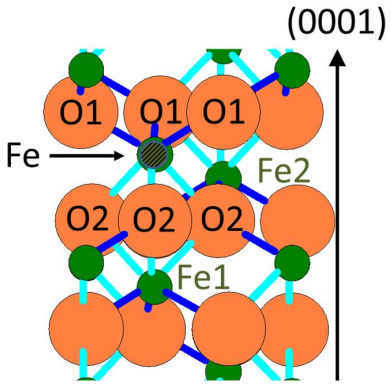

Figure 4.16: Schematic drawing showing the two first layers of neighbours in the hematite structure when the absorbing atom is Fe. From [53].

On figure 4.17, the experimental $k\chi(k)$ EXAFS oscillations spectra are shown together with the fit of the data by FEFF calculations (assuming a corundum structure) for the as-grown and 450-vac samples. It can be seen that the fits are acceptable for both samples.

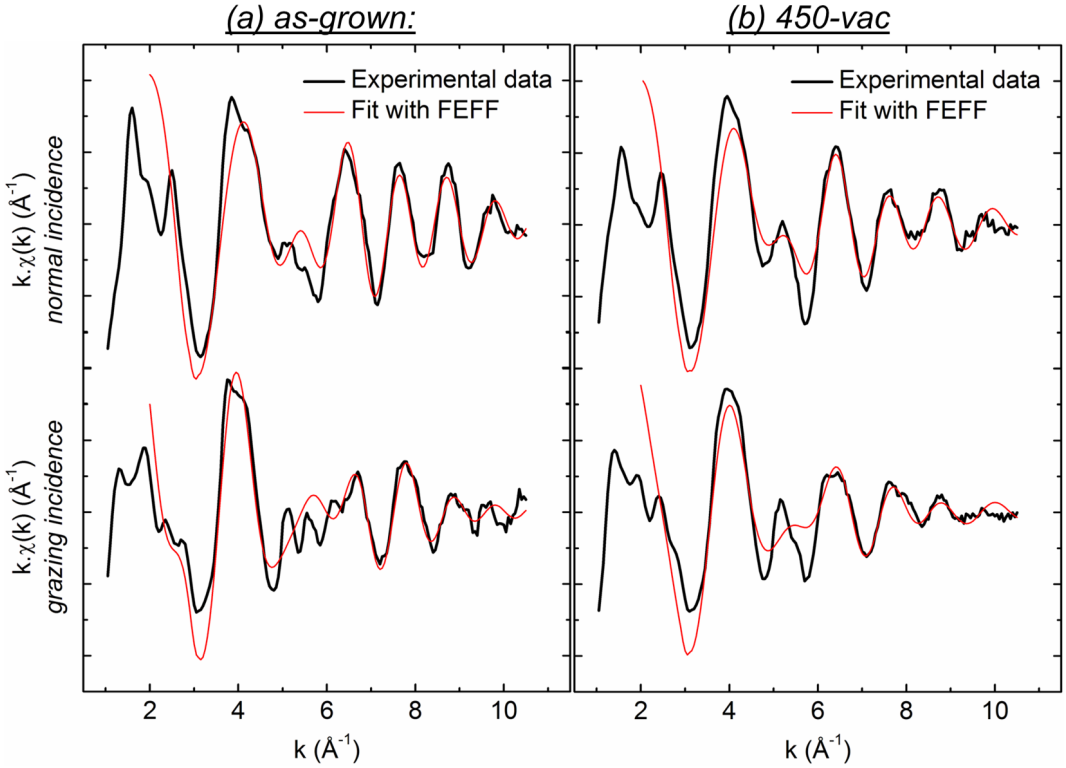

Figure 4.17: Experimental (black thick line) $k\chi(k)$ EXAFS oscillations and fit (red thin line) by FEFF calculations (assuming a corundum structure) obtained in normal (upper curves) and grazing (lower curves) incidences. Samples: (a) as-grown and (b) 450-vac 15 nm thick α-Fe_2O_3 / Pt (111).

The EXAFS oscillations for all the vac-annealed samples were fitted with the same method assuming a hematite (corundum) structure. The obtained structural parameters (interatomic distances and DW factors) for all samples are given in table 4.2 and the evolution of the interatomic distances *vs.* the annealing temperature is depicted on figure 4.18. Consistently with what we observed earlier, visible changes only occur for an annealing temperature higher than 400°C. Other samples feature structural parameters very close to the ones of pure hematite. The DW factors always lie between 1.10^{-3} and 1.10^{-2} Å^{-2}, which is acceptable. From table 4.2 and figure 4.18 it is seen that upon UHV annealing the Fe-O distances seem to converge toward the Fe octa-O distances in pure Fe_3O_4. Analogously, the Fe-Fe distances converge toward the Fe octa-Fe octa distance in pure Fe_3O_4. The largest variation upon annealing is recorded for the Fe-Fe1 distance (*i.e.* the distance to the first out-of-plane Fe neighbour, *cf.* figure 4.16) which is 2.90 Å for the as-grown sample and 2.97 Å for the 450-vac sample.

Sample	Fe-O1 (Å)		Fe-O2 (Å)		Fe-Fe1 (Å)		Fe-Fe2 (Å)	
	R	*DW*	*R*	*DW*	*R*	*DW*	*R*	*DW*
pure α-Fe_2O_3 (FEFF)	1.945		2.11		2.90		2.97	
As-grown	1.95	0.004	2.10	0.005	2.90	0.005	2.99	0.006
200-vac	1.95	0.003	2.10	0.007	2.91	0.003	2.98	0.001
270-vac	1.95	0.006	2.11	0.010	2.91	0.003	2.98	0.004
350-vac	1.95	0.002	2.11	0.005	2.91	0.004	2.98	0.004
400-vac	1.96	0.003	2.08	0.008	2.92	0.006	2.99	0.003
450-vac	1.96	0.007	2.07	0.007	2.97	0.007	2.99	0.005
Fe octa in pure Fe_3O_4 (FEFF)	2.06		2.06		2.97		2.97	

Table 4.2: Structural parameters (interatomic distances (*R*) and DW factors (*DW*)) obtained by EXAFS simulations at the Fe K edge for as-grown and UHV-annealed 15 nm thick hematite films. The interatomic distances (resp. DW factors) are given in Å (resp. $Å^{-2}$), the error bar is ± 0.03 Å (resp. ± 10%). The simulated structure was hematite. Structural parameters for bulk hematite (resp. magnetite) for the two first (resp. first) neighbour shells of an absorbing Fe atom (in octahedral site) obtained from FEFF calculations are also shown.

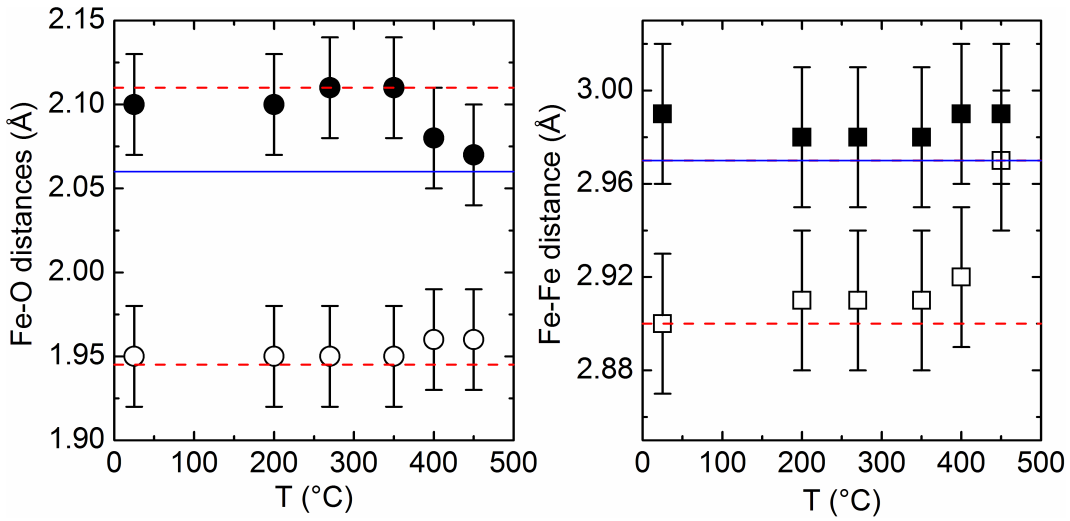

Figure 4.18: Fe-O (left, circles) and Fe-Fe (right, squares) interatomic distances obtained by EXAFS simulations at the Fe K edge for as-grown and UHV-annealed 15 nm thick hematite films for the first (O1, Fe1, empty symbols) and the second (O2, Fe2, full symbols) layers of neighbours. The simulated structure was hematite. Interatomic distances for bulk hematite and bulk magnetite (for the two first neighbour shells of an absorbing Fe atom in octahedral site) obtained from FEFF calculations are also shown (red dashed line and blue line respectively).

Our results suggest that a crystallographic phase transition from hematite to magnetite is initiated at a UHV annealing temperature between 350°C and 400°C, as it can also be seen from the valence point of view in XPS. Bertram et al. studied the reduction upon UHV annealing of maghemite thin films (thickness around 8 nm) deposited on MgO (001) by molecular beam epitaxy [159]. The authors reported that the critical temperature for the reduction from γ-Fe_2O_3 to Fe_3O_4 is 360°C. Our findings are consistent with these results.

4.3.3 Photocurrent measurements

Photocurrent results are shown on figure 4.19 as a map where the X, Y and Z axis represent the applied potential, the annealing temperature and the photocurrent value respectively. Each horizontal line of the map is a photocurrent-voltage curve. Data for not tested temperatures were obtained by linear interpolation of the available experimental data. The optimal oxygen vacancies concentration from the photocurrent point of view is reached for an annealing temperature of 350°C for which the onset potential is reduced by 0.2V and the photocurrent is almost multiplied by two with respect to the as-grown sample. Above this temperature (400-vac and 450-vac samples), the photocurrent decreases, which can be explained by a too large Fe^{2+} concentration which lowers the photocurrent (in the same way than we noticed previously in 4.2) by introducing charge trapping states within the band gap. The sample annealed at 200°C features a photocurrent lower than the as-grown sample. This decrease can not be explained for now. It may originate from sample surface contamination.

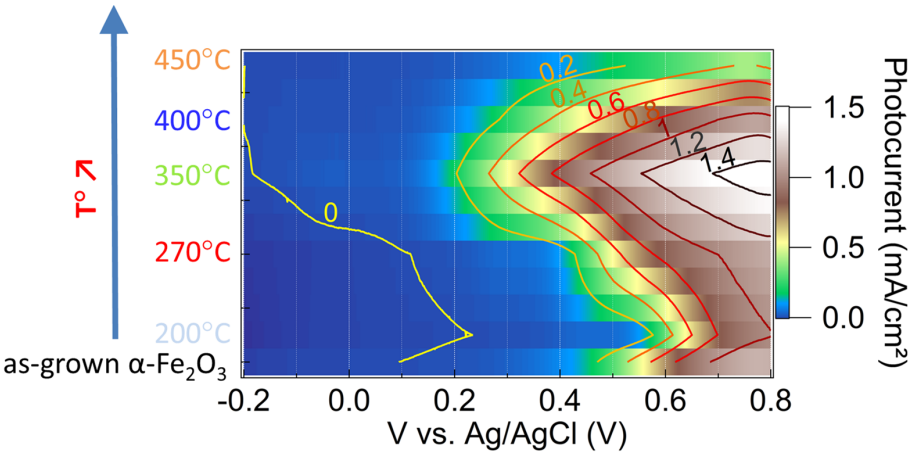

Figure 4.19: Photocurrent map of 15 min UHV-annealed 15 nm hematite samples grown on Pt (111). Iso-photocurrents curves are also shown on the map.

4.3.4 Discussion

It is difficult to compare our photocurrent results with similar studies published in the literature [72, 73] because the studied systems in these papers are completely different from our nanometric single crystalline films. They are often polycrystalline iron oxides films elaborated by a solution-based method, which are not always stoichiometric hematite samples *in fine* (just after elaboration). Moreover the crystallographic structure is highly modified upon oxygen vacancy creation, in particular extra crystallographic orientations appear and a mixed Fe_3O_4 - Fe_2O_3 structure has been reported, accounting for a higher oxygen vacancies concentration than in our systems. Also the authors detected changes in the structure and in the surface chemistry linked to the preparation method (adsorption of gaseous precursors).

The results shown here indicate that for our systems there is a critical Fe^{2+} (*i.e.* oxygen vacancies) concentration above which:

- Fe^{2+} species are detected in XPS by a decrease of the Fe^{3+} shake-up satellite and a slight shift of the Fe$2p_{3/2}$ peak toward lower binding energies;
- The crystallographic structure remains hematite but a phase transition toward the Fe_3O_4 inverse spinel structure is initiated;
- The photocurrent decreases.

This optimal Fe^{2+} concentration is obtained by UHV annealing at 350°C for 15 min (and is exceeded for higher temperatures). However this optimal concentration is below the detection edge of Fe^{2+} presence in hematite by (i) XPS, (ii) Fe K pre-edge analysis or (iii) crystallographic changes recorded in EXAFS. The existence of an optimal Fe^{2+} concentration is consistent with the concomitant effects of reducing Fe^{3+} to Fe^{2+} highlighted at the beginning of this section.

4.4 Summary

Our single crystalline nanometric thin films grown by OPA-MBE proved to be suitable systems to study the structure and oxygen content effect on iron oxides physical and photoelectrochemical properties. Indeed no additional changes due to preparation method or annealing techniques were recorded. The optimal iron oxide crystallographic structure for water photoelectrolysis (among the studied ones) revealed itself to be hematite (0001), whereas the spinel structure showed poor performances.

The gap opening of oxidized Fe_3O_4 occurs through an iron oxidation ($Fe^{2+} \rightarrow Fe^{3+}$), changing the crystallographic structure from pure magnetite to a maghemite/hematite mix, toward a pure hematite structure.

Oxygen vacancies introduced in stoichiometric hematite through annealing in UHV induce changes in the photocurrent. Their concentration can be optimized, since the presence

of Fe^{2+} involves concomitant beneficial and detrimental phenomena. This optimal concentration, doubling the photocurrent and reducing significantly the onset potential with respect to as-grown hematite, is exceeded when Fe^{2+} species are numerous enough to be detected by XPS, Fe K pre-edge analysis or by crystallographic changes in EXAFS.

5 Single layers of Ti-doped hematite

As it was highlighted at the beginning of chapter 4, the main cited drawbacks of pure hematite for photoelectrolysis applications are its low carrier mobility and its low conductivity. A classical way to counter this disadvantage is to dope hematite with donor or acceptor species in the same way than with common semiconductors in microelectronics or photovoltaics. As it was explained in chapter 2, n-type semiconductors are more suited for photoanodes. Therefore one of the simplest way to improve pure hematite properties is to use a donor dopant. The case of hematite doped with Ti is a seductive idea to improve hematite properties and has been the subject of numerous studies in recent years and has proven to greatly enhance the water splitting performances with respect to undoped hematite [51–60]. Indeed, titanium is expected to be a donor in the hematite matrix (Ti^{4+} valence state expected). Moreover Huda et al. predicted Ti as the most promising transition metal dopant for hematite [161]. They reported that Ti-doping decreases the effective mass of electrons in Ti-doped hematite (hence increase their mobility).

However, the improvement of the hematite water splitting performances induced by Ti-doping has not been discussed in details with respect to possible changes of the crystalline structure. As a matter of fact, previous studies concern polycrystalline films or nanostructures including a high density of grain boundaries which may dominate the electric conduction; they can either limit conduction (if the conduction occurs perpendicularly to them) or increase conduction (if the conduction occurs along them). The importance of grain boundaries has been stressed by Glasscock et al. [51], who proposed for polycrystalline magnetron sputtered samples that the passivation of hematite grain boundaries and reduction of the crystalline quality by titanium doping could explain the photoelectrochemical properties enhancement upon doping, whereas silicon doping showed only limited improvements supposedly because of a decrease of grain boundaries size. For hematite films grown by hydrothermal methods, Miao et al. [57] reported that Ti-doping induces a change in nanostructures size and shape and Deng et al. [58] a modification of the type of hematite nanostructure and crystallographic orientation, in agreement with the works of Tang et al. [52, 54], Hahn and Mullins [60]. Therefore, because of the polycrystalline nature of these films, the contributions due to structural, morphological, electronic and crystallographic effects and the intrinsic effects due to Ti-doping are necessarily entangled. It is thus not yet clear if the modifications of hematite water splitting properties upon Ti-doping are linked to the change of crystallographic structure or not. We chose to investigate in section 5.1 Ti-doped hematite single crystalline samples of various Ti-doping levels, which is an elegant way to tackle these questions.

Moreover for undoped and Ti-doped hematite layers, the detailed behavior of the photoelectrochemical properties as a function of the layer thickness, especially for well crystallized

layers, has also been less considered. Previous studies used hematite photoanodes obtained by deposition techniques such as hydrothermal growth [57, 58], chemical vapor deposition [96, 120, 121, 128] or electrodeposition [64], patterned or not. In these approaches, it is very difficult to distinguish which parameter, including preparation issues, morphology or crystal quality (among others), influences the photoelectrochemical properties. Moreover, other works using techniques more suitable for model samples elaboration like atomic layer deposition [56, 65, 122, 162] or sputtering [51, 52, 54], focused mainly on dopants and nanostructuration influence, or on surface kinetics properties. Therefore section 5.1 also aims at studying thin epitaxial undoped and Ti-doped hematite films of different thicknesses as photoanodes.

Further improvement of the performances of Ti-doped hematite films can be achieved upon surface engineering of the films, which has been a widely explored route over the last few years. Major paths were detailed in 2.4.3 and concern the deposition of cocatalysts (*e.g.* cobalt oxides) designed to improve the chemical kinetics [122, 163] or the use of overlayers (*e.g.* alumina) to passivate surface trapping states where photogenerated charges can recombine [128]. Surface chemical treatments (*e.g.* with HF or HCl) are inexpensive experimental processes usually used for samples preparation. These processes are also commonly used to remove native and/or amorphous oxide on semiconductors surfaces (like Si wafers cleaning). In parallel, it has been reported that such wet chemical etching can also improve the surface conductivity and semiconductors photocurrent. For instance, Ziegler et al. [164] reported that a concentrated HCl etching of p-type gallium phosphide removes the native gallium oxide, inducing a 0.2V reduction of the onset potential. Chernomordik et al. [101] reported that a HF treatment on hematite nanowires removes the amorphous iron oxide phase at the surface of the nanowires, resulting in a single crystalline surface and in a reduction of the onset potential by 0.3V. Moreover, Basilio et al. [165] reported that a H_3PO_4 crystallographic wet etching on GaN photocathodes (designed for water reduction) (i) generated a greater surface area (+ 14%), (ii) decreased the surface carrier concentration by cleaning up the surface defects and (iii) made appear stepped edges and etched facets with better photocatalytic activity, resulting in doubling the energy conversion efficiency. Nonetheless, chemical wet-etching of oxides may induce additional deep morphology and electronic structure changes. In section 5.2, we studied the effect of a partial chemical etching in a hydrochloric acid solution on the water splitting performances of epitaxial Ti-doped hematite films. Working on oxide epitaxial thin films deposited on single crystals prevents the formation of a native or amorphous oxide phase at the surface that could lower the water splitting performances or mingle characterizations [101].

5.1 Ti-doping and thickness effects on hematite films properties

In this section, we chose to study the fundamentals of doping hematite with titanium. Ti-doped hematite epitaxial films deposited on Pt (111) using OPA-MBE were investigated to unravel the modification of the intrinsic properties of hematite upon Ti-doping level or film thickness variation. We studied two sets of samples:

- One set consisting in hematite films with various Ti-doping levels (0 - 17 at.% range) and a constant thickness (*ca.* 40 nm);
- One set consisting in hematite films with a constant Ti-doping level of either 0 at.% (undoped) or *ca.* 2 at.% and various thicknesses (5 - 50 nm range).

The RHEED results obtained during the growth are presented in 5.1.1. Afterwards we report observations on the crystallographic structure by EXAFS (5.1.2) and the electronic structure by XPS (5.1.3) and RPES (5.1.4). The influence of the Ti-doping level and of the film thickness on the photoanode properties for photoelectrolysis of water is correlated to the intimate properties of the films (5.1.5 and 5.1.6). Lastly in subsection 5.3 we propose a mechanism to explain the effect of Ti-doping on the properties of our hematite films.

5.1.1 Ti-doped hematite films growth followed by RHEED

Ti-doped hematite thin films were grown on Pt (111) single crystalline substrates by OPA-MBE. The doping level was adjusted by varying the temperature of the Ti Knudsen cell. The thickness of the films was tuned by adjusting the deposition time accordingly. The deposition rate was around 1.5 Å/min.

The precise growth mechanisms of α-Fe_2O_3 (0001) / Pt (111) as a function of the film thickness were previously studied in detail by the "Oxide" group [132, 133]. It was shown that our method allows obtaining single crystalline hematite films with bulk-like properties for thicknesses above 3 nm. More precisely, the early stages of growth (thickness $<$ 3 nm) are dominated by atomic volume maximization favouring the growth of maghemite γ-Fe_2O_3 (001) and the thick layer regime (thickness $>$ 3 nm) by α-Fe_2O_3 (0001), the thermodynamically more stable phase.

Within my PhD work I considered the growth of Ti-doped hematite films on Pt (111) single crystals [55]. The crystallographic structure was followed by *in situ* RHEED and the corresponding patterns are shown on figure 5.1 along with the corresponding surface reciprocal lattices at different deposition times (different thicknesses). We considered the same epitaxial relationship between Pt (111) and γ-Fe_2O_3 or α-Fe_2O_3 than in ref. [132] (*i.e.* cube on cube for γ-Fe_2O_3 (111) / Pt (111) and $\sqrt{3}\times\sqrt{3}$R30° for α-Fe_2O_3 (0001) / Pt (111)), within the considered doping levels (ranging from 0 at.% to 17 at.%). We observe that the thin film has the same structure than undoped hematite. The growth follows a Stranski-Krastanov growth mechanism (layer-plus-islands).

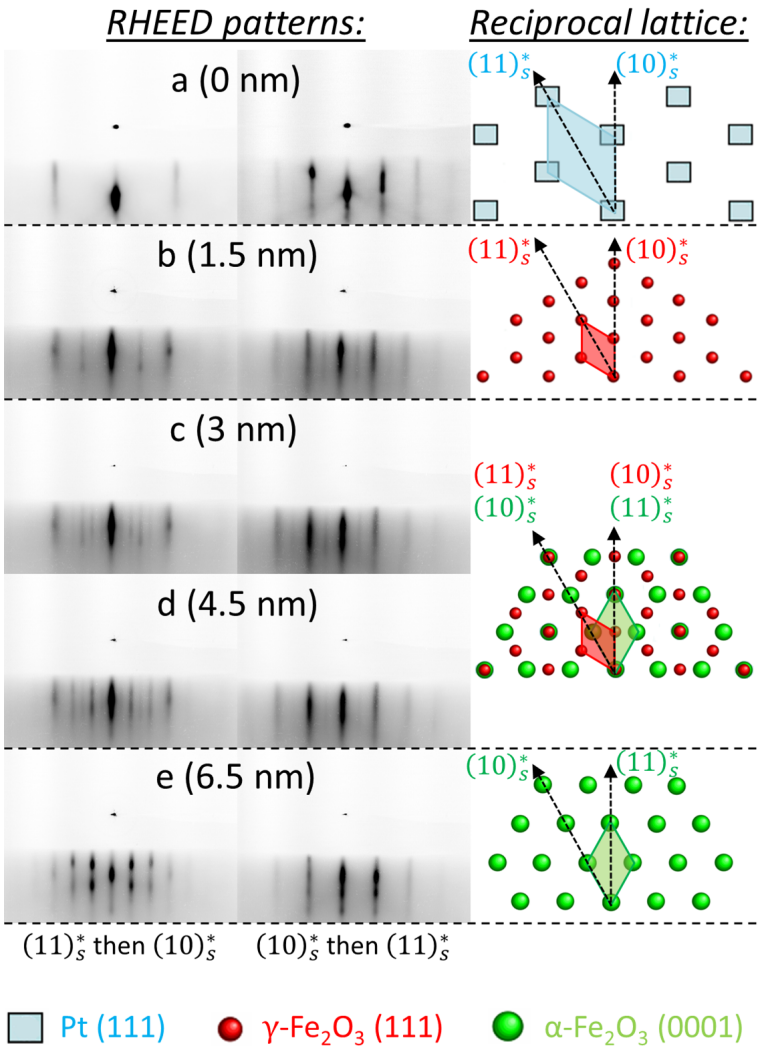

Figure 5.1: (Left panel) RHEED patterns of a 50 nm thick 2 at.% Ti:α-Fe_2O_3 film grown by OPA-MBE (total deposition time of *ca.* 6 hours) at different deposition times/thicknesses (steps a to e) for the two reciprocal space surface diffraction directions of lowest Miller indexes. (Right panel) The corresponding surface reciprocal lattices are represented, making explicit the diffraction directions. (cyan boxes), (small red circles) and (green circles) represent the Pt (111), γ-Fe_2O_3 (111) and α-Fe_2O_3 (0001) surface reciprocal lattices respectively, assuming cube on cube and $\sqrt{3}\times\sqrt{3}$ R30° epitaxial relationship between Pt (111) and γ-Fe_2O_3 and α-Fe_2O_3 respectively. The elementary cell (in the reciprocal space) is also shown with the same color than the corresponding reciprocal lattice. From [55].

Firstly, a 2D Ti:γ-Fe_2O_3 (111) layer grows, evidenced by extra straight lines on the corresponding RHEED patterns (step b in figure 5.1). A phase transition from Ti:γ-Fe_2O_3 (111) to Ti:α-Fe_2O_3 (0001) occurs between 3 and 4.5 nm thickness (steps c and d), where the γ and α phases coexist. After the γ→α transition, an epitaxial growth of Ti-doped hematite (α-Fe_2O_3) with some islands and extra roughness is observed (evidenced by the presence of spots along streaks on RHEED patterns, step e in figure 5.1). The growth mechanism is the same for all Ti-doping levels (from 1 to 17 at.%).

As presented in 3.2.1, we can derive from the RHEED patterns the relaxation of the in-plane lattice parameter. The measurement of the spacing between streaks is homothetic to this lattice parameter. However for other materials than Pt (111), we do not have access directly to the lattice parameter. Since different phases appear during the growth and since they give rise to lattices belonging to different space groups (as evidenced on figure 5.1), it is not straightforward to determine the lattice parameter evolution. Therefore we prefer, with the same approach as Barbier et al. [132], to represent a generic lattice parameter p which is calculated using the RHEED patterns obtained over the particular diffraction direction $(10)_s^*$ of the Pt (111) surface reciprocal lattice (made explicit on figure 5.1.a), which is also the $(11)_s^*$ direction of the hematite surface reciprocal lattice (made explicit on figure 5.1.e). This parameter p is equal to:

- the in-plane lattice parameter in the case of Pt (111);
- $a_{\gamma-Fe_2O_3}/2$ in the case of γ-Fe_2O_3 (where $a_{\gamma-Fe_2O_3}$ is the in-plane lattice parameter of γ-Fe_2O_3 (111), assuming a cube-on-cube epitaxial relationship with respect to Pt (111));
- $a_{\alpha-Fe_2O_3}/\sqrt{3}$ in the case of α-Fe_2O_3 (where $a_{\alpha-Fe_2O_3}$ is the in-plane lattice parameter of α-Fe_2O_3 (0001), assuming a $\sqrt{3}\times\sqrt{3}$ R30° epitaxial relationship with respect to Pt (111)).

Although this parameter p does not correspond to the same lattice parameter for all crystallographic phases, its evolution as a function of the film thickness remains relevant for the overall lattice relaxation and is presented in figure 5.2.

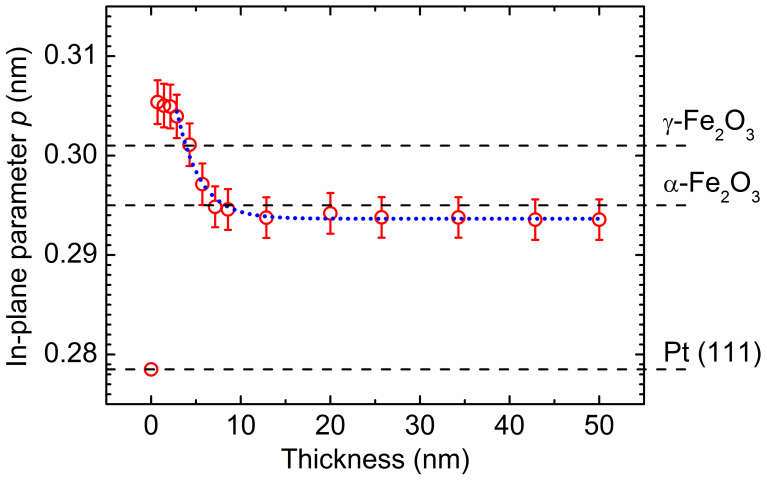

Figure 5.2: In-plane lattice parameter p derived from the $(10)_s^*$ direction of the Pt (111) surface reciprocal lattice (or from the $(11)_s^*$ direction of the hematite surface reciprocal lattice) in RHEED patterns as a function of the film thickness for a 2 at.% Ti-doped α-Fe_2O_3 (0001) film grown by OPA-MBE. Dashed lines stand for the lattice parameter p of bulk γ-Fe_2O_3, α-Fe_2O_3 and Pt (111). Thermal expansion was taken into account. From [55].

Thermal expansion was taken into account considering a linear thermal expansion coefficient of 8.8×10^{-6} K^{-1} for Pt[23], giving a p value of 0.2785 nm at the deposition temperature of 900K for the Pt (111) substrate. The lattice parameter relaxation during the epitaxial growth process with respect to increasing film thickness is consistent with the previous work of the group on pure hematite layers [132]. The parameter p converges to a value of 0.293 ± 0.002 nm, which is very close, or even equal within the experimental error bar, to the expected p value for bulk hematite at 900K (0.295 nm), considering a linear thermal expansion coefficient of 2.38×10^{-5} K^{-1} for hematite [157]. Figure 5.2 shows also that the film relaxes within the first *ca.* 15 nm.

5.1.2 Crystallographic structure investigation by EXAFS

As presented in 3.3.2, EXAFS is a well-suited technique to reveal the local chemical environment of a given species in thin films. EXAFS spectra of 40 nm thick 0 at.%, 5 at.% and 17 at.% Ti-doped α-Fe_2O_3 films were recorded at the Fe and Ti K edges in normal incidence (linear photons polarization parallel to the film surface) and grazing incidence (linear photons polarization perpendicular to the film surface)[24], at room temperature on the SAMBA beamline at synchrotron SOLEIL. Above the Fe K edge, the EXAFS spectra are sensible to the environment of the Fe atoms, whereas above the Ti K edge, the EXAFS spectra are sensible to the environement of the doping Ti atoms. The EXAFS oscillations ($k\chi(k)$ data) are reported in figure 5.3. They show that there is no substantial change with Ti-doping and that for all samples the spectra recorded in normal incidence are different from those recorded in grazing incidence, indicating an anisotropic structure for all doping levels. EXAFS data were analysed according to the approach detailed in 3.3.2 and used in 4.3.2 [53]. The spectra were fitted with HORAE and FEFF 8.4 codes [140–142] assuming a hematite structure (*i.e.* corundum). We did the hypothesis that in the case of a Ti absorbing atom (Ti K edge), the probability of having a Ti neighbour with a length path smaller than 3.8 Å is negligible considering our doping levels. Therefore in the cluster used by the FEFF calculation, all atoms are either Fe or O (except for the Ti K edge where the central absorbing atom which is Ti). We fitted the data with the ARTEMIS software, using 11 parameters[25].

The fit results at the Fe K edge and at the Ti K edge are represented on figure 5.3.a and 5.3.b for undoped, 5 at.% and 17 at.% Ti:α-Fe_2O_3, and corresponding interatomic distances (R), DW factors (DW) and structural expansion factors (α and β) are indicated on table 5.1. The parameters of bulk hematite and bulk ilmenite ($FeTiO_3$, which shares the same

[23] From http://www.webelements.com/
[24] See figure 3.14 in subsection 3.3.2 for more details.
[25] Details about the parameters are given in 4.3.2.

corundum crystal structure) are also indicated. We first observe that the fit parameters are close to the values for bulk hematite, showing that the assumption of a corundum structure is accurate. The good agreement between the data and the best fit calculated lines on figure 5.3 clearly suggests that Ti atoms substitute Fe atoms in α-Fe_2O_3 and that there is no evidence of interstitial Ti.

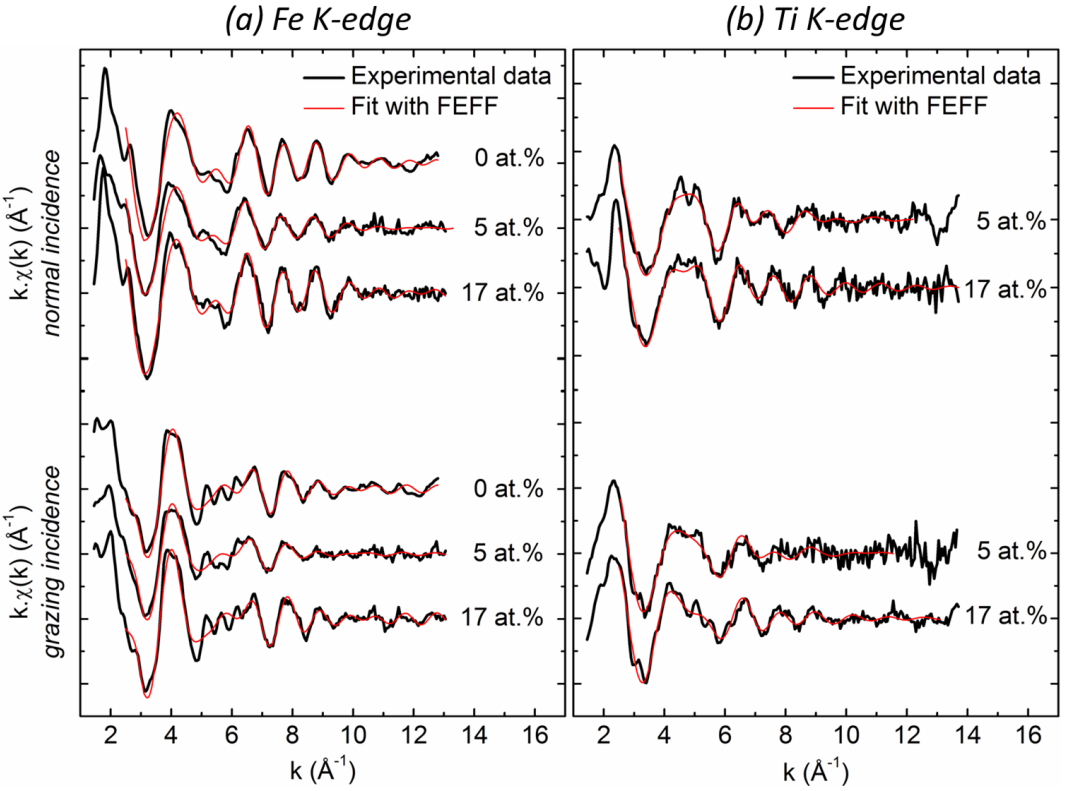

Figure 5.3: Raw (thick black lines) (a) Fe K edge and (b) Ti K edge $k\chi(k)$ EXAFS oscillations for 0 at.%, 5 at.% and 17 at.% Ti:α-Fe_2O_3 40 nm thick films recorded in normal incidence (upper curves) and grazing incidence (lower curves) and fit of the data (thin red lines) by FEFF calculations assuming a corundum structure. From [53].

The corresponding scheme of the crystallographic structure is given on figure 5.4. Accordingly, the obtained interatomic distances (*cf.* table 5.1) show that the Fe environment does not change with Ti-doping and that it is the same as in bulk hematite. However the distances around Ti atoms are slightly different with shorter Ti-O1 and Ti-O2 distances and longer Ti-Fe1 and Ti-Fe2 distances. These distances appear constant with increasing doping level. Comparing these values with the corresponding lengths in bulk ilmenite, we reach the conclusion that the Ti atoms are located in the same site than Fe atoms, but that this site is slightly distorted like in the ilmenite structure. DW factors values lie always between 3.10^{-3} and $1.2.10^{-2}$ $Å^{-2}$ showing that the structure is quite ordered.

Sample	Edge	O1		O2		Fe1		Fe2		α	β
		R	DW	R	DW	R	DW	R	DW		
undoped	Fe	1.96	0.005	2.1	0.011	2.9	0.006	2.98	0.006	0.2	0
5 at.%	Fe	1.97	0.008	2.08	0.012	2.92	0.008	3.01	0.007	1.4	0.6
	Ti	1.91	0.007	1.96	0.009	2.99	0.009	3.07	0.009	3.4	3
17 at.%	Fe	1.96	0.004	2.1	0.007	2.91	0.003	2.99	0.004	0.5	0.2
	Ti	1.89	0.008	2.01	0.010	2.95	0.006	3.02	0.005	1.5	1.8
bulk hematite	Fe	1.945		2.11		2.9		2.97			
bulk ilmenite	Fe	2.07		2.20		2.94		3.002			
	Ti	1.87		2.08		2.94		2.99			

Table 5.1: Interatomic distances (R) and Debye-Waller factors (DW) obtained by EXAFS simulations for 40 nm thick 0 at.%, 5 at.% and 17 at.% Ti-doped hematite films and corresponding lengths in bulk hematite and bulk ilmenite, at Fe (red) and Ti (blue) K edges. The R (resp. DW) values are given in Å (resp. Å^{-2}) and the error bar is ± 0.03 Å (resp. ± 10%). The expansion factors (α and β) are expressed in % and the error bar is ± 0.5%. From [53].

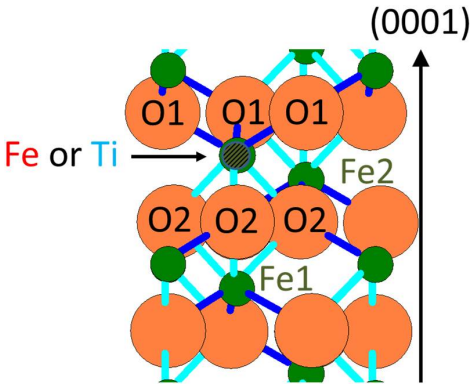

Figure 5.4: Scheme showing the two first layers of neighbours in Ti-doped hematite structure (where Ti substitutes Fe) when the absorbing atom is either Fe or Ti. From [53].

5.1.3 Electronic structure investigation by XPS

We recorded by *in situ* XPS Fe*2p*, Ti*2p*, O*1s* core levels and the valence band region. The reference of binding energies was taken considering the O*1s* line position at 530.1 eV in pure hematite (*cf.* 4.1.3), which is in agreement with other studies [166]. We showed previously by EXAFS that Ti-doping has only a faint effect on the crystallographic structure of hematite (slight distortion of the oxygen octahedron around Fe atoms), therefore we can consider the O*1s* line at the same binding energy in Ti:α-Fe_2O_3 than in α-Fe_2O_3 (up to 17 at.% Ti-doping level), whatever the films thickness. The O*1s* lines were always symmetric, which

excludes hydroxyl or other contaminants incorporation in the layers. The Ti-doping level was measured according to the procedure detailed in 3.2.2.

The spectra for 40 nm thick undoped, 5 at.% and 17 at.% Ti-doped hematite films are shown on figure 5.5.

All Fe*2p* spectra showed the same features with a main Fe$2p_{3/2}$ (resp. Fe$2p_{1/2}$) line at 711.4 eV (resp. 724.8 eV) and a shake-up satellite at 719.4 eV binding energy (*cf.* figure 5.5.a). This shape, shake-up satellite and lines positions are characteristic of the iron +III oxidation state found in hematite either by our group [55, 132, 134] or by others [64, 67, 68, 71, 105, 167] (*cf.* figure 3.7 in subsection 3.2.2). No change could be observed whatever the Ti-doping level, up to 17 at.%. No bump at low binding energy in the Fe$2p_{3/2}$ line, and no decrease of the satellite intensity were observed upon Ti-doping, indicating that Fe^{2+} species are not detected in our samples (within the sensitivity of XPS for this matter), excluding electronic exchange between Fe and Ti cations (according to $Fe^{3+} + Ti^{4+} \rightarrow Fe^{2+} + Ti^{3+}$) in our Ti-doped samples.

The Ti$2p_{3/2}$ (resp. Ti$2p_{1/2}$) line shows a narrow single feature located at 458.1 eV (resp. 463.8 eV) binding energy (*cf.* figure 5.5.b). This binding energy lies between the tabulated Ti$2p_{3/2}$ lines for Ti^{4+} and Ti^{3+} in TiO_2 (458.8 and 457.1 eV respectively) [168]. Since the binding energy of a given photoemission line depends on the chemical environment of the associated atom, the Ti$2p_{3/2}$ line binding energy in the hematite structure is expected to be different from the Ti$2p_{3/2}$ line binding energy in TiO_2. It should be noted that in ref. [50] Zhao et al. measured the same binding energy value for the Ti$2p_{3/2}$ line in Ti:α-Fe_2O_3 on thin films of similar thickness ($\approx$ 50 nm) and Ti-doping level (up to 9 at.%) elaborated with the same growth technique (OPA-MBE). By the way in this reference the authors consider that the titanium is in the Ti^{4+} valence state in these systems. Since EXAFS simulations have shown that the Ti atoms rest in octahedral sites (*cf.* 5.1.2), and that no state in the gap is evidenced (*cf.* figure 5.5.c), we can suggest, as in reference [50], that this binding energy corresponds to Ti^{4+} species included in a hematite host matrix. The Ti*2p* lines being narrow (*i.e.* only one valence state is detected) we can also conclude that there is no detectable Ti^{3+} in XPS.

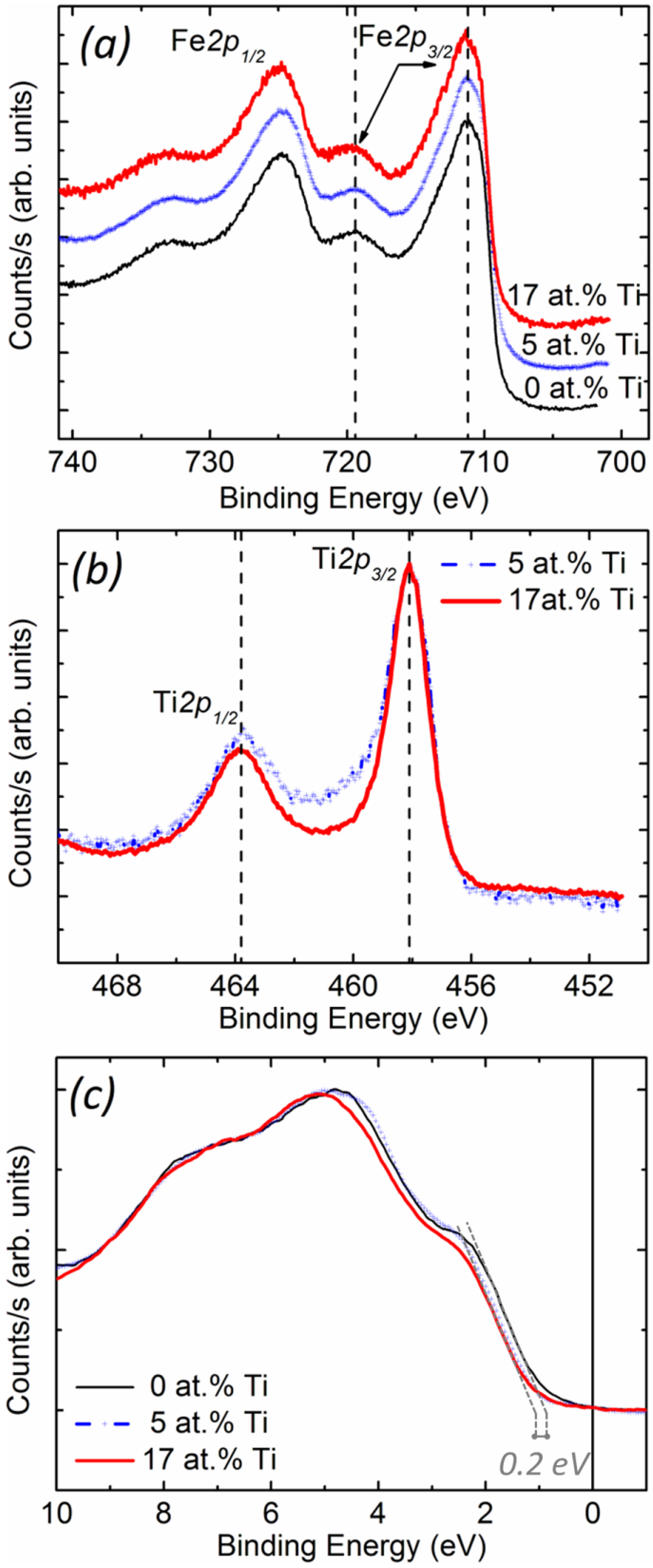

Figure 5.5: (a) Fe*2p* core level, (b) Ti*2p* core level and (c) valence band XPS spectra recorded on 0 at.% (thin black line), 5 at.% (blue plus) and 17 at.% (thick red line) Ti-doped hematite. From [53].

However, we observe changes in the electronic structure within the valence band region (*cf.* figure 5.5.c). The valence band of the Ti-doped samples is shifted by 0.2 eV toward higher binding energies with respect to the undoped sample. These results differ slightly from previous reports. Indeed, Droubay et al. [50, 169] observed no shift in valence band but the presence of Fe^{2+} in the Fe$2p_{3/2}$ line and states in the gap at high doping levels. Moreover these authors suggest that the electronic structure may be influenced by the growth rate and that fast grown samples are more conductive [50]. In our case, OPA-MBE features a very slow growth rate compared to reference [169], which is likely to explain the absence of detectable Fe^{2+} by XPS in our samples.

The set of samples with a constant Ti-doping level of 2 at.% and various thicknesses showed the same results for the Fe*2p* and Ti*2p* core levels [55]. However, as it can be seen on figure 5.6, a lower Ti-doping level (at least up to 2 at.%) does not induce a detectable modification in the valence band XPS spectra. Indeed neither a shift of the spectra nor change in the valence band minimum were recorded for Ti-doping levels lower than 2 at.%.

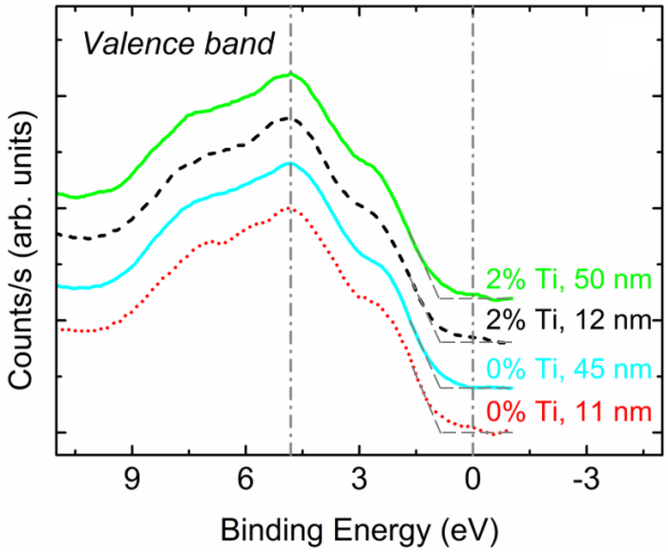

Figure 5.6: Valence band XPS spectra for undoped films of 11 nm (red dotted line) and 45 nm (cyan solid line) and for 2 at.% Ti-doped films of 12 nm (black dashed line) and 50 nm (green solid line). The grey dash-dotted lines highlight the absence of shift and the grey dashed lines are an eye guide for the valence band minimum position derivation. From [55].

5.1.4 Electronic structure investigation by RPES

Resonant photoemission spectroscopy was introduced in 3.3.3. We benefited from the increased sensitivity of RPES as compared to XPS concerning the detection of Fe^{2+} or Ti^{3+} species through the analysis of valence band spectra acquired in resonance conditions (at the Fe L_3 or Ti L_3 edge respectively) for 20 nm thick pure and 2 at.% Ti-doped hematite films.

5.1.4.a RPES at the Fe L_3 edge

On figure 5.7, the Fe L_3 XAS and the corresponding valence band photoemission maps[26] are shown for 20 nm thick pure and 2 at.% Ti-doped hematite films. We see that there are no significant differences between the results for pure and 2 at.% Ti-doped hematite. Indeed neither electronic states in the band gap or valence band shift are detected at the Fe L_3 edge. This means that the shift in the valence band observed earlier occurs only for Ti-doping levels higher than 2 at.%. In addition, these results confirm the very low quantity (if any) of Fe^{2+} species in our samples.

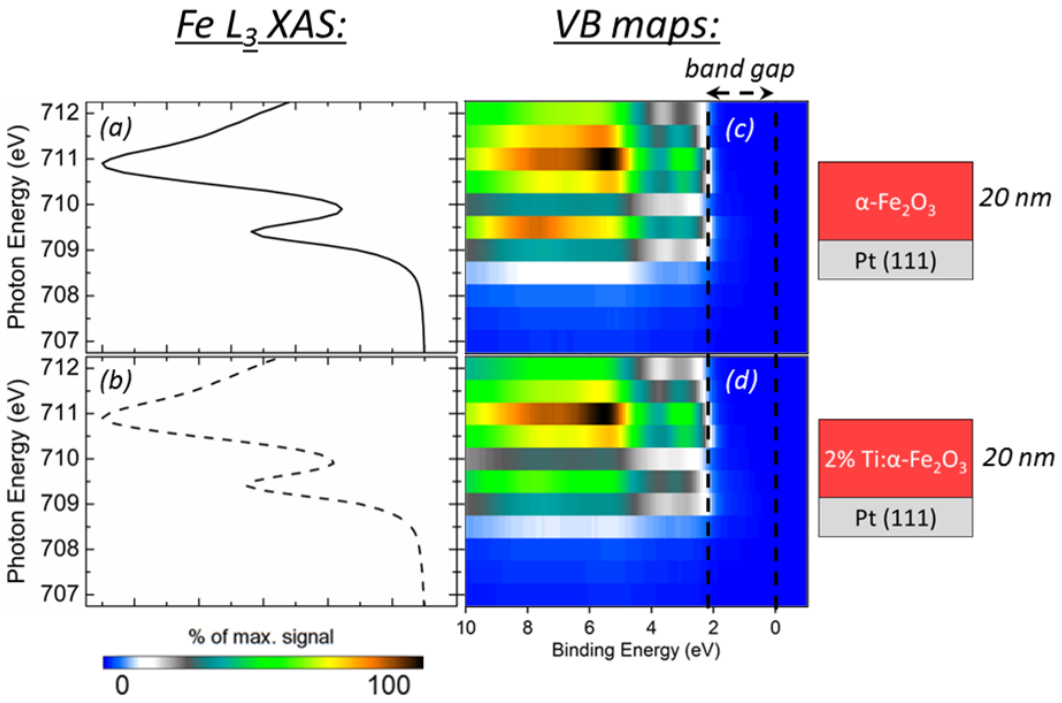

Figure 5.7: Electronic structure measurements done by RPES at the Fe L_3 edge. (Left panel) Fe L_3 X-ray absorption spectra. (Right panel) Corresponding valence band photoemission maps, the colour scale is given at the figure bottom. Samples: (a)+(c) 20 nm pure α-Fe_2O_3 film, (b)+(d) 20 nm 2 at.% Ti:α-Fe_2O_3 film.

[26] See subsection 3.3.3 for more details concerning RPES.

5.1.4.b RPES at the Ti L_3 edge

Resonant photoemission spectroscopy has a higher sensitivity for the detection of Ti^{3+} through the analysis of the valence band in resonant conditions at the Ti L_3 edge. Indeed Ti^{3+} species are expected to create electronic states within the band gap, as it was demonstrated by Le Fèvre et al. [170] in the case of oxygen-deficient TiO_2 studied by RPES. Figure 5.8 shows the Ti L_3 XAS and the corresponding valence band map for a 20 nm 2 at.% Ti:α-Fe_2O_3sample. On this figure we can notice that no electronic states are detected within the band gap, showing that no Ti^{3+} species are detectable, even in resonant conditions at the Ti L_3 edge.

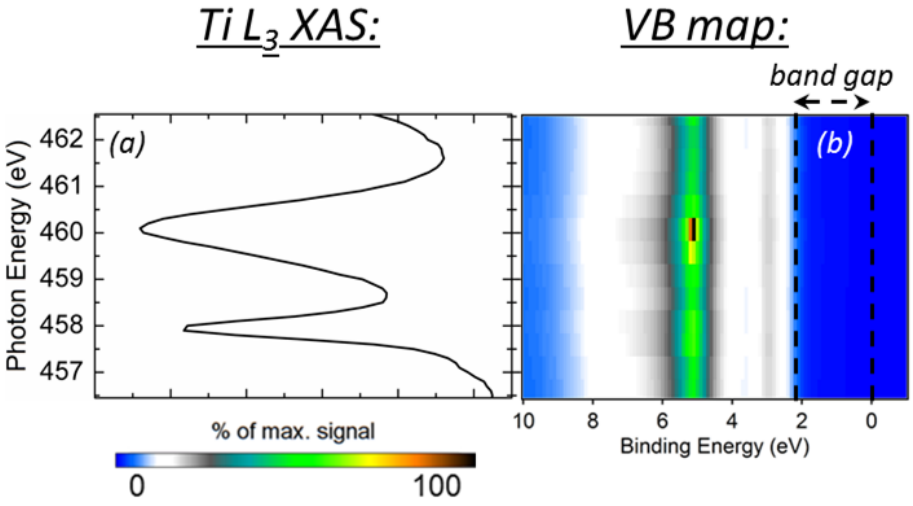

Figure 5.8: Electronic structure measurements done by RPES at the Ti L_3 edge for a 20 nm 2 at.% Ti:α-Fe_2O_3 sample: (a) Ti L_3 X-ray absorption spectra and (b) corresponding valence band photoemission map, the colour scale is given at the figure bottom.

5.1.5 Ti-doping effects on the photocurrent

The photoelectrochemical measurements on 40 nm thick undoped and 17 at.% Ti-doped hematite samples are plotted on figure 5.9.a. We also represented on figure 5.9.b the values of the photocurrent at applied potentials of 0.4V and 0.6V *vs.* Ag/AgCl as a function of the Ti-doping level. The photocurrent density (J_{ph}) was determined from the difference between the stable current measured under illumination and the current in the dark. One observes a clear improvement of the photocurrent upon Ti-doping. For example, at 0.6V *vs.* Ag/AgCl, the photocurrent density (J_{ph}) increases from 8.10^{-3} mA/cm^2 for the undoped film up to 8 mA/cm^2 for the 5 at.% Ti-doped one. This result is consistent with previous experimental papers [51, 52, 59, 60], that also reported an improvement of the photoelectrochemical properties with around 5 at.% Ti-doping. However, in these previous reports it was hard to give a

solid conclusion about which parameter among the doping level, the crystalline alignment or nanostructuring was the major factor contributing to the improvements in PEC properties.

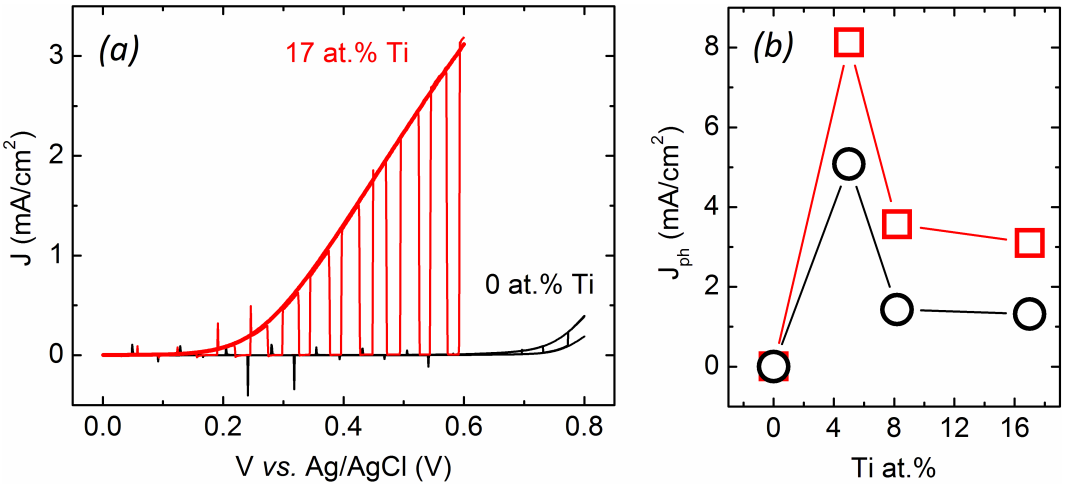

Figure 5.9: (a) Current density *vs.* voltage curves for 40 nm thick undoped (black) and 17 at.% Ti-doped (red) hematite in dark, under illumination and with chopped light. (b) Photocurrent density as a function of the Ti-doping level at 0.4V (black open circle) and 0.6V (red open squares) *vs.* Ag/AgCl. From [53].

At a constant film thickness of 40 nm, Ti-doping greatly increases the photocurrent (by *ca.* three orders of magnitude between the undoped and 5 at.% Ti-doped films). The physical origin of this increase will be discussed more in details in subsection 5.3.

5.1.6 Thickness effects on photoelectrochemical properties

We saw in XPS that a doping level below 2 at.% does not induce measurable changes in the electronic structure. In addition the study of the photocurrent as a function of the hematite film thickness can provide additional insights about the relevant physical parameters and the hematite properties modifications upon Ti-doping.

5.1.6.a Photocurrent

Figure 5.10 presents the photocurrent density *vs.* voltage curves for undoped and 2 at.% Ti-doped hematite films of various thicknesses. The undoped samples have poor photoelectrochemical properties (figure 5.10.a). Indeed below 0.2V *vs.* Ag/AgCl the photocurrent is negative, which indicates a cathode behavior, whereas for larger anodic potentials a positive photocurrent standing for an anode behavior appears. For the Ti-doped samples (figure 5.10.b), only anodic photocurrent appears at positive potentials *vs.* Ag/AgCl. As before, we see that the photocurrent density obtained for Ti-doped samples is higher than for undoped ones by at least two orders of magnitude. Let us note that the increase of photocurrent

with Ti-doping in the present study is much higher than values reported in literature for samples with identical doping levels [56, 58–60] where increases of a factor between 2 and 10 only are reported. These discrepancies in the photocurrent improvement upon Ti-doping between our systems and the ones used in these studies can be attributed to morphology and structure differences.

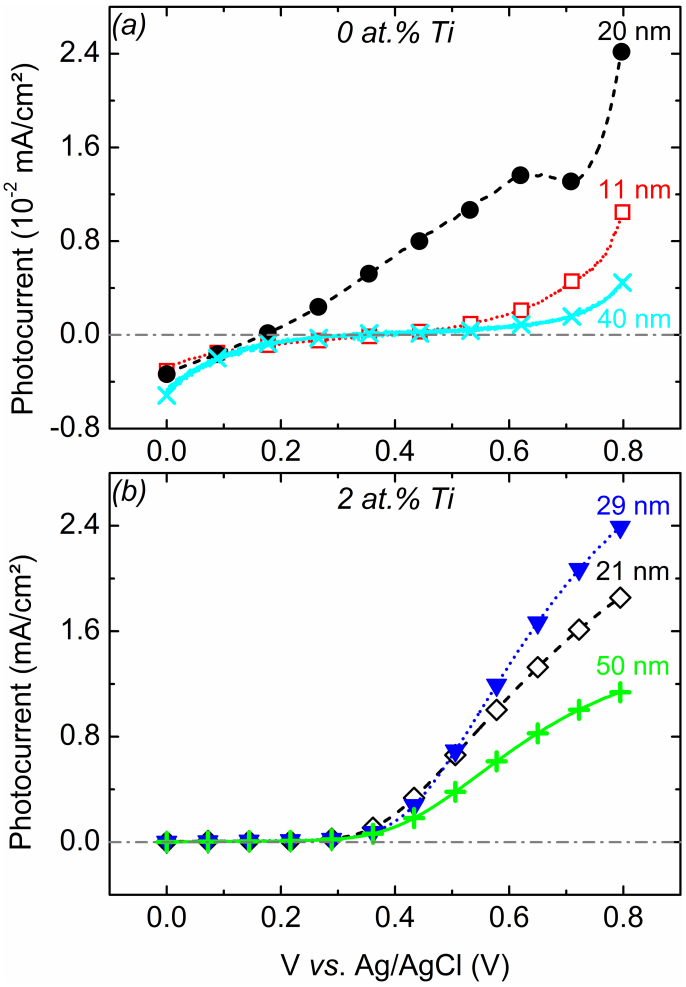

Figure 5.10: Photocurrent density *vs.* voltage curves. (a): undoped hematite films of 11 nm (red empty box), 20 nm (black filled circle) and 40 nm (blue x). (b): 2 at.% Ti-doped hematite films of 21 nm (black open diamond), 29 nm (blue down triangle) and 50 nm (green plus). From [55].

Let us now consider the photocurrent at 0.6V *vs.* Ag/AgCl as a function of the film thickness (figure 5.11, the signal of the undoped film has been multiplied by 75). The dependences of photocurrent with thickness for undoped and doped films are different. For the undoped films we can observe a well-defined sharp photocurrent maximum around 20 nm whereas for the Ti-doped films the curve is smoother and the photocurrent maximum is shifted to a thickness of 30 nm. The shape of the curves at low thicknesses can be easily

understood. Firstly before the maximum, the photocurrent increases when the thickness increases, thanks to an increasing active photon absorption thickness. The much higher photocurrent for Ti-doped hematite compared to undoped hematite is likely due to a higher diffusion length of holes (lower recombination rate) in the depletion layer upon Ti-doping. Secondly at higher thicknesses the decrease of the photocurrent is larger in undoped films ($> 75\%$) than in doped ones ($\approx 50\%$) when the thickness becomes larger than 20 nm and 30 nm respectively.

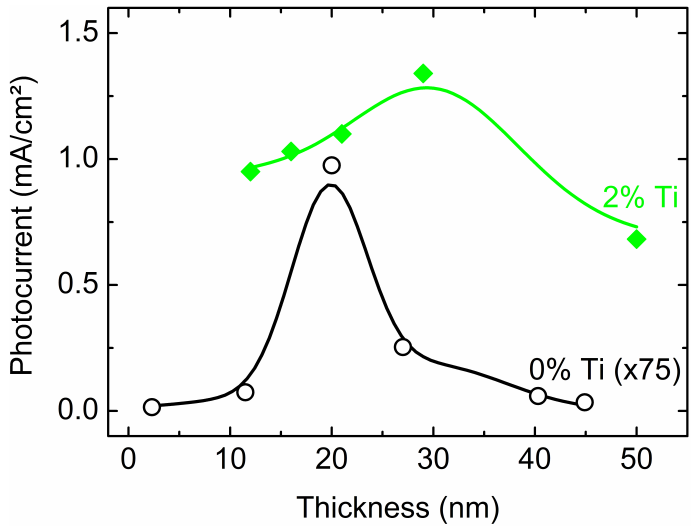

Figure 5.11: Photocurrent density at 0.6V *vs.* Ag/AgCl as a function of the film thickness for undoped (black open circle, multiplied by 75) and 2 at.% Ti-doped (green filled diamond) hematite. Continuous lines are only an eye guide. From [55].

There are very few studies dealing with the variation of water splitting properties with the photoanode thickness [56, 162, 171]. This is usually due to deposition technique limitations making very difficult the production of samples having well defined thicknesses without changing additional important parameters like the crystallographic structure or the surface morphology. Well controlled techniques like atomic layer deposition (ALD) [56, 162], pulsed laser deposition [171] or molecular beam epitaxy (present case) are desirable to make a study on variable thickness. On one hand, Zandi et al. [56] observed on hematite films made by ALD an increase of the photocurrent followed by a saturation when the film thickness increases, which can be explained as follows: when the thickness is larger than the depletion region width, no additional photocurrent is produced since any excess of charge carriers created in the bulk recombines. On the other hand, Dotan et al. [171] showed that with a reflective substrate like platinum, the variation of photocurrent with thickness is due to resonant light trapping in the film and to minority carriers (holes) recombination. Interestingly, our measurements on Ti-doped hematite compare well with the results of Dotan et

al. obtained on Ti-doped hematite films with a platinum substrate where the photocurrent was simulated with a minority carriers (holes) collection length of 20 nm [171]. Multiple reflections and holes recombinations explain thus well the photocurrent *vs.* thickness curve shape in our Ti-doped samples, but not in undoped ones where the amplitude of the photocurrent variation is larger than 75%. In this case, for thicknesses larger than the space charge layer width, we conclude that the photocurrent is limited by the diffusion length of both holes and electrons. In a simple picture this limitation can be illustrated as follows: in undoped samples the holes photogenerated far from the surface recombine before reaching the surface, and the electrons created near the surface cannot reach the substrate because of recombination with holes [70]. This limitation by electrons diffusion length is maybe due to the well-known weak electron mobility in α-Fe_2O_3 (0001) [50]. Our study of photocurrent *vs.* thickness allows understanding the influence of Ti-doping in photoelectrochemical properties. Indeed, we clearly show that the improvement observed in Ti-doped hematite is mainly due to an increase of both electrons and holes diffusion lengths.

5.1.6.b IPCE and PSIPCE

IPCE and PSIPCE measurements[27] at 0.6V *vs.* Ag/AgCl for samples of different thicknesses are reported on figure 5.12. The very weak photoresponse of our undoped samples unfortunately lead to unfavorable signal to noise ratios and made impossible IPCE measurements for these films, therefore only PSIPCE are shown for these films, as a function of the wavelength. Interestingly, on figure 5.12.a, we see that whatever the wavelength, a *ca.* 30 nm thickness for Ti-doped hematite films gives the best IPCE values, which is consistent with the white light response (photocurrent-voltage curve figure 5.10.b and photocurrent-thickness curve figure 5.11). Our efficiency values are of the same order of magnitude than values reported in the literature for the same kind of samples (thicknesses and doping level) [51, 52, 54]. However other studies reported higher IPCE values [56, 58, 60] which is maybe linked to different morphology and/or structure. PSIPCE is not a quantitative measure of efficiency, however by comparing figure 5.12.a and figure 5.12.b one can see that these curves can be used for the study of wavelength dependency. We observe the same behavior for all samples (all thicknesses and the two doping levels): a decrease of efficiency between 400 and 600 nm and a cut-off at 600 nm (equivalent to a band gap of *ca.* 2.07 eV). These results show that the band gap varies neither with the thickness nor with the doping level, which is consistent with valence band XPS spectra analysis.

[27] IPCE and PSIPCE were introduced in 3.4.3 and 3.4.4 respectively.

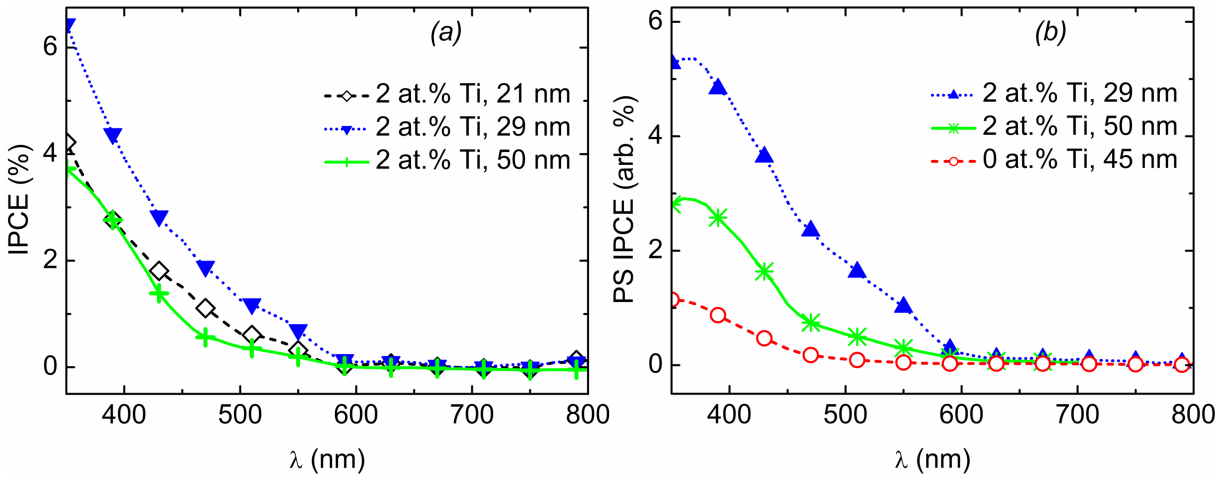

Figure 5.12: (a) IPCE curves at 0.6V *vs.* Ag/AgCl for 2 at.% Ti-doped hematite films of 21 nm (black open diamond), 29 nm (blue down triangle) and 50 nm (green plus) and (b) Phase-Sensitive IPCE (PSIPCE) curves at 0.6V *vs.* Ag/AgCl for 2 at.% Ti-doped hematite films of 29 nm (blue up triangle), 50 nm (green asterisk) and for a 45 nm thick undoped hematite film (red open circle). Experimental data were acquired with steps of 10 nm. From [55].

5.1.7 Discussion

RHEED patterns showed an unmodified crystallographic structure of hematite upon Ti-doping, excluding any morphology or crystallographic structure modifications, which was supported by EXAFS measurements, whatever the thickness (in the 5-50 nm range). XPS and IPCE measurements showed that a *ca.* 2 at.% Ti-doping of hematite, within the experimental uncertainties, does not modify the electronic structure (energy bands, gap, Fermi level). Thus it is legitimate to consider that the improved photoelectrochemical properties upon Ti-doping in our low Ti-doped samples are not linked to any crystallographic or electronic structure modification, but are induced by intrinsic properties changes only. The incorporation of titanium ions on the iron sites dramatically increases the carriers' diffusion lengths in hematite (*i.e.* their mobility), resulting in an overall conductivity increase. This lowers the recombination losses in Ti-doped hematite. The carriers' behavior in undoped and Ti-doped hematite films (thin and thick) is summarized and illustrated on figure 5.13.

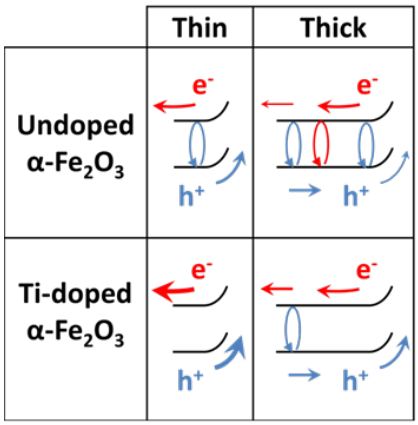

Figure 5.13: Illustration with a band diagram of the carriers' behavior in undoped and Ti-doped hematite films (thin and thick). Simple arrows and cycling arrows stand for charge movement (current) and charge recombination respectively. Carriers concerned are electrons or holes when the line is respectively red or blue. Line thicknesses convey the strength of the corresponding phenomena. From [55].

5.2 Surface chemical etching

In this section, we examine the effect of HCl etching on the surface of Ti-doped hematite epitaxial films deposited by OPA-MBE and the improved photoelectrochemical properties of these films. We studied 20 nm thick 2 at.% Ti-doped hematite thin films patterned by optical lithography and partially HCl-etched, following the protocol detailed in 3.1.3. By UV lithography, we defined on the sample surface micrometric squared (10-50 µm wide) patterns of resist (S1813). The etching time by HCl was 5 seconds for a 2 nm step height. In the end, the morphology of the sample consisted in as-grown Ti-doped hematite patches separated from each other by a partially HCl-etched Ti-doped hematite surface. This makes possible the simultaneous investigation of as-grown and etched surfaces on the very same sample. Topography and spatial-resolved electronic structure measurements were performed by atomic force microscopy (AFM) and X-ray photoemission electron microscopy (X-PEEM) respectively. Microscopy techniques are tools of choice to investigate the local variation of a particular physical property.

We firstly give evidence of a drastic improvement of the water splitting performances of Ti-doped hematite photoanodes upon HCl wet-etching (5.2.1). In addition to the topography investigation by atomic force microscopy (AFM) (5.2.2), a detailed determination of the local electronic structure has been carried out in order to understand the phenomenon. Using X-PEEM, we investigated the X-ray absorption spectral features at the Fe L_3 edge of an as grown surface and of a wet-etched surface on the very same sample thanks to patterning (5.2.3). Results are subsequently discussed (5.2.4).

5.2.1 Photocurrent

Figure 5.14 presents the photocurrent density *vs.* voltage curves for as-grown and after patterning with 10 µm squares 20 nm thick 2 at.% Ti:α-Fe_2O_3 / Pt (111) films (partially HCl-etched, *cf.* inset in figure 5.14, the etching step was about 2 nm). We see that the photocurrent density obtained for the partially HCl-etched sample is at least 25 % higher than for the as-grown one for all the bias voltages used. Moreover, for the partial HCl-etched sample the water splitting onset potential is significantly reduced by 0.1V with respect to the as-grown one.

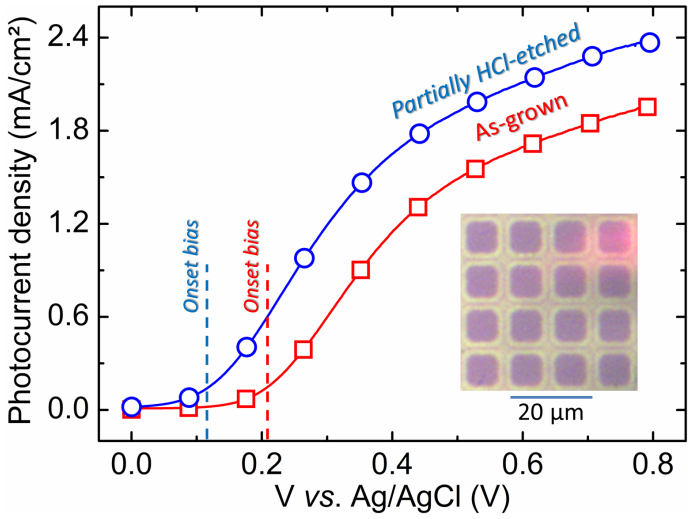

Figure 5.14: Photocurrent density *vs.* voltage curves for a 20 nm thick 2 at.% Ti:α-Fe_2O_3 / Pt (111) film: as-grown (red open squares), and partially HCl-etched (patterned by UV lithography) (blue open circles). The inset shows the used lithography pattern (10 µm squares). Dark zones (resp. bright) correspond to the as-grown surface (resp. etched). From [100].

Etching along the direction normal to the hematite (0001) basal plane will increase the film surface in contact with the electrolyte through the contribution from the step sides. From the inset of figure 5.14 we can estimate that 50% of the surface is etched. Hence a step height of 2 nm on a 20 nm thick film corresponds to a surface increase around 0.2 % due to the step sides contribution, which is much lower than what is observed on figure 5.14. Therefore we can neglect the photocurrent variations due to the contribution of the step sides.

Moreover the partial etching of our films could lead to changes in photocurrent linked to thickness variation. As seen in section 5.1, the photocurrent at 0.6V *vs.* Ag/AgCl for a 18 nm thick 2 at.% Ti:α-Fe_2O_3 film is *ca.* 5% lower than the one for a 20 nm thick 2 at.% Ti:α-Fe_2O_3 film. Then if changes in photocurrent were linked only to a change in the film thickness (from 20 nm to 18 nm for the partially HCl-etched surface which represents 50% of the total surface), a photocurrent decrease of around 2.5% should be observed.

Hence the increase in photocurrent recorded on figure 5.14, taking into account the thickness variation, is around 27.5 %. Therefore we can estimate that for a 20 nm thick 2 at.% Ti:α-Fe_2O_3 the gain in photocurrent upon HCl chemical etching of the whole surface (with a step of 2 nm) is *ca.* 50% (at 0.6V *vs.* Ag/AgCl).

5.2.2 AFM

We used AFM to compare the surface morphology of our samples before and after HCl-etching (*cf.* 3.2.3). Figure 5.15 shows the topography AFM picture (figure 5.15.a) and the height profile (figure 5.15.b) of a film patterned with 10 µm squares (etching step of about 2 nm). We can see that the overall roughness is increased on the HCl-etched surface. More precisely, the root mean square (RMS) roughness increases from 1 nm (as-grown surface) to 4.6 nm (partially HCl-etched surface). This roughness increase likely means that the chemical etching is not uniform. It maybe occurs preferably in the direction perpendicular to the surface, along defects like antiphase boundaries [172].

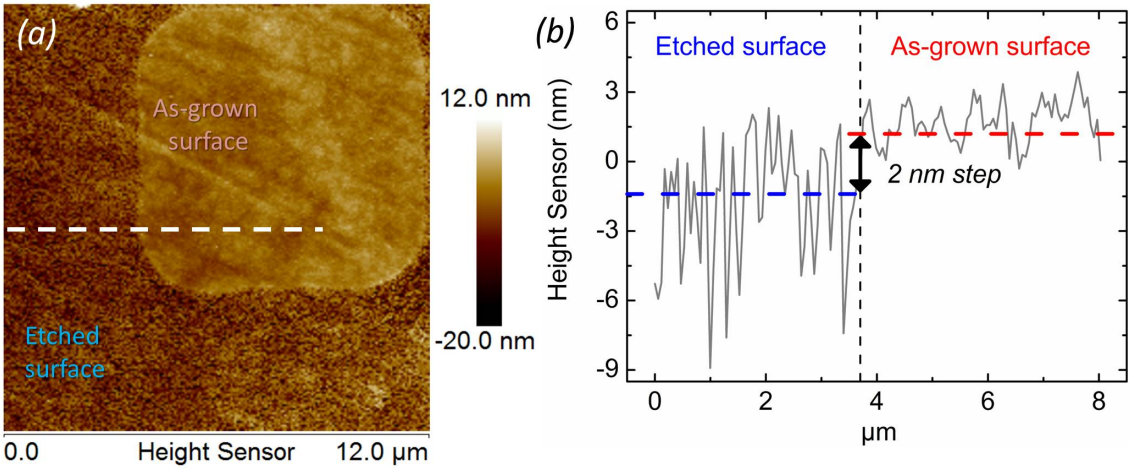

Figure 5.15: (a) 2D topography AFM picture of a patterned 20 nm thick 2 at.% Ti:α-Fe_2O_3 / Pt (111) film (2 nm step height). (b) Height profile along the white dashed line (grey curve). From [100].

5.2.3 X-PEEM

X-PEEM experiments were carried out at room temperature on the I06 Nanoscience beamline at the Diamond Light Source (Didcot-UK). Before analysis and in order to remove any surface contaminant due to air exposure, the samples were annealed under an O_2 partial pressure of 10^{-6} mbar and at a temperature of 300°C for 1 hour. The results presented here were obtained on a thin film patterned with rectangles of various sizes (6 µm to 50 µm) and a step height of *ca.* 2 nm (*cf.* pattern shown on figure 5.16).

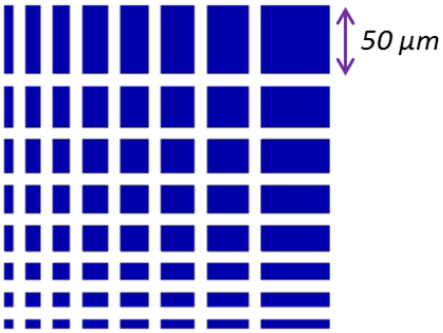

Figure 5.16: Lithography pattern used for X-PEEM measurements, allowing the patterning of rectangles of sizes ranging from 6 µm×6 µm to 50 µm×50 µm. The as-grown (resp. etched) surface is in blue (resp. white)

X-PEEM reveals the local electronic structure of iron in our patterned films on the as-grown and HCl-etched surfaces within the same image. The Fe L_3 absorption edge spectra were selectively recorded on each area[28] and are depicted on figure 5.17 for both surface regions.

The qualitative analysis of the Fe L_3 edge spectra has demonstrated being able to distinguish the electronic configurations of Fe in the different possible oxide environments [132, 138] (as it was shown in subsection 3.3.1). From a simple point of view, the crystal field typical for oxides splits the L_3 edge into two characteristic low and high photons energy contributions labelled L_{3A} and L_{3B} (highlighted on figure 5.17). The shape and relative intensities of these peaks give insights in the valence state of the Fe ions and their location in the lattice. The contribution L_{3A} (resp. L_{3B}), is strengthened in the presence of Fe^{2+} (resp. Fe^{3+}) ions. This interpretation can be derived from the simple comparison between reference spectra of Fe_3O_4 (33 % Fe^{2+}, 67 % Fe^{3+}) [143] and α-Fe_2O_3 (100 % Fe^{3+}) [132, 138] (see inset of figure 5.17) and has already been used by Droubay et al. in the framework of X-ray absorption microspectroscopy of ilmenite [173]. By comparing the two experimental spectra (figure 5.17),

[28] We recorded a XAS image stack (one image per photons energy) of the full field of view and integrated the intensities of the as-grown and etched surfaces to reconstruct their respective XAS spectra (*cf.* 3.3.4 for more details).

we observe a relative increase of the L_{3A} component for the HCl-etched surface with respect to the as-grown surface.

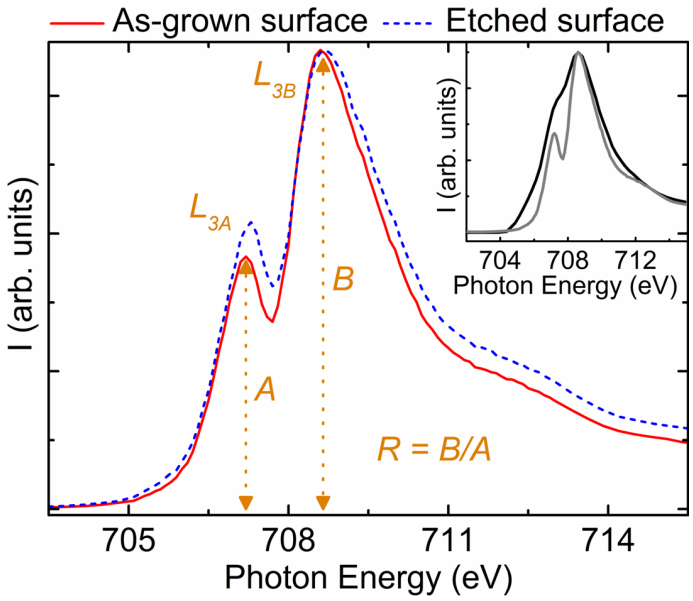

Figure 5.17: Fe L_3 absorption edge for the as-grown (red solid line) and etched (blue dashed line) surfaces of a 20 nm thick 2 at.% Ti:α-Fe_2O_3 / Pt (111) film. Orange items show the positions of the L_{3A} and L_{3B} contributions, as well as the R coefficient graphic determination. The inset shows experimental spectra of reference Fe_2O_3 (grey solid line) and Fe_3O_4 (black solid line) films. All spectra were normalised with the height of the L_{3B} peak. From [100].

In order to see if this behaviour is characteristic of the etched surface we have calculated the ratio R of the intensities of the two peaks of the absorption spectrum (B/A, see figure 5.17) on each point of the X-PEEM image. The map of the ratio R is shown on figure 5.18.b (on a 20 µm square) and a Mirror Electron Microscopy (MEM) picture recorded on the same region is shown on figure 5.18.a.

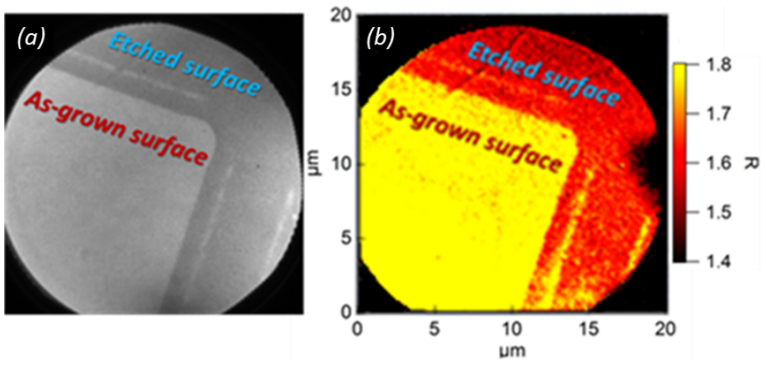

Figure 5.18: (a) MEM image of 20 µm squares (field of view 20 µm) and (b) map of the R ratio in the same region for a 20 nm thick 2 at.% Ti:α-Fe_2O_3 / Pt (111) film. From [100].

As explained in subsection 3.2.4, the MEM mode uses the same setup as X-PEEM, but instead of using photons as excitation source, low energy electrons are used. The MEM images are formed using backscattered low energy electrons and are of high surface morphology sensitivity. As a matter of fact, if the electron energy is not sufficiently high to overcome the surface potential barrier, they are simply reflected by the surface. On figure 5.18.a, the contrast in MEM between the as-grown surface and the HCl-etched surface in our case is linked to a work function variation between the as-grown and the etched surfaces, and/or to a difference of roughness, which is consistent with the AFM results. Lines just next to the pattern edges are due to lithography optical interferences. The R mapping (figure 5.18.b) follows exactly the morphology with a uniform value in the HCl-etched zone. The black areas in the right center on figure 5.18.b are due to inhomogeneous incident beam and channel-plates saturation. These zones are not visible on the MEM pictures (figure 5.18.a) because we used an electron beam as primary source. Moreover R varies from 1.8 on the as-grown surface to 1.6 on the etched one, a value which is intermediate between what is expected for Fe_2O_3 ($\approx$ 1.8 for 0 % Fe^{2+}) and Fe_3O_4 ($\approx$ 1.4 for 33 % Fe^{2+}) (see inset of figure 5.17.a). Assuming a linear variation of the R factor with the Fe^{2+} percentage, we can evaluate the amount of Fe^{2+} in the etched region around 15 %.

Using the same instrument, we also performed measurements of the valence band spectra for the two regions in resonant conditions using photons energies matching the Fe L_{3A} and L_{3B} XAS contributions. The two spectra are almost identical even in resonant conditions, except for the overall intensity of resonance which is different for the L_{3A} and L_{3B} photons energies. Indeed the overall VB signal using a photons energy matching the Fe L_{3A} (resp. L_{3B}) contribution is higher (resp. lower) for the etched surface than for the as-grown surface. This is consistent with the Fe L_3 XAS data (figure 5.17) where the overall XAS signal for photons energy matching the Fe L_{3A} (resp. L_{3B}) contribution is higher (resp. lower) for the etched surface than for the as-grown surface.

Our results show that the Fe^{2+} induced by etching does not reduce the band gap and introduces a very small number of electronic states in the band gap. Patches of sizes different from 20 µm exhibited very similar results.

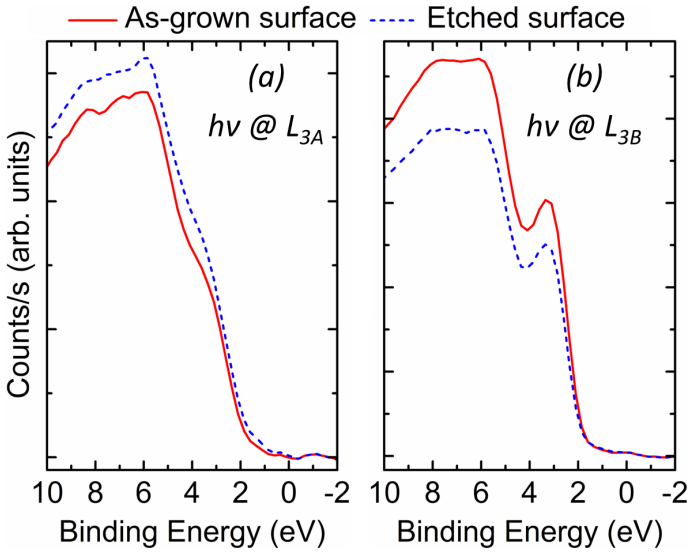

Figure 5.19: Resonant valence band photoemission spectra for the as-grown (red solid line) and etched (blue dashed line) surfaces of a 20 nm thick 2 at.% Ti:α-Fe_2O_3 / Pt (111) film obtained with photons energies matching the (a) L_{3A} and (b) L_{3B} contributions.

5.2.4 Discussion

Unlike Ziegler et al. [164] and Chernomordik et al. [101], the HCl etching effect on our hematite layers does not deal with any amorphous structure removal. Indeed the presence of such a structure would have been noticed by RHEED which is sensitive to the crystalline order of the very top surface layer. In our case, partial HCl wet-etching has a substantial effect on the topography of the films, but also on their electronic structure and on the iron oxidation state. The roughness increase conjugated with the iron oxide reduction can account for a significant improvement of the photoelectrochemical properties. A roughness increase can easily improve the photoelectrochemical properties thanks to a larger reactive surface. Moreover, as in ref. [165], we can reasonably assume that the chemical etching is crystalline surface plane dependent. Hence, the pure (0001) hematite surface may let appear upon etching crystalline planes of higher Miller indexes, which may have better photocatalytic activity than the basal hexagonal one. This phenomenon has also been observed in the case of the thoroughly-studied anatase TiO_2 photoanode material, where water is preferably adsorbed on (001) facets than on (101) facets [174]. Moreover, there is a strong conductivity anisotropy in hematite, the conductivity being 4 times higher in the (0001) basal plane than perpendicularly to it [96, 175]. The presence of Fe^{2+} can also contribute to the water splitting improvement because of an increased carrier mobility [147], as we noticed for the study of hematite samples annealed in UHV (*cf.* 4.3). Interestingly, the introduction of Fe^{2+} with HCl etching occurs without changing the band gap, avoiding any alteration of the semiconducting properties of our films. Analogously to what we observed in the case of a

hematite film annealed in UHV at 350°C (section 4.3), partial HCl etching induces an amount of Fe^{2+} sufficiently low to enhance the photocurrent without changing the crystallographic structure.

However up to now it is far from straightforward to decorrelate the relative contributions of the roughness increase and the iron oxide reduction. It may be possible to use procedures favouring the iron oxide reduction with respect to surface roughness increase. For instance reducing the Ti-doped hematite with a vacuum annealing, as we performed in subsection 4.3, may have little effect on the surface roughness, but we did not investigate the surface topography of our annealed pure hematite films. Reciprocally, an increase in the roughness may be achieved by ion beam etching, possibly with a moderate impact on the iron oxide stoichiometry.

5.3 Summary

In section 5.1, pure and Ti-doped hematite layers were found to have the same corundum (0001) crystallographic structure and to adopt similar Stransky-Krastanov growth mechanisms. Such single crystalline samples are suitable model systems to study independently thickness and Ti-doping effects on the photoelectrochemical properties; we demonstrate that they also allow disentangling intrinsic transport properties from mingled overall properties due to usually unknown contributions from morphology or crystalline structure defects. According to the results reported above, we can now propose a clear mechanism for the enhancement of the photocurrent density with respect to the Ti-doping level:

- We evidenced by EXAFS that Ti substitutes Fe in the hematite lattice inducing a slight distorsion of the oxygen octahedron, showing that Ti-doping does not induce significant structural modifications. In addition, for all doping levels (up to 17 at.%) we observed the same crystalline quality and the same crystallographic orientation. Therefore our samples are well suited to study the effect of Ti-doping on photoelectrochemical properties independently of other structural parameters.

- XPS and RPES spectra revealed that for all doping levels and thicknesses, Ti and Fe have the Ti^{4+} and Fe^{3+} valence state, without any Ti^{3+} or Fe^{2+}, excluding the possibility of increased conductivity through improved polaron hopping in Ti-doped films. The charge compensation is thus probably realized by cation vacancies formation. Assuming perfect charge compensation, we can estimate the cation vacancies concentration (C_{vac}) as function of the Ti concentration (C_{Ti}): $C_{vac} = {}^1\!/_3 C_{Ti}$.

- For doping levels above 5 at.%, Ti-doping induces a shift of the valence band toward higher binding energies. This shift has been theoretically predicted [176] and does not correspond to a gap variation but to a movement of the Fermi level toward the conduction band. This movement induces an increase of the electrical conductivity

and of the flat-band potential (arising larger band bending at the surface), therefore it hinders the recombination of electron-hole pairs and appears as a possible contribution to the improvement of photoelectrochemical properties. Nevertheless, the recombination rate is maybe influenced by the cation vacancies concentration, this can explain a maximum of efficiency around a Ti-doping level of 5 at.%. The shift of the valence band disappears for doping levels below 2 at.%.

– From the second set of samples, we evidenced the existence of an optimum layer thickness, which is higher for 2 at.% Ti-doped samples (30 nm) as compared to undoped ones (20 nm). Our results suggest that this effect is due to higher carriers diffusion lengths in the doped samples. This stresses intrinsic modifications of the hematite layer upon titanium doping that cannot be accounted for simple structural or electronic structure changes.

In section 5.2 the effect of a partial etching by hydrochloric acid on the surface topography and on the electronic structure was investigated by atomic force microscopy and X-ray photoelectron microscopy respectively. It was found that on the one hand HCl etching increases the overall roughness of the surface, providing a higher number of catalytic sites. On the other hand, the etched oxide is locally reduced, as it is shown by the presence of Fe^{2+} ions. These changes in the material properties result in a substantial improvement of the water splitting performances of Ti-doped hematite films (25 % photocurrent increase and onset potential reduction of 0.1V).

6 Photoanode heterojunctions

Combining materials in heterojunctions appears as a very promising way to improve the photoanode performances [177–179], analogously to heterojunctions and multi-junction solar cells in the photovoltaic field [180, 181]. Heterojunctions photoanode systems should not be mistaken with tandem solar water splitting systems where a solar cell is used to provide the bias required to realize water oxidation at the photoanode surface. Here we are considering systems where one expects to increase the photocurrent by benefiting from the phenomena existing in heterojunctions. Some of them are illustrated on figure 6.1:

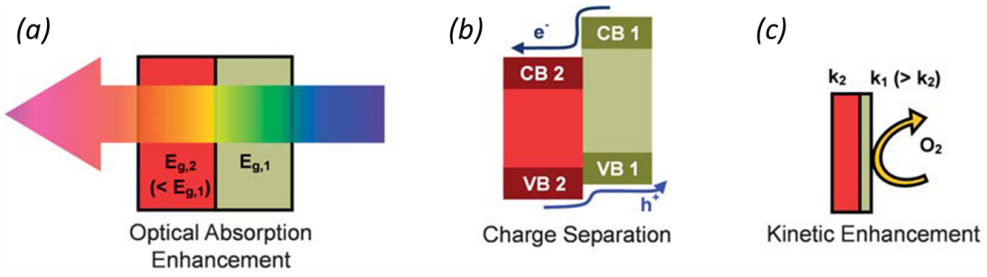

Figure 6.1: Phenomena in heterojunctions expected to increase photoelectrochemical performances: (a) optical absorption enhancement, (b) charge separation, (c) kinetic enhancement. Reproduced from [177].

Indeed, as it was more detailed in 2.4, heterostructuring may allow:

- light absorption optimization (figure 6.1.a) through the use of materials with various gaps. Combining materials with various gaps will increase the absorption efficiency of the whole system by utilizing the maximum number of incident photons.
- better charge separation (figure 6.1.b) thanks to the spontaneous electric field existing at the junction between the two semiconductors.
- kinetic enhancement (figure 6.1.c) thanks to more efficient surface kinetics and/or more appropriate conduction and valence band positions with respect to water oxidation and reduction energy levels.

Various examples from the literature of semiconductor heterojunctions involving hematite and other metal oxides were given in 2.4.

In this chapter we focus on the combination of TiO_2 and Ti:α-Fe_2O_3 to build semiconductor photoanode heterojunctions. As a matter of fact, among metal oxides, TiO_2 and Ti:α-Fe_2O_3 are the most promising candidates as photoanodes for solar water splitting

devices regarding their characteristics. As a reminder, the main advantage of hematite is its low band gap of *ca.* 2.1 eV. However its too low conduction band level requires a large applied potential to drive water oxidation at its surface. Besides TiO_2 features very interesting charge transport properties and electronic structure (conduction and valence band positions with respect to water oxidation and reduction energy levels) in the framework of photoanodes for water splitting, despite a large band gap of *ca.* 3.2 eV [5]. Also both are abundant on earth and very stable in aqueous environments. Combining hematite and TiO_2 in order to build a heterojunction photoanode featuring the advantages of both materials appears appealing.

Several studies reported the use of Fe_2O_3 - TiO_2 heterostructures [85–90, 131]. In these works, the materials are polycrystalline, often in core-shell structure, *e.g.* Fe_2O_3 nanoparticles deposited on TiO_2 nanotubes. In this framework we have studied systems constituted of nanometric single crystalline epitaxial films, allowing the use of resonant photoemission spectroscopy (RPES) in order to characterize the electronic structures of the heterojunction and of the interface between the two materials, which are crucial here. In addition measurements of the photocurrent under steady or modulated illumination regimes bring complementary informations about the charges dynamics in these systems. An encouraging fact about the combination of TiO_2 and hematite in epitaxial systems is the existence of natural crystals where epitaxy between rutile and hematite occurs (*cf.* figure 6.2).

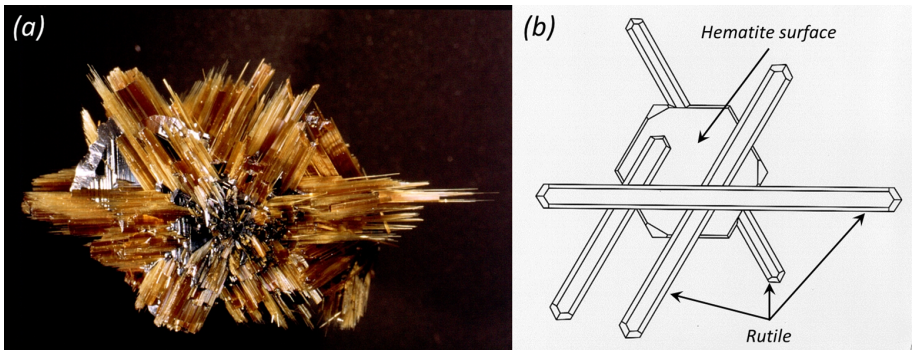

Figure 6.2: Natural epitaxy between rutile and hematite: (a) picture of the mineral and (b) illustration (© Monika Günther, Technische Universität Berlin Mineralogical Collections).

Section 6.1 presents the different samples studied and the results concerning the growth of the films by OPA-MBE (RHEED and XPS). The characterization of the electronic structure of our heterojunctions by RPES is shown in subsection 6.2. Lastly, the photoelectrochemical behaviours of our systems under steady or modulated illumination (OCLIA measurement, presented in subsection 3.4.4) are given in subsections 6.3.1 (white light) and 6.3.2 (monochromatic light) respectively. Lastly subsection 6.4 provides a proposition for the different photocurrent scenarii.

6.1 Growth and structure

The heterojunctions were deposited on single crystalline Pt (111) substrates by OPA-MBE. I have represented the set of realized samples on table 6.1. The terminology of the samples name was chosen as follows: F stands for Ti:α-Fe_2O_3, T stands for TiO_2 and the number before F or T gives the thickness of the corresponding layer in nm. We chose to keep a constant total thickness of 20 nm. This thickness corresponds to a good compromise: it is thick enough to allow acceptable photocurrents in photoelectrochemichal characterization and it is thin enough to allow synchrotron radiation measurements without charge build-up issues. For heterojunctions, we varied the relative thickness of TiO_2 and Ti:α-Fe_2O_3. We also studied single layers as references. The Ti-doping level of hematite was 2 at.% as determined by XPS.

Sample name	Complete architecture
20F	20 nm Ti:α-Fe_2O_3 / Pt (111)
5T/15F	5 nm TiO_2 / 15 nm Ti:α-Fe_2O_3 / Pt (111)
10T/10F	10 nm TiO_2 / 10 nm Ti:α-Fe_2O_3 / Pt (111)
10F/10T	10 nm Ti:α-Fe_2O_3 / 10 nm TiO_2 / Pt (111)
20T	20 nm TiO_2 / Pt (111)

Table 6.1: Set of samples studied in this chapter. For the terminology of the samples name, F stands for Ti:α-Fe_2O_3, T stands for TiO_2 and the number before F or T gives the thickness of the corresponding layer in nm.

6.1.1 RHEED

Figure 6.3 presents the RHEED patterns and the corresponding surface reciprocal lattices for the 20T and 10T/10F samples. The 20F film case corresponds to hematite RHEED patterns and has been discussed in subsection 5.1.1 [55].

In the case of the 20T sample, large dots on the RHEED patterns are visible, indicating a rougher surface and a Volmer-Weber growth mechanism (islands). Lastly for the 10T/10F sample, the RHEED patterns are similar to the 20T patterns, except that streaks are well visible, accounting for a less rough morphology on Ti:α-Fe_2O_3 (0001) than on Pt (111). For both samples, we can notice in both diffraction directions a spacing between RHEED lines divided by two with respect to the Pt (111) substrate. This means that the primitive unit cell (in the direct space) is twice larger for our TiO_2 layers than for Pt (111).

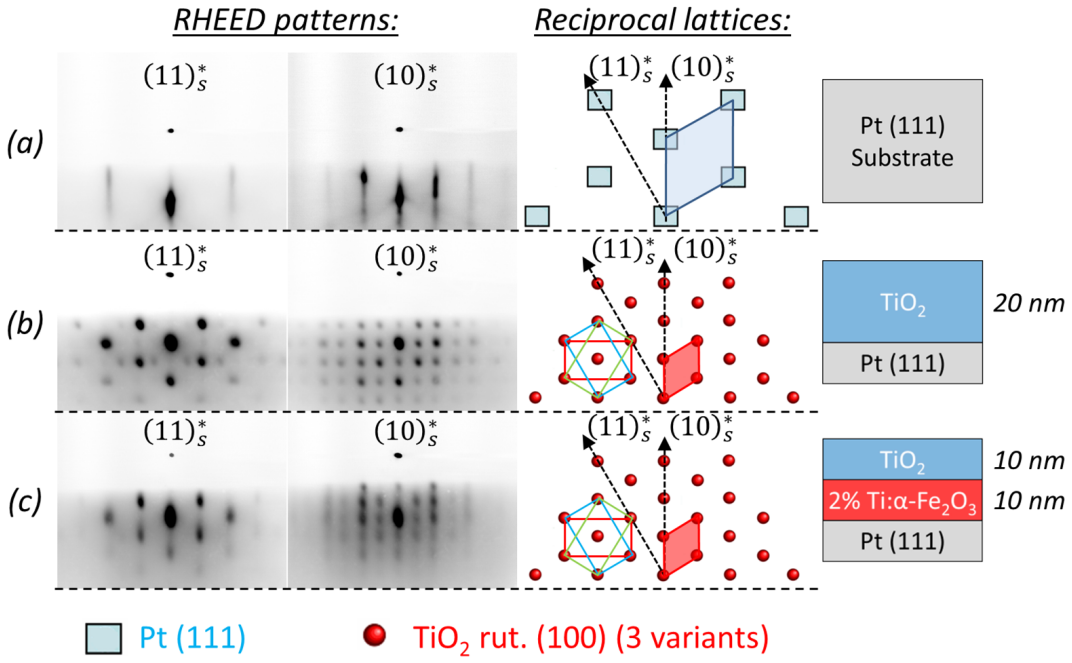

Figure 6.3: (Left panel) RHEED patterns over the two lowest index surface diffraction directions. (Right panel) The corresponding surface reciprocal lattices are represented, assuming a twice larger primitive cell (in the direct space) for TiO_2 with respect to Pt (111). The diffraction directions are also explicited, as well as the 3 variants for TiO_2 rutile (100) (3 coloured rectangles). Samples : (a) Pt (111) substrate, (b) 20T and (c) 10T/10F.

Pt (111) has a 6-fold surface crystallographic network presenting a 2D hexagonal symmetry (*cf.* figure 6.4.a). On Pt (111) (and also on Ti:α-Fe_2O_3 (0001)) the expected crystallographic structure and orientation for TiO_2 is rutile (100) [182], as it is also observed for the natural mineral (natural rutile / hematite epitaxy), *cf.* figure 6.2 above. When a structure with tetragonal symmetry is deposited on a surface with hexagonal symmetry, we can expect 3 variants, *i.e.* the lattice of the deposited material can have three different in-plane orientations. The surface crystallographic lattice expected for the growth of rutile TiO_2 (100) with 3 variants on Pt (111) is shown on figure 6.4.b. From this figure we see that rutile TiO_2 (100) with 3 variants has the same surface lattice symmetry than Pt (111). The RHEED patterns should thus have the same shape with the exception that the spacing between the streaks will change due to epitaxial strain. This is not the case for our RHEED data where we recorded a primitive cell (in the direct space) with a size doubled with respect to Pt (111), indicating most likely a 2×2 surface reconstruction.

Indeed we can calculate the lattice mismatch between Pt (111) and rutile (100). For bulk Pt (111), the relevant in-plane parameters are $\|\overrightarrow{a}\| = 0.277$ nm and $\|\overrightarrow{a} + 2\overrightarrow{b}\| = 0.479$ nm. For bulk rutile TiO_2 (100), the relevant in-plane parameters are 0.296 nm and 0.459 nm. This arises a 6.4 % compressive lattice mismatch for the smaller in-plane parameter and a 4.3 % extensive lattice mismatch for the larger in-plane parameter. These high mismatch values can explain a possible surface reconstruction. Another explanation may be that the structure is not perfectly/entirely rutile (100). However with the RHEED results alone we cannot conclude about the true crystallographic structure of our TiO_2 films. To go further in the analysis, surface X-ray diffraction would be needed to derive the precise crystallographic structure of the TiO_2 films grown on Pt (111) by determining the exact positions of the atoms in the primitive cell.

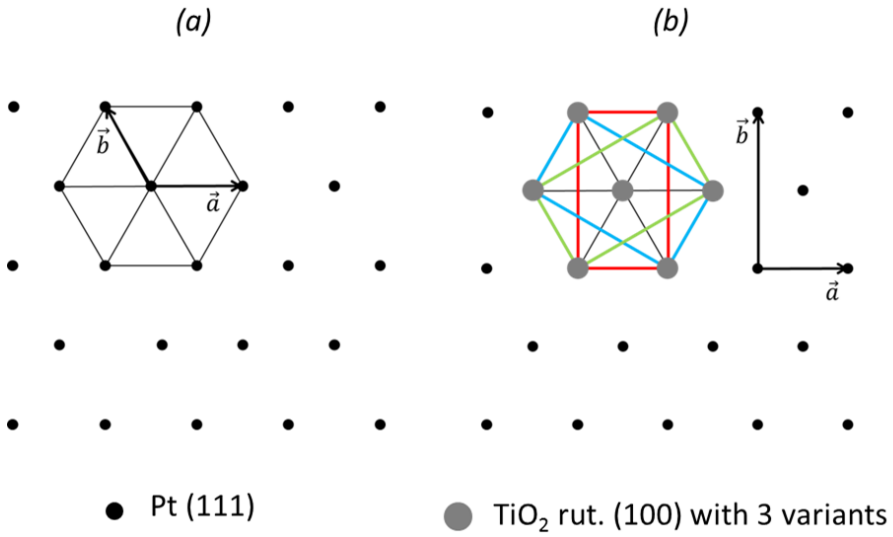

Figure 6.4: Surface crystallographic lattices for (a) Pt (111) (b) expected rutile TiO_2 (100) / Pt (111) with 3 variants (3 coloured rectangles). Small black (resp. large grey) dots represent the Pt (111) (resp. rutile TiO_2(100) with 3 variants) surface crystallographic network nodes. The TiO_2 is supposed to be completely strained.

6.1.2 XPS

The reference of binding energies was obtained through a Pt Fermi level measurement in ultra-thin films (thickness smaller than 5 nm) of α-Fe_2O_3 and TiO_2 deposited on Pt (111). Using this energy reference we showed that the O*1s* line lies respectively at 530.1 eV and 530.7 eV for single Ti:α-Fe_2O_3 and TiO_2 films. For heterojunctions samples, since we could not obtain a binding energy reference through the measurement of a Fermi level, we used the O*1s* line as binding energy reference. More precisely for these samples we considered the O*1s* line at 530.1 eV when the upperlayer is Ti:α-Fe_2O_3 or 530.7 eV when the upperlayer is

TiO_2. Figure 6.5 presents the Fe*2p* and Ti*2p* core levels and the valence band region XPS spectra and relevant measurements are given on table 6.2.

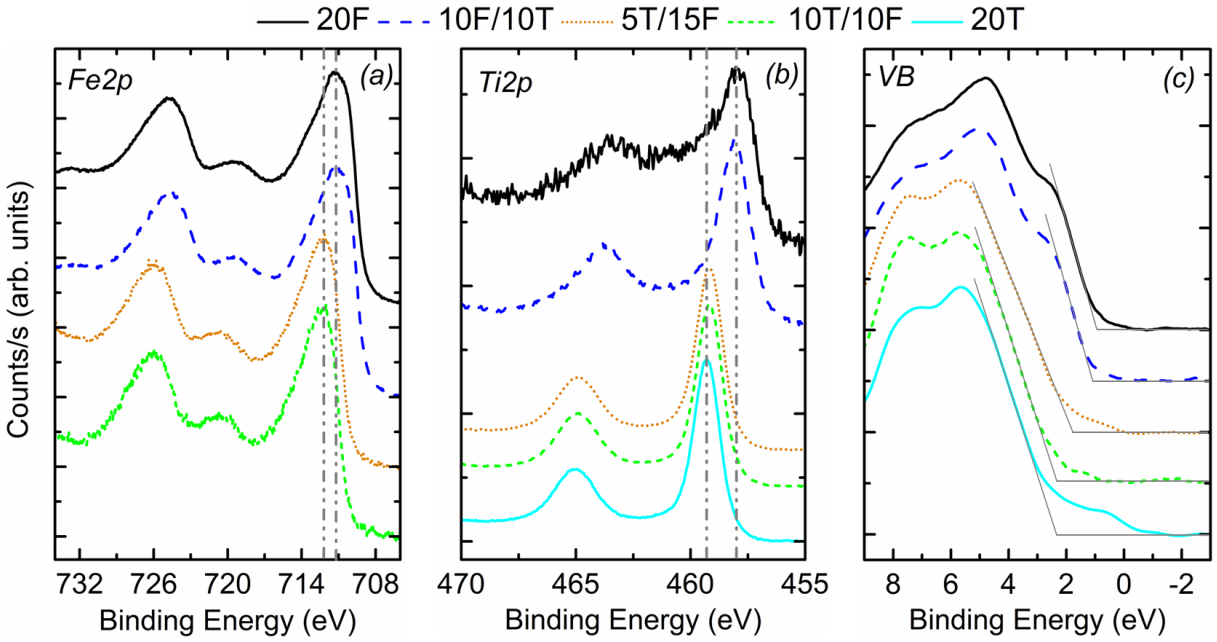

Figure 6.5: XPS spectra of the (a) Fe*2p* , (b) Ti*2p* core level and (c) valence band region. From top to bottom: 20F (black solid line), 10F/10T (blue wide dashed line), 5T/15F (orange dotted line), 10T/10F (green dashed line), and 20T (cyan solid line) samples. The valence band minimum (VBM) determination is also shown on (c) with grey.

Sample	O*1s*	Fe$2p_{3/2}$	Fe*2p* sat.	ΔFe*2p*	Ti$2p_{3/2}$	VBM	*VBO*
20F	530.1	711.2	719.4	8	458	0.95	
10F/10T	530.1	711.2	719.4	8	458.1		-0.15
5T/15F	530.7	712.2	720.4	8	459.2		0.25
10T/10F	530.7	712.2	720.4	8	459.2		0.25
20T	530.7				459.3	2.3	

Table 6.2: XPS results for all samples. The error bar is ± 0.1 eV.

For samples featuring a Ti:α-Fe_2O_3 upperlayer (20F and 10F/10T) we measured binding energies of 711.2 eV for the Fe$2p_{3/2}$ core level and of 719.2 eV for the Fe*2p* shake-up satellite, accounting for a Fe^{3+} ionic state and the absence of detected Fe^{2+} species. However, for samples featuring a TiO_2 upperlayer (5T/15F and 10T/10F) we measured binding energies of 712.2 eV for the Fe$2p_{3/2}$ core level and of 720.2 eV for the Fe*2p* shake-up satellite. The binding energy difference between the Fe$2p_{3/2}$ line and the Fe*2p* shake-up satellite, noted

ΔFe*2p* (and shown on table 6.2) is linked to the iron valence state [134]. For all samples, ΔFe*2p* = 8 eV. We can thus consider that iron is in the Fe^{3+} ionic state of iron in all systems and that no Fe^{2+} species were detected in XPS. However the sensitivity to Fe^{2+} through the analysis of the Fe*2p* shake-up satellite in XPS is quite low (few %). The shift of *ca.* 1 eV of the Fe*2p* lines is higher than the difference between the O*1s* lines positions (0.7 eV) chosen as binding energy reference. Therefore this shift can be attributed to band bending due to heterostructuration.

For the 20F sample, the Ti$2p_{3/2}$ line showed a narrow single feature at a binding energy of 458 eV which corresponds to the binding energy of Ti^{4+} species included in a hematite host matrix, as seen in the previous chapter (5.1) [53, 55]. For the 10F/10T sample we measured the Ti$2p_{3/2}$ line at 458.1 eV, *i.e.* at the same position than for the the 20F sample within the error bar. The Ti$2p_{3/2}$ line for the 20T sample was measured at 459.3 eV. This value is slightly higher than the one tabulated for Ti^{4+} in TiO_2 (458.8 eV) [168]. However, reported Ti$2p_{3/2}$ binding energies values for Ti^{4+} are usually widely spread around this tabulated value with a standard deviation of 1.3 eV [168, 183], which is likely due to various preparation conditions. For heterojunctions featuring a TiO_2 upperlayer (5T/15F and 10T/10F) the Ti$2p_{3/2}$ line was narrow and measured at a binding energy of 459.2 eV, *i.e.* at the same position than for the the 20T sample within the error bar.

Let us note that we were able to acquire a similar Fe*2p* photoemission signal in the case of 5T/15F and 10T/10F samples. This can be due to a not complete coverage of the underlayer by the upperlayer (which can originate from rough surfaces, as seen with RHEED patterns in figure 6.3), or to thicknesses small enough so that the photoelectrons from the underlayer can cross the upperlayer.

Figure 6.5.c shows the valence band spectra for all samples. For the 20T sample, the valence band minimum (VBM) is *ca.* 1.3 eV lower than the VBM of the 20F sample, which is, within the experimental error bar, equal to the difference of band gap between rutile and hematite. Calculating the VBM for heterojunctions has no physical meaning since the overall valence band of samples is measured.

We can apply the widely used formalism of Kraut et al. [135, 184, 185] to calculate the valence band offset (noted VBO) at the interface between the underlayer the upperlayer of the heterojunction. It is equal to the difference of the VBM at the interface between the underlayer and the upperlayer. This model assumes rigid band shift and that the layers forming the heterojunction are identical to the corresponding single layers (*i.e.* without interdiffusion between the two layers). The VBO is noted $VBO^{T/F}$ for the 5T/15F and 10T/10F samples (heterojunctions with an upperlayer of TiO_2 and an under layer of Ti:α-Fe_2O_3). Accordingly it is noted $VBO^{F/T}$ for the 10F/10T sample (heterojunction with an upperlayer of Ti:α-Fe_2O_3 and an underlayer of TiO_2). $VBO^{T/F}$ and $VBO^{F/T}$ are equal to:

$$\begin{cases} VBO^{T/F} = (BE_{Fe2p} - VBM)^{20F} - (BE_{Ti2p} - VBM)^{20T} - (BE_{Fe2p} - BE_{Ti2p})^{T/F} \\ VBO^{F/T} = (BE_{Ti2p} - VBM)^{20T} - (BE_{Fe2p} - VBM)^{20F} - (BE_{Ti2p} - BE_{Fe2p})^{F/T} \end{cases} \quad (6.1)$$

The terms used in equation 6.1 are illustrated on a binding energy diagram on figure 6.6. Using the results given in table 6.2, we calculated VBOs of -0.15 eV, 0.25 eV and 0.25 eV for the 10F/10T, 5T/15F and 10T/10F samples respectively. The difference in absolute values for the VBO between heterojunctions with a Ti:α-Fe_2O_3 upperlayer and heterojunctions with a TiO_2 upperlayer lies within the error bar (0.1 eV). From this result we can conclude that in heterojunctions the VBM of the TiO_2 layer in heterojunctions is always below the VBM of the Ti:α-Fe_2O_3 layer of about 0.2 eV, accounting for a high conduction band offset (*ca.* 0.8 eV considering the expected band gap difference between the two materials). This is important for the drawing of band diagrams needed for further discussion.

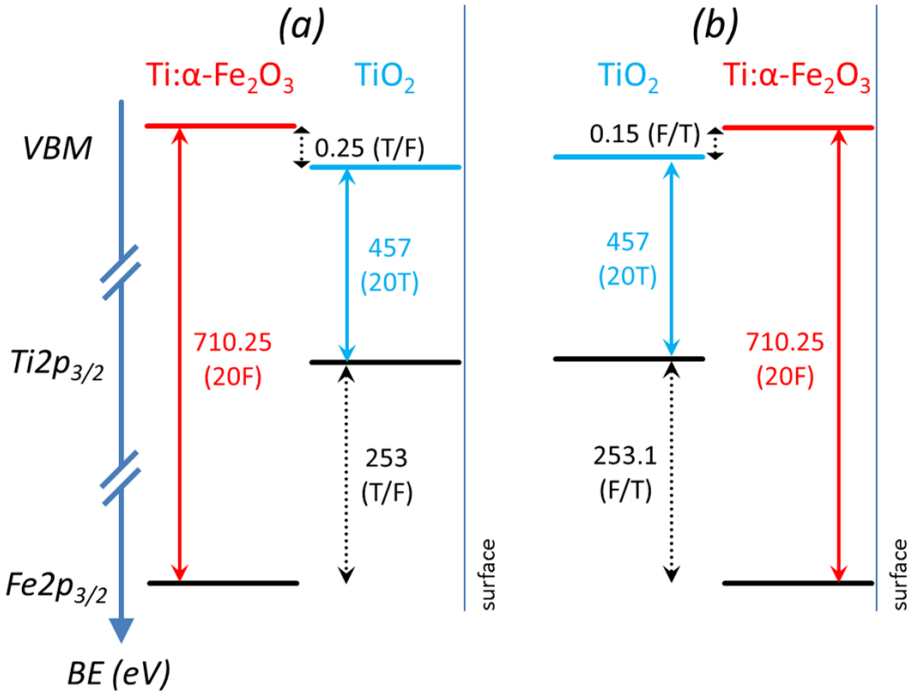

Figure 6.6: Illustrative binding energy diagram showing the terms used in equation 6.1 to calculate (a) $VBO^{T/F}$ and (b) $VBO^{F/T}$. Red, blue and black dotted arrows correspond respectively to binding energies differences calculated in single layers of Ti:α-Fe_2O_3, TiO_2 and in the corresponding heterojunctions.

6.2 Electronic structure investigation by RPES

Assembling different materials together results in an electronic structure modification of all involved materials and in the creation of interfaces. Since the band structure is a key parameter for water splitting, it would be of top interest to selectively determine it for each material and for the interfaces (*e.g.* presence of defects or potential barriers). A very powerful technique to tackle these issues in the case of thin films is resonant photoemission spectroscopy (RPES), which was presented in 3.3.3 [143]. We performed RPES measurements at the Fe and Ti L_3 edges.

6.2.1 RPES at the Fe L_3 edge

Figure 6.7 shows the X-ray absorption spectra and the corresponding resonant photoemission maps of the valence band obtained with photons energies around the Fe L_3 absorption edge for heterojunctions and the 20F sample.

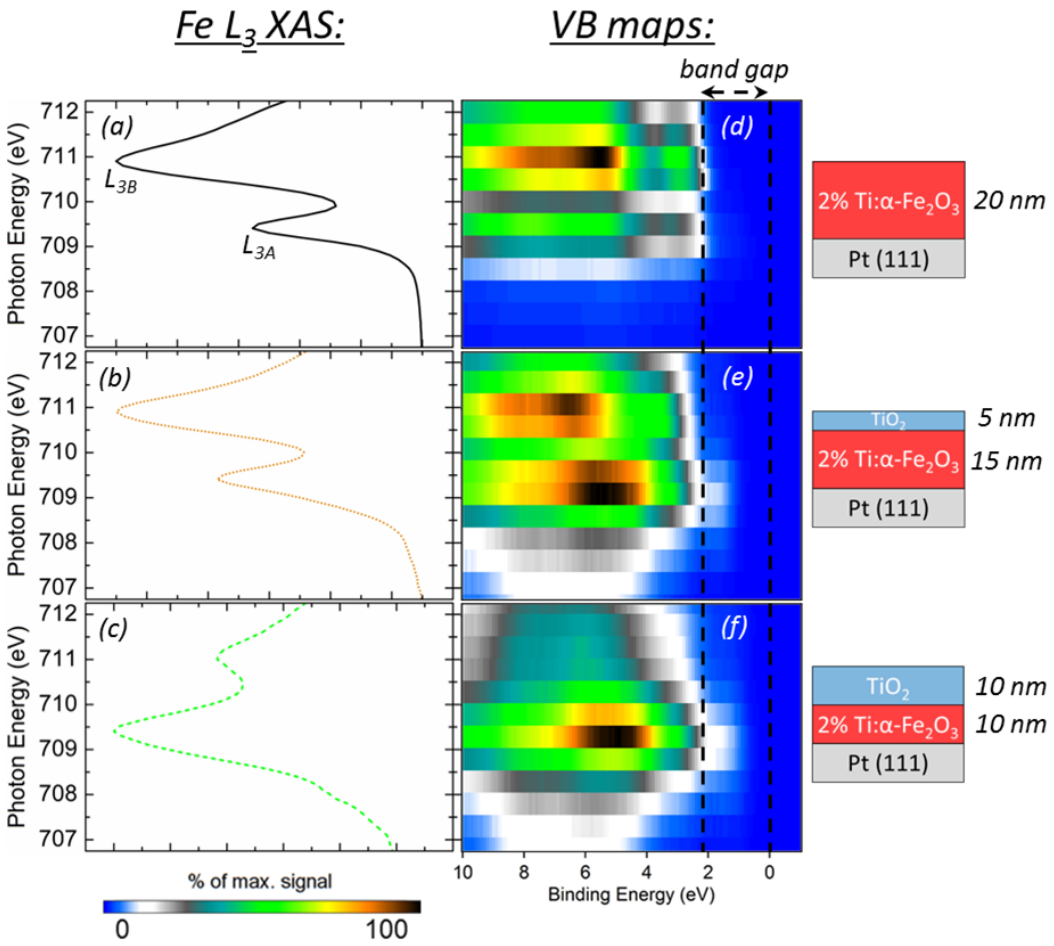

Figure 6.7: Electronic structure measurements done by RPES at the Fe L_3 edge. (Left panel) Fe L_3 X-ray absorption spectra. (Right panel) Corresponding valence band photoemission maps, the colour scale is given at the figure bottom. Samples: (a)+(d) 20F, (b)+(e) 5T/15F, (c)+(f) 10T/10F.

As explained in subsections 5.2.3 and 3.3.1, the qualitative analysis of the Fe L_3 XAS has demonstrated being able to distinguish the electronic configurations of Fe in the different possible oxide environments [132, 138]. The contribution L_{3A} (resp. L_{3B}), is strengthened in the presence of Fe^{2+} (resp. Fe^{3+}) ions. Experimentally we found out that the L_{3A} contribution increases when the hematite film is covered by a TiO_2 film (*cf.* left panel on figure 6.7). In the case of the 10T/10F sample (figure 6.7.c), the L_{3A} contribution is even higher than the L_{3B} contribution, accounting for a high number of detected Fe^{2+} species in the probed zone. However we did not detect by XPS the presence of Fe^{2+} species (*cf.* 6.1.2). Let us note that it is difficult to compare XAS results with XPS results since the probed depth is different in the two experiments. Indeed for the Fe*2p* core level in XPS, the signal of photoelectrons having a kinetic energy around 700 eV was measured, whereas in XAS the kinetic energy of recorded secondary electrons was 35 eV.

Concerning valence band resonant photoemission maps, one can notice an increase of intensity for binding energies below 2 eV (within the band gap, between the two vertical black dotted lines). This zone, which accounts for electronic states within the band gap, widens and intensifies when the TiO_2 upperlayer thickness increases and is visible only at photons energies matching the Fe L_{3A} XAS contribution. Since these states resonate at the photons energy corresponding to Fe^{2+} like in Fe_3O_4 [143], we can conclude that they correspond to Fe^{2+} species which are favoured by the presence of a TiO_2 upperlayer. This result highlights a major advantage of RPES, which is its sensitivity. Indeed these Fe^{2+} species have not been detected in XPS (through the analysis of the Fe*2p* shake-up satellite) because it is much less sensitive than resonant photoemission.

Figure 6.8 shows the valence band spectra obtained at three relevant photons energies (before the edge, at the L_{3A} and at the L_{3B} positions). On figure 6.8.a (valence band obtained with a photons energy below the Fe absorption edge), the valence band edge for the 10T/10F sample is shifted *ca.* 1 eV toward higher binding energies as compared to the 20F sample. The apparent band gap of the 10T/10F sample is then 1 eV higher than the one of the 20F sample, which corresponds to the TiO_2 bandgap. This means that with photons energies lower than the Fe edge, we are mainly sensitive to the TiO_2 upperlayer. However, for photons energies at the Fe L_{3A} and L_{3B} positions, the weak signal is exacerbated thanks to the resonance phenomena since it is coming from Fe atoms. As a consequence, on figures 6.8.b and 6.8.c, the valence band edge of both samples are equal, so they have the same apparent gap (corresponding to the hematite gap). Moreover in the case of the 10T/10F sample we can notice for these two energies a signal increase for binding energies lower than 2 eV as compared to the 20F sample, as we saw earlier on figure 6.7 (Fe^{2+} species due to the TiO_2 upperlayer).

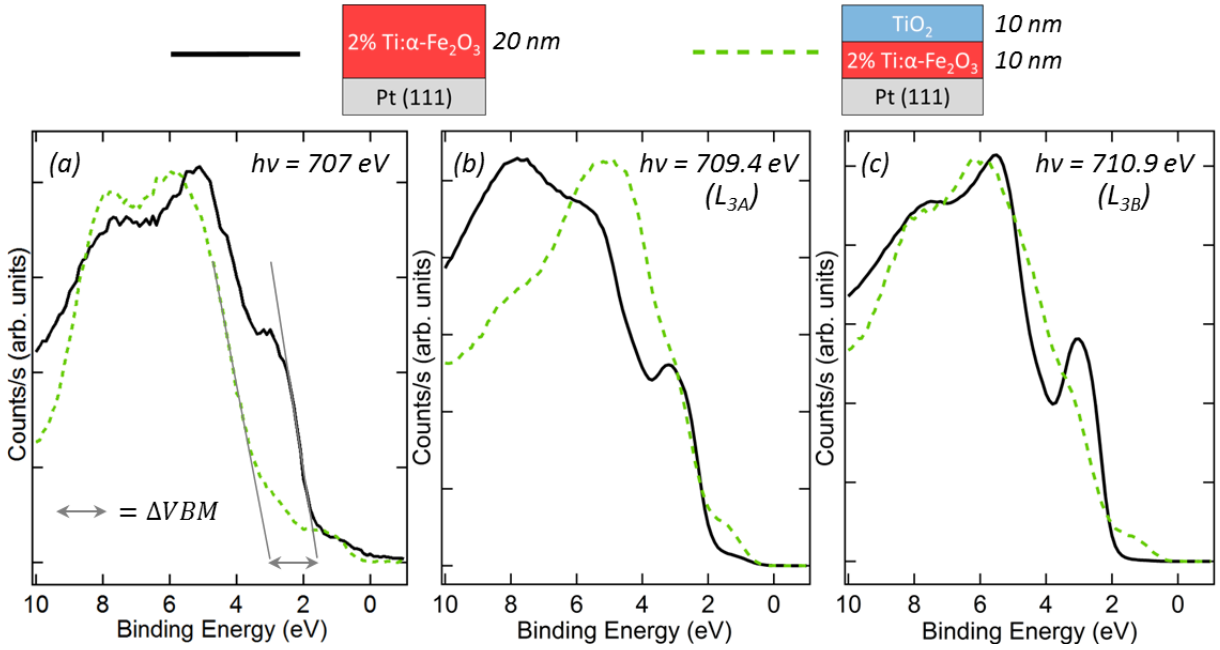

Figure 6.8: Resonant valence band photoemission spectra obtained with photons energies of (a) 707 eV (before Fe L_3 edge), (b) 709.4 eV (L_{3A} contribution) and 710.9 eV (L_{3B} contribution) for samples 20F (black solid line) and 10T/10F (green dashed line).

By comparing the valence band spectra of the 10T/10F heterojunction obtained with photons energies before the Fe L_3 edge (707 eV, figure 6.8.a) and at the Fe L_3 edge (709.4 eV and 710.9 eV, figures 6.8.b and 6.8.c), we can directly calculate the valence band offset between Ti:α-Fe_2O_3 and TiO_2 in the heterojunction, which is *ca.* 1 eV. This is larger than the valence band offset value calculated earlier using XPS data (*ca.* 0.2 eV, *cf.* subsection 6.1.2). In RPES, the photons energy used is around 710 eV, corresponding to a kinetic energy of *ca.* 705 eV for the photoelectrons emitted from the valence band. However in XPS, the photons energy used 1486.7 eV (Al K_α radiation) corresponding to a kinetic energy of *ca.* 1480 eV for the photoelectrons emitted from the valence band. Then the mean free path of valence band photoelectrons is lower in RPES than in XPS. Therefore in the case of heterojunctions, RPES and XPS do not probe the same thickness: indeed RPES is more sensitive to the interface than XPS, which can explain the valence band offset discrepancies.

6.2.2 RPES at the Ti L_3 edge

Figure 6.9 shows X-ray absorption spectra and the corresponding resonant photoemission maps of the valence band obtained with photons energies around the Ti L_3 absorption edge for heterojunctions and the 20T sample. We did not include in this figure the map for the 20F sample because no interesting resonance features were observed (*cf.* figure 5.8 in subsection 5.1.3).

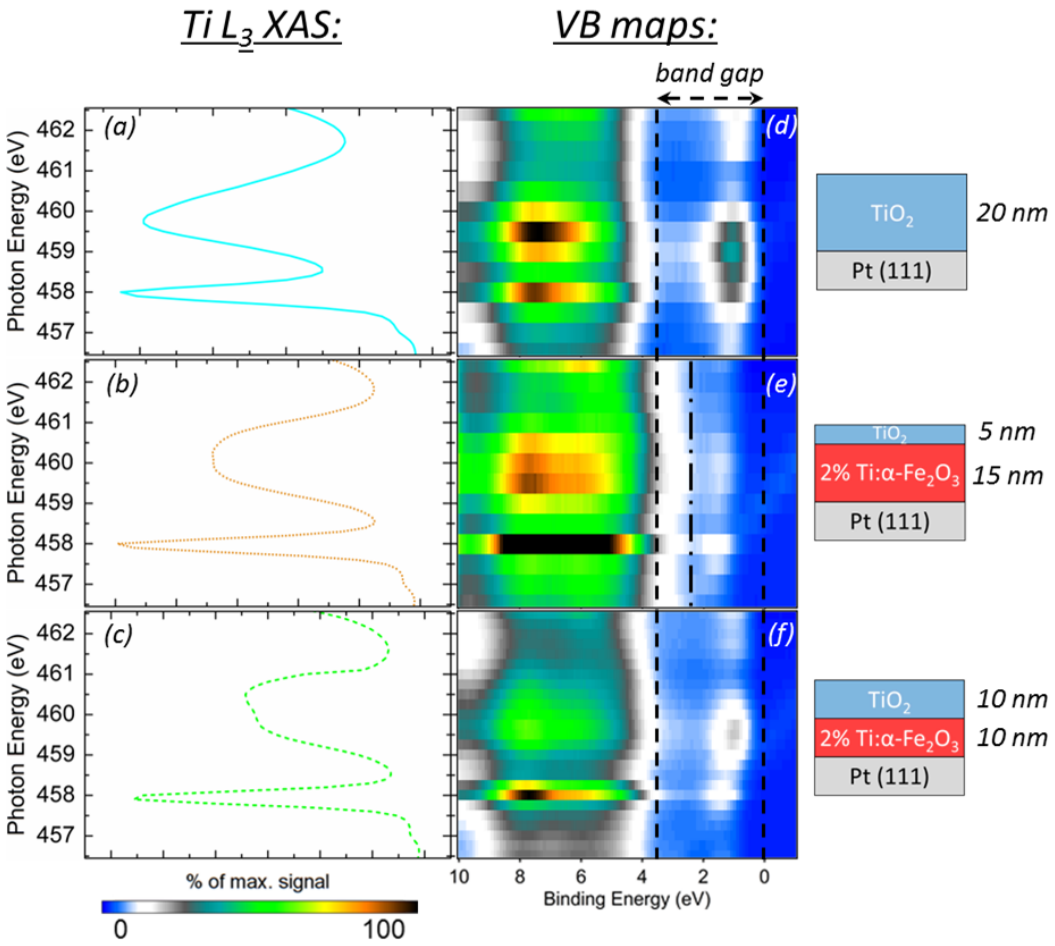

Figure 6.9: Electronic structure measurements done by RPES at the Ti L_3 edge. (Left panel) Ti L_3 X-ray absorption spectra. (Right panel) Corresponding valence band photoemission maps, the colour scale is given at the figure bottom. Samples: (a)+(d) 20T, (b)+(e) 5T/15F, (c)+(f) 10T/10F.

In the case of TiO_2, the analysis of the Ti L_3 absorption spectra can give insights about the crystallographic structure (anatase or rutile), as it has been pointed out by Laskowski and Blaha [186]. More precisely, as it is shown on figure 6.10 Ti L_3 XAS in TiO_2 shows two major features: a sharp peak around 458 eV and a broader component around 460 eV. The latter is also split into two contributions: one around 459.5 eV and the other around 460.5 eV (highlighted by asterisks on figure 6.10). In reference [186], the authors demonstrate that for anatase (resp. rutile) the 459.5 eV contribution is more (resp. less) important than the 460.5 eV one.

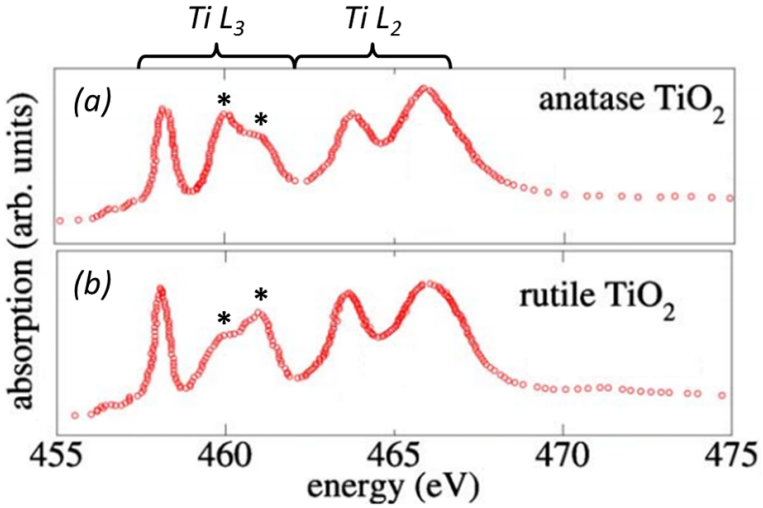

Figure 6.10: Experimental XAS at the Ti $L_{2,3}$ edge for (a) anatase TiO_2 and (b) rutile TiO_2. Asterisks highlight the contributions making possible the distinction between anatase and rutile. Reproduced from [186].

Hence from figure 6.9.a we can conclude that the TiO_2 structure of the 20T sample is anatase. The 460.5 eV contribution increases for heterojunctions, accounting for a more dominant rutile structure. However our *in situ* RHEED patterns (*cf.* figure 6.3 in subsection 6.1) led to the hypothesis of a rutile (100) structure. The comparison between XAS and RHEED results is far from trivial since the probing depth of RHEED (1-2 first atomic layers, *i.e.* few Å) is well below the one of XAS (few nm). Besides the RHEED measurements are done at a temperature around 900K (during the thin film deposition by OPA-MBE), whereas the XAS spectra are acquired at room temperature. Our TiO_2 films are possibly a mix of the two structures.

Valence band maps on figure 6.9 present zones of increased intensity within the band gap, like in the case of the Fe L_3 edge. Those states are likely due to Ti^{3+} species present in the material, as it was demonstrated by Le Fèvre et al. [170] in the case of oxygen-deficient TiO_2 studied by RPES. The fact that for our samples Ti^{3+} was not detected in conventional XPS but detected by RPES is due to the higher sensitivity of RPES. The presence of Ti^{3+} in our samples can be explained by the existence of structural defects (corroborated by a possible mix of anatase and rutile structure) leading to the presence of oxygen vacancies. We can notice an increase of the number of electronic states in the band-gap when the TiO_2 content in the sample (*i.e.* thickness) increases, meaning that the quantity of Ti^{3+} in the system increases when the thickness of the TiO_2 layer increases. Hence the Ti^{3+} species are intrinsically present in our TiO_2 films deposited by OPA-MBE on Pt (111) or Ti:α-Fe_2O_3 (0001) (*i.e.* the appearance of Ti^{3+} occurs during the growth). Lastly, in the case of the 5T/15F sample (figure 6.9.e), a shift of the valence band edge toward lower binding energies is observed (see the increase of the signal between 3 and 2.2 eV of binding energy, between

the dashed and dash-dotted black lines). This is due to the measure of a photoemission signal corresponding to the valence band of the Ti:α-Fe_2O_3 underlayer, which we are able to record even with photons energies below the Fe L_3 edge since the TiO_2 upperlayer for this sample is very thin.

6.2.3 Discussion about RPES results

The presence of Fe^{2+} induced by the deposition of a TiO_2 film on Ti-doped hematite can be due to interdiffusion between the two layers at the interface. In order to investigate the effet of Fe inclusion in TiO_2, we also studied a 0.5 at.% Fe-doped TiO_2 sample (elaborated in the same conditions than the other TiO_2 films). The RHEED patterns during the growth of this material and the Ti*2p* core level XPS spectra were identical to the ones of pure TiO_2 (20T sample, *cf.* figure 6.3.b). The Fe*2p* core level XPS spectra showed classical features for iron oxide however it was not possible to conclude on the Fe valence state because the satellite position could not be determined with such a small doping level (low statistics). The Fe and Ti L_3 XAS together with the corresponding valence band maps are shown on figure 6.11. The Fe L_3 XAS (figure 6.11.a) shows a single feature around 709 eV corresponding to the L_{3A} contribution, with a shoulder after the peak. The shoulder can be associated to a very low (if any) L_{3B} contribution, thus a very small (if any) Fe^{3+} content. This shape presents a lot a resemblance with the Fe L_3 XAS in the FeO environment published by Jiménez-Villacorta et al. [138] where the state of Fe is only Fe^{2+}. We can then conclude that the iron state in our 0.5 at.% Fe-doped TiO_2 is mainly Fe^{2+}. Moreover, the corresponding valence band map (figure 6.11.c) exhibits a substantial photoemission signal for binding energies within the band gap for photons energies matching the L_{3A} contribution. These results show the same behaviour than those measured for heterojunctions at the Fe edge (*cf.* figure 6.7). Therefore a possible hypothesis is that there is an interdiffusion of Fe into TiO_2 upon TiO_2 deposition on Ti-doped hematite, which is expected according to the Ellingham diagrams[29].

The Ti L_3 XAS (figure 6.11.b) has the same shape than the 20T sample one. Since RHEED patterns were also identical, the structure can be considered to be the same (anatase-rutile mix). The corresponding valence band map (figure 6.11.d) shows electronic states within the band gap, but of a smaller amount compared to the 20T sample, accounting for a smaller Ti^{3+} concentration in this sample as compared to undoped TiO_2. We previously considered that the reduction of Ti^{4+} to Ti^{3+} was linked to charge balance restoring due to oxygen vacancies. In the case of Fe:TiO_2, Fe^{2+} species may be more efficient to restore the charge balance than Ti^{3+} species originating from Ti^{4+} reduction. This may explain the decreased Ti^{3+} concentration in Fe:TiO_2 with respect to undoped TiO_2.

[29] The considered Ellingham diagrams can be found at this adress

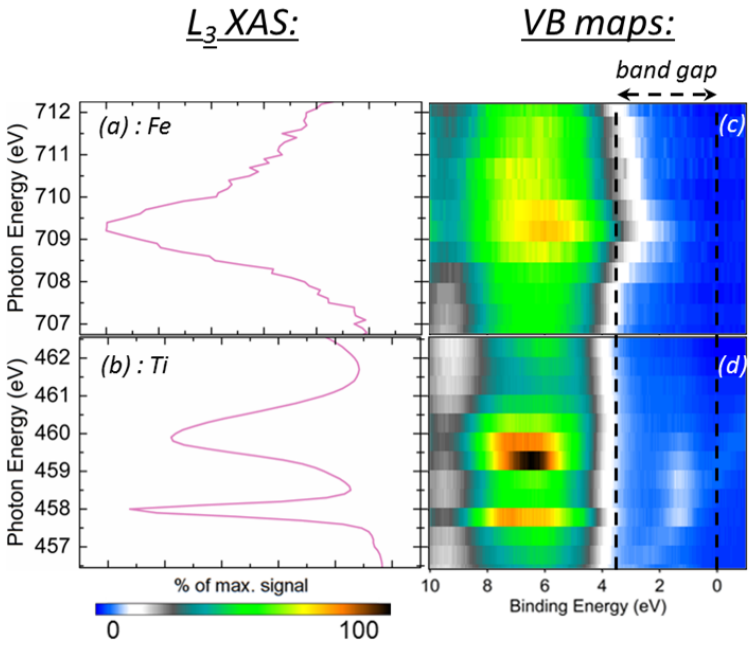

Figure 6.11: Electronic structure measurements done by RPES on a 20 nm Fe:TiO_2 / Pt (111)sample (0.5 at.% Fe-doping level). (Left panel) L_3 X-ray absorption spectra: (a) Fe and (b) Ti edges. (Right panel) (c)+(d) Corresponding valence band photoemission maps. The colour scale is given at the figure bottom.

6.3 Photocurrent measurements

6.3.1 Photocurrent under steady white light illumination

Figure 6.12 presents the photocurrent density *vs.* voltage curves for single layers and heterojunctions obtained with steady white light illumination. In all cases, only anodic photocurrent appears within the chosen range of potentials. In the case of the 20F sample, a good photocurrent is achieved, but at the cost of a high onset potential ($\approx$ 0.2V *vs.* Ag/AgCl). On the opposite, the 20T sample shows a maximum photocurrent almost three times lower, although it is achieved with a low onset potential ($\approx$ -0.4V *vs.* Ag/AgCl). For heterojunctions with a TiO_2 upperlayer (samples 5T/15F and 10T/10F), the photocurrent at high voltage decreases when the TiO_2 thickness increases, with respect to the 20F sample but the onset potential is slightly reduced by *ca.* 0.1V. Lastly, the 10F/10T sample shows very poor photoelectrochemical properties with an onset potential *ca.* 0.7V *vs.* Ag/AgCl and a loss of photocurrent of almost one order of magnitude at 0.8V *vs.* Ag/AgCl with respect to the 20F sample.

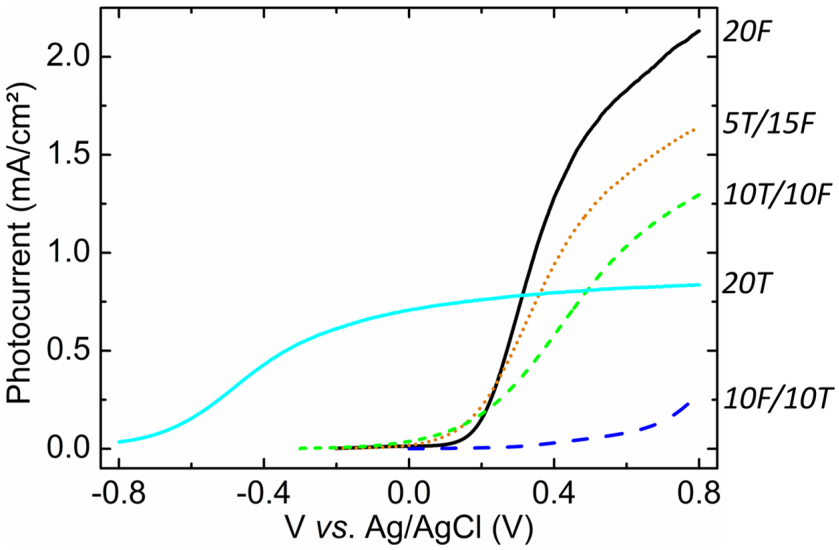

Figure 6.12: Photocurrent density *vs.* voltage curves for the 20F (black solid line), 5T/15F (orange dotted line), 10T/10F (green dashed line), 10F/10T (blue wide dashed line) and 20T (cyan solid line) samples.

To discuss the photocurrent discrepancies between single layers and heterojunctions, we should consider the phenomena that makes an electron-hole pair participate to the water photoelectrolysis photocurrent. The photogenerated electron-hole pair has to fulfil two conditions: (i) it should be created (*i.e.* the photon should be absorbed by the system) and (ii) the associated charges (electron and hole) should reach the interface where they are expected to react. Moreover in the case of heterojunctions the photogenerated charges have to cross the interface between Ti:α-Fe_2O_3 and TiO_2. Therefore a gain (resp. a loss) of photocurrent can be due to an increase (resp. decrease) of the quantity of absorbed photons and/or to an enhancement (resp. degradation) of the charge transport due to heterostructuring.

If photocurrent discrepancies between single layers and heterojunctions could be explained solely by absorption discrepancies due to effective band gap differences, a linear combination of the photocurrent of the single layers should simulate the photocurrent of heterojunctions. Since the penetration depth of photons having wavelength corresponding to the UV and visible range is in the hundreds of nm scale, our linear combination approach is reasonable considering the thicknesses of our samples (tens of nm). We calculated the photocurrent corresponding to the linear combination of the 20T and 20F samples according to the (TiO_2):(Ti:α-Fe_2O_3) content ratio in the different heterojunctions (5:15 for the 5T/15F sample and 10:10 for the 10T/10F and 10F/10T samples). The corresponding curves are shown on figure 6.13. On this figure we see that the photocurrent of the linear combination of single layers is always superior to the photocurrent of the actual heterojunctions. At high applied potentials, the differences are less pronounced (except for the 10F/10T sample), meaning that for this range of potentials the differences between single layers and hetero-

junctions are dominated by absorption discrepancies. However for applied potentials lower than 0.2V *vs.* Ag/AgCl, where only TiO_2 features a substantial photocurrent, the photocurrent in heterojunctions is almost zero. This means that other phenomena, like less efficient surface kinetics or detrimental charge transport due to heterostructuring, are responsible for photocurrent losses.

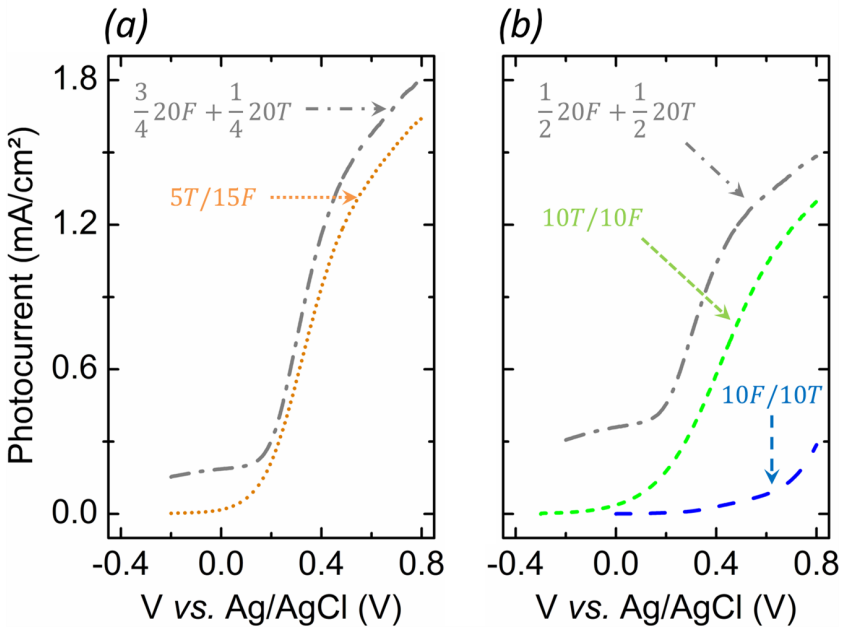

Figure 6.13: Photocurrent obtained by linear combination of the 20F and 20T samples data according to the TiO_2 / Ti:α-Fe_2O_3 content ratio (grey dashed-dotted line) corresponding to the (a) 5T/15F and (b) 10T/10F and 10F/10T heterojunctions. The photocurrent of heterojunctions is also shown.

6.3.2 Photocurrent under monochromatic light

We measured the $J_{ph}(\lambda)$ curve for all samples under steady monochromatic light at applied potentials chosen in the [-0.8V ; +0.8V] *vs.* Ag/AgCl window (photocurrent noted $J_{ph}^{Steady}(\lambda)$). The same curve was acquired under chopped light illumination using the OCLIA method presented in subsection 3.4.4 (photocurrent noted $J_{ph}^{OCLIA}(\lambda)$). At a given potential, the differences between the photocurrent measured in the steady illumination regime ($J_{ph}^{Steady}(\lambda)$) and the one measured with the OCLIA method ($J_{ph}^{OCLIA}(\lambda)$) are due to surface charge recombination. To represent the data together, we considered that a bias of +0.8V *vs.* Ag/AgCl, is strong enough so that the surface charge recombination contributions are negligible resulting in $J_{ph}^{Steady}(0.8V) = J_{ph}^{OCLIA}(0.8V)$.

Figure 6.14 shows $J_{ph}^{Steady}(\lambda)$ and $J_{ph}^{OCLIA}(\lambda)$ curves at applied potentials from -0.2V to +0.8V *vs.* Ag/AgCl for the 20F sample.

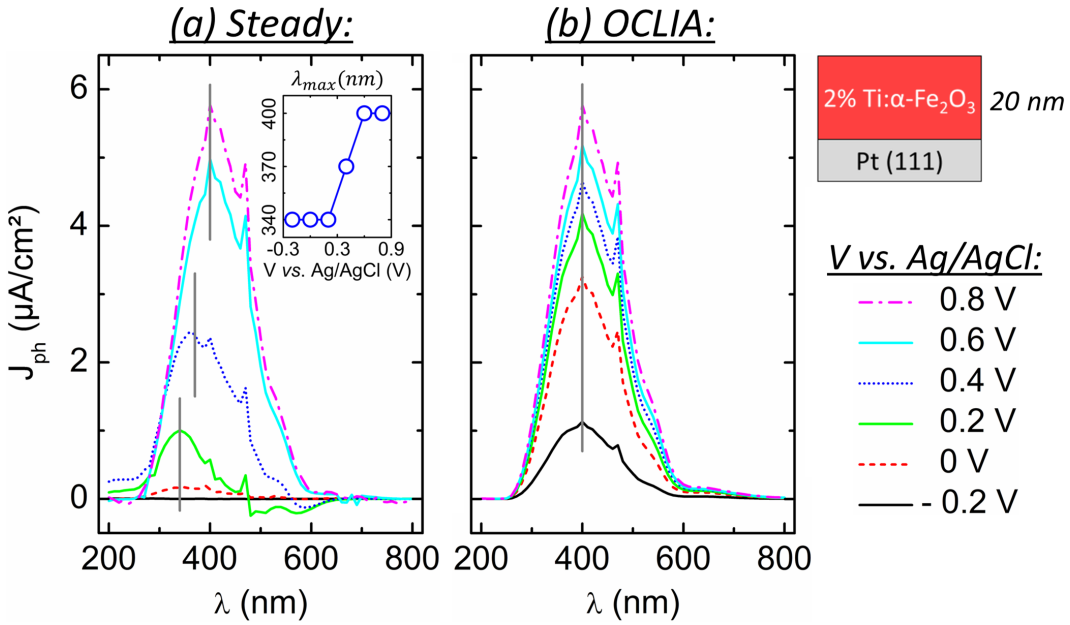

Figure 6.14: $J_{ph}(\lambda)$ curves obtained with (a) steady illumination and (b) with the OCLIA method at various bias potentials *vs.* Ag/AgCl for the 20F sample. From bottom to top: -0.2V (black solid line), 0V (red dashed line), 0.2V (green solid line), 0.4V (blue dotted line), 0.6V (cyan solid line) and 0.8V (magenta dashed-dotted line). Vertical grey lines highlight the wavelength for which the photocurrent maximum is obtained ($\lambda_{max}(20F)$ value) and the inset on figure (a) gives the evolution of $\lambda_{max}(20F)$ *vs.* the applied potential.

The $J_{ph}(\lambda)$ cut-off is always located *ca.* 600 nm, which is equivalent to a band gap of *ca.* 2.07 eV. The small peak at 470 nm on all curves corresponds to the maximum flux of the illumination source (*cf.* figure 3.22 in 3.4.1.a). It is worth noting that in the steady illumination regime the maximum photocurrent is not obtained for the wavelength corresponding to the maximal illumination source output. More precisely from the inset on figure 6.14.a the wavelength λ_{max} for which the maximum photocurrent is obtained is 340 nm for low applied potentials (V $<$ 0.2V *vs.* Ag/AgCl) whereas it is 400 nm for high applied potentials (V $>$ 0.4V *vs.* Ag/AgCl).

The recombination rate is expected to depend on the applied voltage, through the extension of the space charge layer when the potential is more and more anodic (*i.e.* the band bending increases, *cf.* 2.2.3): the higher the applied voltage is, the lower the recombination rate is. Here we show that the recombination rate depends also on the photons wavelength: indeed it is higher at 400 nm than at 340 nm. This is illustrated on figure 6.15 where the monochromatic photocurrent at wavelengths of 340 nm and 400 nm, measured with steady illumination and the OCLIA method, is plotted *vs.* the applied potential. One observes the differences between the steady photocurrent and the OCLIA photocurrent are higher for a wavelength of 400 nm than for a wavelength of 340 nm. For instance at 0.2V *vs.* Ag/AgCl, the OCLIA photocurrent at 340 nm is doubled with respect to the steady photocurrent,

whereas at 400 nm it is multiplied by 10. This means that the carriers generated by the absorption of photons of higher energy (*i.e.* low wavelength) have enough kinetic energy to avoid recombination.

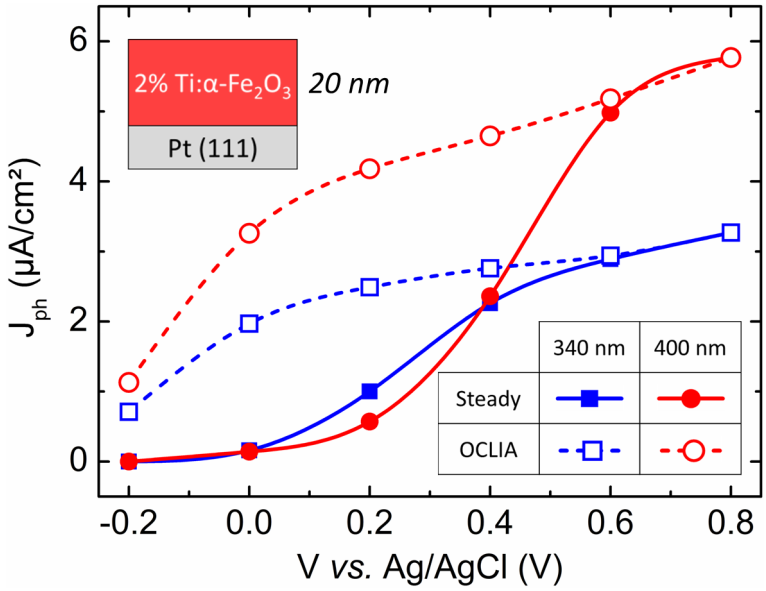

Figure 6.15: Monochromatic photocurrent *vs.* voltage curves of the 20F sample for wavelengths of 340 nm (blue) and 400 nm (red) measured with steady illumination (filled symbols) and with the OCLIA method. Lines are only a guide for the eye.

Figure 6.14.b shows that in conditions where surface charge recombination is reduced (OCLIA measurements), $\lambda_{max}(20F)$ is always equal to 400 nm. Moreover we observe that the $J_{ph}^{OCLIA}(\lambda)$ shape does not depend on the applied potential. In addition we can notice a global signal increase in the [-0.2V ; +0.4V] *vs.* Ag/AgCl window for OCLIA measurements as compared to steady measurements. We can therefore assume that in the steady illumination regime the conversion of photons of high wavelength at low applied potentials is limited by surface charge recombination. Lastly, the high similarity between the data obtained at 0.8V *vs.* Ag/AgCl in both illumination regimes justifies *a posteriori* for this sample the hypothesis about negligible surface charge recombination at high potentials, as stated at the beginning of this subsection.

$J_{ph}^{Steady}(\lambda, V)$ and $J_{ph}^{OCLIA}(\lambda, V)$ data were also acquired for the 20T sample and for heterojunctions. The results are represented as maps where the X, Y and Z axis represent respectively the wavelength (in nm), the applied potential (in V *vs.* Ag/AgCl) and the photocurrent (in µA/cm²) obtained in the steady illumination regime or with the OCLIA method (noted $J_{ph}^{Steady}(\lambda, V)$ and $J_{ph}^{OCLIA}(\lambda, V)$ maps).

Figure 6.16 presents the $J_{ph}^{Steady}(\lambda, V)$ and $J_{ph}^{OCLIA}(\lambda, V)$ maps for the 20F and 20T samples.

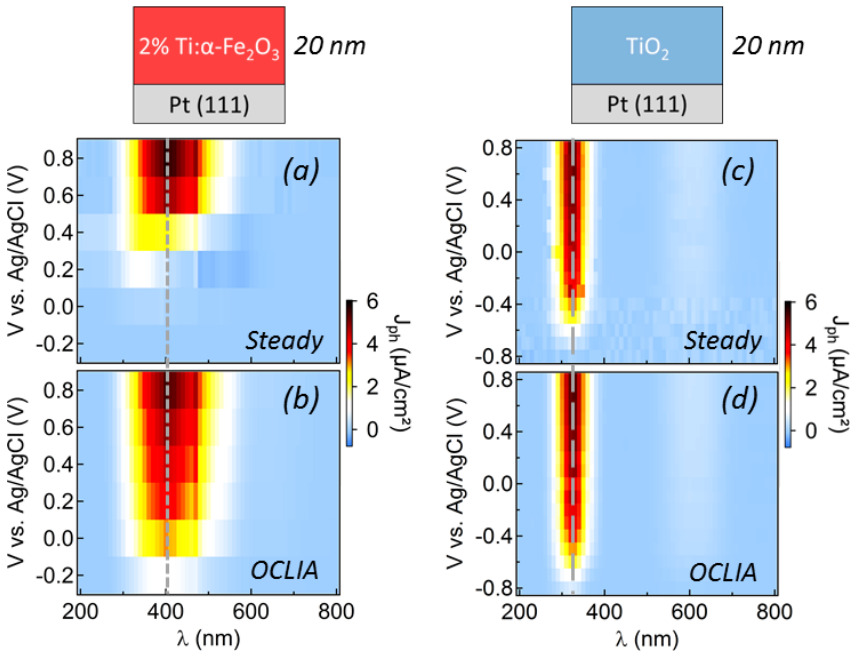

Figure 6.16: Monochromatic photocurrent maps obtained with (top) steady illumination and (bottom) the OCLIA method for (a, b) 20F and (c, d) 20T films. Short (resp. wide) dashed grey lines highlight the wavelength for which the photocurrent is maximum at 0.8V *vs.* Ag/AgCl for the 20F (resp. 20T) film.

Figures 6.16.a and 6.16.b lead to the same conclusions than the ones drawn after the analysis of figure 6.14 except that the results are represented as maps. In particular this facilitates the visualization of the global signal increase in the [- 0.2V ; +0.4V] *vs.* Ag/AgCl window for $J_{ph}^{OCLIA}(\lambda, V)$ with respect to $J_{ph}^{Steady}(\lambda, V)$. The data for the 20T sample (figures 6.16.c and 6.16.d) show that there is almost no difference between $J_{ph}^{Steady}(\lambda, V)$ and $J_{ph}^{OCLIA}(\lambda, V)$, demonstrating that surface charge recombination is not a limiting factor for TiO_2 photoanodes. The signal-to-noise ratio is also improved with the OCLIA method, as it can be seen by a smoother map with respect to the steady illumination regime map. The $\lambda_{max}(20T)$ value is 325 nm (highlighted with a vertical dashed grey line on figures 6.16.c and 6.16.d) and the $J_{ph}(\lambda)$ cut-off is located *ca.* 400 nm, which is equivalent to a band gap of *ca.* 3.10 eV.

Figure 6.17 presents the $J_{ph}^{Steady}(\lambda, V)$ and $J_{ph}^{OCLIA}(\lambda, V)$ maps for the heterojunctions (5T/15F, 10T/10F and 10F/10T samples).

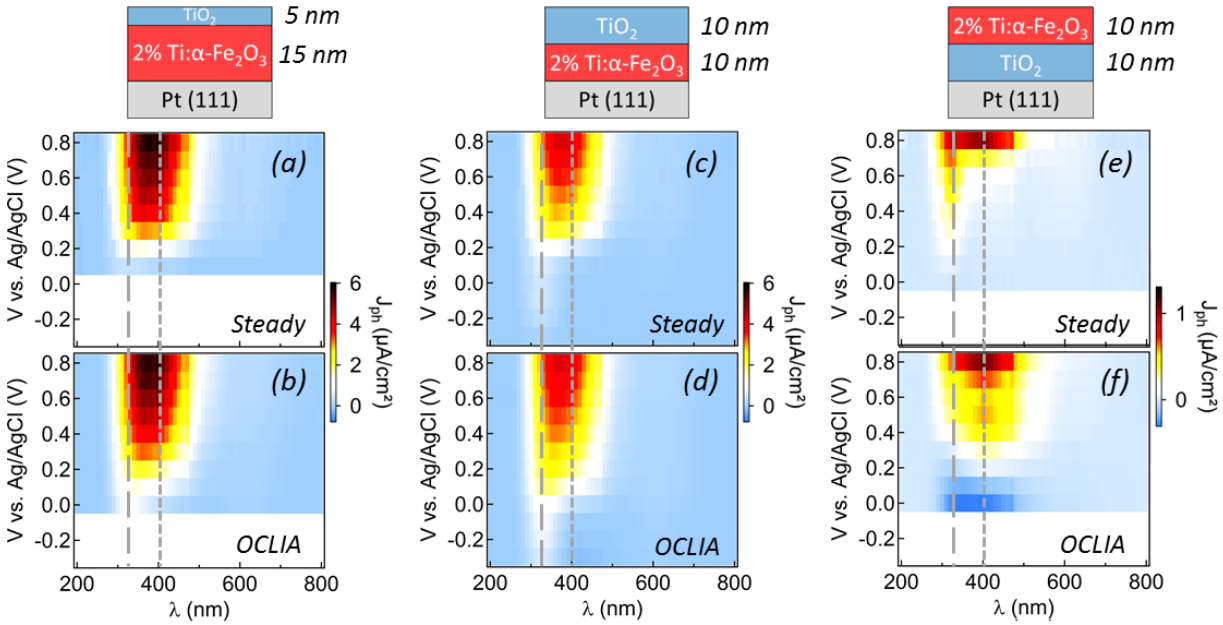

Figure 6.17: Monochromatic photocurrent maps obtained with (top) steady illumination and (bottom) the OCLIA method for (a, b) 5T/15F, (c, d) 10T/10F and (e, f) 10F/10T films (the photocurrent color scale for this sample is different because its signal is very low compared to the others). Short (resp. wide) dashed grey lines highlight the wavelength for which the photocurrent is maximum at 0.8V *vs.* Ag/AgCl for the 20F (resp. 20T) film.

For the 5T/15F and 10T/10F samples (figures 6.17.a to 6.17.d), very little differences are recorded between $J_{ph}^{Steady}(\lambda, V)$ and $J_{ph}^{OCLIA}(\lambda, V)$ (except for low applied potentials below 0.2V *vs.* Ag/AgCl). This behaviour is very similar to the one obtained for the single TiO_2 layer (20T sample, figures 6.17.c and 6.17.d), accounting for a weak limitation due to surface charge recombination. This demonstrates that the deposition of a very thin TiO_2 layer on Ti:α-Fe_2O_3 decreases drastically the photocurrent losses due to surface charge recombination. The λ_{max} value for these samples depends on the applied potential. For low applied potentials, $\lambda_{max}(5T/15F)$ is close to $\lambda_{max}(20T)$, showing that the major contribution to the photocurrent is due to the TiO_2 layer. However for high applied potentials, $\lambda_{max}(5T/15F)$ is close to $\lambda_{max}(20F)$, showing that the major contribution to the photocurrent is due to the Ti:α-Fe_2O_3 layer. Liou et al. [87] observed the same kind of behaviour in the case of polycrystalline TiO_2 / Fe_2O_3 heterojunctions, where the contribution from the Fe_2O_3 increased when the applied potential increased.

On figures 6.17.e and 6.17.f, large discrepancies are observed between the steady and OCLIA maps for the 10F/10T sample. Indeed, like in the case of the 20F sample, strong

photocurrent limitations due to surface recombination are observed, likely due to the Ti:α-Fe_2O_3 surface. Secondly, discrepancies between maps persist until 0.8V *vs.* Ag/AgCl while for the 20F sample surface recombination disappears at a potential of 0.6V *vs.* Ag/AgCl. This means that the recombination rate in this sample is much higher and maybe not negligible at 0.8V *vs.* Ag/AgCl. Moreover, like in the case of the two previous heterojunctions, the major contributor for the photocurrent at low (resp. high) potentials is the TiO_2 (resp. Ti:α-Fe_2O_3) layer. In addition, the overall photocurrent signal on both maps is much lower than the other studied samples, which is consistent with the photocurrent measurements in the white steady light illumination regime (*cf.* subsection 6.3.1, figure 6.12). For the OCLIA data, the maximum photocurrent is always achieved at $\lambda_{max}(10F/10T) = \lambda_{max}(20F) =$ 400 nm. Lastly, at potentials lower than 0.2V *vs.* Ag/AgCl, the photocurrent measured by the OCLIA method is negative, accounting for a cathodic behaviour.

The integration of the $J_{ph}(\lambda)$ curves over the wavelength range for all potentials allows obtaining $J_{ph}^{Steady}(V)$ and $J_{ph}^{OCLIA}(V)$ curves, which are shown on figure 6.18.

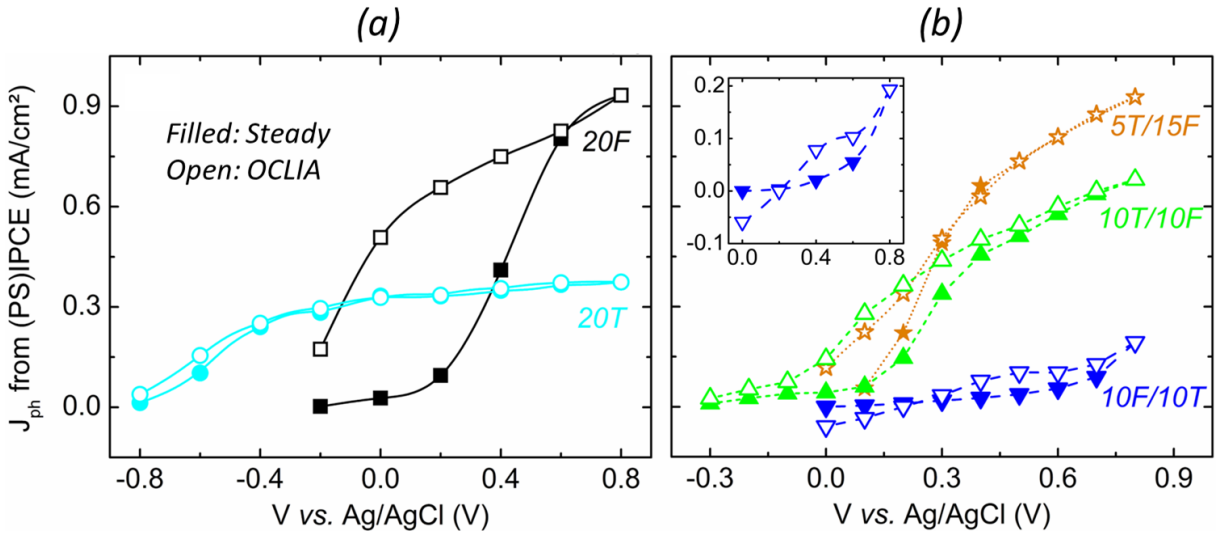

Figure 6.18: Photocurrent *vs.* voltage curves obtained by integration of $J_{ph}(\lambda)$ curves in steady light illumination (filled symbols) and by the OCLIA method (open symbols) for the (a) single layers films and (b) heterojunctions. Samples: 20F (black squares and solid line), 20T (cyan circles and solid line), 5T/15F (orange stars and dotted line), 10T/10F (green up triangles and dashed line) and 10F/10T (blue down triangles and wide dashed line). The inset on figure (b) shows more precisely the data for the 10F/10T sample. Lines are only a guide for the eye.

Figure 6.18.a leads to the same conclusions than previously concerning the 20F and 20T samples. In the case of heterojunctions (figure 6.18.b), the results for the 5T/15F and 10T/10F samples show that a TiO_2 upperlayer diminishes the photocurrent loss due

to surface charge recombination with respect to the 20F sample (the differences between J_{ph}^{Steady} and J_{ph}^{OCLIA} are smaller for these samples than for the 20F sample). This is in agreement with the findings of Yang et al. who reported that an ultra-thin (*ca.* 1 nm thick) TiO_2 film deposited on hematite decreases drastically the surface charge recombination rate of the photoanode [131]. On the contrary, for the 10F/10T sample (*cf.* inset on figure 6.18.b), $J_{ph}^{OCLIA}(V)$ is always higher than $J_{ph}^{Steady}(V)$ by at least a factor of 2. Indeed a Ti:α-Fe_2O_3 upperlayer is not desirable for low surface charge recombination rates as it was seen previously.

Our results are very consistent with the observations reported in ref [108] and summarized figure 6.19. This figure illustrates that the photocurrent onset potential is reduced through surface charge recombination diminution (the so-called "surface state passivation") and the increase in the maximum photocurrent value is increased through an increase in the charge carrier concentration. From the photoelectrochemical characterizations for our samples, a clear statement is that a TiO_2 upperlayer is more desirable for the reduction of surface charge recombination rate (*i.e.* the reduction of the photocurrent onset potential). This induces a decrease in the photocurrent onset potential for heterojunctions with respect to a single layer of Ti:α-Fe_2O_3. However, Ti:α-Fe_2O_3 features a better maximum photocurrent, which is due to a better absorption, *i.e.* a higher increase in charge carrier concentration upon photons absorption as compared with TiO_2, resulting in a higher maximum photocurrent for heterojunctions with respect to a single layer of TiO_2.

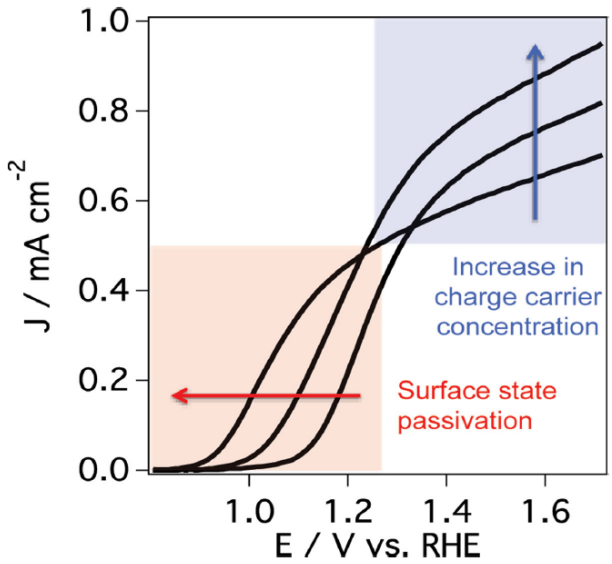

Figure 6.19: Illustration of the mechanisms responsible for modifying the photocurrent *vs.* voltage curves for hematite photoanodes. From [108].

6.4 Photocurrent scenarii for the different heterojunctions

RPES results demonstrated the creation of a diffuse interface inducing Fe^{2+} states within the band gap when combining Ti-doped hematite with TiO_2. Those states are likely to act as recombination centers during charge separation or charge transfer between the two materials. An illustration of this interpretation is given on figure 6.20. Also the concentration of these recombination centers increases when the TiO_2 upperlayer thickness increases.

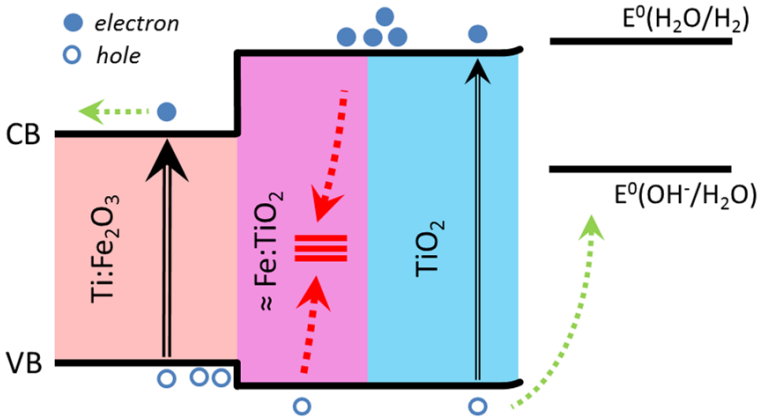

Figure 6.20: Illustration of the detrimental effect of a Fe:TiO_2-like interface between Ti:α-Fe_2O_3 and TiO_2 in the form of a band diagram. Double-lined, green dotted and red dotted arrows convey respectively the photons absorption, the charge transport and the losses due to charge recombination induced by Fe^{2+} states in the band gap at the interface. The band positions were taken from ref. [26] and the band offsets between TiO_2 and Ti:α-Fe_2O_3 were determined using XPS.

Figure 6.21 shows the interpretation of charge recombination mechanisms ruling the photocurrent in heterojunctions at small or large applied bias potentials. For the sake of clarity, the Fe:TiO_2-like interface and the Fe^{2+} states within the band gap for this interface are not shown. To convey the charge recombination due to this interface, red dotted arrows are sketched. We can now propose a mechanism to explain the photocurrent behaviour at any applied potential within the chosen window for the two types of heterojunctions we investigated: heterojunctions with a TiO_2 upperlayer or with a Ti:α-Fe_2O_3 upperlayer.

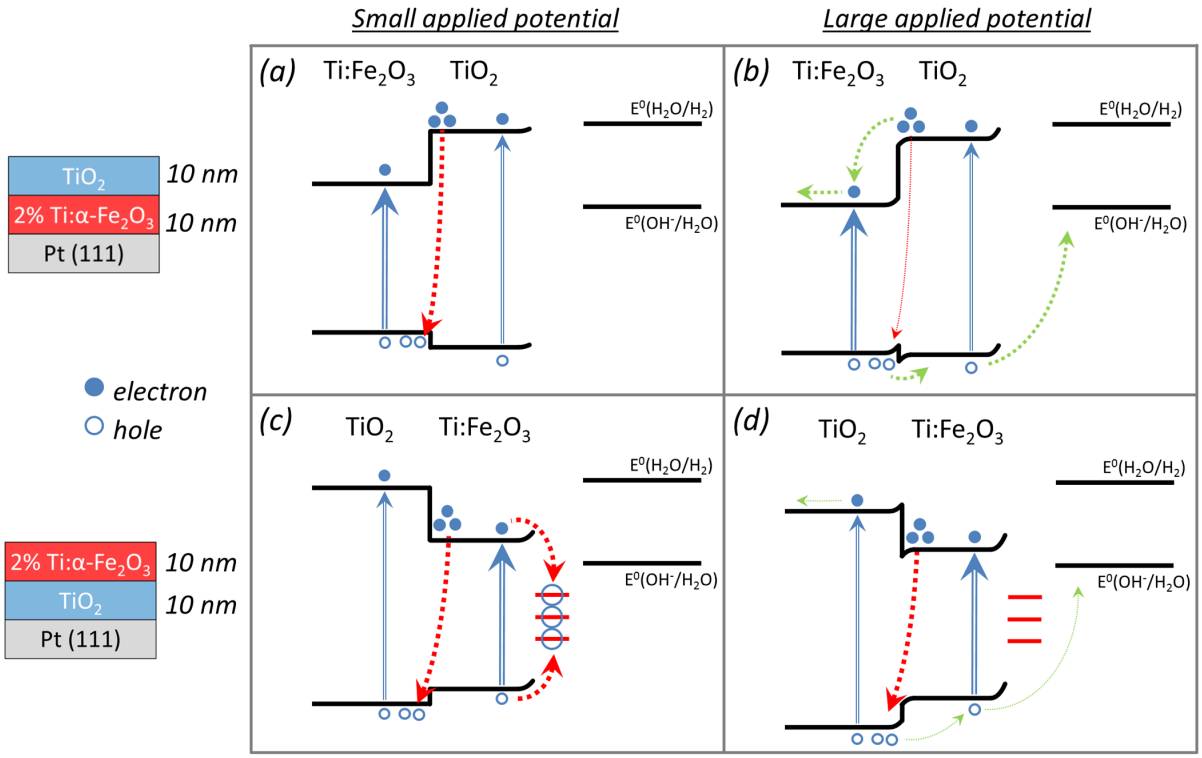

Figure 6.21: Interpretation of charge recombination mechanisms ruling the photocurrent in heterojunctions illustrated by band diagrams for a heterojunction with a TiO_2 or Ti:α-Fe_2O_3 upperlayer at small (a or c) or large (b or d) applied bias potentials. Red dotted arrows stand for the recombination at the Ti:α-Fe_2O_3 - TiO_2 interface due to Fe^{2+} states within the band gap. Green dotted arrow convey the photocurrent. Blue double arrows stand for the photons absorption in materials. The thickness of arrows are significant of the strength of the phenomena. The band positions were taken from ref [26] and the band offsets between TiO_2 and Ti:α-Fe_2O_3 were determined using XPS.

We will first discuss the case of a heterojunction with a TiO_2 upperlayer. For applied voltages lower than 0V *vs.* Ag/AgCl, only the charges photogenerated in the TiO_2 upperlayer contribute to the photocurrent. However most of the electrons recombine at the interface with Ti:α-Fe_2O_3 before going in the external circuit because of the Fe^{2+} states within the band gap. Therefore the signal is much lower than for the single layer of TiO_2. When the potential increases the recombination rate diminishes and around 0.1V *vs.* Ag/AgCl some electrons coming from TiO_2 can participate to the signal. This is confirmed by the monochromatic photocurrent maps which showed that for this range of potentials the main contribution comes from the TiO_2 layer. At higher potentials, both layers can contribute to the photocurrent. Therefore the photocurrent of heterojunctions can be approximated by a linear combination of the single layers photocurrent (*cf.* figure 6.13). However our XPS results revealed unfavourable valence band offsets for the hole transfer from the Ti:α-Fe_2O_3 to the TiO_2 layer. This is illustrated on figure 6.21 by small energy barriers at

the interface. With large applied potentials, one can expect to assist this hole transfer and therefore the photogenerated holes in Ti:α-Fe_2O_3 can contribute to the photocurrent in heterojunctions with a TiO_2 upperlayer. This can explain the increasing Ti:α-Fe_2O_3 contribution with the increasing applied potential which was demonstrated thanks to the measurement of $J_{ph}^{Steady}(\lambda, V)$ and $J_{ph}^{OCLIA}(\lambda, V)$ maps.

The huge photocurrent variations between the 10T/10F and 10F/10T samples show that the photocurrent discrepancies cannot be explained only by different absorption efficiencies and recombination centers creation at the interface, because the contributions are the same for both samples. In the case of photoanodes it is desirable to bring electrons toward the substrate direction, therefore an electron transfer from the upperlayer to the underlayer is mandatory. If TiO_2 is deposited on Ti:α-Fe_2O_3, the conduction band offset between the two materials is favourable to this transfer. We have measured in XPS (*cf.* subsection 6.1.2) a valence band offset of 0.15 eV for the 10F/10T sample, accounting for a conduction band offset of 0.85 eV considering the band gap difference between Ti:α-Fe_2O_3 and TiO_2. Then for the 10T/10F sample (*cf.* figure 6.21.a and 6.21.b) the electron transfer from TiO_2 to Ti:α-Fe_2O_3 is favoured. *A contrario* for the 10F/10T sample (*cf.* figure 6.21.c and 6.21.d) the electron transfer from Ti:α-Fe_2O_3 to TiO_2 is not favoured at all.

To summarize, the study of our nanometric Ti:α-Fe_2O_3 - TiO_2 systems highlighted concomitant effects due to heterostructuring:

- the creation of a detrimental interface between the two materials, inducing (bulk) charge recombination which limits the overall photocurrent;
- a beneficial effect in the case of a TiO_2 upperlayer for which surface recombination losses are drastically reduced.

For our systems, the combination of two materials together with a view to benefit from the assets of each material is dominated by surface and interface effects. However we highlighted a possible use of TiO_2 as a surface treatment in order to reduce the surface charge recombination, which is similar to the findings of Yang et al. [131]. Such a configuration, where only few layers of TiO_2 would be deposited on the top of Ti-doped hematite, may fulfil the final objective stated at the beginning of this chapter, which was the creation of a photoanode featuring the advantageous absorption properties of hematite and the well-suited band structure and surface kinetics properties of TiO_2.

7 Ferroelectric layers as photocurrent enhancers

The use of an internal electric field as photoelectrochemical properties enhancer is a widely explored route to drive the separation of photogenerated carriers and hence reducing the recombination rate, as it was detailed in 2.4.1. A ferroelectric material, which features a spontaneous electric polarization, is able to provide an internal electric field in a photoanode system. The use of such materials is an emerging lead in the framework of photoanodes for solar water splitting, following the "perovskite fever" [187] in the solar cells community. We recently started to investigate this possibility using the prototypical ferroelectric material $BaTiO_3$. Our first results concern the study of ferroelectric thin films of $BaTiO_3$ deposited on Nb:$SrTiO_3$ single crystals. Indeed, given our approach, a mandatory step is to understand the behaviour of the ferroelectric system alone before combining it with a conventional photoanode material like hematite or TiO_2,

In this chapter I will present our first results concerning the impact of ferroelectricity on the properties of $BaTiO_3$ / Nb:$SrTiO_3$ photoanodes systems. The first section (7.1) introduces the general problematic of the chapter where the physics of ferroelectricity (7.1.1) are presented, highlighting its interest in the framework of photoanodes for solar water splitting, as well as a short literature review of the applications of ferroelectrics in the fields of photovoltaics and photocatalysis (7.1.2). The results about growth and structure of our systems will be given in 7.2, and section 7.3 presents the photocurrent measurements. The characteristics of the samples and the influence of ferroelectricity on the electronic structure is studied by PFM and X-PEEM in sections 7.4 and 7.5 respectively. Lastly, section 7.6 provides a discussion about the relation between the ferroelectric polarization and the photocurrent.

7.1 Ferroelectricity physics - applications in photovoltaics and photochemistry

7.1.1 Ferroelectricity physics in $BaTiO_3$

A ferroelectric material is a material that exhibits, over some range of temperature, a spontaneous electric polarization [91]. Bulk $BaTiO_3$ is a prototypical ferroelectric material at room temperature with a para- to ferro- electric phase transition at about 130°C accompanied by a cubic to tetragonal structural transition upon decreasing temperature; the electrical polarization orientation lies along the (001) tetragonal axis [188]. The Curie temperature (T_C) of the paraelectric / ferroelectric transition increases fairly for strained epitaxial $BaTiO_3$ layers. Figure 7.1 presents the $BaTiO_3$ elementary cell configuration above and below T_C, for upward and downward polarizations. Above T_C (figure 7.1.a), the $BaTiO_3$ elementary cell is cubic, no internal polarization exists: the material is paraelectric. Below T_C, the $BaTiO_3$ ele-

mentary cell is tetragonal, and the Ti^{4+} cation is moved with respect to the central position. This induces an electric dipole, *i.e.* an electric polarization, oriented toward upward (figure 7.1.b) or downward (figure 7.1.c) directions (with respect to the surface normal), labelled as $\overrightarrow{P_{up}}$ and $\overrightarrow{P_{down}}$ in the rest of the chapter.

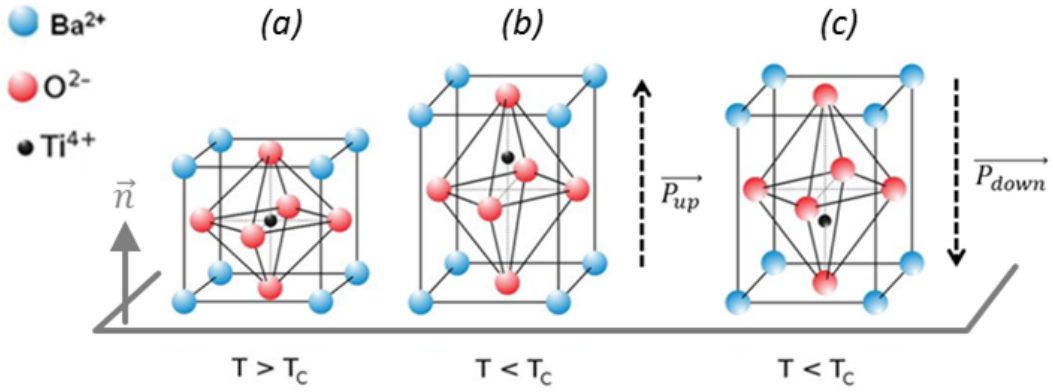

Figure 7.1: $BaTiO_3$ elementary cell (a) above the Curie temperature T_C (cubic, not ferroelectric), and above T_C with Ti^{4+} cation position inducing an (b) upward or (c) downward remnant polarization. $\overrightarrow{n}$ is the surface normal. Reproduced from https://en.wikibooks.org/.

Various remnant internal polarizations can be obtained through the use of external poling procedures, namely the application of an external electric field. Ideally in such procedures, the external field ($\overrightarrow{E_{ext}}$) should be applied between the upper and lower surfaces of the ferroelectric material. By convention positive (resp. negative) poling corresponds to the application of a positive (negative) potential difference between the surface and the back of the sample. The potential applied on the surface of the sample will be referred to as poling potential in the rest of the chapter. Figure 7.2 details the steps during the positive poling in the $BaTiO_3$ (001) / Nb:$SrTiO_3$ (001) system. The first step is the application of $\overrightarrow{E_{ext}}$ (figure 7.2.a). The ions in the material will move because of the electric force $\overrightarrow{F_{elec}}$ to which they are submitted (according to $\overrightarrow{F_{elec}} = q \times \overrightarrow{E_{ext}}$, where q is the electric charge of the ion). More precisely, in the ferroelectric cell, cations (Ti^{4+}) will be displaced toward the back and anions (O^{2-}) will be displaced toward the surface. This will lead to a downward internal polarization $\overrightarrow{P_{down}}$. The electric field $\overrightarrow{E_{pol}}$ created by this $\overrightarrow{P_{down}}$ polarization is equal to the electric field created by a fictive charge density $\sigma_{down} = \overrightarrow{P_{down}} \cdot \overrightarrow{n}$ [135]. In the following, we will call the fictive charges "polarization bound charges" (indicated by red circles in figure 7.2). Therefore $\overrightarrow{E_{pol}} = -\dfrac{\overrightarrow{P_{down}}}{\varepsilon\varepsilon_0}$ where ε is the dielectric constant of $BaTiO_3$. We can note that $\overrightarrow{E_{pol}}$ is opposed to $\overrightarrow{E_{ext}}$, following Le Châteliers's principle[30]. After removal of the external applied field, the

[30]"Any change in *status quo* prompts an opposing reaction in the responding system" (from this page)

$\overrightarrow{P_{down}}$ polarization will remain and screening phenomena will occur, for which the driving force is to reduce the electric field $\overrightarrow{E_{pol}}$ inside the material. This is illustrated on figure 7.2.c where positive charges screen the negative polarization bound charges at the surface, and negative charges screen the positive polarization bound charges at the bottom. In realistic systems, the screening mechanism is not perfect. Accordingly, negative poling will induce $\overrightarrow{P_{up}}$ polarization, which will be subsequently screened by negative charges at the surface and positive charges at the back.

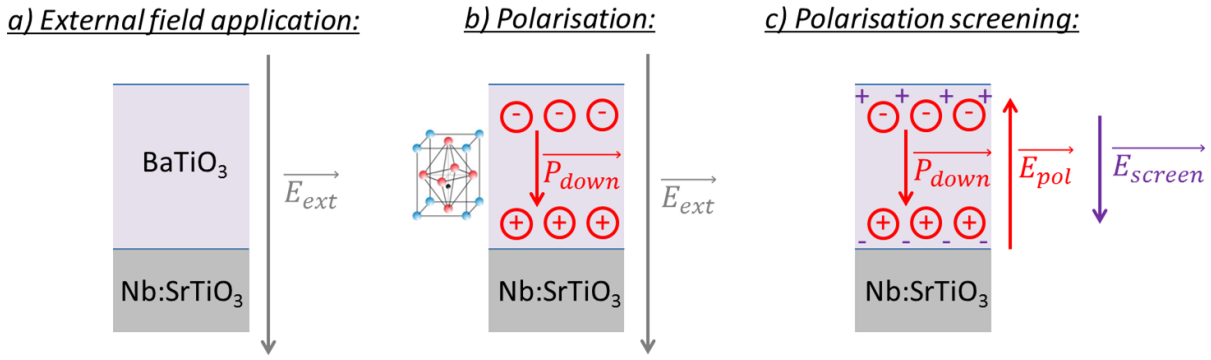

Figure 7.2: Positive poling steps: (a) external field ($\overrightarrow{E_{ext}}$) application, (b) Internal polarization process in $BaTiO_3$ by dipole alignment along $\overrightarrow{E_{ext}}$, arising $\overrightarrow{P_{down}}$ polarization and (c) internal polarization screening after external field removal, inducing the screening field $\overrightarrow{E_{screen}}$. Red circled charges stand for the polarization bound charges (fictive charges) and purple charges stand for charges which screen the internal polarization. System: $BaTiO_3$ (001) / Nb:$SrTiO_3$ (001).

Screening in ferroelectrics can arise from multiple phenomena [135], some are illustrated on figure 7.3. Namely screening phenomena can occur through:

- mobile charges screening (figure 7.3.a), for instance by doping or the creation of oxygen vacancies;
- domain ordering (figure 7.3.b) where the internal polarization is opposite between two adjacent domains so that they screen each other;
- external screening (figure 7.3.c) through adsorption of chemical species.

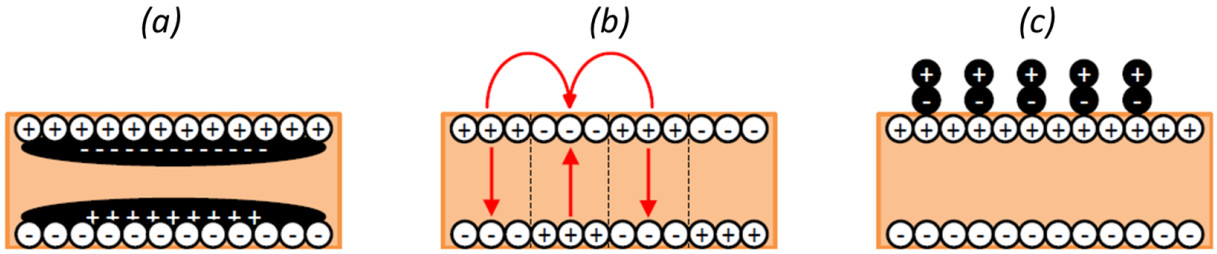

Figure 7.3: Phenomena involved in the screening of the $\overrightarrow{P_{down}}$ polarization bound charges (white spheres): (a) internal screening (by mobile charges), (b) domain ordering and (c) external screening (by adsorbates). Reproduced from [135].

Polarization screening will induce band bending at the ferroelectric surface. The challenge is to take advantage from this band bending in order to enhance the photoanode properties of our systems. On figure 7.4 the band diagram of the interface between an aqueous solution and $BaTiO_3$ is shown for $\overrightarrow{P_{up}}$ and $\overrightarrow{P_{down}}$ polarizations domains (with the hypothesis of complete screening in the bulk (no residual field), *i.e.* flat bands). As seen on figure 7.4.a, the screening of positive polarization bound charges will result in an accumulation of negative charges at the surface, *i.e.* downward band bending. This means that $\overrightarrow{P_{up}}$ polarization would favour (by means of screening) the electron transfer from the ferroelectric surface to an electrolyte (reduction reaction). This is of top interest in the framework of photocathodes for solar water splitting (water reduction). The reverse behaviour (*i.e.* upward band bending) is observed for $\overrightarrow{P_{down}}$ polarization (figure 7.4.b). This means that $\overrightarrow{P_{down}}$ polarization would favour (by means of screening) the hole transfer from the ferroelectric surface to an electrolyte (oxidation reaction). This is of top interest in the framework of photoanodes for solar water splitting (water oxidation).

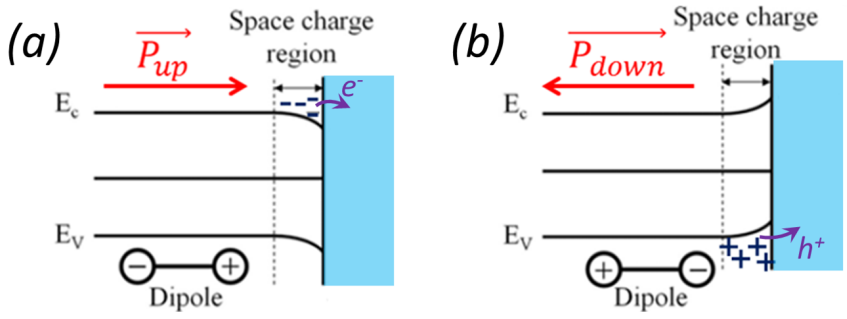

Figure 7.4: Energy level diagrams for a ferroelectric photoelectrode in aqueous solution, without illumination, for (a) $\overrightarrow{P_{up}}$ polarization, and (b) $\overrightarrow{P_{down}}$ polarization. E_V is the valence band edge, E_C is the conduction band edge, and the blue zone stand for the the aqueous solution. Reproduced from [93].

7.1.2 Ferroelectricity applications in photovoltaics and photochemistry

Recently ferroelectrics have attracted much attention as promising candidates for photovoltaic materials [189, 190] since it has been shown that the spontaneous electrical polarization promotes the desirable separation of photogenerated carriers [92]. In addition and contrary to conventional p-n junctions where the photovoltage is limited to the electronic bandgap, ferroelectrics exhibit photovoltages that are significantly higher than the band gap (several tens of V), thanks to the existence of the bulk photovoltaic effect in these noncentrosymmetric crystals [189]. Zenkevich et al. reported recently a further improvement of this bulk photovoltaic effect for $BaTiO_3$ thin films as compared to bulk materials [191]. The high band gap of $BaTiO_3$ (3.2 eV) may be considered to be an obstacle to the relevancy of $BaTiO_3$ in energy applications. Fortunately, Upadhyay et al. showed that doping $BaTiO_3$ with Fe can reduce this value down to 2.8 eV (for a 2 at.% doping level) [192].

The impact of ferroelectricity in the framework of photocatalytic applications has recently been studied [93, 94]. In particular it has been proposed that photooxidation (resp. photoreduction) reactions occur preferably on ferroelectric surfaces featuring $\overrightarrow{P_{down}}$ (resp. $\overrightarrow{P_{up}}$) polarization. This selectivity is associated to the band bending originating from screening phenomena, which favours oxidation or reduction reactions [193–195], as we saw earlier in this chapter (7.1.1).

This chemical selectivity was widely studied by the group of Steve Dunn (Queen Mary University of London). They demonstrated that various ferroelectrics such as $BaTiO_3$ [193, 196, 197], $BiFeO_3$ [198], $Pb(Zr,Ti)O_3$ [199], and $LiNbO_3$ [200, 201] exhibit this behaviour, in the framework of silver ions photoreduction or dye photodecomposition (*e.g.* Rhodamine B). In a different context (CO_2 adsorption), Cabrera et al. reported the same kind of observations [202].

Interestingly in the case of TiO_2 / $BaTiO_3$ heterostructures, Burbure et al. reported that the internal electric field in the ferroelectric $BaTiO_3$ modifies the band bending in the semiconducting TiO_2 and here again creates different spatial sites for oxidation and reduction reactions at the surface of TiO_2 [203].

The potential use of such materials in the framework of photoelectrolysis of water is very promising [93]. Inoue et al. showed that H_2 evolution using ferroelectric $Pb(Zr,Ti)O_3$ photocathodes occurs preferentially on surfaces featuring $\overrightarrow{P_{up}}$ polarization [204]. Ji et al. reported in the case of $BiFeO_3$ thin films photoanodes a reduction of the onset potential of *ca.* 0.02V and an increase in the overall photocurrent by *ca.* 30% for the samples with a $\overrightarrow{P_{down}}$ polarization with respect to the ones with a $\overrightarrow{P_{up}}$ polarization [95]. Cao et al. reported for polycrystalline $BiFeO_3$ samples an increase (resp. decrease) of the photooxidation of water performances upon positive (resp. negative) poling with respect to the native samples [205]. Park et al. studied the performance of suspended ferroelectric particles as catalysts for hydrogen evolution as a function of the internal polarization direction [206]. In particular they

reported an increase in the H_2 production when the ferroelectric exhibit a $\overrightarrow{P_{up}}$ polarization, but no change in the case of $\overrightarrow{P_{down}}$ polarization.

7.1.3 Our approach

Experimentally, assessing unambiguously the influence of the electric polarization field is tricky because it is difficult to master electric polarization on large size samples that need to be continuous and flat with a very well controlled structure. For example, in the case of powder samples, Jones and Dunn reported that the photodeposition of Ag ions on lead titanate is more influenced by the films structure and defects than by the ferroelectric domains orientation [199]. Hence it can be difficult to decorrelate mingled morphology and ferroelectricity effects on systems which are hard to control in terms of structure.

In this chapter, we studied photoanode architectures incorporating a ferroelectric single crystalline $BaTiO_3$ epitaxial upperlayers. The thin films were deposited by OPA-MBE on Nb:$SrTiO_3$ (001) single crystals. Such single crystalline systems allow a high level of control of the remnant polarization and are well suited in the framework of the study of the influence of the ferroelectricity on the system material properties. As it will be more detailed in 7.3.3, the Nb:$SrTiO_3$ substrate is a photoactive n-type semiconductor suitable as photoanode, as it has already been reported in previous works [45, 46]. Therefore the samples studied in this chapter are heterojunctions where the influence of the ferroelectricity of the upperlayer ($BaTiO_3$) on the properties of the whole architecture is investigated. These heterojunctions have to be considered as "model systems" to study the influence of ferroelectricity on the photoanode performance. Indeed due to its high band gap, undoped $BaTiO_3$ is clearly not a promising material for solar water splitting applications.

7.2 Growth and structure

7.2.1 *In situ* RHEED

$BaTiO_3$ (001) films were grown on Nb:$SrTiO_3$ (001) single crystals by OPA-MBE. The use of strontium titanate single crystalline substrates allows good epitaxy conditions (2 % compressive lattice mismatch) and identical perovskite crystalline structure [156]. The growth monitoring of the deposition of $BaTiO_3$ on pure $SrTiO_3$ (001) single crystals has already been studied in details by Barbier et al. in reference [156]. Our results are very similar with this previous work, which was expected since Nb:$SrTiO_3$ and pure $SrTiO_3$ have the same lattice parameter and crystallographic structure for the Nb doping level considered (1 at.%). RHEED patterns at various deposition times (*i.e.* various thicknesses) for 28 nm $BaTiO_3$ film grown by OPA-MBE on Nb:$SrTiO_3$ (total deposition time of 4 hours) are shown on figure 7.5 (steps a to d) along with the corresponding surface reciprocal lattice (figure 7.5.e). The RHEED patterns slightly degrades during the first nanometers of deposited

material (figure 7.5, step b) with respect to the initial substrate sharp lines (figure 7.5, step a). In optimal growth conditions very well contrasted RHEED patterns with intense 2D streaks corresponding to a perovskite crystal structure are obtained up to 10 nm thickness (figure 7.5, step c). For higher thicknesses, 3D spots appear in the patterns indicating islands on the top surface, which can be more or less present from one sample to another (figure 7.5, step d).

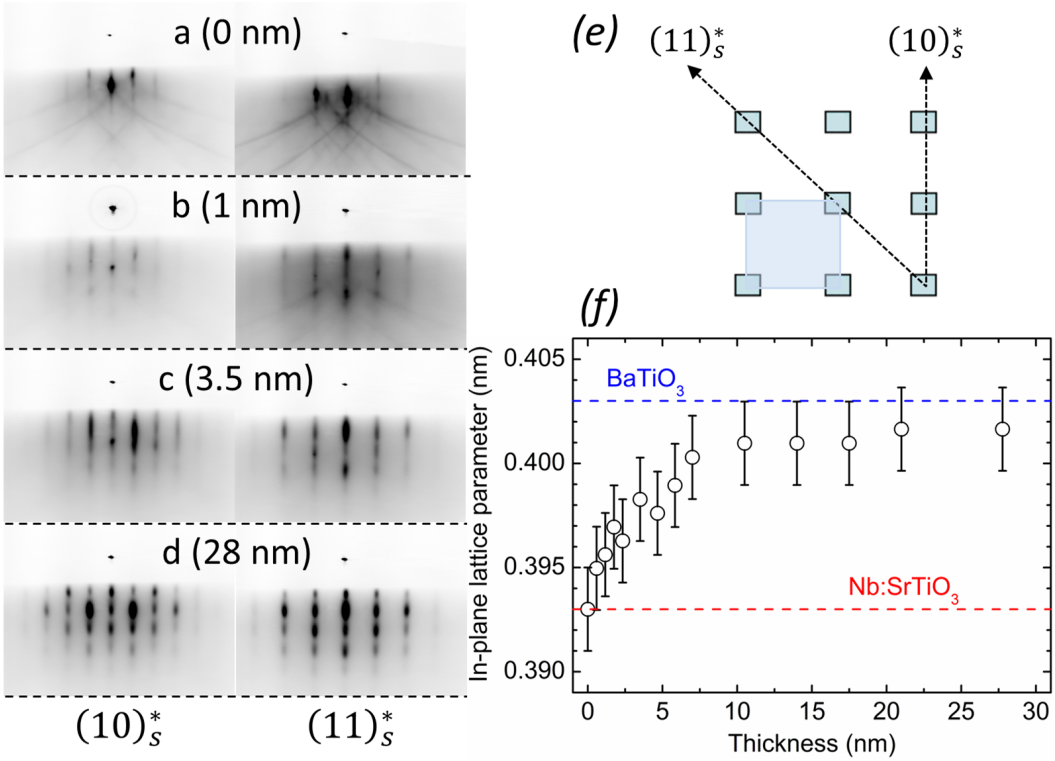

Figure 7.5: (Left panel) RHEED patterns of a 28 nm $BaTiO_3$ film grown by OPA-MBE (4h deposition time) on Nb:$SrTiO_3$ at different deposition times/thicknesses (steps a to d) over the two lowest index surface diffraction directions. (e) The corresponding surface reciprocal lattice is represented, making explicit the diffraction directions, the elementary cell (in the reciprocal space) is also shown. (f) In-plane lattice parameter derived from the $(10)^*_s$ direction of the Nb:$SrTiO_3$ surface reciprocal lattice in RHEED patterns as a function of the film thickness for the same film. Dashed lines stand for the in-plane lattice parameter of bulk $BaTiO_3$(blue) and Nb:$SrTiO_3$ (red) at the deposition temperature (taking into account the thermal expansion). From [99].

In the same manner than in the previous chapters, we calculated from the RHEED patterns the in-plane lattice parameter (*cf.* 3.2.1, 5.1.1) [55, 132, 156]. The in-plane lattice parameter derived from the RHEED patterns obtained over the diffraction direction $(10)^*_s$ of the Nb:$SrTiO_3$ (001) surface reciprocal lattice is plotted figure 7.5.f. Since Nb:$SrTiO_3$ and $BaTiO_3$ have the same perovskite structure, on this figure we see simply the relaxation of the

in-plane lattice parameter from the value for Nb:$SrTiO_3$ (001) (0.393 nm at the deposition temperature taking into account the thermal expansion [156]) to the value for the $BaTiO_3$ (001) film. Our results are, within the experimental error bar, very similar to the previous work of Barbier et al. [156]. The evolution of the in-plane lattice parameter is consistent with an in-plane compressive epitaxial strain: it progressively increases from the substrate lattice parameter to an asymptotic value. This asymptotic value can be estimated *ca.* 0.402 ± 0.002 nm, which is close to the expected value for bulk $BaTiO_3$ at a deposition temperature of 900K (highlighted with a blue dashed line in figure 7.5.f) [156].

7.2.2 *In situ* XPS

Figure 7.6 shows the XPS spectra of the Ba*3d*, Ti*2p* core levels and valence band region for the $BaTiO_3$ / Nb:$SrTiO_3$ system. By convention we considered the O*1s* line at 529.6 eV [207]. The analysis of Ba*3d* (figure 7.6.a) and Ti*2p* (figure 7.6.b) core levels show features consistent with the previous work of our group concerning the growth of $BaTiO_3$ thin films on pure $SrTiO_3$ substrates [156]. More precisely here the Ti$2p_{3/2}$ line is at a binding energy of 458.2 eV, corresponding to Ti^{4+} species.

The Ti/Ba atomic ratio can be calculated by XPS through the ratio of the Ti$2p_{3/2}$ and Ba$3d_{7/2}$ lines area, normalized in the same way than for the calculation of titanium doping level in the case of Ti:α-Fe_2O_3 (*cf.* 3.2.2). The fine correlation between the Ti/Ba ratio in XPS and the growth features observed by RHEED has already been analysed in details in ref. [156], but we will briefly give some informations here, extracted from this reference. For a homogeneous layer, one would expect a Ti/Ba ratio of 1 in the case of stoichiometric $BaTiO_3$. However in our systems a Ti/Ba ratio of 1 in XPS is not correlated with a satisfactory growth process, *i.e.* RHEED patterns featuring a 2D-growth mechanism with well-defined perovskite lines are not observed. A satisfactory growth, with the same features than what was presented in 7.2.1, is achieved when the Ti/Ba ratio in XPS lies between 0.6 and 0.75. Indeed in our systems, the presence of a Ba-rich surface layer is required to fulfil 2D growth conditions (surfactant effect). This Ba-rich layer will severely impact the Ti/Ba ratio in XPS. It is finally worth noting that an ethanol bath removes this Ba-rich layer and that the Ti/Ba ratio in XPS measured after this bath equals 1, but leads to a rougher surface.

The valence band spectrum shows a substantial photoemission signal within the band gap (binding energies lower than the valence band minimum). It is maybe due to oxygen vacancies that can originate from structural defects and/or internal polarization screening.

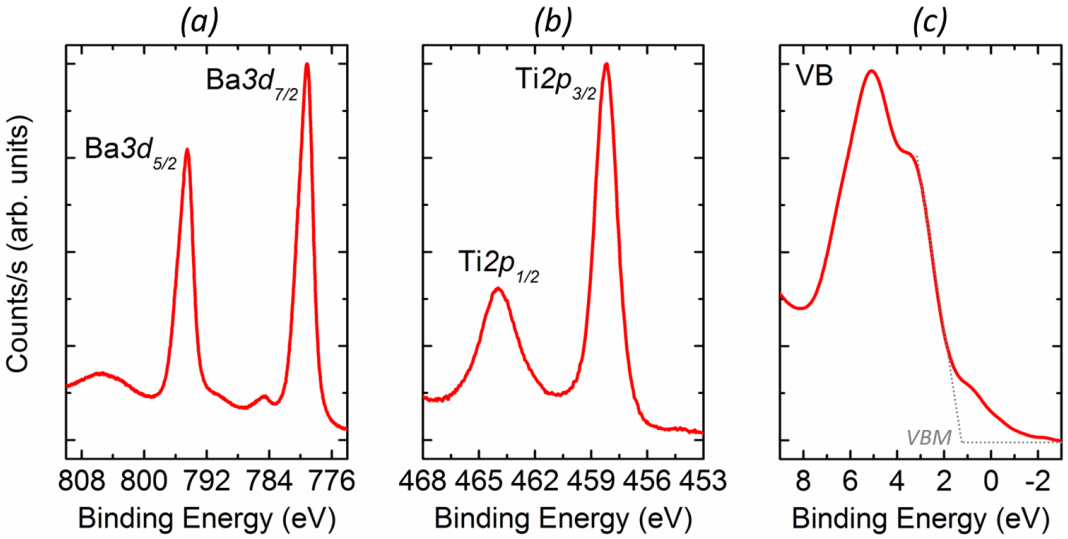

Figure 7.6: XPS spectra of the (a) Ba*3d* , (b) Ti*2p* core level and (c) valence band region after the growth of a 20 nm $BaTiO_3$ / Nb:$SrTiO_3$ film by OPA-MBE. Grey dotted lines on (c) highlight the range of binding energies lower than the valence band minimum (VBM).

7.3 Photoelectrolysis as a function of $BaTiO_3$ internal polarization

In this section I will present the photoelectrochemistry properties of our photoanodes systems incorporating a ferroelectric $BaTiO_3$ film. The challenge was to study systems with various internal polarization states. Subsections 7.3.1 and 7.3.2 present the mounting and the external poling procedures respectively. Then, the photoelectrolysis current densities for our systems are presented in 7.3.3.

7.3.1 Mouting and poling procedures

For photoelectrochemical measurements, the sample mounting involves screwing the sample holder into the photoanode holder to ensure impermeability, so that the electrolyte is only in contact with the thin film surface. This induces mechanical stresses on the sample, located at the edges of the illuminated surface. In the case of samples incorporating a ferroelectric thin film, mechanical stresses will have an effect on the ferroelectricity since a ferroelectric is also piezoelectric. On figure 7.7, the photocurrent *vs.* voltage curves are plotted for a 28 nm $BaTiO_3$ / Nb:$SrTiO_3$ sample mounted three different times. The spread in the photocurrent values (standard deviation *ca.* 27 %), illustrated by the arrows of various lengths, shows that this sample mounting is not reproducible. We conclude that it is not desirable for studying the ferroelectricity impact on the photoelectrochemical properties.

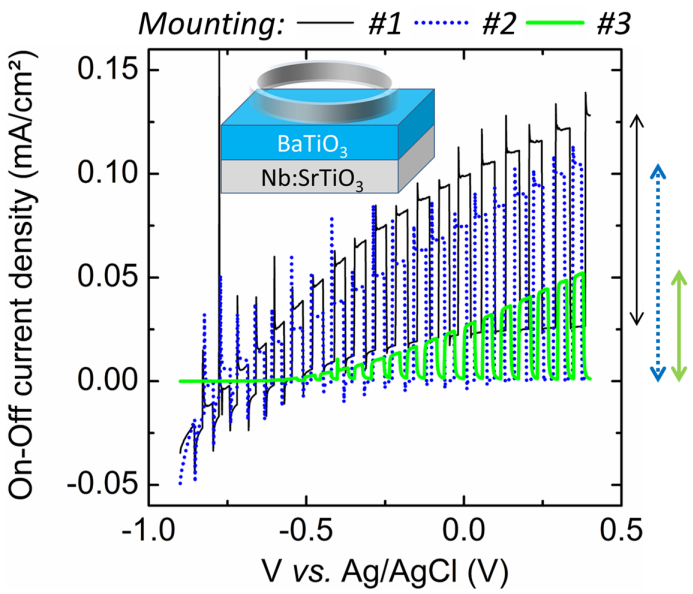

Figure 7.7: On-Off current density *vs.* voltage curves for a 28 nm $BaTiO_3$ / Nb:$SrTiO_3$ film mounted three times. Arrows give the photocurrent value at 0.4V *vs.* Ag/AgCl for the corresponding mounting. The grey ring represents the joint ensuring impermeability, which here would induce mechanical stresses in the $BaTiO_3$ layer after mounting.

Therefore a first challenge was to find a reproducible mounting procedure which does not involve mechanical stresses. The chosen solution consisted in patterning the $BaTiO_3$ thin film in the form of a disk (diameter 8 mm) small enough so that no physical contact exists between the sample holder and the ferroelectric film. The "anti-disk" was designed by laser lithography and the etching was performed by an Ar^+ ion beam etching (at a pressure of 10^{-5} mbar with an energy beam of 4 kV). On figure 7.8, which is the analogue of figure 7.7 but in the case of a sample which was patterned as a disk, it is clear that there is no spread in the photocurrent values due to different mountings anymore (standard deviation *ca.* 1 %). Differences in the dark current (and hence in the light current) are due to changes in the electrical contact resistance between the sample and the sample holder for the different mountings.

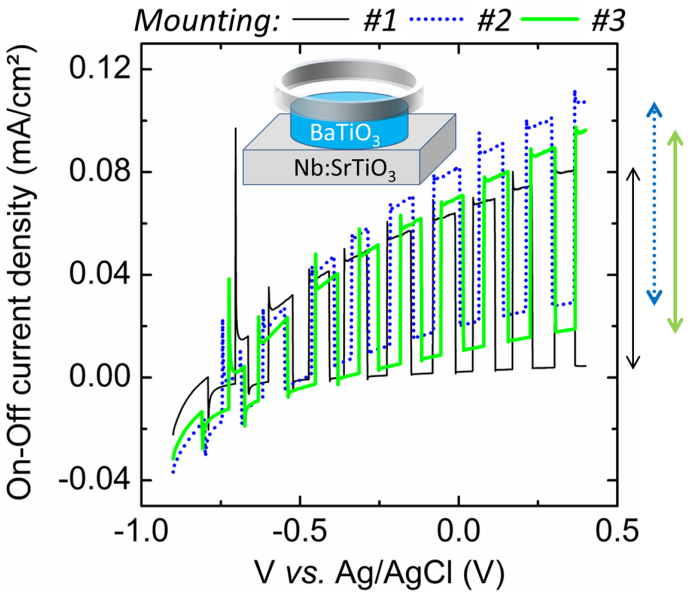

Figure 7.8: On-Off current density *vs.* voltage curves for a 28 nm $BaTiO_3$ / Nb:$SrTiO_3$ film patterned in the form of a circle mounted three times. Arrows give the photocurrent value at 0.4V *vs.* Ag/AgCl for the corresponding mounting. The grey ring represents the joint ensuring impermeability, which here would not induce any mechanical stresses in the $BaTiO_3$ layer after mounting.

7.3.2 Electrochemical poling procedure

Ideally, if one desires to study the effect of the electric polarization on photoelectrochemical properties, the control of this electric polarization (at least its direction) is mandatory. As a consequence a second challenge for our study dealt with the effective macroscopic poling of the samples. Indeed a poling procedure that involves the application of an external field on a macroscopic surface (*i.e.* the whole sample, 1×1 cm^2 surface) is far from trivial. Different methods of macroscopic poling were tested: (i) poling with a conductive plate on the sample as top electrode and (ii) poling using aluminium patches deposited on the surface as top electrodes and subsequently dissolved in a NaOH 0.1 M solution. Both procedures turned out to be unsuccessful (no effect on the samples ferroelectric properties). Cao et al. recently tackled this issue by macroscopically poling $BiFeO_3$ thin films deposited by spin-coating (thickness of hundreds of nm) in an electrochemical cell containing two electrodes and a non-aqueous electrolyte (0.1 M $LiClO_4$ in propylene carbonate) [205]. The choice of the poling potential value depends on the required field to reverse the polarization (the coercive field) of the ferroelectric and on the eventual potential losses because the external field is not directly applied between the surface and the bottom of the ferroelectric thin film. Kim et al. reported that the coercive field in single crystalline $BaTiO_3$ (001) thin films of thickness between 5 and 30 nm lies in the 10^3 kV/cm range [208]. This corresponds to a required

poling potential of 0.1V if it is applied exactly between the surface and the back of the film. If we neglect the potential drops in the Nb:$SrTiO_3$ substrate and in the electrolyte, poling potentials of hundreds of mV would be sufficient. However neither Nb:$SrTiO_3$ or the electrolyte used for poling are perfect conductors. As a matter of fact Cao et al. observed that poling potentials higher than 5V are necessary to macroscopically pole their $BiFeO_3$ samples [205]. This justifies the necessity of an electrolyte for which no chemical reactions occur in a potential range of approximately [-10V, +10V]. Such an electrolyte is said to have a large electrochemical window and is *a fortiori* non aqueous. To macroscopically apply an external field on our samples, we implemented the procedure of Cao et al. [205]. The electrochemical poling (noted EC-poling in the rest of the manuscript) procedure is illustrated on figure 7.9.

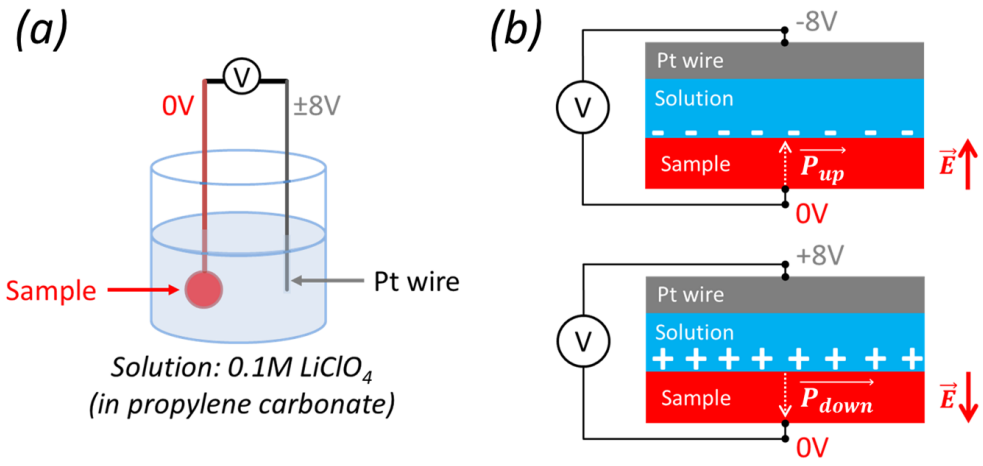

Figure 7.9: (a) Scheme of the electrochemical poling (EC-poling) procedure. (b) Scheme of the external field $\overrightarrow{E}$ induced by EC-poling with a -8V or +8V potential applied on the Pt counter electrode. The corresponding expected remnant internal polarization vector in the sample is also shown.

In a two electrodes cell, the sample and a Pt wire were mounted as the working and counter electrodes respectively. Potentials of +8V and -8V were applied alternatively 2 or 3 times on the platinum counter electrode (during 10 seconds each) and the sample was kept at 0V. The last potential was either +8V or -8V in order to obtain a remnant $\overrightarrow{P_{down}}$ (resp. $\overrightarrow{P_{up}}$) polarization. This poling method is efficient, as it will be seen hereinafter (subsection 7.3.3). However we observed that if the current flowing between the sample and the Pt electrode is too high ($>$ 2 mA), the $BaTiO_3$ film can be destroyed (no Ba signal in XPS). Therefore during the EC-poling procedure we monitored the current and managed to keep it below 1 mA.

7.3.3 On-Off current density measurements

7.3.3.a Bare $Nb:SrTiO_3$ substrate

First of all, it should be noted that the use of $Nb:SrTiO_3$ single crystals or thin films as photoanode for solar water splitting has been reported in the literature [45, 46]. However $Nb:SrTiO_3$ is not ferroelectric at room temperature, therefore EC-poling is not expected to have an effect on its photocurrent. We measured the photoelectrolysis current density on a bare $Nb:SrTiO_3$ single crystal in unpoled and +8V EC-poled conditions (*cf.* figure 7.10). The results evidence that the photocurrent of the bare $Nb:SrTiO_3$ substrate is not modified upon +8V EC-poling. In addition the data from figure 7.10 compare well with the results reported by Yin et al. in the case of $Nb:SrTiO_3$ single crystals used as photoanode [45].

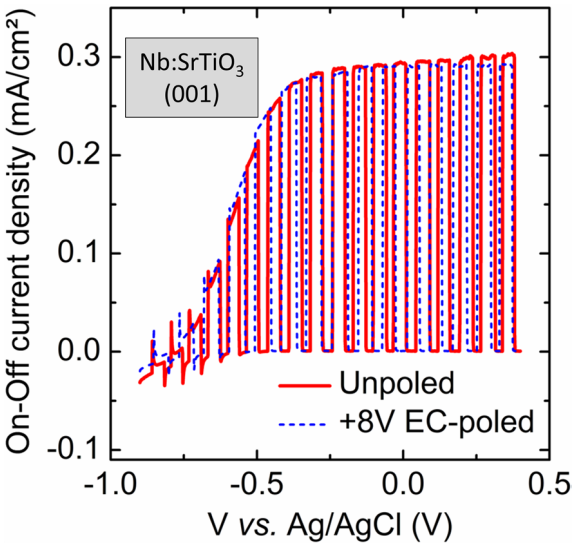

Figure 7.10: On-Off current density *vs.* voltage curves of a bare $Nb:SrTiO_3$ single crystal substrate for (a) unpoled (red solid line) and +8V EC-poled (blue dashed line) situations.

As it was highlighted in 7.1.3, the $BaTiO_3$ / $Nb:SrTiO_3$ system should be treated as a semiconductor heterojunction. In this case light absorption occurs in both materials, and in a photoanode system it is desirable to transfer the holes (resp. electrons) from $Nb:SrTiO_3$ (resp. $BaTiO_3$) to $BaTiO_3$ (resp. $Nb:SrTiO_3$). Since $BaTiO_3$ and $Nb:SrTiO_3$ have the same band gap, we cannot apply the same method than in the case of the γ^*-Fe_2O_3 / $Nb:SrTiO_3$ system (*cf.* appendix A.3). In the latter case we were able to separate the contributions from Fe_2O_3 and $Nb:SrTiO_3$ because of the gap difference between the two materials (2.07 eV and 3.26 eV respectively).

7.3.3.b $BaTiO_3$ / $Nb:SrTiO_3$ system

In this paragraph our first results concerning the effect of EC-poling on the photocur-

rent of a 25 nm $BaTiO_3$ / Nb:$SrTiO_3$ sample are shown. Figure 7.11 shows the photoelectrolysis current density measurements done on unpoled, -8V and +8V EC-poled 25 nm $BaTiO_3$ / Nb:$SrTiO_3$ samples. From figure 7.11.a we can observe that the photocurrent density of the -8V EC-poled sample is very similar to the one of the unpoled sample. In the case of a +8V EC-poling (figure 7.11.b), the photocurrent density is higher than the one for the unpoled sample by more than a factor of 2. Also the onset potential for the +8V EC-poled sample is significantly reduced by 0.2V. We also observe discrepancies for the dark current between the samples, for which the origin is not understood yet. Hence our results suggest that the transfer of holes from Nb:$SrTiO_3$ to $BaTiO_3$ and from $BaTiO_3$ to the electrolyte (and reciprocally for electrons) is more efficient in the case of the +8V EC-poled systems with respect to the unpoled system, resulting in an overall increase of the photoelectrochemical performances.

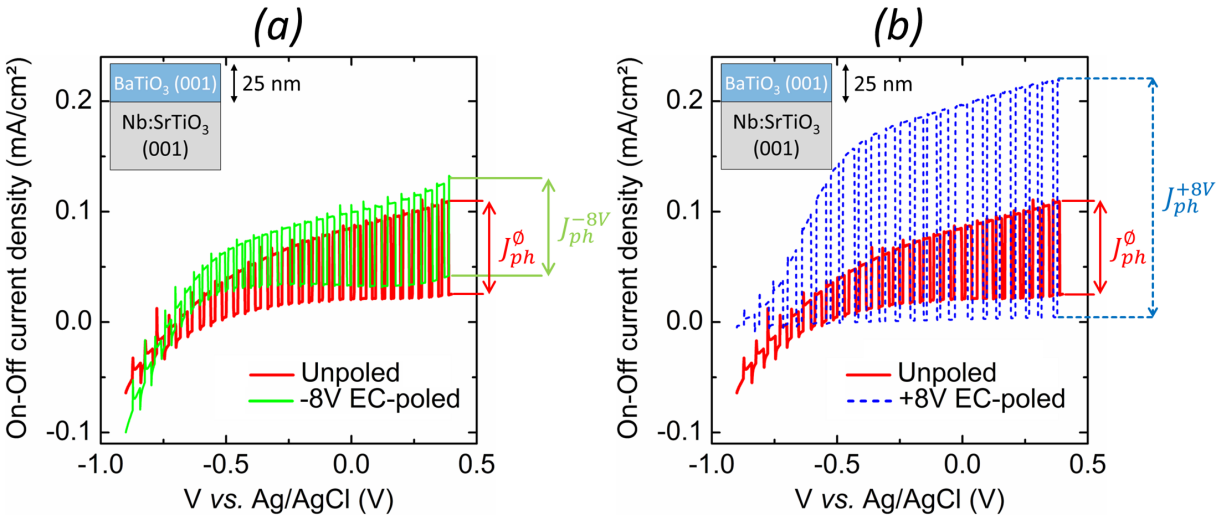

Figure 7.11: On-Off current density *vs.* voltage curves of a 25 nm $BaTiO_3$ / Nb:$SrTiO_3$ sample for (a) unpoled (red solid line) and -8V EC-poled (green solid line) and (b) unpoled and +8V EC-poled (blue dashed line) situations. Arrows give the photocurrent value ($J_{ph}^{\emptyset}$, J_{ph}^{-8V} and J_{ph}^{+8V}) at 0.4V *vs.* Ag/AgCl for the unpoled, -8V and +8V EC-poled situations. From [99].

Park et al. studied suspended ferroelectric particles as catalysts for hydrogen evolution and reported that the H_2 production (water reduction) between native and $\overrightarrow{P_{down}}$ polarized samples is very similar [206]. It is like our case where a -8V EC-poling (which is expected to arise $\overrightarrow{P_{up}}$ polarization) does not induce significant change in the O_2 production photocurrent (water oxidation) with respect to the unpoled system.

To the best of our knowledge, only one publication [95] concerns the use of a ferroelectric photoanode for solar water splitting with a detailed study of the variation of the photocurrent with the electric polarization. This work was published by Ji et al. [95] where they

studied $BiFeO_3$ (001) epitaxial films of hundreds of nm thicknesses grown by radio-frequency sputtering. Authors reported a reduction of the onset potential of *ca.* 0.02V and an increase in the overall photocurrent by *ca.* 30% for the positively poled films with respect to the negatively poled films. This behaviour is similar to our results, however our effect is much stronger and obtained for much thinner films. The low effect recorded by Ji et al. can originate from the (001) orientation of their films, which can be detrimental since the internal polarization in $BiFeO_3$ is oriented along the (111) axis. In our case, the internal polarization is oriented along the same direction than the carriers transport, which is the (001) axis.

7.3.4 Effect of EC-poling on the XPS peaks

In order to understand the mechanism responsible for the photocurrent changes upon EC-poling, we firstly checked that it does not originate from a modification of the $BaTiO_3$ film morphology or coverage upon the EC-poling procedure. Therefore we acquired *ex situ* XPS spectra of the Ti*3p* and Ba*4d* core levels before and after EC-poling. In addition we performed high resolution XPS experiments on the CASSIOPEE beamline at synchrotron SOLEIL with a photons energy of 500 eV (figure 7.12). For both EC-poling situations, we observed no change in the $BaTiO_3$ layer overall photoemission signal. This suggests no change in the $BaTiO_3$ quantity upon EC-poling.

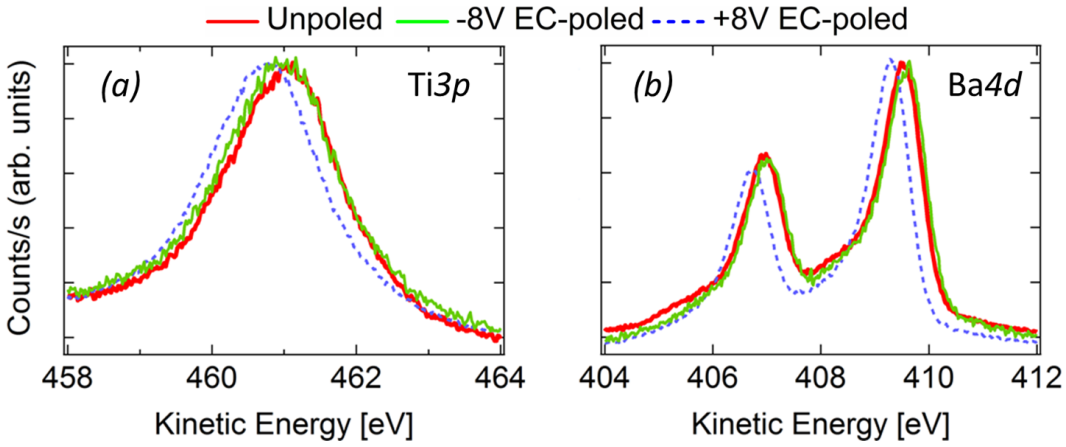

Figure 7.12: High resolution XPS spectra of the (a) Ti*3p* and (b) Ba*4d* core levels for a 25 nm $BaTiO_3$ / Nb:$SrTiO_3$ sample unpoled (red solid line), -8V (green solid line) and +8V EC-poled (blue dashed line) obtained with a photons energy of 500 eV.

Additional information can be extracted from the analysis of the peaks position. For these experiments, the samples were mounted so that only the back of the sample is connected to the sample holder in order to be sensitive to the effect of EC-poling on the photoemission peaks. In the case of a -8V EC-poling, almost no change in the XPS core level peaks position

was observed. However in the case of +8V EC-poling, we recorded a clear XPS peaks shift toward lower kinetic energies (by *ca.* 0.2 eV) for both Ti*3p* and Ba*4d* core levels. This suggests that EC-poling modifies the electronic structure of the $BaTiO_3$ layer. We observe that +8V EC-poling causes the same kind of photoemission peak shift than the well-known charge effect in conventional XPS, where exiting photoelectrons can be slowed down due to an excess of positive charges at the surface. This results in a shift of the photoemission peaks toward lower kinetic energies.

These results are consistent with our photoelectrolysis current density measurements. Indeed we see only changes when the sample is +8V EC-poled. The origin of the photoemission peak shift will be discussed later (section 7.5).

7.4 Piezoresponse Force Microscopy (PFM)

PFM (introduced in subsection 3.2.3) is sensitive to the local polarization state and is the technique of choice to study the ferroelectric properties of our systems. It was used in writing mode in order to define µm-sized ferroelectric domains on our samples, by applying various potentials on the tip (PFM-poling), *i.e.* on the sample surface. Figure 7.13 shows the direction of the remnant internal polarization expected after postive or negative PFM-poling. As it was detailed in subsection 7.1.1, the remnant internal polarization is expected to be parallel to the applied external poling field. Hence PFM-poling with a positive (resp. negative) potential applied on the sample surface is expected to induce a remnant $\overrightarrow{P_{down}}$ (resp. $\overrightarrow{P_{up}}$) polarization inside the $BaTiO_3$ layer.

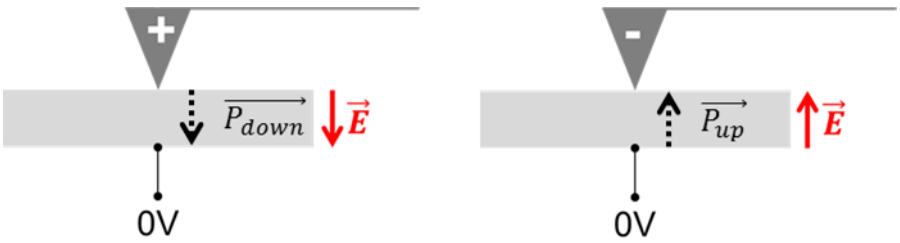

Figure 7.13: PFM-poling geometry and expected remnant internal polarization as a function of the PFM-poling potential sign: (left) positive and (right) negative. As it was detailed in subsection 7.1.1, the remnant internal polarization is expected to be parallel to the applied external poling field.

PFM was used to characterize the ferroelectric state of the $BaTiO_3$ layer after OPA-MBE deposition (unpoled) and after PFM-poling (results shown on figure 7.14). The PFM pattern used for PFM-poling is given (figure 7.14.a) as well as and the corresponding PFM phase images (in reading mode) for a 15 nm $BaTiO_3$ / Nb:$SrTiO_3$ sample unpoled (figure 7.14.b)

and PFM-poled (figure 7.14.c). The well-defined phase contrast of $\Delta\varphi = 110°$ between the two PFM-poled regions at +8V and -8V (shown on the phase profile figure 7.14.d) demonstrates the existence of two different orientations of the remnant electrical polarization after ± 8V saturation, confirming the ferroelectric character of our $BaTiO_3$ films. Moreover the hysteresis cycle obtained in PFM (figure 7.14.e) proves that tip potentials of +8V and -8V are sufficient to saturate the ferroelectric polarization, hence inducing $\overrightarrow{P_{down}}$ and $\overrightarrow{P_{up}}$ polarizations respectively. It is worth noting that we were able to write ferroelectric domains with two different out-of-plane orientations by PFM-poling.

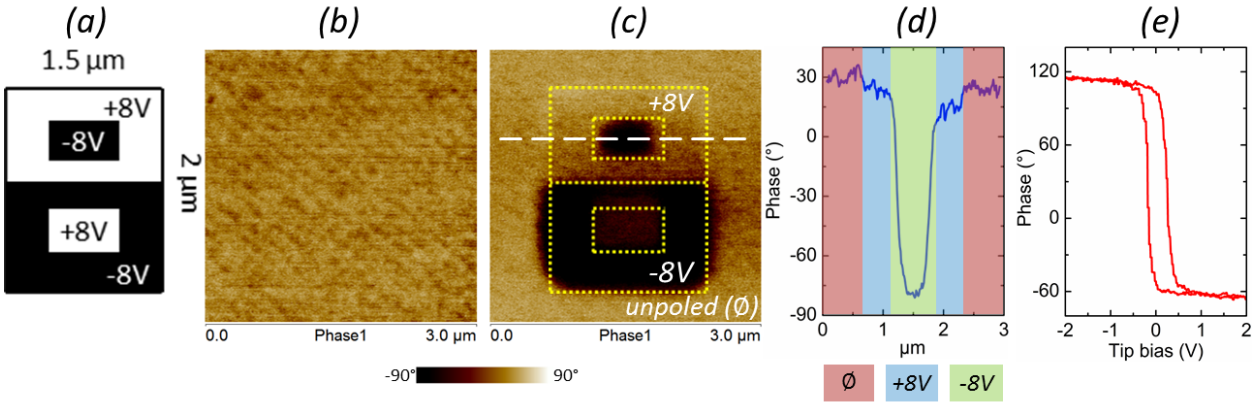

Figure 7.14: PFM data of a 15 nm $BaTiO_3$ / Nb:$SrTiO_3$ sample: (a) PFM pattern applied, (b) PFM phase image of after OPA-MBE deposition (unpoled) and (c) after PFM-poling through the writing of the PFM pattern highlighted with yellow dotted lines (PFM-poled). (d) PFM phase profile along the white dashed line shown on (c) (the ∅ symbol stands for unpoled), and (e) hysteresis cycle.

Moreover, there is very few phase contrast between the unpoled and +8V PFM-poled regions, meaning that for this sample, the $BaTiO_3$ film deposited on Nb:$SrTiO_3$ natively features an internal polarization which is mostly downward oriented. The internal ferroelectric polarization is aligned along the (001) axis and exists in $BaTiO_3$ as soon as the elementary cell is tetragonal. In the case of the growth of $BaTiO_3$ on Nb:$SrTiO_3$, we saw in 7.2.1 that the substrate induces an in-plane compressive strain. According to the Poisson effect, an in-plane compressive strain induces an out-of-plane extensive strain. Therefore on Nb:$SrTiO_3$ the $BaTiO_3$ elementary cell will be natively tetragonal with the tetragonal axis parallel to the (001) axis. This explains why our $BaTiO_3$ layers are natively out-of-plane polarized. The origin for a self-polarization mostly oriented toward the substrate (mostly $\overrightarrow{P_{down}}$ polarization) is not trivial. As it was mentioned earlier, Nb:$SrTiO_3$ is an n-type semiconductor [45, 46] with a reported work function smaller than the one of $BaTiO_3$. The built-in Schottky junction between the $BaTiO_3$ film and the Nb:$SrTiO_3$ substrate may explain the

mostly downward oriented native polarization. Indeed $\overrightarrow{P_{down}}$ polarization will be screened more easily than $\overrightarrow{P_{up}}$ polarization by the n-type Nb:$SrTiO_3$ substrate, through the electron injection from Nb:$SrTiO_3$ to $BaTiO_3$[31]. However in the literature a self $\overrightarrow{P_{down}}$ polarization is not always reported in the case of $BaTiO_3$ thin films deposited on substrates inducing in-plane compressive epitaxial strain. As a matter of fact, Chen et al. reported a native $\overrightarrow{P_{up}}$ polarization for $BaTiO_3$ films deposited on both p-type and n-type surfaces, however without proposing a clear mechanism for this preferential native orientation [209]. The same team reported similar observations in the case of another widely studied ferroelectric material, Pb(Zr,Ti)O_3 [210].

7.5 X-PEEM measurements

To investigate the impact of ferroelectricity (*i.e.* the remnant internal polarization orientation) on the electronic structure, we chose to characterize our systems by X-PEEM. Various remnant polarizations states were obtained through PFM-poling. The combination of X-PEEM and PFM has the advantage to allow studying on the very same sample surfaces featuring various polarization directions. In addition, we demonstrated in section 7.4 that PFM-poling allows obtaining both $\overrightarrow{P_{up}}$ and $\overrightarrow{P_{down}}$ remnant polarization. In this section we studied a 15 nm $BaTiO_3$ / Nb:$SrTiO_3$ sample (the same as for the PFM results shown on figure 7.14).

The written PFM pattern is shown on figure 7.15. In order to locate the PFM-poled zone, gold landmarks were applied on the samples by laser lithography. In addition figure 7.16 shows the three types of measurements performed using X-PEEM[32].

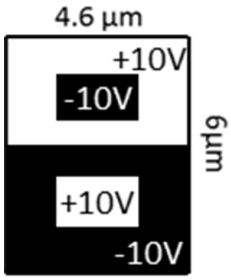

Figure 7.15: PFM pattern used for X-PEEM measurements.

[31] As a reminder (*cf.* 7.1.1), in the case of $\overrightarrow{P_{down}}$ polarization, the polarization bound charges at the interface between $BaTiO_3$ and Nb:$SrTiO_3$ are positive. Hence these charges are expected to be screened by negative charges.

[32] We recorded X-PEEM image stacks (one image per photons energy or incident electron energy) of the full field of view and integrated the intensities of the unpoled and PFM-poled surfaces to reconstruct their respective spectra (*cf.* 3.3.4 for more details).

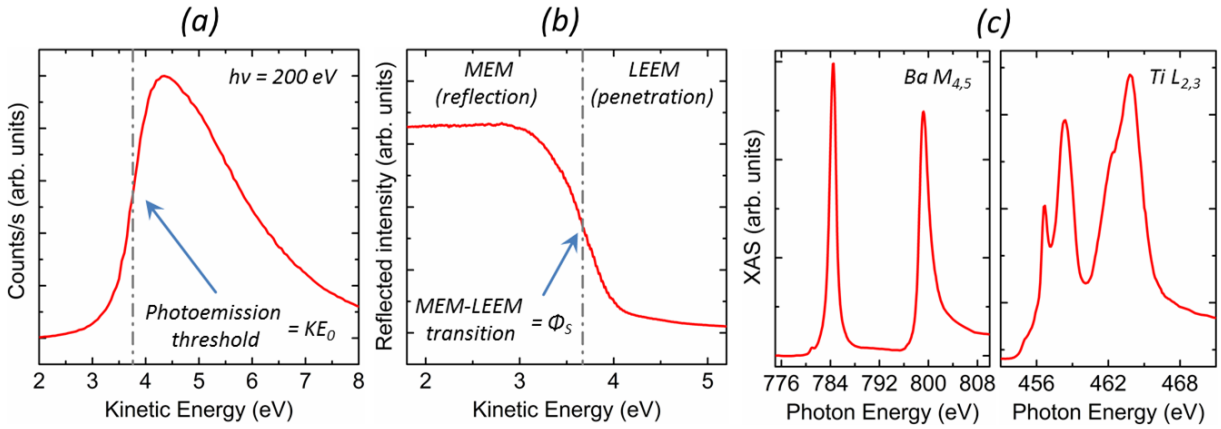

Figure 7.16: Illustration of the realized X-PEEM measurements: (a) photoemission threshold spectra showing the KE_0 value, (b) MEM-LEEM transition spectra showing the Φ_S value and (c) XAS spectra at the Ba $M_{4,5}$ and Ti $L_{2,3}$ edges. Sample: 15 nm $BaTiO_3$ / Nb:$SrTiO_3$ (unpoled region).

A relevant physical property for our study is the photoemission threshold. It corresponds to the lowest kinetic energy experimentally reachable for the exiting photoelectrons. To measure it, we scanned the photoemission signal for low kinetic energies (2 to 8 eV) upon excitation with photons of 200 eV (energy well above the work function). Its value, noted KE_0, is defined as the inflexion point of this curve (*cf.* figure 7.16.a). We obtained the KE_0 map by calculating the photoemission threshold value for each pixel of the probed spatial area.

We also measured the MEM-LEEM transition potential from reflectivity curves in LEEM mode, which was introduced in 3.2.4. Briefly, below the MEM-LEEM transition potential (MEM regime), electrons are reflected elastically by the sample surface and above (LEEM regime) their energy is large enough to penetrate the sample. The MEM-LEEM transition energy is defined as the inflection point of the reflectivity curve (*cf.* figure 7.16.b). This value is called surface potential (noted Φ_S) and corresponds to the minimum energy for which incident electrons can penetrate in the sample.

Finally we performed XAS measurements at the Ba $M_{4,5}$ and Ti $L_{2,3}$ edges (*cf.* figure 7.16.c). The XAS signal was recorded by counting the photoelectrons of a given kinetic energy just above the photoemission threshold (around 4.5 eV) as a function of the incident photons energy. Ferroelectricity in $BaTiO_3$ is linked to the tetragonality of the elementary cell through the displacement of Ti^{4+} cations. In the tetragonal phase, the ferroelectric polarization is aligned with the (001) axis. Since the (001) axis is not equivalent to the (100) axis, one expects anisotropic XAS spectra when the linear synchrotron radiation polarization is either parallel to the (001) plane or perpendicular to it. Therefore one can expect to probe ferroelectricity by measuring the linear dichroism in XAS spectra (charges anisotropy).

We measured the XAS spectra using two different photons polarizations, linear horizontal (LH) or linear vertical (LV) (*cf.* 3.3), corresponding respectively to a photons polarization orientation mainly parallel to the (001) plane or perpendicular to it (*cf.* details about the X-PEEM geometry experiment in 3.3.4).

Our X-PEEM experiments were carried out on the I06 Nanoscience beamline at the Diamond Light Source (Didcot-UK). Before analysis and in order to remove any surface contamination due to air exposure, the samples were annealed under UHV at a temperature of 80°C for one hour. This procedure is a good compromise allowing enough outgasing without changing the signal due to ferroelectric polarization. Experiments were performed *ca.* one week after the writing of the PFM pattern so that any excess charge at the surface due to PFM-poling is evacuated [135].

7.5.1 Photoemission threshold KE_0

The photoemission threshold spectra and the KE_0 map for a 15 nm $BaTiO_3$ / Nb:$SrTiO_3$ film are shown on figure 7.17.

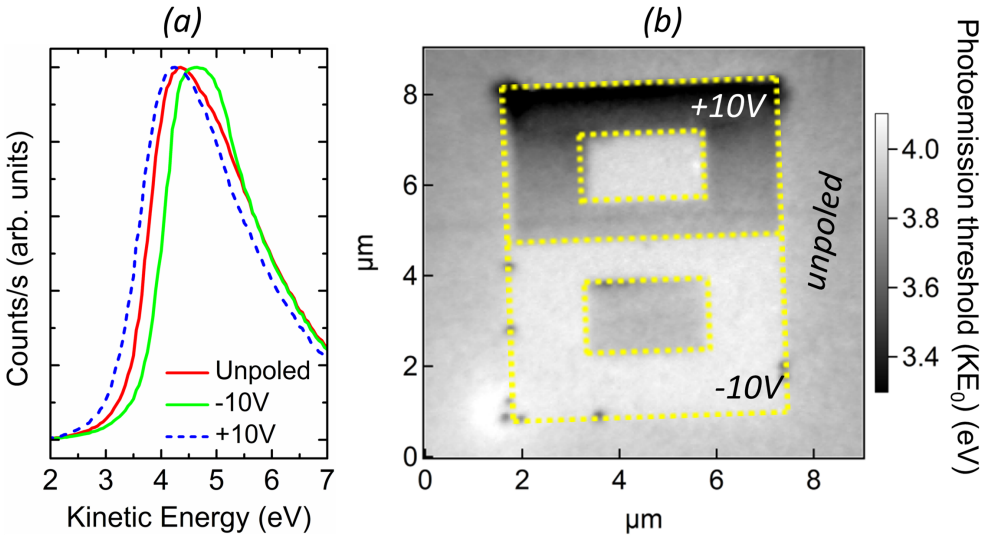

Figure 7.17: (a) Integrated photoemission threshold spectra on unpoled (red solid line), -10V (green solid line) and +10V (blue dashed line) PFM-poled regions and (b) KE_0 map at the PFM-poling pattern location for a 15 nm $BaTiO_3$ / Nb:$SrTiO_3$ sample. The yellow dotted lines highlight the PFM pattern location as well as the integration zones used to reconstruct the spectra of (a). From [99].

The photoemission threshold curve for the +10V (resp. -10V) PFM-poled surface is shifted toward lower (resp. higher) kinetic energies with respect to the unpoled surface (*cf.* figure 7.17.a). Hence $KE_0(+10V) < KE_0(unpoled) < KE_0(-10V)$. Accordingly, on the KE_0 map (figure 7.17.b) the +10V (resp. -10V) PFM-poled surface appears uniformly

darker (resp. uniformly lighter) than the unpoled surface. This shows that a +10V (resp. -10V) PFM-poling induces a remnant electric field at the surface of the $BaTiO_3$ layer which decelerates (resp. accelerates) the outcoming photoelectrons with respect to the unpoled region.

7.5.2 MEM-LEEM transition Φ_S

The reflectivity curve and the Φ_S map for a 15 nm $BaTiO_3$ / Nb:$SrTiO_3$ sample are shown on figure 7.18. The reflectivity curve for the +10V (resp. -10V) PFM-poled surface is shifted toward lower (resp. higher) kinetic energies with respect to the unpoled surface (*cf.* figure 7.18.a). Hence $\Phi_S(+10V) < \Phi_S(unpoled) < \Phi_S(-10V)$. Accordingly on the Φ_S map (figure 7.18.b) the +10V (resp. -10V) PFM-poled surface appears uniformly darker (resp. uniformly lighter) than the unpoled surface. This shows that a +10V (resp. -10V) PFM-poling induces a remnant electric field at the surface of the $BaTiO_3$ layer which favours (resp. penalizes) the penetration of incoming electrons with respect to the unpoled region. This is consistent with the results obtained from the previous photoemission threshold measurements (7.5.1).

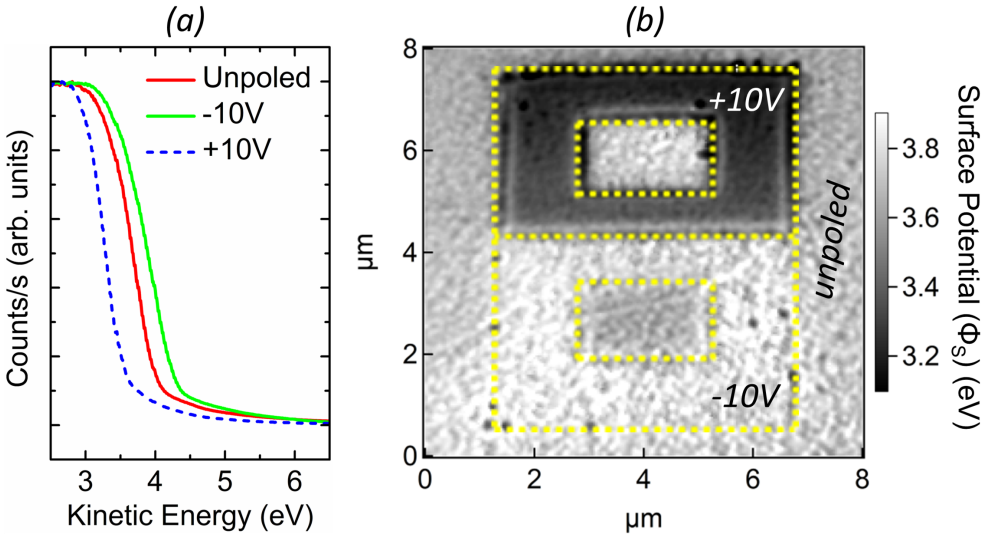

Figure 7.18: (a) Integrated MEM-LEEM transition spectra on unpoled (red solid line), -10V (green solid line) and +10V (blue dashed line) PFM-poled regions and (b) Φ_S map at the PFM-poling pattern location for a 15 nm $BaTiO_3$ / Nb:$SrTiO_3$ sample. The yellow dotted lines highlight the PFM pattern location as well as the integration zones used to reconstruct the spectra of (a).

7.5.3 XAS at the Ba $M_{4,5}$ edge

Figure 7.19 shows the XAS obtained at the Ba $M_{4,5}$ edge for LH and LV incident photons polarization.

The overall XAS signal of the -10V PFM-poled surface is higher than the one of the +10V PFM-poled surface, which is itself higher than the one of the unpoled surface. We indicated earlier that the XAS signal is recorded through the counting of photoelectrons having a kinetic energy just above the photoemission threshold (around 4.5 eV). Since the photoemission threshold is different for the three surfaces (*cf.* 7.5.1), the choice of a single kinetic energy will arise different photoemission yields for the three surfaces, thus the overall XAS signal will be different.

However a result independent on the measurement strategy is that the branching ratio (relative M_5 / M_4 peak intensities) for a given incident photons polarization changes with the remnant polarization state. The branching ratio is shown in table 7.1. We can see that:

- the branching ratio for PFM-poled surfaces is always higher than the branching ratio of the unpoled surface;
- for unpoled and PFM-poled surfaces the branching ratio changes with the incident photons polarization;
- this branching ratio anisotropy is more pronounced for the PFM-poled surfaces than for the unpoled surface.

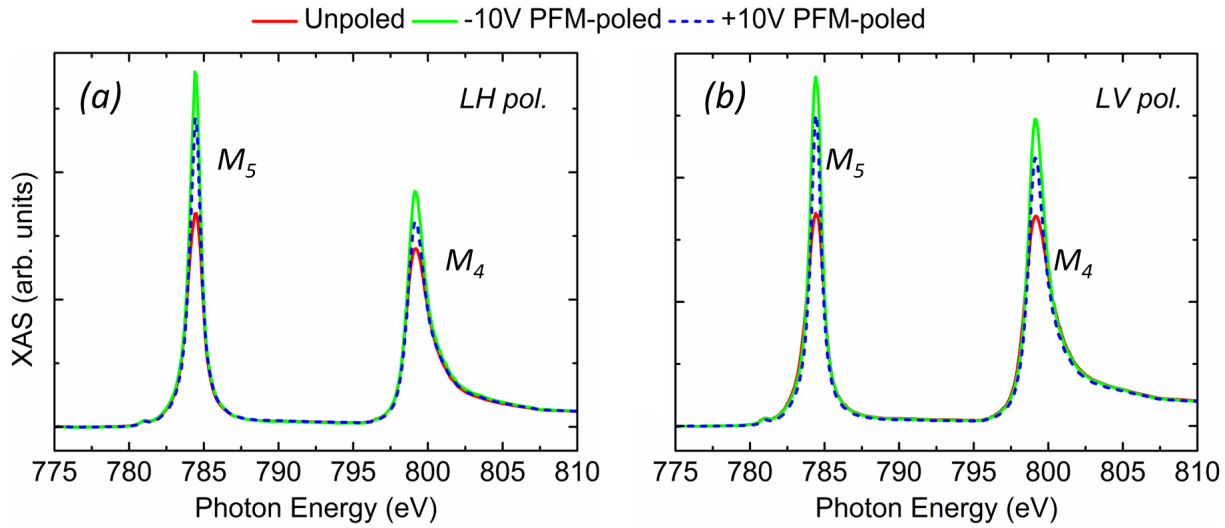

Figure 7.19: Ba $M_{4,5}$ edge XAS of a 15 nm $BaTiO_3$ / Nb:$SrTiO_3$ sample measured with (a) LH and (b) LV incident photons polarization for unpoled (red solid line), -10V (green solid line) and +10V (blue dashed line) PFM-poled regions.

Photons polarization	PFM-poling		
	unpoled	-10V	+10V
LH	1.19	1.51	1.49
LV	1.00	1.13	1.18

Table 7.1: Branching ratio at the Ba $M_{4,5}$ edge of a 15 nm $BaTiO_3$ / Nb:$SrTiO_3$ sample obtained with LH or LV incident photons polarization for unpoled, -10V and +10V PFM-poled regions.

Usually a high branching ratio is linked to a high spin-orbit coupling [211]. To the best of our knowledge, a branching ratio dependence as a function of the remnant polarization in $BaTiO_3$, and more generally the evolution of the Ba $M_{4,5}$ XAS as a function of the remnant polarization have not been investigated in the literature. It would be very interesting to investigate this matter using simulation approaches, like multiplet calculations, in order to be able to link properly the ferroelectricity to the electronic structure (branching ratio and spin-orbit coupling). Although the physical origin of the branching ratio change upon PFM-poling is not understood yet, its amplitude seems to be linked to the remnant ferroelectric polarization amplitude and (perhaps) direction. We can imagine using this property for the characterization of EC-poled samples.

7.5.4 XAS at the Ti $L_{2,3}$ edge

The very few studies dealing with the influence of ferroelectric polarization on the XAS spectra focus on the Ti $L_{2,3}$ XAS. This was explored by Polisetty et al. [212] and Arenholz et al. [213] in the case of $PbZr_{0.2}Ti_{0.8}O_3$ films. Indeed in this material (like in $BaTiO_3$) the orientation and amplitude of the ferroelectric polarization vector are directly dependent on the position of the Ti^{4+} cations in the primitive cell. In these studies the authors observe strong discrepancies in the XAS signal at the Ti $L_{2,3}$ edge when the photons polarization is perpendicular or parallel to the ferroelectric polarization vector. In our case we have measured the XAS at the Ti $L_{2,3}$ edge for the three relevant regions of our sample (unpoled, +10V and -10V PFM-poled) using LH and LV photons polarizations. No significant dichroïsm signal was observed, confirming that in our sample the ferroelectric polarization is always perpendicular to the film surface (*i.e.* along the (001) axis, $\overrightarrow{P_{up}}$ or $\overrightarrow{P_{down}}$ polarization).

7.6 Discussion

By comparing figure 7.12 and figure 7.17, one observes that positive EC-poling and positive PFM-poling both induce a shift of the photoemission peaks toward lower kinetic energies. Therefore both poling procedures induce the same remnant polarization (in terms of orientation), which is $\overrightarrow{P_{down}}$ polarization. Moreover the observed shift is in the same direction than for the "charge effect" in XPS, where an excess of positive charges remains at the surface. For $\overrightarrow{P_{down}}$ polarization, the scheme of charges repartition is represented on figure 7.20, where positive screening charges are present near the surface. We can then conclude that the internal field highlighted by XPS and X-PEEM results is due to the positive screening charges.

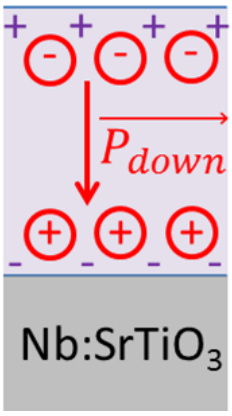

Figure 7.20: Expected charges repartition for a $\overrightarrow{P_{down}}$ polarization of the $BaTiO_3$ layer deposited on Nb:$SrTiO_3$. Red circled charges stand for the polarization bound charges (fictive charges) and purple charges stand for charges which screen the internal polarization.

Concerning negative PFM-poling and negative EC-poling, the results are different. Negative PFM-poling induces a shift of the photoemission peaks in the opposite direction with respect to positive PFM-poling, as it was observed by X-PEEM. This shift can be easily understood considering a $\overrightarrow{P_{up}}$ polarization and negative screening charges. However negative EC-poling produces no effect in XPS or in water photoelectrolysis, showing that negative EC-poling is not effective.

According to the previous results, we investigated experimentally of the effects of internal ferroelectric polarization of $BaTiO_3$ on the charges dynamics in the $BaTiO_3$ / Nb:$SrTiO_3$ system. We demonstrated by X-PEEM measurements that $\overrightarrow{P_{up}}$ polarization obtained by negative poling induces, through the polarization screening, an electric field favouring electron accumulation at the surface which is very helpful for reduction reactions. Reciprocally $\overrightarrow{P_{down}}$ polarization obtained by positive poling induces an electric field that hinders electrons

from the bulk to cross the surface, which is equivalent to attract holes from the bulk to the surface, favouring oxidation reactions.

Our findings are illustrated on figure 7.21 (reproduced from ref. [214]), where the band diagram of the interface between an aqueous solution and $BaTiO_3$ is shown for unpoled, $\overrightarrow{P_{up}}$ and $\overrightarrow{P_{down}}$ polarizations (with the hypothesis of complete screening in the bulk, *i.e.* flat bands far from the surface). In the case of photocathodes, the objective is to realize water reduction at the photocathode/electrolyte interface. This reaction occurs through electron transfer from the photocathode to the electrolyte, therefore to increase the efficiency, driving the electron accumulation at the photocathode surface is desirable. We showed that it can be achieved trough negative poling (*i.e.* $\overrightarrow{P_{up}}$ polarization). This is illustrated on figure 7.21.a by downward band bending at the surface (with respect to the unpoled surface). In the case of photoanodes, the objective is to realize water oxidation at the photoanode/electrolyte interface. This reaction involves a transfer of holes from the photoanode to the electrolyte, therefore to increase the efficiency it is desirable to drive the hole accumulation (*i.e.* the electron depletion) at the surface, which we managed to do thanks to positive poling (*i.e.* $\overrightarrow{P_{down}}$ polarization). This is illustrated on figure 7.21.c by an upward band bending (with respect to the unpoled surface). Indeed the photocurrent of our $BaTiO_3$ / Nb:$SrTiO_3$ system was more than doubled upon +8V EC-poling. This is consistent with the findings of groups studying the impact of ferroelectricity in photocatalysis applications (*cf.* 7.1.2).

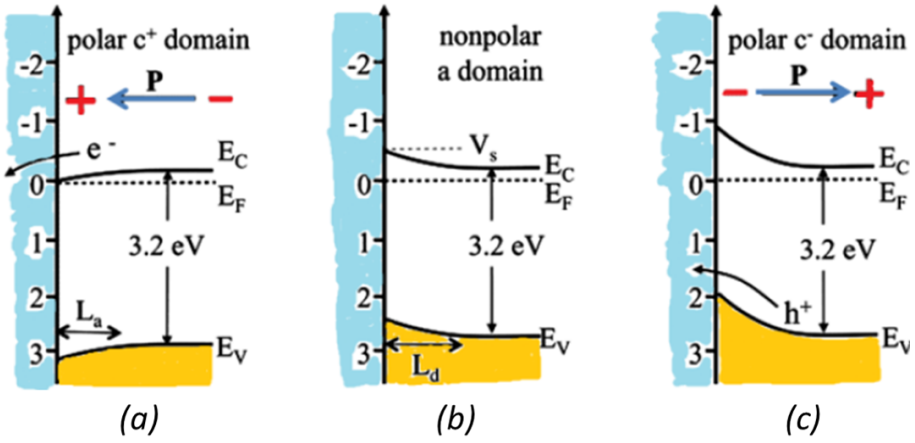

Figure 7.21: Energy level diagrams for $BaTiO_3$ in aqueous solution, without illumination, for (a) $\overrightarrow{P_{up}}$ polarization, (b) unpoled, and (c) $\overrightarrow{P_{down}}$ polarization. The energies on the vertical axes are on the standard hydrogen electrode scale. E_V is the valence band edge, E_F is the Fermi level, E_C is the conduction band edge, V_s is the surface potential, L_d is the width of the space charge layer in depletion, and L_a is the width of the space charge layer in accumulation. The electrolyte is coloured in blue. From [214].

To summarize, we have directly correlated the physical phenomena induced by remnant polarization to photocurrent variations in the case of $BaTiO_3$ / Nb:$SrTiO_3$ photoanodes. As

a matter of fact, the photocurrent can be strongly enhanced by the ferroelectric polarization, through the induced internal electric field within the ferroelectric layer. The results presented in this chapter are very encouraging for the combination of ferroelectric materials with conventional metal oxide photoanodes like hematite. Our study is a first step toward the tailoring of the photoelectrochemical properties through ferroelectricity.

8 Conclusion and outlook

This aim of this thesis work was to study hematite-based single crystalline nanometric films to be used as photoanodes in the framework of solar water splitting. This was a new research topic started in 2010 in the "Oxide" group. Oxygen plasma assited molecular beam epitaxy revealed itself as a well-suited technique to elaborate model samples, making possible the use of high-end characterization techniques, in particular using synchrotron radiation, as well as the photoelectrochemical measurement setup. Such systems allow studying independently the effect of a single parameter, while the use of chemical routes may make water splitting performances depend on multiple origins like changes in morphology or crystalline structure. In addition we measured the photoelectrochemical properties of our systems, through the development of a complete photoelectrochemical characterization setup, as well as experiments protocols. Further experience will provide a stronger expertise in the rich range of methods offered by this setup, thanks to various illumination (steady, modulated, white or monochromatic light) and applied potential (steady or modulated) regimes. We were able to propose an original contribution to the research effort in the field of hematite-based photoanodes for solar water splitting, with a fundamental research approach.

Despite its drawbacks, hematite is still to be considered as the top candidate for solar water splitting photoanodes. It has indeed, thanks to its low band gap, the highest theoretical solar-to-hydrogen efficiency among abundant and low-cost metal oxides (*ca.* 13%). In chapters 4 and 5 of this manuscript we considered various approaches to improve the water splitting performances of hematite single layers: tuning the iron oxide crystallographic structure and its oxygen content (4), doping hematite with titanium and varying the thin film thickness (5.1), as well as applying a surface chemical treatment (5.2).

We demonstrated in chapter 4 that the most favourable iron oxide phase in the case of nanometric thin films is hematite. Further improvement of the photocurrent (two-fold increase) and reduction of the onset potential (by *ca.* 0.2V) can be obtained through the introduction of oxygen vacancies upon annealing in ultra high vacuum. The optimal concentration of these oxygen vacancies is exceeded when Fe^{2+} can be detected by XPS in the material, which results in a slight modification of the crystallographic structure, as it was seen by EXAFS.

As it was investigated in chapter 5, doping hematite with Ti has been proven to be a very efficient strategy for our films since it multiplied the photocurrent by more than 100 and reduced the onset potential down to 0.2V *vs.* Ag/AgCl. Investigating single crystalline samples made possible studying the effects of thickness and Ti-doping level independently. We showed thanks to EXAFS measurements that the corundum structure is conserved upon Ti-doping and that titanium substitutes iron, resulting in a slight distortion of the oxygen

octahedron. A moderate doping level of 2 at.% increases both electrons and holes diffusion lengths. In addition, doping levels of 5 at.% or more induce a shift of the Fermi level toward the conduction band, increasing the band bending between hematite and the electrolyte for these doping levels. Further improvement of 2 at.% Ti-doped hematite performances (25% increase in the photocurrent and 0.1V onset potential reduction) can be achieved upon partial chemical etching in a hydrochloric acid solution. This partial etching increases the overall roughness of the surface, as it was measured by AFM, providing a higher surface area able to realize water oxidation. In addition an iron oxide reduction at the etched surface was revealed by the presence of Fe^{2+} ions detected by X-PEEM, which were not numerous enough to induce detrimental recombination centers within the band gap.

Semiconductor heterojunctions is a very interesting approach for improving photoanodes performances, especially through more efficient charge separation and photons absorption. We studied in chapter 6 the Ti:α-Fe_2O_3 - TiO_2 system, where the ultimate goal was to benefit from the TiO_2 surface kinetics and band structure (valence band and conduction band positions) and from the advantageous absorption properties of hematite. Resonant photoemission spectroscopy revealed the creation of a Fe^{2+}-rich interface between the two materials. Moreover the concentration of these Fe^{2+} species was sufficient enough to introduce energy states within the band gap, which are tremendous for the photocurrent since they favour carriers recombination. We showed that this interface is likely to rule the charges dynamics in these systems. Nonetheless, photocurrent measurements using steady or modulated monochromatic light showed that a TiO_2 surface is desirable in order to reduce the high surface recombination rate inherent to hematite. It opens to the possibility of using TiO_2 as a surface treatment in order to reduce the surface charge recombination.

The success of ferroelectric surfaces in photochemistry applications can make one very confident concerning the use of ferroelectric polarization as an internal electric field in photoanodes. A mandatory stage is to completely understand the behaviour of the single ferroelectric system, before introducing it in a heterojunction with hematite for example. A first step toward the comprehension of the relationship between the ferroelectric polarization and the photocurrent changes was conducted in chapter 7 where ferroelectric $BaTiO_3$ thin films deposited on Nb:$SrTiO_3$ single crystals were studied. Poling and mounting methods were developed, allowing the photoelectrochemical characterization of ferroelectric photoanodes featuring various macroscopic polarization states. A major finding is that the photocurrent of a 25 nm $BaTiO_3$ / Nb:$SrTiO_3$ sample was more than doubled in the case of downward polarization. This was explained by XPS and X-PEEM measurements which brought the experimental proof that downward polarization induces an electric field that lowers the photoelectrons kinetic energy, favouring water oxidation at the surface.

These results are a first step toward the use of ferroelectric polarization to enhance, or at least act, on the photoelectrochemical properties of photoanodes.

This PhD was the first in the Oxide group at the Service de Physique de l'Etat Condensé which focused on the study of single crystalline metal oxide thin films as photoanodes dedicated to solar water splitting. A photoelectrochemical characterization setup was developed and a new field of research was successfully implemented in the group. Our approach penetrated well the solar water splitting community, as it was confirmed by accepted research projects, published articles or participations to conferences. All these points, as well as the scientific wealth offered by this topic, promise a bright future and arise numerous outlooks, which are detailed below.

Doping is a very powerful degree of freedom for tuning the electrical properties of hematite, as well as its electronic structure. Gradient doping would be an interesting approach since it can arise new properties as compared to homogeneous doping. Indeed gradient doping can induce, through the local shift of the Fermi level, a continuous band bending all along the thin film. This can improve the electron-hole pairs separation and possibly increase the optimal thickness of hematite films, thus the quantity of absorbed photons and the overall photocurrent. In the light of the study of Ti-doped hematite in chapter 5, gradient doping using titanium as dopant seems very encouraging. Indeed we showed that there is a comfortable latitude concerning the Ti-doping range since the corundum structure of hematite films is preserved upon Ti-doping, up to a doping level of 17 at.%. Moreover the versatility of the OPA-MBE technique facilitates the tuning of the doping level during thin films deposition. In addition we can also imagine the building of p-Fe_2O_3 / n-Fe_2O_3 homojunctions, which is subjected to finding the right dopant for obtaining p-Fe_2O_3.

Another path to investigate emerged after discovering that a TiO_2 layer deposited on hematite reduces the surface charge recombination rate. The use of overlayers is a recognized strategy to improve the performances of photoanodes. Using our OPA-MBE apparatus, it is possible to grow aluminium, cobalt or nickel oxides. These oxides were proven to enhance photoelectrochemical properties of metal oxide photoanodes, as surface recombination passivation layers or cocatalysts materials. Here the point would be to characterize the effect of such overlayers on the electronic structure of the photoanode, which is of top interest. Does the overlayer modify the valence band or/and change the band bending at the surface ? What is the mechanism responsible for the suppression of surface recombination ? The approach used in chapter 6, in particular the use of resonant photoemission spectroscopy, may provide new insights in this field.

The use of an internal field through ferroelectricity appears as a very promising degree of freedom to improve the performances of photoanodes. The first results obtained on $BaTiO_3$ (001) films deposited on Nb:$SrTiO_3$ (001), studied in chapter 7, are very encouraging. However some questions remain largely open: is the photocurrent improvement only related to an improved electron-hole separation, or also to more efficient surface kinetics ? What is the screening mechanism ? A first short-term work should be to confirm the results presented in this chapter on similar samples in order to tackle these challenging open questions and to improve and validate the developed poling and mounting methods.

Secondly, it may be interesting to focus on using metallic substrates instead of n-type semiconducting Nb:$SrTiO_3$ ones for the growth of $BaTiO_3$. Nb:$SrTiO_3$ is the substrate of choice to grow single crystalline $BaTiO_3$ films, however using metallic substrates would make possible the study of the properties of $BaTiO_3$ only, so that the system is much simpler than a semiconductor heterojunction. An on-going work on this matter in the group deals with the use of Pt (111) substrates. Besides, the use of different substrates orientations would also provide results about the influence of the crystallographic orientation of $BaTiO_3$, such as (001) or (111) directions, on the ferroelectricity (in particular the ferroelectric polarization orientation) and hence on the photoelectrochemical properties.

Moreover, it was demonstrated that domain walls in ferroelectrics have very interesting properties in the field of ferroelectric photovoltaics, such as photovoltages above the band gap and increased photoconductivity with respect to the inside of the domain [189]. In addition it was suggested by Frost et al. that the large carrier diffusion length in ferroelectric thin films originates from the existence of "ferroelectric highways", different for electrons and holes, favoured by ferroelectric domains walls [215]. Therefore, the investigation of the ferroelectric domain walls properties in our systems and especially their role in the water splitting performances appears particularly relevant.

Then, a route worthy to be explored is $BaTiO_3$ doping in order to reduce the band gap without destroying the ferroelectricity. As already mentioned in 7.1.2, Upadhyay et al. showed that a modest Fe doping level of 2 at.% reduces the band gap of $BaTiO_3$ down to 2.8 eV [192], and a recent work of our group demonstrated that ferroelectric properties are preserved upon Fe doping (up to 4 at.%) [216]. Our OPA-MBE apparatus allows the consideration of other metals like Ni, Al or Co, to see if a further lowering of the band gap can be achieved. This approach can be followed in the framework of using $BaTiO_3$ as a single photoanode material, or integrated as a photocurrent enhancer in a heterojunction with (Ti:)α-Fe_2O_3 or TiO_2.

Lastly, the future study of (Ti:)Fe_2O_3 / $BaTiO_3$ / Nb:$SrTiO_3$ samples will initiate the investigation of a new type of semiconductor heterojunctions where the ferroelectric polarization of $BaTiO_3$ will likely modify the electronic structure (and hence the charge dynamics) of Fe_2O_3. However, using poling procedures (PFM or electrochemical poling) on these heterojunctions opens new questions, *e.g.* the possibility of ions migration in the ferroelectric layer upon poling or the influence of interfaces. Such challenging emerging systems promise exciting new developments in the field of photoanodes for solar water splitting.

A Appendixes

A.1 Estimation of the Xe arc lamp flux

Acquisition of $J(\lambda)$ data for IPCE calculations made possible the estimation of the mean monochromator transmission between 200 and 1000 nm. Let us consider the following equations at a given applied potential:

$$\begin{cases} J_L^{WL} \times K_{200s} = \int \dfrac{J_L(\lambda)}{T_{mono}(\lambda)} d\lambda \\ \int P_{in}(\lambda) d\lambda = \int \dfrac{P_{out}(\lambda)}{T_{mono}(\lambda)} d\lambda \end{cases} \tag{A.1}$$

Where:

- J_L^{WL} is the current density in white light illumination conditions just after the potential application (in mA/cm^2), measured by the Power Suite software in $J(V)$ curves;
- $J_L(\lambda)$ is the current density (in mA/cm^2) measured in monochromatic light illumination conditions detailed in subsection 3.4.3;
- K_{200s} is the current damping factor after 200 s of voltage application (in %), supposed independent of the wavelength;
- $P_{in}(\lambda)$ (resp. $P_{out}(\lambda)$) is the light flux incoming (resp. outcoming) in (resp. from) the monochromator (in mW/cm^2);
- $T_{mono}(\lambda)$ is the λ-dependent transmission of the monochromator (in %).

The first equation is valid if the lamp outgoing flux or the photocurrent is negligible for wavelengths outside the [200 ; 1000] nm range. Therefore, we performed on a 50 nm thick 2 at.% Ti:α-Fe_2O_3 / Pt (111) sample the following measurements:

- measurement of the J_L^{WL} *vs.* time curves in white light illumination conditions, at an applied bias of 0.6V *vs.* Ag/AgCl (equivalent to the curve on figure 3.25), using a home-made LabView program. We can then estimate the K_{200s} value around 57% for the used sample.
- measurement of the $J_L(\lambda)$ curve (by applying the potential 200 s prior measurement);
- calculus of the overall current in monochromatic light using $J_L^{\lambda} = \int J_L(\lambda) d\lambda$;
- measurement of the light flux coming out of the monochromator $P_{out}(\lambda)$ using the power meter;

– calculus of the overall light flux coming out of the monochromator using $P_{out} = \int P_{out}(\lambda)d\lambda$.

If we suppose that $T_{mono}(\lambda)$ is independent on λ, equation A.1 becomes:

$$\begin{cases} 57\% \times J_L^{WL} = \dfrac{J_L^{\lambda}}{T_{mono}} \\ P_{in} = \dfrac{P_{out}}{T_{mono}} \end{cases} \tag{A.2}$$

Where P_{in} is the overall light flux entering the monochromator. Therefore T_{mono} is estimated to 53%. This is in agreement with transmission curves provided by Newport in the user manual of Cornerstone 130 monochromators [217].

Using our power meter, we measured a value of the mean monochromatic flux outgoing from the monochromator $P_{out} = 55$ mW/cm^2 (between 200 and 1000 nm). Considering the overall transmission of *ca.* 53%, we can estimate that it corresponds to a white light flux incoming on the monochromator $P_{in} = 104$ mW/cm^2 ($\pm$ 5%).

A.2 More details about the functioning of a potentiostat

A simplified electrical scheme of how a potentiostat works is depicted on figure A.1 [218]. It features the following mandatory modules:

- a control amplifier to allow the stability and application of the desired potential;
- an electrometer to measure the applied potential;
- a current/voltage converter to measure the current flowing between the working and counter electrodes.

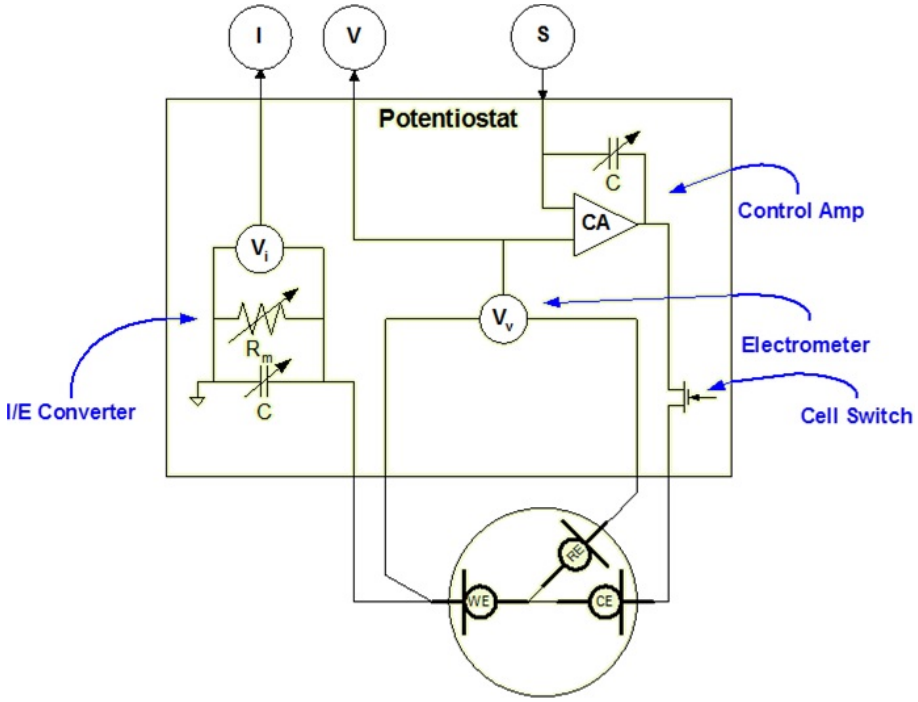

Figure A.1: Simplified electrical scheme of a potentiostat [218].

The working principle of a potentiostat is often explained alternatively using the following definition. When one desires to apply (or measure) a potential on the working electrode (with respect to the reference electrode), it may result in a current flow between the working and reference electrodes, yet if a current flows through the reference electrode, its potential will vary and it will lose its absolute reference status. To overcome this issue, a third electrode (the counter electrode) is introduced. The potentiostat then imposes a current flow between the working and counter electrode to "counter" the current flow in the reference electrode[33] and then suppresses the potential/current interdependency. The resulting measure is the same.

[33] http://www.customsensorsolutions.com/ap-pstat.html

A.3 γ*-Fe_2O_3 photocurrent contribution in γ*-Fe_2O_3 / Nb:$SrTiO_3$

To extract the photocurrent contribution specific to the γ*-Fe_2O_3 layer in the 15 nm γ*-Fe_2O_3 / Nb:$SrTiO_3$ sample (*cf.* subsection 4.1.5), we used the fact that γ*-Fe_2O_3 is expected to have a lower band gap than Nb:$SrTiO_3$, so that the signal specific to γ*-Fe_2O_3 can be extracted from monochromatic photocurrent measurements. On the one hand, in 4.1.3 we observed in XPS that γ*-Fe_2O_3 and α-Fe_2O_3 have the same band gap. Its value was calculated around 2.07 eV in the case of α-Fe_2O_3 (*cf.* IPCE measurements in 5.1.6.b). On the other hand, the band gap of Nb:$SrTiO_3$ is expected to be around 3.4 eV [45, 46].

Figure A.2 shows the monochromatic photocurrent data obtained with the OCLIA method ($J_{ph}^{OCLIA}(\lambda)$) at potentials ranging from -0.2V to +0.8V *vs.* Ag/AgCl for a Nb:$SrTiO_3$ (001) single crystal, 15 nm γ*-Fe_2O_3 / Nb:$SrTiO_3$ and 15 nm α-Fe_2O_3 / Pt (111) samples[34]. The results are represented as maps where the X, Y and Z axis represent respectively the wavelength (in nm), the applied potential (in V *vs.* Ag/AgCl) and the photocurrent (in µA/cm²) obtained with the OCLIA method ($J_{ph}^{OCLIA}(\lambda, V)$ maps). On figure A.2.a it is observed that the $J_{ph}^{OCLIA}(\lambda)$ cut-off for the Nb:$SrTiO_3$ single crystals is at 380 nm, which corresponds to a band gap of 3.26 eV. Also a substantial photocurrent signal is measured around 600 nm. The origin of this peak around 600 nm is not completely understood yet. No photocurrent is measured between 380 nm and 510 nm (range between the two grey dashed lines). However from figure A.2.b one can see that between 380 nm and 510 nm, a photocurrent signal is measured for the 15 nm γ*-Fe_2O_3 / Nb:$SrTiO_3$ sample. This signal necessarily originates from the γ*-Fe_2O_3 layer only.

The overall value of the photocurrent contribution specific to γ*-Fe_2O_3 can be measured by integrating the signal between 380 nm and 510 nm, noted $J_{ph,380-510}^{OCLIA}(V)$. To evaluate the overall value of the photocurrent specific to γ*-Fe_2O_3 between 200 nm and 1000 nm, noted $J_{ph,200-1000}^{OCLIA}(V)$, we assumed that the photocurrent wavelength dependence is the same for γ*-Fe_2O_3 and α-Fe_2O_3 (*i.e.* the absorption coefficients are the same). Therefore we used the $J_{ph}^{OCLIA}(\lambda)$ data of a 15 nm α-Fe_2O_3 / Pt (111) sample (shown on figure A.2.c) to calculate at each applied potential $J_{ph,200-1000}^{OCLIA}(V)$ for γ*-Fe_2O_3 using:

$$\frac{J_{ph,200-1000}^{OCLIA}(V)}{J_{ph,380-510}^{OCLIA}(V)}(\gamma * -Fe_2O_3) = \frac{J_{ph,200-1000}^{OCLIA}(V)}{J_{ph,380-510}^{OCLIA}(V)}(\alpha - Fe_2O_3) \tag{A.3}$$

[34] As it is detailed in 3.4.4 and 5.1.6.b, the OCLIA method is necessary to measure the monochromatic photocurrent of our pure hematite samples .

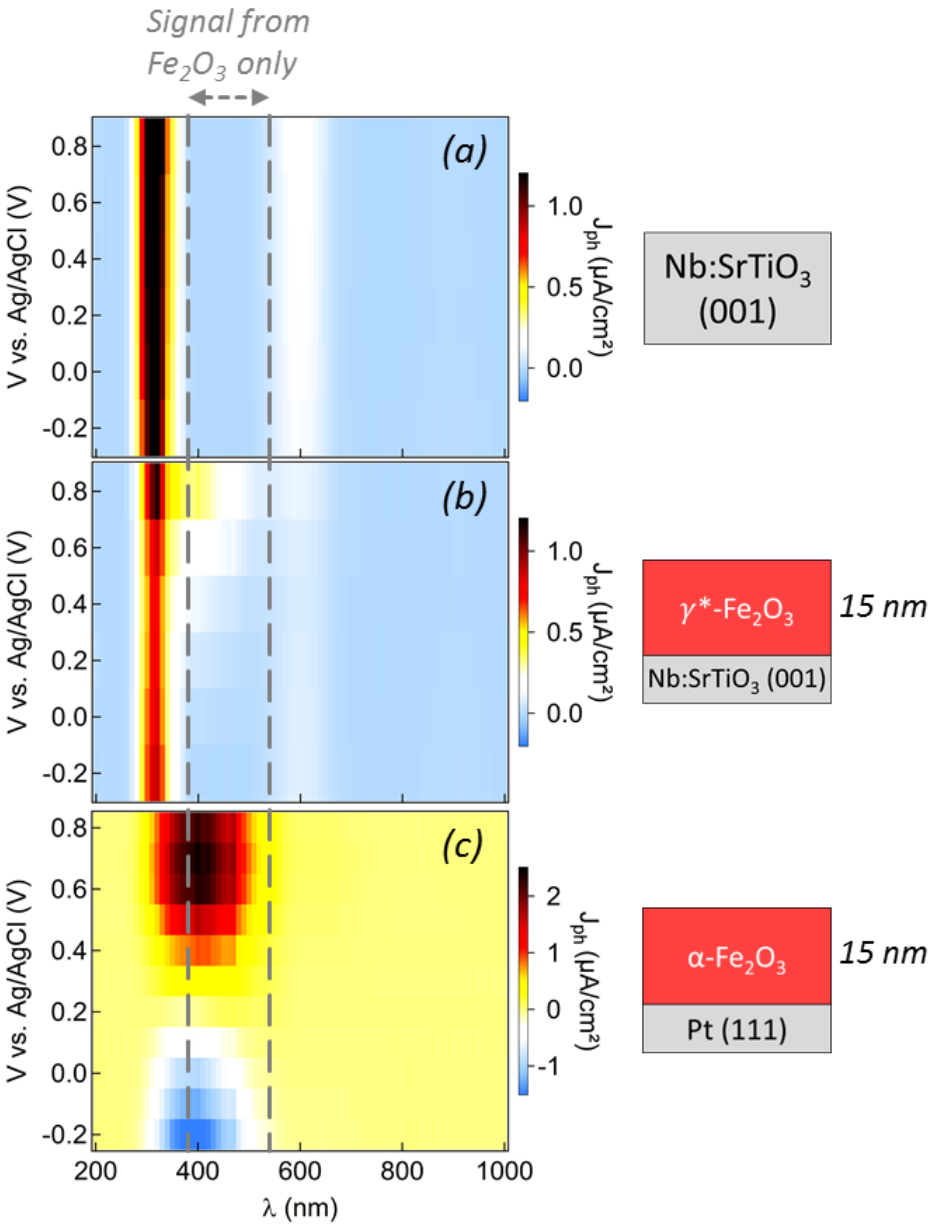

Figure A.2: Monochromatic photocurrent maps obtained with the OCLIA method for (a) Nb:$SrTiO_3$ (001) single crystal, (b) 15 nm γ*-Fe_2O_3 / Nb:$SrTiO_3$ and (c) 15 nm α-Fe_2O_3 / Pt (111) samples. Grey dashed lines highlight the wavelength range for which only Fe_2O_3 participates to the photocurrent for the 15 nm γ*-Fe_2O_3 / Nb:$SrTiO_3$ sample.

Afterwards, we assumed that the voltage-dependent recombination rate is the same for γ*-Fe_2O_3 and α-Fe_2O_3 (*i.e.* the differences between the steady and OCLIA photocurrents are the same). Therefore we can calculate the photocurrent in steady white light at a given applied potential V (noted $J_{ph,WL}^{steady}(V)$) for γ*-Fe_2O_3 using the following equation:

$$\frac{J_{ph,WL}^{steady}(V)}{J_{ph,200-1000}^{OCLIA}(V)}(\gamma* - Fe_2O_3) = \frac{J_{ph,WL}^{steady}(V)}{J_{ph,200-1000}^{OCLIA}(V)}(\alpha - Fe_2O_3) \tag{A.4}$$

In addition this method does not take into account the existence of a semiconductor junction at the interface between the γ^*-Fe_2O_3 and the Nb:$SrTiO_3$ substrate which could be detrimental or beneficial for the transfer of electrons from the γ^*-Fe_2O_3 to the substrate and then to the external circuit.

The evaluated photocurrent in steady white light as a function of the applied potential is plotted on figure 4.8.

References

[1] P. C. K. Vesborg and T. F. Jaramillo, RSC Advances **2**, 7933 (2012).

[2] A. Cho, Science **329**, 786 (2010).

[3] Editorial, Nature **454**, 805 (2008).

[4] T. Abbasi and S. A. Abbasi, Renewable and Sustainable Energy Reviews **15**, 3034 (2011).

[5] R. van de Krol, Y. Liang, and J. Schoonman, Journal of Materials Chemistry **18**, 2311 (2008).

[6] F. Le Formal, *On the Morphology and Interfaces of Nanostructured Hematite Photoanodes for Solar-Driven Water Splitting*, Ph.D. thesis, Ecole Polytechnique Fédérale de Lausanne, Switzerland (2011).

[7] T. J. Jacobsson, V. Fjällström, M. Edoff, and T. Edvinsson, Energy & Environmental Science **7**, 2056 (2014).

[8] A. Duret, *Mesoscopic thin films of hematite as photoanode for water photoelectrolysis*, Ph.D. thesis, Ecole Polytechnique Fédérale de Lausanne, Switzerland (2005).

[9] B. A. Pinaud, J. D. Benck, L. C. Seitz, A. J. Forman, Z. Chen, T. G. Deutsch, B. D. James, K. N. Baum, G. N. Baum, S. Ardo, H. Wang, E. Miller, and T. F. Jaramillo, Energy & Environmental Science **6**, 1983 (2013).

[10] K. Sivula, The Journal of Physical Chemistry Letters **6**, 975 (2015).

[11] K. Sivula, Chimia **67**, 155 (2013).

[12] A. J. Bard, G. M. Whitesides, R. N. Zare, and F. W. McLafferty, Accounts of Chemical Research **28**, 91 (1995).

[13] A. J. Bard and M. A. Fox, Accounts of Chemical Research **28**, 141 (1995).

[14] M. Grätzel, Nature **414**, 338 (2001).

[15] A. Fujishima and K. Honda, Nature **238**, 37 (1972).

[16] Z. Chen, T. F. Jaramillo, T. G. Deutsch, A. Kleiman-Shwarsctein, A. J. Forman, N. Gaillard, R. Garland, K. Takanabe, C. Heske, M. Sunkara, E. W. McFarland, K. Domen, E. L. Miller, J. A. Turner, and H. N. Dinh, Journal of Materials Research **25**, 3 (2010).

[17] S. Protti, A. Albini, and N. Serpone, Physical Chemistry Chemical Physics **16**, 19790 (2014).

[18] T. Hisatomi, H. Dotan, M. Stefik, K. Sivula, A. Rothschild, M. Grätzel, and N. Mathews, Advanced Materials **24**, 2699 (2012).

[19] K. Maeda, K. Teramura, D. Lu, T. Takata, N. Saito, Y. Inoue, and K. Domen, Nature **440**, 295 (2006).

[20] R. Van Noorden, "Secrets of artificial leaf revealed," (2011).

[21] S. Y. Reece, J. A. Hamel, K. Sung, T. D. Jarvi, A. J. Esswein, J. J. H. Pijpers, and D. G. Nocera, Science **334**, 645 (2011).

[22] J. W. Phair and S. P. S. Badwal, Science and Technology of Advanced Materials **7**, 792 (2006).

[23] J. W. Ager, M. R. Shaner, K. A. Walczak, I. D. Sharp, and S. Ardo, Energy & Environmental Science **8**, 2811 (2015).

[24] J. Luo, J.-H. Im, M. T. Mayer, M. Schreier, M. K. Nazeeruddin, N.-G. Park, S. D. Tilley, H. J. Fan, and M. Grätzel, Science **345**, 1593 (2014).

[25] B. Scrosati, Pure and Applied Chemistry **59**, 1173 (1987).

[26] Y. Xu and M. A. A. Schoonen, American Mineralogist **85**, 543 (2000).

[27] C. A. Koval and J. N. Howard, Chemical Reviews **92**, 411 (1992).

[28] S. M. Sze and K. K. Ng, "Physics and properties of semiconductors - a review," in *Physics of Semiconductor Devices* (John Wiley & Sons, Inc., 2006).

[29] M. G. Walter, E. L. Warren, J. R. McKone, S. W. Boettcher, Q. Mi, E. A. Santori, and N. S. Lewis, Chemical Reviews **110**, 6446 (2010).

[30] K. Gelderman, L. Lee, and S. W. Donne, Journal of Chemical Education **84**, 685 (2007).

[31] Z. Zhang and J. T. Yates Jr., Chemical Reviews **112**, 5520 (2012).

[32] K. Sivula, F. Le Formal, and M. Grätzel, ChemSusChem **4**, 432 (2011).

[33] O. Khaselev and J. A. Turner, Science **280**, 425 (1998).

[34] Z. Li, W. Luo, M. Zhang, J. Feng, and Z. Zou, Energy & Environmental Science **6**, 347 (2013).

[35] L. M. Peter, K. G. U. Wijayantha, and A. A. Tahir, Faraday Discussions **155**, 309 (2012).

[36] S. Cho, J.-W. Jang, K.-H. Lee, and J. S. Lee, APL Materials **2**, 010703 (2014).

[37] L. Kavan, M. Grätzel, S. E. Gilbert, C. Klemenz, and H. J. Scheel, Journal of The American Chemical Society **118**, 6716 (1996).

[38] M. Radecka, M. Rekas, A. Trenczek-Zajac, and K. Zakrzewska, Journal of Power Sources **181**, 46 (2008).

[39] M. J. Katz, S. C. Riha, N. C. Jeong, A. B. F. Martinson, O. K. Farha, and J. T. Hupp, Coordination Chemistry Reviews **256**, 2521 (2012).

[40] X. Liu, F. Wang, and Q. Wang, Physical Chemistry Chemical Physics **14**, 7894 (2012).

[41] G. Li, T. Varga, P. Yan, Z. Wang, C. Wang, S. A. Chambers, and Y. Du, Physical Chemistry Chemical Physics **17**, 15119 (2015).

[42] Q. Jia, K. Iwashina, and A. Kudo, PNAS **109**, 11564 (2012).

[43] F. F. Abdi, N. Firet, and R. van de Krol, ChemCatChem **5**, 490 (2013).

[44] J. G. Mavroides, J. A. Kafalas, and D. F. Kolesar, Applied Physics Letters **28**, 241 (1976).

[45] J. Yin, J. Ye, and Z. Zou, Applied Physics Letters **85**, 689 (2004).

[46] A. N. Pinheiro, E. G. S. Firmiano, A. C. Rabelo, C. J. Dalmaschio, and E. R. Leite, RSC Advances **4**, 2029 (2014).

[47] J. Hou, Z. Wang, C. Yang, H. Cheng, S. Jiao, and H. Zhu, Energy & Environmental Science **6**, 3322 (2013).

[48] J. Hou, H.-J. Cheng, O. Takeda, and H. Zhu, Energy & Environmental Science **8**, 1348 (2015).

[49] K. Srinivasu, B. Modak, and S. K. Ghosh, The Journal of Physical Chemistry C **118**, 26479 (2014).

[50] B. Zhao, T. C. Kaspar, T. C. Droubay, J. McCloy, M. E. Bowden, V. Shutthanandan, S. M. Heald, and S. A. Chambers, Physical Review B **84**, 245325 (2011).

[51] J. A. Glasscock, P. R. F. Barnes, I. C. Plumb, and N. Savvides, The Journal of Physical Chemistry C **111**, 16477 (2007).

[52] H. Tang, M. A. Matin, H. Wang, T. Deutsch, M. Al-Jassim, J. Turner, and Y. Yan, Journal of Applied Physics **110**, 123511 (2011).

[53] H. Magnan, D. Stanescu, M. Rioult, E. Fonda, and A. Barbier, Applied Physics Letters **101**, 133908 (2012).

[54] H. Tang, W.-J. Yin, M. A. Matin, H. Wang, T. Deutsch, M. M. Al-Jassim, J. A. Turner, and Y. Yan, Journal of Applied Physics **111**, 073502 (2012).

[55] M. Rioult, H. Magnan, D. Stanescu, and A. Barbier, The Journal of Physical Chemistry C **118**, 3007 (2014).

[56] O. Zandi, B. M. Klahr, and T. W. Hamann, Energy & Environmental Science **6**, 634 (2013).

[57] C. Miao, T. Shi, G. Xu, S. Ji, and C. Ye, ACS Applied Materials & Interfaces **5**, 1310 (2013).

[58] J. Deng, J. Zhong, A. Pu, D. Zhang, M. Li, X. Sun, and S.-T. Lee, Journal of Applied Physics **112**, 084312 (2012).

[59] M. Zhang, W. Luo, Z. Li, T. Yu, and Z. Zou, Applied Physics Letters **97**, 042105 (2010).

[60] N. T. Hahn and C. B. Mullins, Chemistry of Materials **22**, 6474 (2010).

[61] V. M. Aroutiounian, V. M. Arakelyan, G. E. Shahnazaryan, H. R. Hovhannisyan, H. Wang, and J. A. Turner, Solar Energy **81**, 1369 (2007).

[62] S. S. Shinde, R. A. Bansode, C. H. Bhosale, and K. Y. Rajpure, Journal of Semiconductors **32**, 013001 (2011).

[63] V. R. Satsangi, S. Kumari, A. P. Singh, R. Shrivastav, and S. Dass, International Journal of Hydrogen Energy **33**, 312 (2008).

[64] A. Kleiman-Shwarsctein, Y.-S. Hu, A. J. Forman, G. D. Stucky, and E. W. McFarland, The Journal of Physical Chemistry C **112**, 15900 (2008).

[65] Y. Lin, Y. Xu, M. T. Mayer, Z. I. Simpson, G. McMahon, S. Zhou, and D. Wang, Journal of the American Chemical Society **134**, 5508 (2012).

[66] Gurudayal, D. Sabba, M. H. Kumar, L. H. Wong, J. Barber, M. Grätzel, and N. Mathews, Nano Letters **15**, 3833 (2015).

[67] Y. Liu, Y.-X. Yu, and W.-D. Zhang, Electrochimica Acta **59**, 121 (2012).

[68] Y.-S. Hu, A. Kleiman-Shwarsctein, A. J. Forman, D. Hazen, J.-N. Park, and E. W. McFarland, Chemistry of Materials **20**, 3803 (2008).

[69] J. Y. Kim, G. Magesh, D. H. Youn, J.-W. Jang, J. Kubota, K. Domen, and J. S. Lee, Scientific Reports **3**, 2681 (2013).

[70] I. Cesar, K. Sivula, A. Kay, R. Zboril, and M. Grätzel, The Journal of Physical Chemistry C **113**, 772 (2009).

[71] A. Bak, W. Choi, and H. Park, Applied Catalysis B: Environmental **110**, 207 (2011).

[72] Y. Ling, G. Wang, J. Reddy, C. Wang, J. Z. Zhang, and Y. Li, Angewandte Chemie **124**, 4150 (2012).

[73] T.-Y. Yang, H.-Y. Kang, U. Sim, Y.-J. Lee, J.-H. Lee, B. Koo, K. T. Nam, and Y.-C. Joo, Physical Chemistry Chemical Physics **15**, 2117 (2013).

[74] R. F. G. Gardner, F. Sweett, and D. W. Tanner, Journal of Physics and Chemistry of Solids **24**, 1183 (1963).

[75] P. Merchant, R. Collins, R. Kershaw, K. Dwight, and A. Wold, Journal of Solid State Chemistry **27**, 307 (1979).

[76] G. Wang, Y. Ling, and Y. Li, Nanoscale **4**, 6682 (2012).

[77] J. H. W. de Wit, A. F. Broersma, and M. Stroband, Journal of Solid State Chemistry **37**, 242 (1981).

[78] H.-P. Wang, K. Sun, S. Y. Noh, A. Kargar, M.-L. Tsai, M.-Y. Huang, D. Wang, and J.-H. He, Nano Letters **15**, 2817 (2015).

[79] K.-S. Ahn, Y. Yan, M.-S. Kang, J. Y. Kim, S. Shet, H. Wang, J. Turner, and M. Al-Jassim, Applied Physics Letters **95**, 022116 (2009).

[80] M. G. Ahmed, T. A. Kandiel, A. Y. Ahmed, I. Kretschmer, F. Rashwan, and D. Bahnemann, The Journal of Physical Chemistry C **119**, 5864 (2015).

[81] E. S. Kim, H. J. Kang, G. Magesh, J. Y. Kim, J.-W. Jang, and J. S. Lee, ACS Applied Materials & Interfaces **6**, 17762 (2014).

[82] E. S. Kim, N. Nishimura, G. Magesh, J. Y. Kim, J.-W. Jang, H. Jun, J. Kubota, K. Domen, and J. S. Lee, Journal of the American Chemical Society **135**, 5375 (2013).

[83] S. J. Hong, S. Lee, J. S. Jang, and J. S. Lee, Energy & Environmental Science **4**, 1781 (2011).

[84] A. Mao, J. K. Kim, K. Shin, D. H. Wang, P. J. Yoo, G. Y. Han, and J. H. Park, Journal of Power Sources **210**, 32 (2012).

[85] S. Kuang, L. Yang, S. Luo, and Q. Cai, Applied Surface Science **255**, 7385 (2009).

[86] L. Peng, T. Xie, Y. Lu, H. Fan, and D. Wang, Physical Chemistry Chemical Physics **12**, 8033 (2010).

[87] F.-T. Liou, C. Y. Yang, and S. N. Levine, Journal of The Electrochemical Society **129**, 342 (1982).

[88] H.-J. Oh, K.-J. Noh, B.-R. Kim, W. Kang, S.-C. Jung, and S.-J. Kim, Japanese Journal of Applied Physics **52**, 01AC15 (2013).

[89] H. Zhao, W. Fu, H. Yang, Y. Xu, W. Zhao, Y. Zhang, H. Chen, Q. Jing, X. Qi, J. Cao, X. Zhou, and Y. Li, Applied Surface Science **257**, 8778 (2011).

[90] M. Wang, M. Pyeon, Y. Gönüllü, A. Kaouk, S. Shen, L. Guo, and S. Mathur, Nanoscale **7**, 10094 (2015).

[91] IEEE, ANSI/IEEE Std 180-1986 , 1 (1986).

[92] Y. Yuan, Z. Xiao, B. Yang, and J. Huang, Journal of Materials Chemistry A **2**, 6027 (2014).

[93] D. Tiwari and S. Dunn, Journal of Materials Science **44**, 5063 (2009).

[94] C. R. Bowen, H. A. Kim, P. M. Weaver, and S. Dunn, Energy & Environmental Science **7**, 25 (2014).

[95] W. Ji, K. Yao, Y.-F. Lim, Y. C. Liang, and A. Suwardi, Applied Physics Letters **103**, 062901 (2013).

[96] A. Kay, I. Cesar, and M. Grätzel, Journal of the American Chemical Society **128**, 15714 (2006).

[97] C. Y. Cummings, F. Marken, L. M. Peter, K. G. U. Wijayantha, and A. A. Tahir, Journal of the American Chemical Society **134**, 1228 (2012).

[98] H. Jun, B. Im, J. Y. Kim, Y.-O. Im, J.-W. Jang, E. S. Kim, J. Y. Kim, H. J. Kang, S. J. Hong, and J. S. Lee, Energy & Environmental Science **5**, 6375 (2012).

[99] M. Rioult, S. Datta, D. Stanescu, S. Stanescu, R. Belkhou, F. Maccherozzi, H. Magnan, and A. Barbier, Applied Physics Letters **107**, 103901 (2015).

[100] M. Rioult, R. Belkhou, H. Magnan, D. Stanescu, S. Stanescu, F. Maccherozzi, C. Rountree, and A. Barbier, Surface Science **641**, 310 (2015).

[101] B. D. Chernomordik, H. B. Russell, U. Cvelbar, J. B. Jasinski, V. Kumar, T. Deutsch, and M. K. Sunkara, Nanotechnology **23**, 194009 (2012).

[102] H. Wang and J. A. Turner, Journal of The Electrochemical Society **157**, F173 (2010).

[103] V. A. N. de Carvalho, R. A. de S. Luz, B. H. Lima, F. N. Crespilho, E. R. Leite, and F. L. Souza, Journal of Power Sources **205**, 525 (2012).

[104] A. Boudjemaa, S. Boumaza, R. Bouarab, and A. Bouguelia, International Journal of Hydrogen Energy **34**, 4268 (2009).

[105] A. A. Tahir, K. G. U. Wijayantha, S. Saremi-Yarahmadi, M. Mazhar, and V. McKee, Chemistry of Materials **21**, 3763 (2009).

[106] P.-S. Li and H. Teng, Journal of the Chinese Institute of Chemical Engineers **38**, 267 (2007).

[107] P. Hiralal, S. Saremi-Yarahmadi, B. C. Bayer, H. Wang, S. Hofmann, K. G. U. Wijayantha, and G. A. J. Amaratunga, Solar Energy Materials and Solar Cells **95**, 1819 (2011).

[108] L. Steier, I. Herraiz-Cardona, S. Gimenez, F. Fabregat-Santiago, J. Bisquert, S. D. Tilley, and M. Grätzel, Advanced Functional Materials **24**, 7681 (2014).

[109] T. Hisatomi, J. Brillet, M. Cornuz, F. Le Formal, N. Tétreault, K. Sivula, and M. Grätzel, Faraday Discussions **155**, 223 (2012).

[110] J. Cao, Y. Zhang, H. Tong, P. Li, T. Kako, and J. Ye, Chemical Communications **48**, 8649 (2012).

[111] Y. J. Hwang, A. Boukai, and P. Yang, Nano Letters **9**, 410 (2009).

[112] A. Kargar, K. Sun, Y. Jing, C. Choi, H. Jeong, G. Y. Jung, S. Jin, and D. Wang, ACS Nano **7**, 9407 (2013).

[113] M. T. Mayer, C. Du, and D. Wang, Journal of the American Chemical Society **134**, 12406 (2012).

[114] X. Wang, K.-Q. Peng, Y. Hu, F.-Q. Zhang, B. Hu, L. Li, M. Wang, X.-M. Meng, and S.-T. Lee, Nano Letters **14**, 18 (2014).

[115] J.-W. Jang, C. Du, Y. Ye, Y. Lin, X. Yao, J. Thorne, E. Liu, G. McMahon, J. Zhu, A. Javey, J. Guo, and D. Wang, Nature Communications **6**, 7447 (2015).

[116] M. A. Holmes, T. K. Townsend, and F. E. Osterloh, Chemical Communications **48**, 371 (2012).

[117] E. Thimsen, F. Le Formal, M. Grätzel, and S. C. Warren, Nano Letters **11**, 35 (2011).

[118] I. Thomann, B. A. Pinaud, Z. Chen, B. M. Clemens, T. F. Jaramillo, and M. L. Brongersma, Nano Letters **11**, 3440 (2011).

[119] K. Sivula, The Journal of Physical Chemistry Letters **4**, 1624 (2013).

[120] S. D. Tilley, M. Cornuz, K. Sivula, and M. Grätzel, Angewandte Chemie International Edition **49**, 6405 (2010).

[121] L. Badia-Bou, E. Mas-Marza, P. Rodenas, E. M. Barea, F. Fabregat-Santiago, S. Gimenez, E. Peris, and J. Bisquert, The Journal of Physical Chemistry C **117**, 3826 (2013).

[122] S. C. Riha, B. M. Klahr, E. C. Tyo, S. Seifert, S. Vajda, M. J. Pellin, T. W. Hamann, and A. B. F. Martinson, ACS Nano **7**, 2396 (2013).

[123] C. Du, X. Yang, M. T. Mayer, H. Hoyt, J. Xie, G. McMahon, G. Bischoping, and D. Wang, Angewandte Chemie International Edition **52**, 12692 (2013).

[124] C. C. L. McCrory, S. Jung, J. C. Peters, and T. F. Jaramillo, Journal of the American Chemical Society **135**, 16977 (2013).

[125] B. Klahr, S. Gimenez, F. Fabregat-Santiago, J. Bisquert, and T. W. Hamann, Journal of the American Chemical Society **134**, 16693 (2012).

[126] X. Sala, I. Romero, M. Rodríguez, L. Escriche, and A. Llobet, Angewandte Chemie International Edition **48**, 2842 (2009).

[127] R. Liu, Z. Zheng, J. Spurgeon, and X. Yang, Energy & Environmental Science **7**, 2504 (2014).

[128] F. Le Formal, K. Sivula, and M. Grätzel, The Journal of Physical Chemistry C **116**, 26707 (2012).

[129] F. Le Formal, N. Tétreault, M. Cornuz, T. Moehl, M. Grätzel, and K. Sivula, Chemical Science **2**, 737 (2011).

[130] T. Hisatomi, F. Le Formal, M. Cornuz, J. Brillet, N. Tétreault, K. Sivula, and M. Grätzel, Energy & Environmental Science **4**, 2512 (2011).

[131] X. Yang, R. Liu, C. Du, P. Dai, Z. Zheng, and D. Wang, ACS Applied Materials & Interfaces **6**, 12005 (2014).

[132] A. Barbier, R. Belkhou, P. Ohresser, M. Gautier-Soyer, O. Bezencenet, M. Mulazzi, M.-J. Guittet, and J.-B. Moussy, Physical Review B **72**, 245423 (2005).

[133] O. Bezencenet, *Propriétés et couplage d'échange dans le système modèle : Co / alpha-Fe_2O_3*, Ph.D. thesis, Université Pierre et Marie Curie, Paris, France (2008).

[134] S. Gota, E. Guiot, M. Henriot, and M. Gautier-Soyer, Physical Review B **60**, 14387 (1999).

[135] J. Rault, *Structure chimique et électronique des interfaces métal / ferroélectrique en fonction de la polarisation ferroélectrique*, Ph.D. thesis, Université Pierre et Marie Curie, Paris, France (2013).

[136] E. Soergel, Journal of Physics D: Applied Physics **44**, 464003 (2011).

[137] J. Stöhr, in *X-Ray Absorption: Principles, Applications, Techniques of EXAFS, SEXAFS and XANES*, edited by D. C. Koningsberger and R. Prins (Wiley, New York, 1987) Chap. SEXAFS: everything you always wanted to know about SEXAFS but were afraid to ask, pp. 443–571.

[138] F. Jiménez-Villacorta, C. Prieto, Y. Huttel, N. D. Telling, and G. van der Laan, Physical Review B **84**, 172404 (2011).

[139] H. Magnan, *Etude par EXAFS de l'ordre local dans des films minces métastables de fer et de cobalt*, Ph.D. thesis, Université de Paris-Sud, Orsay, France (1990).

[140] A. L. Ankudinov, B. Ravel, J. J. Rehr, and S. D. Conradson, Physical Review B **58**, 7565 (1998).

[141] B. Ravel and M. Newville, Journal of Synchrotron Radiation **12**, 537 (2005).

[142] M. Newville, Journal of Synchrotron Radiation **8**, 322 (2001).

[143] H. Magnan, P. Le Fèvre, D. Chandesris, P. Krüger, S. Bourgeois, B. Domenichini, A. Verdini, L. Floreano, and A. Morgante, Physical Review B **81**, 085121 (2010).

[144] K. L. Hardee and A. J. Bard, Journal of The Electrochemical Society **123**, 1024 (1976).

[145] M. P. Dare-Edwards, J. B. Goodenough, A. Hamnett, and P. R. Trevellick, Journal of the Chemical Society, Faraday Transactions 1: Physical Chemistry in Condensed Phases **79**, 2027 (1983).

[146] J. Lee and S. Han, Physical Chemistry Chemical Physics **15**, 18906 (2013).

[147] P. H. Borse, H. Jun, S. H. Choi, S. J. Hong, and J. S. Lee, Applied Physics Letters **93**, 173103 (2008).

[148] A. Pu, J. Deng, M. Li, J. Gao, H. Zhang, Y. Hao, J. Zhong, and X. Sun, Journal of Materials Chemistry A **2**, 2491 (2014).

[149] M. Li, J. Deng, A. Pu, P. Zhang, H. Zhang, J. Gao, Y. Hao, J. Zhong, and X. Sun, Journal of Materials Chemistry A **2**, 6727 (2014).

[150] J. Deng, X. Lv, J. Gao, A. Pu, M. Li, X. Sun, and J. Zhong, Energy & Environmental Science **6**, 1965 (2013).

[151] A. Bataille, *Etude des propriétés physiques des films de Fe_3O_4 épitaxiés et de la polarisation en spin à l'interface Fe_3O_4 / γ-Al_2O_3*, Ph.D. thesis, Université Paris-XI, Orsay, France (2005).

[152] E. Guiot, *Epitaxie assistée par plasma d'oxygène atomique de couches minces d'oxydes de fer sur α-Al_2O_3*, Ph.D. thesis, Université Paris VI, Paris, France (1998).

[153] R. Grau-Crespo, A. Y. Al-Baitai, I. Saadoune, and N. H. De Leeuw, Journal of Physics: Condensed Matter **22**, 225401 (2010).

[154] Z. Somogyváari, E. Sváb, G. Mészáros, K. Krezhov, I. Nedkov, I. Sajó, and F. Bourée, Applied Physics A **74**, s1077 (2002).

[155] M. Friák, A. Schindlmayr, and M. Scheffler, New Journal of Physics **9**, 5 (2007).

[156] A. Barbier, C. Mocuta, D. Stanescu, P. Jegou, N. Jedrecy, and H. Magnan, Journal of Applied Physics **112**, 114116 (2012).

[157] J. R. Smyth, S. D. Jacobsen, and R. M. Hazen, Reviews in Mineralogy and Geochemistry **41**, 157 (2000).

[158] J. A. Moyer, R. Gao, P. Schiffer, and L. W. Martin, Scientific Reports **5**, 10363 (2015).

[159] F. Bertram, C. Deiter, K. Pflaum, M. Suendorf, C. Otte, and J. Wollschläger, Journal of Applied Physics **110**, 102208 (2011).

[160] A. J. Berry, H. St.C. O'Neill, K. D. Jayasuriya, S. J. Campbell, and G. J. Foran, American Mineralogist **88**, 967 (2003).

[161] M. N. Huda, A. Walsh, Y. Yan, S.-H. Wei, and M. M. Al-Jassim, Journal of Applied Physics **107**, 123712 (2010).

[162] B. M. Klahr, A. B. F. Martinson, and T. W. Hamann, Langmuir **27**, 461 (2011).

[163] L. Xi, P. D. Tran, S. Y. Chiam, P. S. Bassi, W. F. Mak, H. K. Mulmudi, S. K. Batabyal, J. Barber, J. S. C. Loo, and L. H. Wong, The Journal of Physical Chemistry C **116**, 13884 (2012).

[164] J. Ziegler, D. Fertig, B. Kaiser, W. Jaegermann, M. Blug, S. Hoch, and J. Busse, Energy Procedia **22**, 108 (2012).

[165] A. M. Basilio, Y.-K. Hsu, W.-H. Tu, C.-H. Yen, G.-M. Hsu, O. Chyan, Y. Chyan, J.-S. Hwang, Y.-T. Chen, L.-C. Chen, and K.-H. Chen, Journal of Materials Chemistry **20**, 8118 (2010).

[166] T. Fujii, F. M. F. de Groot, G. A. Sawatzky, F. C. Voogt, T. Hibma, and K. Okada, Physical Review B **59**, 3195 (1999).

[167] Y. Gao and S. A. Chambers, Journal of Crystal Growth **174**, 446 (1997).

[168] J. F. Moulder, W. F. Stickle, P. E. Sobol, and K. D. Bomben, in *Handbook of X-Ray Photoelectron Spectroscopy* (Physical Electronics, 1995).

[169] T. Droubay, K. M. Rosso, S. M. Heald, D. E. McCready, C. M. Wang, and S. A. Chambers, Physical Review B **75**, 104412 (2007).

[170] P. Le Fèvre, J. Danger, H. Magnan, D. Chandesris, J. Jupille, S. Bourgeois, M.-A. Arrio, R. Gotter, A. Verdini, and A. Morgante, Physical Review B **69**, 155421 (2004).

[171] H. Dotan, O. Kfir, E. Sharlin, O. Blank, M. Gross, I. Dumchin, G. Ankonina, and A. Rothschild, Nature Materials **12**, 158 (2013).

[172] A. Barbier, O. Bezencenet, C. Mocuta, J.-B. Moussy, H. Magnan, N. Jedrecy, M.-J. Guittet, and M. Gautier-Soyer, Materials Science and Engineering: B **144**, 19 (2007).

[173] T. Droubay, G. Mursky, and B. P. Tonner, Journal of Electron Spectroscopy and Related Phenomena **84**, 159 (1997).

[174] W. Q. Fang, X.-Q. Gong, and H. G. Yang, The Journal of Physical Chemistry Letters **2**, 725 (2011).

[175] T. Nakau, Journal of the Physical Society of Japan **15**, 727 (1960).

[176] X. Y. Meng, G. W. Qin, S. Li, X. H. Wen, Y. P. Ren, W. L. Pei, and L. Zuo, Applied Physics Letters **98**, 112104 (2011).

[177] C. X. Kronawitter, L. Vayssieres, S. Shen, L. Guo, D. A. Wheeler, J. Z. Zhang, B. R. Antoun, and S. S. Mao, Energy & Environmental Science **4**, 3889 (2011).

[178] S. J. A. Moniz, S. A. Shevlin, D. J. Martin, Z.-X. Guo, and J. Tang, Energy & Environmental Science **8**, 731 (2015).

[179] S. Choudhary, S. Upadhyay, P. Kumar, N. Singh, V. R. Satsangi, R. Shrivastav, and S. Dass, International Journal of Hydrogen Energy **37**, 18713 (2012).

[180] S. De Wolf, A. Descoeudres, Z. C. Holman, and C. Ballif, Green **2**, 7 (2012).

[181] H. Cotal, C. Fetzer, J. Boisvert, G. Kinsey, R. King, P. Hebert, H. Yoon, and N. Karam, Energy & Environmental Science **2**, 174 (2009).

[182] L. Artiglia, A. Zana, G. A. Rizzi, S. Agnoli, F. Bondino, E. Magnano, E. Cavaliere, L. Gavioli, and G. Granozzi, The Journal of Physical Chemistry C **116**, 12532 (2012).

[183] U. Diebold and T. E. Madey, Surface Science Spectra **4**, 227 (1996).

[184] E. A. Kraut, R. W. Grant, J. R. Waldrop, and S. P. Kowalczyk, Physical Review Letters **44**, 1620 (1980).

[185] Q. Guo, K. Takahashi, K. Saito, H. Akiyama, T. Tanaka, and M. Nishio, Applied Physics Letters **102**, 092107 (2013).

[186] R. Laskowski and P. Blaha, Physical Review B **82**, 205104 (2010).

[187] Editorial, Nature Materials **13**, 837 (2014).

[188] K. J. Choi, M. Biegalski, Y. L. Li, A. Sharan, J. Schubert, R. Uecker, P. Reiche, Y. B. Chen, X. Q. Pan, V. Gopalan, L.-Q. Chen, D. G. Schlom, and C. B. Eom, Science **306**, 1005 (2004).

[189] S. Y. Yang, J. Seidel, S. J. Byrnes, P. Shafer, C.-H. Yang, M. D. Rossell, P. Yu, Y.-H. Chu, J. F. Scott, J. W. Ager III, L. W. Martin, and R. Ramesh, Nature Nanotechnology **5**, 143 (2010).

[190] I. Grinberg, D. V. West, M. Torres, G. Gou, D. M. Stein, L. Wu, G. Chen, E. M. Gallo, A. R. Akbashev, P. K. Davies, J. E. Spanier, and A. M. Rappe, Nature **503**, 509 (2013).

[191] A. Zenkevich, Yu. Matveyev, K. Maksimova, R. Gaynutdinov, A. Tolstikhina, and V. Fridkin, Physical Review B **90**, 161409 (2014).

[192] S. Upadhyay, J. Shrivastava, A. Solanki, S. Choudhary, V. Sharma, P. Kumar, N. Singh, V. R. Satsangi, R. Shrivastav, U. V. Waghmare, and S. Dass, The Journal of Physical Chemistry C **115**, 24373 (2011).

[193] Y. Cui, J. Briscoe, and S. Dunn, Chemistry of Materials **25**, 4215 (2013).

[194] J. L. Giocondi and G. S. Rohrer, Chemistry of Materials **13**, 241 (2001).

[195] J. L. Giocondi and G. S. Rohrer, The Journal of Physical Chemistry B **105**, 8275 (2001).

[196] S. V. Kalinin, D. A. Bonnell, T. Alvarez, X. Lei, Z. Hu, J. H. Ferris, Q. Zhang, and S. Dunn, Nano Letters **2**, 589 (2002).

[197] Y. Cui, S. M. Goldup, and S. Dunn, RSC Advances **5**, 30372 (2015).

[198] C. Hengky, X. Moya, N. D. Mathur, and S. Dunn, RSC Advances **2**, 11843 (2012).

[199] P. M. Jones and S. Dunn, Nanotechnology **18**, 185702 (2007).

[200] S. Dunn and D. Tiwari, Applied Physics Letters **93**, 092905 (2008).

[201] M. Stock and S. Dunn, The Journal of Physical Chemistry C **116**, 20854 (2012).

[202] A. L. Cabrera, F. Vargas, and J. C. Albers, Surface Science **336**, 280 (1995).

[203] N. V. Burbure, P. A. Salvador, and G. S. Rohrer, Journal of the American Ceramic Society **89**, 2943 (2006).

[204] Y. Inoue, K. Sato, and H. Miyama, The Journal of Physical Chemistry **90**, 2809 (1986).

[205] D. Cao, Z. Wang, Nasori, L. Wen, Y. Mi, and Y. Lei, Angewandte Chemie **126**, 11207 (2014).

[206] S. Park, C. W. Lee, M.-G. Kang, S. Kim, H. J. Kim, J. E. Kwon, S. Y. Park, C.-Y. Kang, K. S. Hong, and K. T. Nam, Physical Chemistry Chemical Physics **16**, 10408 (2014).

[207] M. Wegmann, L. Watson, and A. Hendry, Journal of the American Ceramic Society **87**, 371 (2004).

[208] Y. S. Kim, D. H. Kim, J. D. Kim, Y. J. Chang, T. W. Noh, J. H. Kong, K. Char, Y. D. Park, S. D. Bu, J.-G. Yoon, and J.-S. Chung, Applied Physics Letters **86**, 102907 (2005).

[209] J. Chen, Y. Luo, X. Ou, G. Yuan, Y. Wang, Y. Yang, J. Yin, and Z. Liu, Journal of Applied Physics **113**, 204105 (2013).

[210] Y. Luo, X. Li, L. Chang, W. Gao, G. Yuan, J. Yin, and Z. Liu, AIP Advances **3**, 122101 (2013).

[211] J. P. Clancy, N. Chen, C. Y. Kim, W. F. Chen, K. W. Plumb, B. C. Jeon, T. W. Noh, and Y.-J. Kim, Physical Review B **86**, 195131 (2012).

[212] S. Polisetty, J. Zhou, J. Karthik, A. R. Damodaran, D. Chen, A. Scholl, L. W. Martin, and M. Holcomb, Journal of Physics: Condensed Matter **24**, 245902 (2012).

[213] E. Arenholz, G. van der Laan, A. Fraile-Rodríguez, P. Yu, Q. He, and R. Ramesh, Physical Review B **82**, 140103 (2010).

[214] L. Li, P. A. Salvador, and G. S. Rohrer, Nanoscale **6**, 24 (2014).

[215] J. M. Frost, K. T. Butler, F. Brivio, C. H. Hendon, M. van Schilfgaarde, and A. Walsh, Nano Letters **14**, 2584 (2014).

[216] A. Barbier, T. Aghavnian, V. Badjeck, C. Mocuta, D. Stanescu, H. Magnan, C. L. Rountree, R. Belkhou, P. Ohresser, and N. Jedrecy, Physical Review B **91**, 035417 (2015).

[217] Newport Corporation, "Cornerstone 130 1/8m monochromator family," User's Manual (2015).

[218] Gamry Instruments, "Care and Feeding of Computer-controlled Potentiostats," Corrosion: Fundamentals and Experimental Methods (Fourteenth Annual Penn State Short Corrosion course) (2010).

Abstract

Using hydrogen as an energy carrier for solar energy storage and/or fuel alternative to oil is very appealing, especially as it can be cleanly produced by solar water splitting. In this process, electron-hole pairs, generated in illuminated semiconductors dipped in an aqueous solution, realize the water oxidoreduction reactions (oxygen production at the photoanode and hydrogen production at the photocathode). Transition metal oxides, in particular hematite (α-Fe_2O_3) which features a quasi ideal band-gap for this application, are the most promising photoanodes materials.

Hematite thin films were deposited on single crystals by oxygen plasma assisted molecular beam epitaxy. These model samples along with the use of high-end techniques, in particular using synchrotron radiation, make possible the identification of the relevant parameters affecting the photoelectrochemical properties. I firstly focused on the impact of the crystallographic structure, the stoichiometry and the surface morphology. Then the effects of doping with titanium were investigated, demonstrating the existence of an optimal doping level and an increase of the charges diffusion length inducing a high photocurrent gain. In addition, I studied the electronic structure and the surface recombinations dynamics of TiO_2 - Ti-doped hematite heterojunctions, revealing a diffuse interface. Lastly, the internal electric field created by a ferroelectric thin film of $BaTiO_3$/Nb:$SrTiO_3$ was considered in order to enhance the performances of photoanodes. A first step toward the comprehension of the link between ferroelectric polarization and photocurrent was achieved through the evidence of an internal electric field favourable for the separation of charges.

Keywords: *hematite, thin film, molecular beam epitaxy, solar water splitting, photoanode.*

Résumé

Utiliser l'hydrogène en tant que vecteur énergétique pour stocker l'énergie solaire et/ou remplacer le pétrole comme carburant est très attrayant, d'autant qu'il peut être produit de façon propre par photo-électrolyse de l'eau. Dans ce procédé, des paires électron-trou, générées par éclairement dans des semi-conducteurs immergés dans une solution aqueuse, réalisent les réactions d'oxydo-réduction de l'eau (production d'oxygène à la photo-anode et production d'hydrogène à la photo-cathode). Les oxydes de métaux de transition, en particulier l'hématite (α-Fe_2O_3) qui présente un gap quasi-idéal pour cette application, sont les matériaux de photo-anode les plus prometteurs.

Des films minces d'hématite ont été déposés sur des monocristaux par épitaxie par jets moléculaires assistée par plasma d'oxygène. Ces échantillons modèles ainsi que l'utilisation de techniques de pointe, notamment utilisant le rayonnement synchrotron, rendent possible l'identification des paramètres pertinents influençant les propriétés de photo-électrolyse. Je me suis d'abord intéressé à l'impact de la structure cristallographique, de la stœchiométrie et de la morphologie de surface. Ensuite, les effets d'un dopage avec du titane ont été analysés, montrant l'existence d'un taux de dopage optimal et l'augmentation de la longueur de diffusion des porteurs de charges induisant un fort gain en photo-courant. J'ai également étudié la structure électronique et la dynamique des recombinaisons en surface d'hétérojonctions TiO_2 - hématite dopée Ti, révélant une interface diffuse. Enfin, le champ électrique interne créé par un film mince ferroélectrique de $BaTiO_3$/Nb:$SrTiO_3$ a été considéré pour améliorer les propriétés des photo-anodes. Un premier pas vers la compréhension du lien entre polarisation ferroélectrique et photo-courant a été fait, mettant en évidence un champ électrique interne favorable pour séparer les charges.

Mots-clés: *hématite, film mince, épitaxie par jets moléculaires, photo-électrolyse de l'eau, photo-anode.*